

# Collective Electronic Excitations in Spectroscopy of Conjugated and Aggregated Molecules

by

**Sergei Tretiak**

Submitted in Partial Fulfillment

of the

Requirements for the Degree

Doctor of Philosophy

Supervised by

Professor **Shaul Mukamel**

Department of Chemistry

College of Arts and Science

University of Rochester

Rochester, New York

1998

# Curriculum Vitae

The author was born in Mariupol, Ukraine on November 2, 1968. He attended Moscow Institute of Physics and Technology from 1987 to 1994. He received the Bachelor of Science degree in 1992. In September 1994, he began graduate studies in physics under the supervision of Professor E. A. Ryabov at the Institute of Spectroscopy of Russian Academy of Sciences. He graduated with 'Red Diploma' (Diploma with Honor) and received the Master of Science degree in Physics in 1994. His master thesis is devoted to the Raman spectroscopy studying of ultrafast energy transfer in molecular gases.

He came to the University of Rochester in the fall 1994 for pursuing a Ph.D. degree. Stimulated by curiosity in Nonlinear Optical Spectroscopy, he began studies in Theoretical Chemical Physics under the direction of Professor Shaul Mukamel and received the Master of Science degree in Chemistry in 1996.

The author was the recipient of a Sherman Clarke Graduate Fellowship during the 1995-1996 school year, an Elon Huntington Hooker Graduate Fellowship during the 1996-1997 school year, an Arnold Weissberger Graduate Fellowship during the 1997-1998 school year, and received 1996 Graduate Student Award in Computational Chemistry supported by American Chemical Society Division of Physical Chemistry, the Subdivision of Theoretical Chemistry, IBM, and the Cornell Theory Center.

# List of Publications

1. S. Tretiak, V. Chernyak, and S. Mukamel, "Collective electronic oscillators for nonlinear optical response of conjugated molecules," *Chem. Phys. Lett.*, **259**, 55-61 (1996).
2. S. Tretiak, V. Chernyak, and S. Mukamel, "Chemical bonding and size scaling of nonlinear polarizabilities of conjugated polymers," *Phys. Rev. Lett.*, **77**, 4656-4660 (1996).
3. S. Tretiak, V. Chernyak, and S. Mukamel, "Recursive density-matrix-spectral-moment algorithm for molecular nonlinear polarizabilities," *J. Chem. Phys.*, **105**, 8914-8928 (1996).
4. T. Meier, S. Tretiak, V. Chernyak, and S. Mukamel, "Electronic-oscillator analysis of femtosecond four-wave mixing in conjugated polyenes," *Phys. Rev. B*, **55**, 4960-4978 (1997).
5. S. Mukamel, S. Tretiak, Th. Wagersreiter, and V. Chernyak, "Electronic coherence and collective optical excitations of conjugated molecules," *Science*, **277**, 781-787 (1997).
6. S. Tretiak, V. Chernyak, and S. Mukamel, "Two-dimensional real-space analysis of optical excitations in acceptor-substituted carotenoids," *J. Am. Chem. Soc.*, **119**, 11408-11419 (1997).
7. S. Tretiak, V. Chernyak, and S. Mukamel, "Origin, scaling, and saturation of second order polarizabilities in donor/acceptor polyenes," *Chem. Phys. Lett.*, **287**, 75-82 (1998).
8. S. Tretiak, V. Chernyak, and S. Mukamel, "Localized electronic excitations in phenylacetylene dendrimers," *J. Phys. Chem. B*, **102**, 3310-3315 (1998).

9. G. C. Bazan, W. J. Oldham, Jr., R. J. Lachicotte, S. Tretiak, V. Chernyak, and S. Mukamel, "Stilbenoid dimers: Dissection of a paracyclophane chromophore," *J. Am. Chem. Soc.*, **120**, 9188-9204 (1998).
10. S. Tretiak, V. Chernyak, and S. Mukamel, "Excited electronic states of carotenoids: Time-dependent density-matrix-response algorithm," *Int. J. Quant. Chem.*, **70**, 711-727 (1998).
11. S. Tretiak, V. Chernyak, and S. Mukamel, "Real-space analysis of electronic excitations in free-base ( $H_2P$ ) and magnesium ( $MgP$ ) porphins," *Chem. Phys. Lett.*, **297**, 357-364.
12. E. V. Tsiper, V. Chernyak, S. Tretiak, and S. Mukamel, "Ground-State-Density-Matrix Algorithm for Excited State Adiabatic Surfaces; Application to Polyenes," *Chem. Phys. Lett.* (in press).
13. E. Poliakov, V. Chernyak, S. Tretiak, and S. Mukamel, "Exciton Scaling and Optical Excitations of Self-Similar Phenylacetylene Dendrimers," *J. Chem. Phys.* (in press).
14. V. Chernyak, S. Tretiak, E. V. Tsiper, T. Meier, and S. Mukamel "Semi-classical Effective Hamiltonian for Coupled Electronic and Nuclear Optical Response," *CMT22 (Vanderbilt) Workshop Proceedings, Vol. 14, Condensed Matter Theories* (in press).
15. E. V. Tsiper, V. Chernyak, S. Tretiak, and S. Mukamel, "Density Matrix Spectroscopic Algorithm for Excited State Adiabatic Surfaces and Molecular Dynamics of a Protonated Schiff Base," *J. Chem. Phys.* (in press).
16. V. Chernyak, E. Poliakov, S. Tretiak, and S. Mukamel, "Localized Optical Excitations and Two-Exciton Spectroscopy of Phenylacetylene Dendrimers," *Mat. Res. Soc. Proc.* (in press).
17. S. Tretiak, V. Chernyak, and S. Mukamel, "Electronic Screening in Second Order Optical Polarizabilities of Elongated Donor/Acceptor Polyenes," *Chem. Phys.* (in press).

# Acknowledgements

I would like to express my most sincere gratitude to my research advisor, Professor Shaul Mukamel, for all of his dedicated guidance and encouragement during my years at the University of Rochester. Shaul's love for science, continued ideas, and enthusiasm made this thesis possible.

I wish to thank to all members of the Shaul Mukamel research group for their invaluable support and friendship. Especially, I would like to thank to Senior Scientist Vladimir Chernyak for numerous useful discussions and assistance throughout this work. I would like to thank Professor M. C. Zerner for providing us with the ZINDO program and for his help in using it. Special thanks go to our collaborators, Dr. W. J. Oldham and Professor G. C. Bazan. Their valuable suggestions and assistance help us to understand complex photochemistry of stilbenoid aggregates. I wish to thank Professor W. E. Torruelas for providing us with the linear absorption data of acceptor-substituted carotenoids and for numerous useful discussions. I would like to thank Dr. S. F. Swallen and Professor R. Kopelman for providing us with the linear absorption data of phenylacetylene dendrimers and for most valuable discussions. Special thanks go to the Rochester Theory Center for Optical Science and Engineering at the University of Rochester for the stimulating atmosphere and discussion.

The financial support of the Air Force Office of Scientific Research, the National Science Foundation, Center for Photoinduced Charge Transfer at the University of Rochester is gratefully acknowledged. Most of the calculations were conducted using the resources of the Cornell Theory Center, which receives major funding from the NSF and New York State.

Finally, I would like to thank my wife Natalia and my daughter Oksana for all their support, patience, and encouragement throughout my graduate career.

# Abstract

This thesis focuses on the development of a theoretical approach that relates the electronic properties of large conjugated molecules directly to the motions of electron-hole pairs in real space. A physical picture is obtained using collective electronic oscillators (CEO) which represent the dynamics of the optically-driven reduced single-electron density matrix. This representation is displayed using two-dimensional electronic mode matrices. It pinpoints the origin of each optical transition and identifies spatial coherences and the underlying saturation sizes.

The CEO are calculated using the Time-Dependent Hartree-Fock approximation for the equation of motion for the time-dependent reduced single-electron density matrix. These electronic normal modes are computed directly as eigenmodes of  $K^2 \times K^2$  Liouville operator,  $K$  being the basis set size. An iterative Density-Matrix-Spectral-Moments-Algorithm (DSMA) has been developed to diagonalize this operator. The DSMA computational time (and memory) requirements scale very favorably with system size:  $\sim N^3$  (and  $N^2$ ). Linear and nonlinear optical polarizabilities of large organic molecules with hundreds of heavy atoms have been calculated with moderate computational effort. Connection to molecular excited states has been made as well. Simple expressions have been derived which predict the trends for the off-resonant optical polarizabilities of polyene chains and reproduce well the magnitudes of polarizabilities and their scaling with molecular size and bond-length alternation.

A Fortran 77 code, which calculates molecular electronic spectra using the DSMA algorithm, was developed. This code interfaces the CEO with standard quantum chemistry programs, employs the ZINDO package to generate the INDO/S hamiltonian using *ab-initio* optimized molecular geometry, experimental X-ray diffraction, or NMR data.

Several applications of the CEO are made. These include size-scaling and crossover to the bulk of the optical nonlinearities of polyacetylene (up to 300 repeat units and seventh order response); real-space two-dimensional analysis of collective optical excitations in Poly(p-phenylene vinylene) (PPV) oligomers, stilbenoid aggregates, acceptor-substituted carotenoids, porphins, and phenylacetylene dendrimers. The origin, scaling, and saturation of second order polarizabilities in donor/acceptor polyenes and femtosecond four-wave mixing in conjugated polyenes are discussed.

# Contents

Curriculum Vitae	i
List of Publications	ii
Acknowledgements	iv
Abstract	v
Contents	vii
List of Tables	x
List of Figures	xi
<b>1 Introduction</b>	<b>1</b>
<b>2 Collective Electronic Oscillator (CEO) Representation of Optical Response</b>	<b>10</b>
2.1 The Pariser-Parr-Pople (PPP) and the Intermediate Neglect of Differential Overlap / Spectroscopy (INDO/S) Hamiltonians . . .	10
2.2 The Single-Electron Density Matrix and the TDHF equations .	14
2.3 Properties of the Electronic Normal Modes . . . . .	19
2.4 The Density–Matrix–Spectral–Moment Algorithm (DSMA) . . .	20
2.5 Real-space CEO analysis of electronic response. . . . .	29
2.6 Density matrices vs. eigenstates; advantages of the CEO representation. . . . .	31
2.7 Appendix A. Relations between the Inter- and Intraband Components of the Density Matrix. . . . .	35
2.8 Appendix B. Short-time Evolution of the density-matrix response function. . . . .	35
2.9 Appendix C. Solution of Eqs. (2.53) . . . . .	36



<b>3</b>	<b>Time-Dependent Density-Matrix-Response-Functions (DMRF) Algorithm for calculating Excited States.</b>	<b>39</b>
3.1	Density matrix response functions and material properties . . .	39
3.2	Classical Electronic Oscillators in the TDHF Approach: . . . .	42
3.3	Intrastate and Transition Electronic Density Matrices for the Effective Multilevel System . . . . .	45
3.4	Merits of the DMRF method. . . . .	50
3.5	Appendix A. Response Function for the Classical TDHF approach	51
3.6	Appendix B. Sum-over-States Polarizabilities of the Effective Multilevel System . . . . .	54
3.7	Appendix C. Nonlinear response of systems with Coordinate-dependent anharmonicities . . . . .	56
<b>4</b>	<b>Chemical Bonding and Size-Scaling of Off-Resonant Nonlinear Polarizabilities.</b>	<b>58</b>
4.1	Electronic Normal Modes and Size-Scaling of Optical Polarizabilities of Polyacetylene Oligomers . . . . .	59
4.2	Single-Oscillator Approximation for Off-Resonant Polarizabilities	65
<b>5</b>	<b>Linear Optical Excitations in PPV Oligomers</b>	<b>74</b>
5.1	Electronic Normal Modes and Optical Absorption (PPP hamiltonian) . . . . .	75
5.2	Electronic Normal Modes and Optical Absorption (INDO/S hamiltonian) . . . . .	81
5.3	Molecular Orbital Representation of Electronic Oscillators . . .	85
<b>6</b>	<b>Linear Optical Excitations in Acceptor-substituted Carotenoids.</b>	<b>89</b>
6.1	Size-Scaling of the Ground - State Density Matrix. . . . .	90
6.2	Electronic Normal Modes and Optical Absorption . . . . .	95
6.3	The Ground-State of Long Polyacetylenes: Solitons . . . . .	104
6.4	Excited States Density Matrices of Acceptor-Substituted Carotenoids. . . . .	107
6.5	Quantum Confinement and Coherence Sizes . . . . .	114

<b>7</b>	<b>Localized Electronic Excitations in Phenylacetylene Dendrimers</b>	<b>116</b>
7.1	Collective Electronic Excitations in Linear Oligomers . . . . .	119
7.2	Spectra and Energy funneling in Dendrimers . . . . .	125
<b>8</b>	<b>Charge-Transfer Electronic Excitations in Free-Base (<math>H_2P</math>) and Magnesium (<math>MgP</math>) Porphins.</b>	<b>128</b>
8.1	The Linear Absorption Spectra. . . . .	131
8.2	Collective Electronic Excitations. . . . .	135
8.3	Conclusions. . . . .	140
<b>9</b>	<b>Linear Electronic Excitations in Stilbenoid Aggregates</b>	<b>142</b>
9.1	Electronic modes of the monomeric building blocks . . . . .	143
9.2	Electronic modes of dimers . . . . .	148
9.3	Emission Spectra and Radiative Decay Rates . . . . .	152
<b>10</b>	<b>Scaling and Saturation of Second Order Off-Resonant Polarizabilities in Donor/Acceptor Polyenes.</b>	<b>155</b>
10.1	Real-space Two-Dimensional analysis of Substitution Effects . .	157
10.2	Size-scaling of optical polarizabilities . . . . .	160
<b>11</b>	<b>Electronic-oscillator analysis of femtosecond four-wave mixing in conjugated polyenes.</b>	<b>167</b>
11.1	The CEO Representation of Resonant Response . . . . .	168
11.1.1	Equations of motion for electron-hole oscillators . . . . .	169
11.1.2	Two-oscillator representation of resonant four-wave mixing	172
11.2	Numerical results . . . . .	178
11.2.1	The Hückel model . . . . .	178
11.2.2	The PPP model . . . . .	187
11.3	Appendix A. Equations of motion for two-pulse nonlinear optical response . . . . .	198
11.4	Appendix B. Iterative calculation of the four-wave mixing signal	200
11.5	Appendix C. Elimination of off-resonant oscillators . . . . .	202
<b>12</b>	<b>Conclusions</b>	<b>207</b>
	<b>Bibliography</b>	<b>209</b>

# List of Tables

8.1	Calculated and experimental excitation energies of the free base porphin. Energies are in $eV$ . Oscillator strengths are given in parentheses. . . . .	132
8.2	Calculated excitation energies of the magnesium porphin. Experimental energies are given for Mg etioporphin (MgEtio) and Mg tetraphenylporphin (MgTTP). Energies are in $eV$ . Oscillator strengths are given in parentheses. . . . .	133
11.1	Mode frequencies and anharmonic coupling constants for the Hückel and the PPP models. . . . .	179

# List of Figures

- 2.1 Decomposition of the single-electron density matrix to the particle-hole : hole-particle (interband) and particle-particle : hole-hole (intraband) parts shown in the molecular orbital basis set representation. The dimensionality of density matrix  $\rho$  defined by the basis set size is  $K \times K$ . We assume  $N$  occupied and  $K - N$  unoccupied orbitals: the ground-state density matrix  $\bar{\rho}$  is then diagonal in the particle-particle block and zero otherwise in molecular orbitals. The dimensionality of interband and intraband parts are  $2N(K - N)$  and  $N^2 + (K - N)^2$  respectively. 16
- 2.2 Variation of electronic oscillator frequencies  $\Omega_\nu$ , effective dipole moments  $\mu_\nu^{(1)}$ , and first ( $\alpha$ ), third ( $\gamma$ ), fifth ( $\delta$ ), and seventh ( $\zeta$ ) off-resonant polarizabilities with the number of modes used for octateraene (N=8). The polarizabilities will be defined later in this Section. Here convergence of the DSMA to the full TDHF calculation ( $M = 16$  is demonstrated. The magnitudes of polarizabilities are normalized at their converged values:  $\alpha = 3.2 \times 10^{-23} \text{ esu}$ ,  $\gamma = 6.6 \times 10^{-35} \text{ esu}$ ,  $\delta = 1.4 \times 10^{-46} \text{ esu}$ ,  $\zeta = 2.3 \times 10^{-59} \text{ esu}$ . . . . . 23
- 2.3 Convergence of the linear absorption (the imaginary part of  $\alpha$  (Eq. (1.5))) with the number of modes used for N=40 atom oligomer. The linewidth is  $\epsilon = 0.2eV$ . Note, that the fundamental band at  $2.57 \text{ eV}$  with strength  $109 \text{ e\AA}^2/V$  [ $1.57 \times 10^{-21} \text{ esu}$ ] remains basically the same in all panels. . . . . 24

- 2.4 **A - C)** convergence of the lowest three nonvanishing polarizabilities ( $\alpha$ ,  $\gamma$ , and  $\delta$ ) of polyacetylene chains (up to 40 carbon atoms) with the number of modes used for calculations. The polarizabilities will be defined later in this Section. Here convergence of the DSMA is demonstrated. The results obtained with the full TDHF calculations (panel **(A)** and **(B)**) and with  $M = 12$  modes (panel **(C)**) are shown by solid lines. Note that  $M = 7$  modes approximation gives good values for hyperpolarizabilities  $\gamma$ , and  $\delta$  . . . . . 25
- 2.5 Two-dimensional representation and physical interpretation of electronic modes. Each mode  $\xi_\nu$  is an  $N \times N$  matrix,  $N$  being the molecular size. By displaying this matrix in two-dimensions we establish a direct real-space connection between the optical response and motions of charges in the molecule upon optical excitation. The x axis represents an electron on site  $n$ , the y axis describes a hole on site  $m$ . An incident light moves an electron from some occupied to an unoccupied orbitals, creating an electron-hole pair (or exciton). The state of this pair can be characterized by two lengthscales: First, the distance between electron and hole (i.e., how far the electron can travel apart from the hole). This coherence size  $L_c$  is the "width" of the density matrix along the anti-diagonal direction. The second length  $L_d$  describes the exciton center of mass position (i.e., where the optical excitation resides within the molecule).  $L_d$  is the "width" of the density matrix along the diagonal direction. Finally charge transfer processes can be characterized by the asymmetry of mode with respect to the diagonal.  $(\xi_\nu)_{mn} \sim (\xi_\nu)_{nm}$  means that there is no preferable direction of motion for electrons (or holes), whereas  $(\xi_\nu)_{mn} \gg (\xi_\nu)_{nm}$  shows the motion of electron from m to n. . . . . 30
- 3.1 The four steps involved in constructing the effective multilevel system (EMS) out of the original quantum Fermion Model (QFM). 41

- 4.1 Scaling of linear  $\alpha$  third order  $\gamma$ , fifth order  $\delta$ , and seventh order  $\zeta$  polarizabilities with size. Shown are the magnitudes of polarizability normalized at its saturated value  $\frac{\chi^{(j)}(N)}{N\chi_{sat}^{(j)}}$ , where  $\chi_{sat}^{(j)} = \frac{\chi^{(j)}(N)}{N}$  at  $N \rightarrow \infty$ ,  $j=1,3,5,7$ . The magnitudes of saturated polarizabilities are:  $\alpha_{sat} = 1.7 \times 10^{-23}$  *esu*,  $\gamma_{sat} = 1.1 \times 10^{-33}$  *esu*,  $\delta_{sat} = 1.9 \times 10^{-43}$  *esu*,  $\zeta_{sat} = 5.2 \times 10^{-53}$  *esu*. . . . . 60
- 4.2 Upper panel: size dependence of mode frequencies, lower panel: the number of dominant modes, needed to compute susceptibilities with 0.1% accuracy compared with the full  $N^2/4$  modes TDHF calculations. . . . . 60
- 4.3 The effective dipole moments  $\mu_\nu$  vs. Electronic Oscillator Frequencies  $\Omega_\nu$  for an  $N = 100$  polyacetylene chain. Shown are the dominant modes in first, third, fifth, and seventh orders of nonlinearity. . . . . 61
- 4.4 The effective dipole moments  $\mu_\nu$  vs. Electronic Oscillator Frequencies  $\Omega_\nu$  for an  $N = 100$  polyacetylene chain. Shown are the dominant modes in second, fourth, and sixth orders of nonlinearity. 62
- 4.5 **A)** Contour plots of  $\bar{\rho}$  (a) and the dominant modes (b-f) that contribute to the responses up to the seventh order for the system of Figs. 4.3 and 4.4 ( $N = 30$ ). Shown are the absolute values of the density matrices smoothed over four points to eliminate fast oscillations and to highlight the long range behavior. The axes are labeled by the carbon atoms along the chain. Exciton confinement effects are clearly seen in panels c, d, e, f. Frequencies of modes b-f are 2.6, 4.0, 4.8, 5.2, and 5.6 *eV*, respectively. **B)** Same as **A** but for a longer chain ( $N = 100$ ). Frequencies of b-f modes are 2.4, 3.9, 4.5, 4.7, and 5.1 *eV*, respectively. . . . . 63
- 4.6 Variation of the scaling exponents  $b \equiv d[\ln\chi]/d[\ln N]$ ,  $\chi = \alpha, \gamma, \delta$ , and  $\zeta$  with size. Note that both the maximum value of  $b$  and the size where the maximum is attained increase with the degree of nonlinearity. . . . . 65

- 4.7 The ratio of the interband contribution ( $a = \chi_{p-h}^{(j)}/\chi^{(j)}$ ) to  $\gamma$ ,  $\delta$ , and  $\zeta$  polarizabilities. Note that for small chain lengths the particle-hole contributions to the high order polarizabilities are negative, and the interband contribution decreases with increased degree of nonlinearity. The ratio saturates to the values  $a_\gamma = 0.4$ ;  $a_\delta = 0.26$ ;  $a_\zeta = 0.19$ . . . . . 66
- 4.8 Scaling of the first  $f^{(1)}$  [ $e^3 \text{\AA}^2 V$ ] and second  $f^{(2)}$  [ $e^5 \text{\AA}^2 V^3$ ] moments of the linear absorption with number of carbon atoms for different values of bond-length alternation. Calculations were made using the DSMA algorithm. . . . . 69
- 4.9 Upper panels: variation of the coefficients ( $f_1^{(2)}$  [ $e^5 \text{\AA}^2 V^3$ ] and  $f_0^{(2)}$  [ $e^5 \text{\AA}^2 V^3$ ]) in the Taylor expansion of the second moment with the bond length alternation  $\Delta$  [ $\text{\AA}$ ]. Calculations were made using the DSMA algorithm. Bottom panels: The  $\Delta$  [ $\text{\AA}$ ] dependence of the coherence size  $L$  and the optical gap  $\tilde{\Omega}$  [eV]. Solid lines - full TDHF calculations. Dashed line - Eq. (4.6) . . . . . 70
- 4.10 Scaling of the first third and fifth order polarizabilities ( $\alpha$ ,  $\gamma$ , and  $\delta$  are in the units of  $e\text{\AA}^2 V^{-1}$  [ $1.441 \times 10^{-23} esu$ ],  $e\text{\AA}^4 V^{-3}$  [ $1.297 \times 10^{-34} esu$ ], and  $e\text{\AA}^6 V^{-5}$  [ $1.167 \times 10^{-45} esu$ ]) of polyacetylene chains with the numbers of carbon atoms for various values of the bond length alternation parameter  $\Delta = 0.03\text{\AA}$ ,  $0.05\text{\AA}$ ,  $0.07\text{\AA}$ , and  $0.09\text{\AA}$ , as indicated, solid line - full TDHF calculation, dashed line - Eq. (4.8) . . . . . 72
- 4.11 Variation of the dimensionless parameters  $k_j$  with the bond length alternation  $\Delta$  [ $\text{\AA}$ ].  $k_j$  were obtained by fitting Eq.(7) to the TDHF (see Fig. 4.10). . . . . 73
- 5.1 Geometry and atom labeling of PPV oligomers. Bond angles are  $120^\circ$ , except  $\alpha(r_{6,7}, r_{7,8}) = 128^\circ$ , and the distances are:  $r_{1,2} = r_{2,3} = r_{3,4} = r_{4,5} = r_{5,6} = r_{6,1} = 1.39\text{\AA}$ ,  $r_{6,7} = 1.44\text{\AA}$ ,  $r_{7,8} = 1.33\text{\AA}$ . 75

- 5.2 **(A)** Absorption spectrum of PPV(10) (the imaginary part of  $\alpha$  Eq.(1)). Dashed line: experimental absorption of a PPV thin film. Solid and dotted lines: absorption lineshapes of PPV(10) obtained with 12 effective modes calculations and linewidth  $\Gamma_\nu = 0.1eV$  using PPP and INDO/S hamiltonians, respectively; The sticks represent oscillator strengths  $f_\nu$ ,  $\nu = 1, N^2/4$  of PPV(10) obtained by the full TDHF with PPP hamiltonian. **(B)** The frequency – dependent participation ratio of the induced density matrix. . . . . 76
- 5.3 Contour plots of density matrices. **(A)**  $\bar{\rho}$  of PPV(10); **(B)** magnified region of **(A)** representing the single unit of polymer chain and the color maps; **(C)** momentum, and **(D)** coordinate of PPV(10), and **(E)** coordinate of PPV(20) of the lowest absorption peak (I); **(F)**, **(G)**, **(H)** are the same quantities as in **C** to **E** but for the second absorption peak (II). The axis labels represent the repeat units, except in **(B)** where the axes represents the individual carbon atoms as numbered in Fig. 5.1. . . . . 78
- 5.4 Contour plots of density matrices. **(A)** Momentum, and **(B)** coordinate in the real space, and **(C)** coordinate in the molecular orbital representation of the peak (III) of PPV(10). **(D)** Momentum, and **(E)** coordinate of PPV(10) for the fourth absorption peak (IV), and **(F)** magnified area of **(E)** representing the single unit of polymer chain. **(G, H, and I)** the same quantities as in **B** to **F** but for the fifth absorption peak (V). The axis of **(A)**, **(B)**, **(D)**, **(E)**, **(G)**, and **(H)** are labeled to the repeat units of polymer chain. The axis of **(C)** denote the molecular orbitals. Labeling using the number of carbon atoms according to Fig. 5.1 is used for panels **(F)** and **(I)** . . . . . 80
- 5.5 Contour plots of electronic modes  $\xi_\nu$  dominating the absorption spectrum of PPV(10). Panels **A, B, C, D, E, F** represent the modes corresponding to transitions I, Ia, II, IIIa, IV, V, VI in spectrum shown by dotted line in Fig. 5.2. The axis labels represent the repeat units. The ordinate and abscissa label electron and hole respectively. . . . . 83



- 5.6 (A) Origin of the collective electronic oscillators. Each transition between an occupied and an unoccupied orbital represents an electron-hole oscillator. In a molecule with  $N_e$  occupied (electron) and  $N_h$  unoccupied (hole) orbitals we have altogether  $N_e \times N_h$  oscillators. For a system with a filled valence and empty conduction band described by a “minimal basis set”  $N_e = N_h = N/2$  and the number of oscillators is  $N^2/4$ . The collective oscillators  $Q_\nu$  can be represented as superpositions of the electron-hole oscillators (see Eq. (5.2)). The participation ratio  $P^\nu$  measures the effective number of electron-hole pairs contributing to a given collective oscillator. (B) The molecular orbital contributions and the inverse participation ratios of orbital pairs corresponding to the five dominant modes of PPV(10) absorption. . . . . 86
- 6.1 Six acceptor-substituted carotenoids [1,2] listed in order increasing acceptor strength. Repeat units numbering used in two-dimensional plots is given for molecule 1. . . . . 91
- 6.2 Contour plots of ground state density matrices for (A) neutral  $N(10)$  (compound 1) and (B) polar  $P(10)$  (compound 6) molecules. The color code is shown in the upper panel. The structures at the ends of molecules are shown by rectangles. . . . . 92
- 6.3 Dipole moments (A), total charge on the acceptor (B), frequency of the lowest transition (C), linear  $\alpha(0)$  (D), quadratic  $\beta(0)$  (E), and cubic  $\gamma$  (F) off-resonant polarizabilities for six carotenoids. The ordinate axes are labeled by compound number according to Fig. 6.1.  $\alpha, \beta$ , and  $\gamma$  are in the units of  $e\text{\AA}^2V^{-1}$  [ $1.441 \times 10^{-23}esu$ ],  $e\text{\AA}^3V^{-2}$  [ $4.323 \times 10^{-29}esu$ ], and  $e\text{\AA}^4V^{-3}$  [ $1.297 \times 10^{-34}esu$ ]. . . . . 93
- 6.4 Structures of the neutral  $N(n)$  and polar  $P(n)$  (substituted by the strongest acceptor) molecules. Calculations were done for chain lengths of  $n = 10, 15, 20, 30, 40$  double bonds. . . . . 94

- 6.5 Variation of the bond-length alternation (A), total charge  $Q_A$  (B), total atomic charge  $q_A$  (C), diagonal elements of modes  $a$  and  $b$  in polar  $P(n)$  molecule (D and E), and modes  $a'$  and  $b'$  in neutral  $N(n)$  molecule (F and G)) along the chain for chain length  $n = 40$  double bonds. . . . . 95
- 6.6 Calculated (solid lines) and experimental (dashed lines) linear absorption spectra [1,2] of six carotenoids. Panels are numbered according to Fig. 6.1. The absolute values of linear polarizability are given in arbitrary units. Theoretical spectra were calculated with linewidth  $\Gamma = 0.2$  eV. Peak  $i$  at 4.5 eV appearing on all experimental spectra originates from the anti-oxidant added to samples. . . . . 96
- 6.7 Linear absorption spectra calculated with linewidth  $\Gamma = 0.2$  eV of the neutral  $N(n)$  (dashed lines) and polar  $P(n)$  (solid lines) molecules shown in Fig. 6.4. The relative values of linear polarizability are given in arbitrary units. . . . . 99
- 6.8 Contour plots of density matrices for neutral  $N(n)$  molecule. Top panel: coordinates of the first  $a'$  (A) and second  $b'$  (B) absorption peaks for chain length  $n = 40$  double bonds. Middle and bottom panels display the same quantities but for chain lengths of  $n = 20$  and  $n = 10$  double bonds, respectively. The structures at the ends of molecules are shown by rectangles. . . 100
- 6.9 Sketch of the dipole moments  $\mu = Tr(\mu Q)$  gain for dominant modes in neutral  $N(n)$  and polar  $P(n)$  molecules with chain length  $n = 40$  double bonds. . . . . 101
- 6.10 Contour plots of density matrices for polar  $P(n)$  molecule. Top panels: coordinates of the first  $a$  (A) and second  $b$  (B) absorption peaks for chain length  $n = 40$  double bonds. Middle and bottom panels display the same quantities but for chain length  $n = 20$  and  $n = 10$  double bonds, respectively. The structures at the ends of molecules are shown by rectangles. . . . . 102

- 6.11 Schematic variation of bond - length alternation pattern in the long acceptor substituted molecules with increasing acceptor strength (panels A to C). Two possible configurations corresponding to ground states with  $\delta l_{II} = \delta \bar{l}$  and  $\delta l_{II} = -\delta \bar{l}$  are shown by solid and dashed lines respectively. Panel A. No acceptor, the ground state is non-degenerate and has to  $\delta l_{II} = \delta \bar{l}$  (solid line), the state with  $\delta l_{II} = -\delta \bar{l}$  (dashed line) has a higher energy needed to form two solitons. Panel B Intermediate-strength acceptor: the ground state with  $\delta l_{II} = \delta \bar{l}$  is nondegenerate (solid line) and contains a soliton in the acceptor region. A state with  $\delta l_{II} = -\delta \bar{l}$  (dashed line) contains two solitons and has a higher energy. Panel C. Very strong acceptor; The molecule is separated into the acceptor with the charge  $-e$  and anion with the charge  $+e$  and  $(N-1)$  carbon atoms with the ground state representing the charged soliton. The ground state of an anion may become degenerate since a soliton can be formed anywhere (this is represented by the dashed line). However Coulomb interaction between the acceptor and the soliton leads to its localization near the acceptor (solid line). Panel D: Molecule substituted by a donor and an acceptor of intermediate strength. Two ground states with  $\delta l_{II} = \delta \bar{l}$  (solid line) and  $\delta l_{II} = -\delta \bar{l}$  (dashed line) have the same energy (cyanine like). . . . . 105
- 6.12 Structures and atom labeling of the neutral  $N$  and polar  $P$  (substituted by the strong acceptor) molecules. . . . . 108
- 6.13 The dipole moments  $\mu_\nu$  are displayed vs. electronic mode frequencies  $\Omega_\nu$  for the molecules shown in Fig. 6.12. Shown are the dominant modes in the first two orders of nonlinearity. The dipoles are given in arbitrary units. . . . . 109

6.14	Contour plots of ground and excited state density matrices which dominate the linear absorption of molecules N. The axis labels represent the individual carbon atoms as labeled in Fig. 6.12. Panel labels indicate the molecule (Fig. 6.12) and the state corresponding to the peak in Fig. 6.13. $\rho^{gg}$ ground state density matrix; $\Delta\rho^{\nu\nu} \equiv \rho^{\nu\nu} - \rho^{gg}$ the difference between the density matrices of state $\nu$ and the ground state; $\rho^{\nu\eta}$ the transition density matrices. . . . .	111
6.15	Same as in Fig. 6.14 but for the polar molecule P. . . . .	113
7.1	Structures of the two families of phenylacetylene dendrimers [3]. The compact dendrimers (A) are made of the same linear building block P1. The extended dendrimers (B) have a varying linear unit length which decreases for higher generations. . . . .	117
7.2	Calculated (solid lines) [3] and experimental (dashed lines) absorption spectra of the dendrimers shown in Fig. 7.1 . . . . .	118
7.3	The generations (shown by different colors) in the extended dendrimers have a varying linear segment length. Their absorption frequency is blue-shifted for higher generations. . . . .	119
7.4	Structures and atom labeling of the linear <i>para</i> - oligomers $P_n$ with $n = 1, 2, 3, 4, 7$ repeat units (triple bonds), and the M7 oligomer made of the P1, P2, P3 units conjugated at <i>meta</i> -position. . . . .	120
7.5	Calculated linear absorption (oscillator strengths $f_\nu$ vs. transition frequencies $\Omega_\nu$ ) of the molecules shown in Fig. 7.4. Mode frequencies of P1 ( $\Omega_a = 3.90$ eV, $\Omega_b = 5.87$ eV); P2 ( $\Omega_a = 3.49$ eV, $\Omega_b = 5.78$ eV); P3 ( $\Omega_a = 3.31$ eV, $\Omega_b = 5.71$ eV); P7 ( $\Omega_a = 3.11$ eV, $\Omega_b = 5.60$ eV); M7 ( $\Omega_{a1} = 3.86$ eV, $\Omega_{a2} = 3.48$ eV, $\Omega_{a3} = 3.31$ eV, $\Omega_b = 5.60$ eV). . . . .	121
7.6	Contour plots of the ground state density matrices of oligomers P1, P7, and M7. The axes represent the carbon atoms as labeled in Fig. 7.4. The panels are labeled the molecule (Fig. 7.4) and the electronic mode (Fig. 7.5) (e.g. P1( $\rho$ ) is the ground state density matrix of molecule P1). The aromatic ring units are shown by solid rectangles. The color code is given in the top panel. . . . .	122

7.7	Contour plots of the electronic modes which dominate the absorption spectra of the oligomers shown in Fig. 7.4. The axes represent the carbon atoms as labeled in Fig. 7.4. The panels indicate the molecule (Fig. 7.4) and the electronic mode (Fig. 7.5). The linear units in M7 are shown by solid rectangles. The color code is given in Fig. 7.6. . . . . .	124
8.1	Structures and atom labeling of the Free-Base Porphin ( $H_2P$ ) (top) and Magnesium Porphin ( $MgP$ ) (bottom) . . . . .	129
8.2	Contour plots of the ground state density matrices of Free-Base Porphin ( $H_2P$ ( $\rho$ )), Magnesium Porphin ( $MgP$ ( $\rho$ )), and charge transfer electronic mode TX (panel $MgP$ ( $TX$ )). The axes represent the carbon atoms as labeled in Fig. 8.1. The ordinate and abscissa label electron and hole respectively. The color code is given in the bottom left panel. . . . .	136
8.3	Contour plots of the electronic modes which dominate the absorption spectra of Free-Base and Magnesium Porphin shown in Fig. 8.1. The axes represent the carbon atoms as labeled in Fig. 8.1. The ordinate and abscissa label electron and hole respectively. Each panel indicates the molecule (Fig. 8.1) and the electronic mode (Tables 8.1 and 8.2). The color code is given in Fig. 8.2. . . . .	137
8.4	Variation of the diagonal elements of modes $H_2P$ ( $N_{  }$ ) (solid line) and $MgP$ ( $N_{  }$ ) (dashed line). The X axis represents the carbon atoms as labeled in Fig. 8.1. The dotted line represents the difference of atomic contributions to the transition dipole of mode N in molecules $H_2P$ and $MgP$ : $\mu_n^{MgP} - \mu_n^{H_2P}$ , $n = 1 \dots 24$ .	139
9.1	Structures and atom labeling of [2,2]paracyclophane (Pc), stilbenoid monomers (1c, 2c) and dimers (1a, 2a, 1b, 2b). . . . .	144
9.2	Calculated (solid lines) and experimental (dashed lines) absorption spectra and experimental (dotted lines) fluorescence spectra of the molecules presented in Fig. 9.1. . . . .	145

- 9.3 Contour plots of ground state density matrices and the electronic modes which dominate the optical absorption of monomers 1c and 2c. The axis labels represent the individual carbon atoms as labeled in Fig. 9.1. The panels indicate the molecule (Fig. 9.1) and the electronic mode (Fig. 9.2) (e.g. 1c( $\rho$ ) is the ground state density matrix of molecule 1c; Pc(III) is mode III of [2,2]paracyclophane Pc). The aromatic ring units are shown by solid rectangles. The color code is given in the bottom row. Mode frequencies of 1c ( $\Omega_{II} = 4.12$  eV,  $\Omega_{IIIA} = 5.36$  eV,  $\Omega_{IIIB} = 5.73$  eV); 2c ( $\Omega_{II} = 3.53$  eV,  $\Omega_{III} = 5.25$  eV); Pc ( $\Omega_{IA} = 3.95$  eV,  $\Omega_{IB} = 4.77$  eV,  $\Omega_{III} = 5.5$  eV) . . . . . 147
- 9.4 Contour plots of electronic modes which dominate the absorption dimers. The axis labels represent the individual carbon atoms as labeled in Fig. 9.1. The panels indicate the molecule (Fig. 9.1) and the electronic mode (Fig. 9.2). The monomers 1c and 2c units are shown by solid rectangles. The paracyclophane Pc unit is shown by dashed rectangle. The color code is given in Fig. 9.3. Mode frequencies of 1a ( $\Omega_{IA} = 2.91$  eV,  $\Omega_{IB} = 3.03$  eV,  $\Omega_{IIA} = 3.69$  eV,  $\Omega_{IIB} = 4.02$  eV,  $\Omega_{III} = 5.46$  eV); 1b ( $\Omega_{IA} = 2.92$  eV,  $\Omega_{IB} = 3.01$  eV,  $\Omega_{IIA} = 3.72$  eV,  $\Omega_{IIB} = 4.59$  eV,  $\Omega_{III} = 5.47$  eV); 2a ( $\Omega_{IA} = 2.91$  eV,  $\Omega_{IB} = 3.03$  eV,  $\Omega_{IIA} = 3.29$  eV,  $\Omega_{IIB} = 3.61$  eV,  $\Omega_{III} = 5.29$  eV); 2b ( $\Omega_{IA} = 2.92$  eV,  $\Omega_{IB} = 3.01$  eV,  $\Omega_{IIA} = 3.41$  eV,  $\Omega_{IIB} = 3.86$  eV,  $\Omega_{III} = 5.30$  eV) . . . . . 150
- 10.1 Structures of the neutral  $N(n)$ , Donor  $D(n)$ , Acceptor  $A(n)$ , and Donor/Acceptor  $DA(n)$  substituted molecules. Calculations were performed for bridges with  $n = 5, 10, 15, 20, 30, 40$  double bonds. . . . . 158
- 10.2 Contour plots of the ground state density matrix  $\bar{\rho}(\mathbf{A})$ , and the density matrices induced by a static electric field  $\delta\rho^{(1)}(\mathbf{B})$ ,  $\delta\rho^{(2)}(\mathbf{C})$ , and  $\delta\rho^{(3)}(\mathbf{D})$  of molecule DA(15). The part of the density matrix corresponding to the bridge is marked by a rectangle. The axes are labeled by the bridge carbon atoms. Atom 1 (30) correspond to the donor (acceptor) ends. . . . . 159

- 10.3 Top row: Contour plots of the ground state difference matrices  $\Delta\bar{\rho} = \bar{\rho}_{DA} - \bar{\rho}_N$  for  $n=9$  (**A**),  $n=15$  (**B**), and  $n=30$  (**C**) shown for the bridge part of the matrix. Axes are labeled by the bridge carbon atoms with atom 1 on the donor side and atom  $2n$  on the acceptor side. The second, the third, and the fourth rows display the difference matrices to various orders in the field  $\Delta\rho^{(1)}$ ,  $\Delta\rho^{(2)}$ , and  $\Delta\rho^{(3)}$  respectively. . . . . 161
- 10.4 Scaling with size and saturation of the ground state dipole moment  $\mu_{gg}$  (**A**), the first (**B**), second (**C**), and third (**D**) orders off-resonant polarizabilities of the molecules displayed in Fig. 10.1. **▲** Neutral (no substitutions) N; **▼** acceptor substituted (A); **●** donor substituted (D); **□** in panels **A** and **C** show the sum of molecules (A) and (D). The additivity of  $\mu_{gg}$  and  $\beta$  at large sizes reflects the independent effect of the donor and acceptor. Note the similar saturation behavior of  $\alpha/n$ ,  $\gamma/n$  and  $\beta$ . . . . . 163
- 10.5 Variation of the scaling exponents  $b_\chi \equiv d[\ln \chi]/d[\ln n]$ ,  $\chi = \alpha, \gamma, \delta$  with size for the curves shown in Fig. 10.4. At large sizes  $b_\alpha$  and  $b_\gamma$  tend to 1 whereas  $b_\beta$  approaches 0. These reflect the saturation of  $\alpha/n, \gamma/n$ , and  $\beta$  shown in Fig. 10.4. . . . . 164
- 11.1 Frequencies of all  $B_u$  and  $A_g$  oscillators for the Hückel model of a 30 carbon atom polyacetylene chain. There are 113  $B_u$  and 112  $A_g$  oscillators. The frequencies of the first eight  $B_u$  ( $A_g$ ) oscillators are: 2.28, 3.35, 3.46, 3.46, 4.63, 4.66, 4.66, and 4.79eV (2.82, 2.82, 3.99, 3.99, 4.13, 4.13, 5.30, and 5.30eV). . . . 180
- 11.2 (a) Ground state density matrix and (b) absolute value of density matrix representing the  $1B_u$  oscillator for the Hückel model. (c) Ground state density matrix and absolute value of density matrix representing the  $1B_u$  (d),  $3A_g$  (e), and  $5A_g$  (f) oscillators for the PPP model. (Large=blue, green, yellow, red=small) . . . 181
- 11.3 Convergence of anharmonicities for the Hückel model as function of number of virtual  $A_g$  oscillator variables. Shown is the relative percent difference of the quantity to its converged value. 182

11.4	(a) Time-resolved amplitude and (b) phase of the FWM signal for time-delay $\tau = 0fs$ for the Hückel model. Solid line: model IH, dashed: model IIH, dotted: model IIIH, and dashed-dotted: laser pulse envelope. . . . .	183
11.5	Absolute value of second-order density matrix $\rho^{(2)}(t)$ at $t = 20fs$ representing transient-grating ( $\mathbf{k}_2 - \mathbf{k}_1$ ) for (a) model IH, Eq. (27), (b) model IP, Eq. (28), (c) model IIP, Eq. (27), and (d) two-photon resonances ( $2\mathbf{k}_2$ ) for model IIIP, Eq. (29). . . . .	185
11.6	Time-integrated FWM for the Hückel model. Solid line: model IH, dashed: model IIIH, and dashed-dotted: laser pulse envelope.	186
11.7	$B_u$ and $A_g$ oscillator frequencies for the PPP model for a 30 carbon atom polyacetylene chain. There are 113 $B_u$ and 112 $A_g$ oscillators. The frequencies of the first eight $B_u$ ( $A_g$ ) oscillators are: 2.28, 3.49, 4.10, 4.57, 4.59, 4.95, 5.48, and $5.62eV$ (2.89, 3.73, 4.06, 4.52, 5.05, 5.12, 5.13, and $5.37eV$ ). . . . .	188
11.8	(a) Time-resolved amplitude and (b) phase of the FWM signal for time-delay $\tau = 0fs$ for the PPP model: Solid line: model IP, dashed: model IIP, dotted: model IIIP, and dashed-dotted: laser pulse envelope. . . . .	191
11.9	Convergence of the $X$ anharmonicities for the PPP model as function of number of virtual $A_g$ oscillator variables. Shown is the relative percent difference of the quantity to its converged value. . . . .	192
11.10	Same as Fig. 11.9 but for the $Y$ anharmonicities. . . . .	194
11.11	(a) Time-resolved amplitude and (b) phase of the FWM signal for time-delay $\tau = 0fs$ for the PPP model. Solid line: model VP, dashed: model IVP, and dashed-dotted: laser pulse envelope.	197
11.12	Time-integrated FWM for the PPP model. Solid line: model VP, dashed: model IVP. . . . .	198



# Chapter 1

## Introduction

Investigating the electronic structure of organic materials constitutes an important fundamental task of modern chemistry. The electronic excitations, charge-transfer, energy-transfer, and isomerization of such systems have been thoroughly studied and form the basis for our understanding of the photo-physics and photochemistry of complex molecules [4–7]. For example, photosynthesis and other photochemical biological processes which constitute the basis of our life on the Earth involve conjugated chromophores such as porphyrins and chlorophylls. These fundamental studies are closely connected to the technological applications. The nonlinear optical properties of large conjugated and aggregated polymers have been studied in search for new organic optical materials with large nonlinear polarizabilities [8–11,1,12–15] with potential applications to light emitting diodes, ultrafast switches, photodetectors and optical limiting materials [16–22].

One of the most important tools in the study of molecular electronic structures is optical spectroscopy which allows chemists and physicists to probe the dynamics of vibrations and electronic excitations within molecules and solids. Spectroscopic experimental investigations of organic molecules are more difficult than inorganic semiconductors due to problems related to sample-quality, controlled synthesis and poor solubility of large molecules [23,24]. The theoretical models used for describing molecular spectra versus those for extended

solids are usually quite different, and certain systems, such as clusters and polymers, are not readily described by either of these limiting cases.

The prediction and interpretation of spectroscopic measurements usually involves solving the many-electron problem, which requires an extensive numerical effort. The molecular methods can be classified into two major types, depending on the way they treat the coupling to the optical field. The first is based on a variational and perturbative treatment of the ground state in the presence of the electric field. For example, the Coupled-Perturbed Hartree-Fock (CPHF) procedure computes off-resonant optical polarizabilities by evaluating energy derivatives of molecular Hamiltonian perturbed by external static field. It involves expensive *ab initio* calculations with basis sets including diffuse and polarized functions, that are substantially larger than those required for computing the ground-state properties [10]. The second type uses time-dependent perturbation theory, which relates optical response to the properties of the excited states. For example, the Configuration-Interaction / Sum-over-States (CI/SOS) method [11,25] based on the expansion of the Stark energy of the molecule in powers of electric field, involves the calculations of both the ground state and excited states wavefunctions and the transition dipole moments between them [26,27]. Despite straightforward implementation of the procedure and the interpretation of the results in terms of quantum states (which is common in quantum chemistry), special care needs to be taken when choosing the right configurations. In addition, this method is not size-consistent [28,29] i.e. intrinsic interference effects resulting in an almost cancellation of very large contributions further limit its accuracy. The CI/SOS approach has been widely applied using semiempirical Hamiltonians (e.g. simple tight-binding or Hückel,  $\pi$ -electron Pariser-Par-Pople (PPP), Valence Effective Hamiltonians (VEH), Complete Neglect of Differential Overlap (CNDO), and Intermediate Neglect of Differential Overlap (INDO) models)

[10,11,30–37].

On the other hand, large polymers can also be treated using semiconductor band theories that focus on the dynamics of electron-hole pairs as opposed to the molecular viewpoint [38]. The size-scaling of the optical response, and the transition between these two regimes has not been fully explored for the lack of adequate theoretical methods. The global eigenstates carry too much information about the system, which makes it hard to use them efficiently in the interpretation of optical response and in the prediction of various trends. Band theories neglect electronic correlation effects in the  $G$  and  $S_i$ , and because they are formulated in momentum ( $k$ ) space they do not lend themselves very easily to real-space chemical intuition.

To formulate a hybrid formulation that bridges the gap between the chemical and semiconductor points of view we have to define **I**) an appropriate amount of information about the many-electronic system necessary to calculate molecular optical response, and **II**) an approximation which allows to solve this many-body problem.

**I. The reduced single-electron density matrix.** The complete information on the optical response of a quantum system is contained in its set of many-electron eigenstates  $|\nu\rangle, |\eta\rangle, \dots$  and energies  $\epsilon_\nu, \epsilon_\eta, \dots$  [26]. Using the many-electron wavefunctions it is possible to calculate all  $n$ -body quantities and correlations. Most of this information is, however, rarely used in the calculation of common observables (energies, dipole moments, spectra, *etc.*) which only depend on the expectation values of one- and two- electron quantities. In addition, since the number of states increases exponentially with the number of electrons, exact calculations become impractical even for fairly small molecules with a few atoms. A reduced description which only keeps a small amount of relevant information is called for. An important example of such a method is the density-functional theory (DFT) [39–43] which only retains the ground

state charge density profile:

$$\bar{\rho}_{nn} = \langle g | c_n^+ c_n | g \rangle , \quad (1.1)$$

where  $|g\rangle$  denotes the ground-state many-electron wavefunction and  $c_n^+$  ( $c_n$ ) is the Fermi annihilation (creation) operators for the n-th basis set orbital. Hohenberg and Kohn's theorem proves that the ground state energy is a unique and a universal functional of  $\rho_{nn}$  [44,45], making it possible to compute self consistently the charge distribution and the ground state energy. This approach has been remarkably successful, and extensions to excited states have been made as well [42,43].

In this thesis a reduced description is built using the single-electron density matrices [46–51]

$$\rho_{nm}^{\nu\eta} \equiv \langle \nu | c_n^+ c_m | \eta \rangle . \quad (1.2)$$

$|\nu\rangle$  and  $|\eta\rangle$  represent the global electronic states of the system, whereas n and m denote the atomic basis functions. These quantities carry more information than  $\bar{\rho}_{nn} \equiv \rho_{nn}^{gg}$ <sup>1</sup>, yet considerably less than the complete set of eigenstates.  $\rho^{\nu\nu}$  is the reduced single-electron density matrix in the state  $\nu$ . For  $\nu \neq \eta$   $\rho^{\nu\eta}$  is the density-matrix associated with the transition between  $\nu$  and  $\eta$ . When the system is driven by an optical field, its wavefunction becomes a coherent superposition of states

$$\Psi(t) = \sum_{\nu} a_{\nu}(t) |\nu\rangle , \quad (1.3)$$

and its density matrix is given by

$$\rho_{nm}(t) \equiv \langle \Psi(t) | c_n^+ c_m | \Psi(t) \rangle = \sum_{\nu\eta} a_{\nu}^*(t) a_{\eta}(t) \rho_{nm}^{\nu\eta} . \quad (1.4)$$

$\rho_{nm}^{\nu\eta}$  are thus the building blocks for the time-dependent single-electron density matrix  $\rho_{mn}(t)$ .

---

<sup>1</sup>Abbreviated notation  $\bar{\rho}$  for the ground state density matrix  $\rho^{gg}$  will be used throughout this thesis

The optical response involves only reduced information about the global eigenstates. This information is contained in the matrices  $\rho^{\nu n}$ . To illustrate this let us consider the frequency-dependent linear polarizability  $\alpha(\omega)$  which assumes the form

$$\alpha(\omega) = \sum_{\nu} \frac{2\Omega_{\nu}\mu_{g\nu}\mu_{g\nu}^*}{\Omega_{\nu}^2 - (\omega + i\Gamma)^2} \quad (1.5)$$

where  $\Gamma$  is a relaxation rate,  $\mu_{g\nu} = \langle g|\mu|\nu\rangle$  are the transition dipoles, and  $\Omega_{\nu} \equiv \epsilon_{\nu} - \epsilon_g$  are the transition frequencies. The molecular dipole  $\mu$  is a single-electron operator which may be expanded in the form

$$\mu = \sum_{nm} \mu_{nm} c_n^{\dagger} c_n, \quad (1.6)$$

and we have

$$\mu_{g\nu} \langle g|\mu|\nu\rangle = \sum_{nm} \mu_{nm} \rho_{nm}^{g\nu}. \quad (1.7)$$

Thus the matrices  $\rho^{g\nu}$  and the corresponding frequencies  $\Omega_{\nu}$  contain all necessary information for calculating the linear optical response. Higher order polarizabilities and other spectroscopic observables are computed in Chapters 2, 10, and 11.

**II. The time-dependent Hartree-Fock approximation.** Calculating  $\rho^{g\nu}$  through Eq. (1.2) implies that one first needs to calculate the eigenstates  $|\nu\rangle$  and  $|g\rangle$  and then use them to compute the matrix elements. However, the matrices  $\rho^{g\nu}$  and frequencies  $\Omega_{\nu}$  can be calculated directly using the time-dependent Hartree-Fock (TDHF) approach which allows us to avoid the tedious calculations of global eigenstates [52–56]. This approximation assumes that the many-body wavefunction is given by a single Slater determinant at all times and can be formulated in terms of closed equations of motion for the single-electron density matrix (see Chapter 2). These equations suggest an oscillator (quasiparticle) picture of optical response: the linear part of the equations describes the oscillators whereas the nonlinear terms represent anharmonicities that are responsible for the nonlinear optical response. The matrices  $\rho^{g\nu} \equiv \xi_{\nu}$

<sup>2</sup> appear as eigenmodes of the linearized TDHF equation with eigenfrequencies  $\Omega_\nu$ .

The TDHF equation of motion for the single-electron density matrix (Eq. (2.21) in Chapter 2) was first derived by Dirac in 1930 [57]. This equation has been introduced and explicitly applied in nuclear physics by Ferrel [58]. Since then the TDHF description was widely used in nuclear many-body physics in 50-60th [52,53]. Sekino and Bartlett derived the TDHF expressions for molecular optical polarizabilities using a density matrix formalism [54,33,34]. This approach was further successfully applied to conjugated polymer chains. The equations of motion for the time-dependent density matrix of polyenic chain were first derived and solved in [59]. Then the TDHF approach based on the Pariser-Par-Pople (PPP) hamiltonian was formulated and applied to linear and nonlinear optical response of neutral polyenes (up to 40 repeat units) [60] and PPV (up to 10 repeat units) [61]. The electronic oscillators <sup>3</sup> contributing to the response were identified and the size-scaling of optical susceptibilities was analyzed. The PPP hamiltonian [62] has  $K/2$  occupied and  $K/2$  unoccupied orbitals,  $K$  being the basis set size. Computations require calculating  $K^2$  electronic oscillators (eigenvectors of a  $K^2 \times K^2$  matrix representing the linearized TDHF equations) which are linear combination of all possible pairs of orbitals. It limited the studies to the PPP hamiltonian parameterized only for carbon and nitrogen, and moderate chain sizes (few tens of heavy atoms). The development of the classical TDHF representation and algebra of electronic oscillators [63,56] reduced the number of variables to  $K^2/4$  electron-hole oscillators which only represent occupied-unoccupied orbital pairs.

---

<sup>2</sup>Abbreviated notation  $\xi_\nu$  for the family of single-electron density matrices  $\rho^{g\nu}$  will be used throughout this thesis

<sup>3</sup>We shall refer to eigenmodes of the linearized TDHF equation  $\xi_\nu$  with eigenfrequencies  $\Omega_\nu$  as *electronic oscillators* since they represent collective motions of electrons and holes (see Chapter 2)

This thesis further advances of the CEO method. In Chapter 2 the Pariser-Parr-Pople (PPP) and the Intermediate Neglect of Differential Overlap / Spectroscopy (INDO/S) semiempirical molecular hamiltonians are introduced. The solution of the TDHF equations of motion for the reduced single-electron density matrix is expressed using electronic normal modes. An iterative DSMA procedure for direct computation of dominant electronic oscillators is further formulated and the efficiency of the DSMA calculations is illustrated. Finally, the real-space CEO analysis is outlined and the advantages of the density matrices versus states for representation of molecular optical response are discussed. In Chapter 3 the CEO is extended by calculating the response of the single-electron density matrix of a many-electron system to an external field. A Time-Dependent Density-Matrix-Response-Function Algorithm (DMRF) for inverting the resulting nonlinear response functions to obtain an effective quantum multilevel system that has the same response is developed. The number of effective states is gradually increased as higher-order nonlinearities are computed. The complete set of matrices  $\rho^{\nu n}$  out of computed electronic modes  $\rho^{g\nu}$  and excited state energies can be calculated.

In Chapter 4 the size-scaling and saturation of off-resonant polarizabilities (up to seventh order) of polyacetylene oligomers with up to 300 carbon atoms is analyzed in terms of collective electronic oscillators computed using the DSMA combined with the PPP hamiltonian. Simple analytical expressions for size and bond-length alternation dependence of off-resonant polarizabilities are derived using a single-oscillator approximation. Chapter 5 presents the CEO analysis of absorption spectra of Poly(p-phenylene vinylene) (PPV) oligomers. Collective electronic normal modes are calculated using the DSMA combined with the PPP hamiltonian. Spatial coherence displayed in two-dimensional plots of the five electronic normal modes which dominate the optical response of PPV oligomers with up to 50 repeat units (398 carbon atoms) in the 1.5 to 8

eV frequency range suggests a saturation to bulk behavior at about 5 repeat units. Linear absorption and off-resonant quadratic and cubic polarizabilities of substituted carotenoids with varying acceptor strength are investigated in Chapter 6 using CEO combined with the INDO/S hamiltonian. By varying the polyene chain length we show that the response of symmetric molecules is controlled by “bulk” delocalized excitations with coherence size  $\sim 12$  double bonds whereas the response of short polar molecules is dominated by a localized “charge-transfer” excitation created at the acceptor end with coherence and diagonal lengths  $\sim 12$  and  $\sim 17$  double bonds respectively. The DMRF technique is applied to calculate the excited electronic states of carotenoids. In Chapter 7 the absorption spectra of two families of dendrimers are analyzed by combining the CEO with the INDO/S hamiltonian. Electron-hole pairs created upon optical excitation of conjugated dendrimers (fractal antenna macromolecules) are shown to be localized within segments connected by benzene rings substituted at the *meta*- position. These results may be used in the design of artificial Light harvesting antennae with controlled energy funneling pathways.

In Chapter 8 the CEO analysis of the absorption spectra of Free-Base and Magnesium Porphins is presented. High frequency (4-6 eV) charge-transfer type excitations are identified. Electronic spectra of a family of stilbenoid dimers are calculated using CEO in Chapter 9. Comparison of the electronic modes of molecular aggregates with the corresponding monomers identifies the origin of the various optical transitions. The observed trends in absorption, fluorescence, and radiative lifetime of these molecules are fully accounted for. In Chapter 10 the size-scaling of polarizabilities of donor/acceptor substituted elongated polyenes is investigated. Collective electronic normal modes are obtained using the DSMA combined with the INDO/S hamiltonian. The second order polarizability ( $\beta$ ) is shown to originate from localized regions at the



donor/acceptor ends and therefore saturates to a constant value, independent on polyene size  $n$ , for large  $n$ . In contrast, the linear ( $\alpha$ ) and cubic ( $\gamma$ ) polarizabilities have contributions from the entire chain and grow linearly with  $n$ . The relevant electronic coherence sizes that control the optical response and may be valuable in the design of new optical materials are identified.

Equations of motion which describe the nonlinear optical response of conjugated polyenes using the CEO representation are derived in Chapter 11. Specific signatures of electronic correlations which enter as anharmonicities and scattering between oscillators are predicted in ultrafast resonant four-wave mixing. Only few resonant oscillators need to be considered explicitly; effects of the remaining (off resonant) oscillators are introduced via renormalized anharmonic coupling coefficients. The connection with inorganic semiconductors is established. Finally the main results of the thesis are discussed and summarized in Chapter 12.

# Chapter 2

## Collective Electronic Oscillator (CEO) Representation of Optical Response

### 2.1 The Pariser-Parr-Pople (PPP) and the Intermediate Neglect of Differential Overlap / Spectroscopy (INDO/S) Hamiltonians

Let us consider a general system of  $N$  electrons which can occupy  $K$  single-electron states ( $N \leq K$ ) and interact with an external field. The Hamiltonian is most generally is given by [51]

$$\hat{H} = \sum_{mn\sigma} t_{mn} c_{m\sigma}^+ c_{n\sigma} + \sum_{\substack{nmkl \\ \sigma\sigma'}} \langle nm|kl \rangle c_{m\sigma}^+ c_{n\sigma'}^+ c_{k\sigma'} c_{l\sigma} - \mathcal{E}(t) \sum_{mn\sigma} \mu_{mn} c_{m\sigma}^+ c_{n\sigma}, \quad (2.1)$$

where subscripts  $i, j, k, l$  run over known spatial atomic basis functions  $\{\chi_n\}$  and  $\sigma, \sigma'$  label spin components. These atomic orbitals are assumed to be orthogonal

$$\langle n|m \rangle = \int d\mathbf{r}_1 \chi_n^*(1) \chi_m(1) = \delta_{nm}. \quad (2.2)$$

$c_n^+(c_n)$  are the creation (annihilation) operators which satisfy the Fermi anti-commutation relations

$$c_{m\sigma} c_{n\sigma'}^+ + c_{n\sigma'}^+ c_{m\sigma} = \delta_{mn} \delta_{\sigma\sigma'}, \quad (2.3)$$

and all other anticommutators of  $c^+$  and  $c$  vanish.

The first term in Eq. (2.1) is the core-hamiltonian describing the kinetic energy and nuclear attraction of an electron

$$t_{nm} = \langle n | -\frac{1}{2}\nabla_1^2 - \sum_A \frac{Z_A}{|\mathbf{r}_1 - \mathbf{R}_A|} | m \rangle \equiv \int d\mathbf{r}_1 \chi_n^*(1) \left( \nabla_1^2 - \sum_A \frac{Z_A}{|\mathbf{r}_1 - \mathbf{R}_A|} \right) \chi_m(1), \quad (2.4)$$

where  $\mathbf{R}_A$  is the nuclear coordinate of atom  $A$ . The second term represents electron-electron Coulomb interactions where

$$\langle nm | kl \rangle = \int d\mathbf{r}_1 d\mathbf{r}_2 \chi_n^*(1) \chi_m^*(2) \frac{1}{r_{12}} \chi_k(1) \chi_l(2) \quad (2.5)$$

are the two-electron integrals. The interaction between the electrons and the external electric field  $\mathcal{E}(\mathbf{t})$  polarized along the chosen z-axis is given by the last term in Eq. (2.1),  $\mu$  being the dipole operator

$$\mu_{nm} = \langle n | \mu_z | m \rangle \equiv \int d\mathbf{r}_1 \chi_n^*(1) z_1 \chi_m(1). \quad (2.6)$$

To solve the Schrödinger equation

$$\hat{H}\Psi = E\Psi, \quad (2.7)$$

for the ground state we assume the simplest antisymmetric wavefunction i.e a single Slater determinant  $\Psi = |\phi_1(1)\phi_2(2)\dots\phi_N(N)\rangle$  [51] (Hartree-Fock approximation). Here  $\{\phi_\alpha\}$  are the molecular orbitals. Following Roothaan's procedure [51] they are expanded as linear combinations of spatial atomic basis functions  $\{\chi_n\}$

$$\phi_\alpha = \sum_i^K C_{\alpha i} \chi_i. \quad (2.8)$$

The essence of the Hartree-Fock approximation is to replace the complicated many-body problem by a one-electron problem in which electron-electron repulsion is treated in an average way. By minimizing the ground state energy

with respect to the choice of molecular orbitals one can derive a Hartree-Fock eigenvalue equation:

$$FC = C\epsilon. \quad (2.9)$$

This equation may be recast in the form

$$[F(\bar{\rho}), \bar{\rho}] = 0. \quad (2.10)$$

Hereafter we will focus on closed-shell molecules and exclude spin variables [51]. Generalization to the unrestricted opened-shell case is straightforward. For closed-shells the ground-state density matrix is related to the molecular orbital expansion coefficients (Eq. (2.8)) as

$$\bar{\rho}_{nm} = 2 \sum_a^{N/2} C_{na} C_{ma}^*. \quad (2.11)$$

$F(\bar{\rho})$  is the Fock matrix with matrix elements

$$F_{nm}(\bar{\rho}) = t_{nm} + V_{nm}(\bar{\rho}), \quad (2.12)$$

and the matrix representation of the Coulomb electronic operator  $V$  in the atomic basis set  $\{\chi_n\}$  is

$$V(\bar{\rho})_{mn} = \sum_{k,l}^K \bar{\rho}_{kl} [\langle mk|nl \rangle - \frac{1}{2} \langle mn|kl \rangle]. \quad (2.13)$$

The Hartree-Fock equation (2.9) is nonlinear and should be solved iteratively (the self consistent field (SCF) procedure). SCF starts by calculating the average Coulomb field  $V$  from the initial guess of molecular orbitals. Then the new set of orbitals is obtained solving the eigenvalue problem (2.9). Using these new orbitals, we can obtain new field  $V$  and repeat the procedure until self-consistency is reached.

In this Chapter we first consider a Pariser-Parr-Pople (PPP) parameterization of the hamiltonian (2.1):

$$\hat{H} = \sum_{mn\sigma} t_{mn} c_{m\sigma}^+ c_{n\sigma} + \frac{1}{2} \sum_{\substack{mn \\ \sigma\sigma'}} V_{nm} c_{m\sigma}^+ c_{n\sigma'}^+ c_{n\sigma'} c_{m\sigma} - \mathcal{E}(t) \sum_{n\sigma} \mu_{nn} c_{n\sigma}^+ c_{n\sigma}. \quad (2.14)$$

Here each carbon atom has a single  $\pi$  orbital [60,55,61,62].  $K$  then coincides with the number of carbon atoms. PPP hamiltonian reproduces many important properties of conjugated polyenes [62]. The first term of Eq. (2.1) is the Hückel hamiltonian, where  $t_{nn} = \sum_m V_{nm}$  is the Coulomb integral at the  $n$ -th atom and  $t_{mn}$  ( $m \neq n$ ) is the nearest-neighbor transfer integral between the  $n$ -th and  $m$ -th atoms:  $t_{n,n\pm 1} = \beta - \beta' l_n$  and  $l_n$  is the deviation of the  $n$ -th bond length from the mean bond length along the chain. The second term (Eq. (2.13)) representing electron-electron Coulomb interactions has the form:

$$V(\bar{\rho})_{mn} = -V_{mn}\bar{\rho}_{mn} + 2\delta_{mn} \sum_l V_{ml}\bar{\rho}_{ll}. \quad (2.15)$$

The repulsion between the  $n$ -th and  $m$ -th sites is given by Ohno's formula:

$$V_{nm} = \frac{U}{\sqrt{1 + (r_{nm}/a_0)^2}} \quad (2.16)$$

where  $U = U_0/\epsilon$  is the on-site Hubbard repulsion and  $\epsilon$  is the static dielectric constant. The basis set is localized so that the dipole moment is diagonal  $\mu_{nm} = e\mathbf{r}_n\delta_{nm}$ . The parameters of the PPP model were adjusted to reproduce the energy gap for polyacetylene ( $2.0eV$ ):  $U_0 = 11.13eV$ ,  $\beta_0 = -2.4eV$ ,  $\beta_1 = -3.5eV\text{\AA}^{-1}$ ,  $\epsilon = 1.5$ ,  $a_0 = 1.2935\text{\AA}$  [60,55]. This hamiltonian was parametrized only for carbon and nitrogen and, therefore, it allows to treat only a narrow range of conjugated molecules.

The more rigorous semiempirical (INDO/S) hamiltonian reproduces the spectra of simple chromophores at the singly excited CI level. The INDO approximation [64–67] limits the basis set to valence orbitals of Slater type. The exchange terms in the two-electron interaction are permitted only among orbitals located on the same atom

$$\langle \chi_n^A \chi_k^B | \chi_m^A \chi_l^B \rangle = \begin{cases} \langle \chi_n^A \chi_k^A | \chi_m^A \chi_l^A \rangle & A = B \\ \langle \chi_n^A \chi_k^B | \chi_m^A \chi_l^B \rangle \delta_{nm} \delta_{kl} & A \neq B \end{cases} \quad (2.17)$$

where  $\chi_n^A$  belongs to atom A and  $\chi_n^B$  to atom B. The four-dimensional matrix  $\langle \chi_n \chi_k | \chi_m \chi_l \rangle$  thus becomes block-diagonal in two dimensions. The parameters of the INDO/S hamiltonian are given in [64–67]. INDO/S (Spectroscopy)

hamiltonian first introduced by Pople [64,65] and parameterized in the original works of Zerner and collaborators [66–69] gains wide popularity in optical response computations. INDO-CI calculations have been previously successfully applied to studies of electronically excited states in a wide variety of chromophores, including transition metals [66,67,69]. The ZINDO code developed by Zerner and co-workers serves as a convenient platform for these calculations. We found that the INDO/S hamiltonian works extremely well without further reparameterization with the TDHF for a broad range of molecules. This combination made it possible to calculate the optical properties of a broad range of molecules.

## 2.2 The Single-Electron Density Matrix and the TDHF equations

The TDHF approach provides a convenient approximation scheme for calculating the optical response of large molecules. The reduced single-electron density matrix Eq. (1.4) representing the molecule driven by an external field is given by  $\rho(t) = \bar{\rho} + \delta\rho(t)$  where the ground-state density matrix  $\bar{\rho}$  is the key input to this calculations. The diagonal element of  $\rho_{nm}$  ( $n = m$ ) represents the charge at the  $n$ 'th atomic orbital, and

$$q_A = \sum_{n \in A} \bar{\rho}_{nn} - Z_A \quad (2.18)$$

is the net charge on the atom  $A$ . The off-diagonal elements ( $n \neq m$ ) represent the electronic coherences between atomic orbitals. In particular,  $\bar{\rho}_{n_A m_B}$  describe the chemical bonding strength (bond-order) between atoms  $A$  and  $B$ . The matrix elements of  $\delta\rho_{nm}(t)$  represent the changes in these quantities induced by the electric field.

We start with the Heisenberg equation of motion for  $\rho_{nm}(t) = \langle c_n^\dagger c_m \rangle$ :

$$i \frac{\partial \rho_{nm}}{\partial t} = \langle [c_n^\dagger c_m, H] \rangle, \quad (2.19)$$

where hamiltonian  $H$  is given by Eq (2.1). Equation (2.19) is exact but not closed since higher order products (two-electron density matrices  $\rho_{nmn'm'}^{(2)}(t) = \langle c_n^+ c_m^+ c_{n'} c_{m'} \rangle(t)$ ) show up in the right hand side. Writing equations of motion for these higher products will yield increasingly higher products. This is the famous hierarchy of many-body dynamics that is common to classical and quantum mechanics. To overcome this difficulty one need a truncation procedure. The simplest assumes that the many-body wavefunction is given by a single Slater determinant at all times. This yields the time dependent Hartree-Fock factorization [70,55,56,63]

$$\langle c_n^+ c_m^+ c_{n'} c_{m'} \rangle(t) = \langle c_n^+ c_{n'} \rangle \langle c_m^+ c_{m'} \rangle(t) + \langle c_n^+ c_{m'} \rangle \langle c_m^+ c_{n'} \rangle(t). \quad (2.20)$$

Applying this approximation to Eq. (2.19) we obtain the following closed equations of motion for the single-electron density matrix  $\rho(t)$ .

$$i \frac{\partial \rho(t)}{\partial t} = i \frac{\partial \delta \rho(t)}{\partial t} = [F(\rho), \rho] - \mathcal{E}(t) \cdot [\mu, \rho]. \quad (2.21)$$

To zero order in the field we recover the stationary solution Eq. (2.10).

This set of  $K \times K$  matrix equations may be solved numerically for  $\delta \rho(t)$  either in frequency [60,61] or time [71] domain. We can further restrict the number of equation to variables which contain only occupied-unoccupied orbital pairs and develop an convenient algebra of electronic oscillators [63,56]. To that end we first decompose  $\delta \rho(t)$  into two components

$$\delta \rho(t) = \xi(t) + T(\xi(t)), \quad (2.22)$$

where  $\xi$  represents the particle-hole (interband) and  $T(\xi)$  represents the particle-particle and the hole-hole (intraband) parts. This decomposition is illustrated by Fig 2.1.

Since the many-electron wavefunction is represented by a single Slater determinant, the total density matrix  $\rho(t)$  must be a projector at all times [52,72,56]:

$$(\bar{\rho} + \delta \rho(t))^2 = \bar{\rho} + \delta \rho(t). \quad (2.23)$$

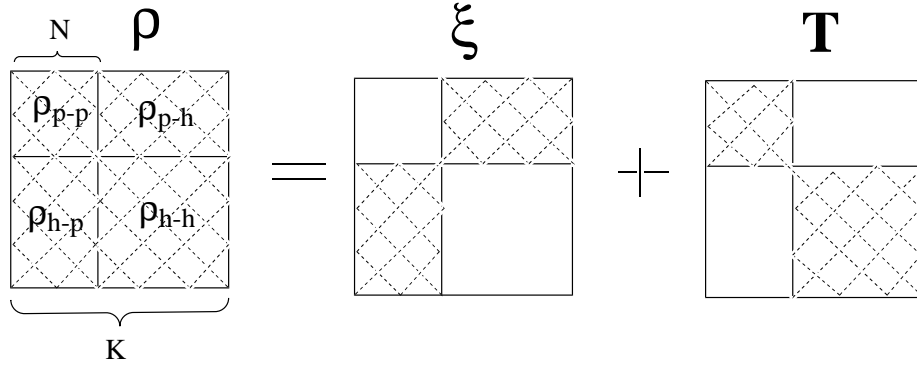


Figure 2.1: Decomposition of the single-electron density matrix to the particle-hole : hole-particle (interband) and particle-particle : hole-hole (intraband) parts shown in the molecular orbital basis set representation. The dimensionality of density matrix  $\rho$  defined by the basis set size is  $K \times K$ . We assume  $N$  occupied and  $K - N$  unoccupied orbitals: the ground-state density matrix  $\bar{\rho}$  is then diagonal in the particle-particle block and zero otherwise in molecular orbitals. The dimensionality of interband and intraband parts are  $2N(K - N)$  and  $N^2 + (K - N)^2$  respectively.

This property of  $\bar{\rho}$  allows us to project any matrix  $\xi$  into the particle-hole ( $p-h$ ) subspace

$$\xi_{p-h} = [[\xi, \bar{\rho}], \bar{\rho}], \quad (2.24)$$

Consequently, not all matrix elements are independent. The number of degrees of freedom of  $\delta\rho$  subject to the condition Eq. (2.23) is precisely the number of its particle-hole matrix elements [56]. In Appendix 2.7  $T(\xi)$  is expressed in terms of  $\xi$

$$T(\xi) = \left( \bar{\rho} - \frac{I}{2} \right) \left( I - \sqrt{I - 4\xi^2} \right), \quad (2.25)$$

where  $I$  is the unit  $K \times K$  matrix. Eq. (2.25) can be expanded in powers of  $\xi$

$$T(\xi) = (I - 2\bar{\rho})(\xi^2 + \xi^4 + 2\xi^6 + \dots). \quad (2.26)$$

An alternative expansion is given in Ref. [56,70]

$$T(\xi) = \frac{1}{2!} [[\xi, \bar{\rho}], \xi] + \frac{1}{4!} [[\xi, \bar{\rho}], [[\xi, \bar{\rho}], [[\xi, \bar{\rho}], \xi]]] + \dots \quad (2.27)$$

In Eqs (2.26) and (2.27), all  $\xi$  are taken at time  $t$ ,  $\xi = \xi(t)$ . The expansions (2.26) and (2.27) are identical. For example, to second order in  $\xi$ ,



Eq. (2.27) reads  $\frac{1}{2!}[[\xi, \bar{\rho}], \xi] = \xi \bar{\rho} \xi - \frac{1}{2}(\bar{\rho} \xi^2 + \xi^2 \bar{\rho})$ . The projection property of  $\bar{\rho}$  [56] implies the following relations for any interband density matrix  $\xi$ :  $\xi = \bar{\rho} \xi + \xi \bar{\rho}$  and  $\bar{\rho} \xi^2 = \xi^2 \bar{\rho}$  (note, that  $\xi^2$  is an intraband matrix). Using these identities we recover the second order term in Eq. (2.26).

Projecting Eq. (2.21) to the particle-hole subspace using Eq. (2.24) we obtain the following closed equations of motion for  $\xi$ .

$$i \frac{\partial \xi}{\partial t} - L \xi = R(\xi)_{p-h} - \mathcal{E}(t) \cdot [\mu, \bar{\rho}], \quad (2.28)$$

where  $L$  is a linear operator in Liouville space (i.e. superoperator) [73,70,55,56] given by

$$L \xi = [F(\bar{\rho}), \xi] + [V(\xi), \bar{\rho}], \quad (2.29)$$

and

$$R(\xi) = [F(\xi), \xi + T(\xi)] + [F(T(\xi)), \bar{\rho} + \xi] - \mathcal{E} \cdot [\mu, \xi + T(\xi)] \quad (2.30)$$

is the nonlinear part of the equation projected onto the particle-hole subspace (Eq. (2.24)). The Fock operator  $F$  and the Coulomb operator  $V$  are defined by Eqs (2.12) and (2.13).

The time-dependent polarization which determines all optical properties is finally given by

$$P(t) = Tr(\mu \xi(t)) + Tr(\mu T(\xi(t))). \quad (2.31)$$

Eqs. (2.28) and (2.25) constitute the basic TDHF equations [56]. They may be solved by expanding the density matrix in powers of the external field

$$\xi = \xi^{(1)} + \xi^{(2)} + \dots, \quad T(\xi) = T^{(2)}(\xi) + T^{(3)}(\xi) + \dots, \quad (2.32)$$

where  $T^{(j)}(t)$  is expressed in terms of  $\xi^{(j)}$  by comparing Eq. (2.26) (or Eq. (2.27)) with Eq. (2.32):

$$T^{(1)}(t) \equiv 0,$$

$$\begin{aligned}
T^{(2)}(t) &= (I - 2\bar{\rho})(\xi^{(1)}(t))^2, \\
T^{(3)}(t) &= (I - 2\bar{\rho})(\xi^{(2)}(t)\xi^{(1)}(t) + \xi^{(1)}(t)\xi^{(2)}(t)), \\
T^{(4)}(t) &= (I - 2\bar{\rho})(\xi^{(3)}(t)\xi^{(1)}(t) + \xi^{(2)}(t)\xi^{(2)}(t) + \xi^{(1)}\xi^{(3)}(t)).
\end{aligned} \tag{2.33}$$

The polarization to  $j$ 'th order in the external field  $\mathcal{E}(t)$  is calculated by taking the expectation value of the dipole operator  $\mu$  with respect to the time dependent density matrix

$$P^{(j)}(t) = Tr(\mu\delta\rho^{(j)}(t)), \tag{2.34}$$

with

$$\delta\rho^{(j)}(t) = \xi^{(j)}(t) + T^{(j)}(t). \tag{2.35}$$

The original nonlinear equation (2.28) is then transformed into a hierarchy of linear inhomogeneous equations. To  $j$ -th order we have

$$i\frac{\partial\xi^{(j)}(t)}{\partial t} - L\xi^{(j)}(t) = \eta^{(j)}(t), \tag{2.36}$$

where  $\eta^{(j)}(t)$  is given in terms of  $\bar{\rho}$  and lower order  $\xi^{(k)}$   $k < j$ ,

$$\begin{aligned}
\eta^{(1)}(t) &= -\mathcal{E}(t)[\mu, \bar{\rho}], \\
\eta^{(2)}(t) &= \left[ \left( [V(\delta\rho^{(1)}(t)), \delta\rho^{(1)}(t)] + [V(T^{(2)}(t)), \bar{\rho}] - \mathcal{E}(t)[\mu, \delta\rho^{(1)}(t)] \right), \bar{\rho} \right], \\
\eta^{(3)}(t) &= \left[ \left( [V(\delta\rho^{(2)}(t)), \delta\rho^{(1)}(t)] + [V(\delta\rho^{(1)}(t)), \delta\rho^{(2)}(t)] \right. \right. \\
&\quad \left. \left. + [V(T^{(3)}(t)), \bar{\rho}] - \mathcal{E}(t)[\mu, \delta\rho^{(2)}(t)] \right), \bar{\rho} \right].
\end{aligned} \tag{2.37}$$

The linear and non-linear optical response is calculated by solving Eq. (2.36) either in the frequency domain or in the time domain. In the frequency domain, the procedure involves diagonalizing the linearized Liouville operator  $L$  which requires a large memory ( $\sim N^4$  where  $N$  is the total number of orbitals in the system). Time-domain calculations do not require a large memory ( $\sim N^2$ ) and may be applied for larger systems. However evaluating

commutators in Eqs. (2.29) and (2.30) is time consuming. These difficulties limit the application of the TDHF to basis set size of about 100 functions <sup>1</sup>.

## 2.3 Properties of the Electronic Normal Modes

Here a few properties of the tetradic linear  $M_0 = N \times (K - N)$  dimensional space defined by the Liouville operator  $L$  [73,70,55,56] are reviewed. A scalar product of any two interband  $K \times K$  matrices  $\xi$  and  $\eta$  which are the elements of this space is defined by [73,70,56]

$$\langle \xi | \eta \rangle \equiv Tr(\bar{\rho}[\xi, \eta]). \quad (2.38)$$

We have used the bra (ket) to underline the similarity with Dirac's Hilbert space notation. The Liouville operator  $L$  is Hermitian with respect to this scalar product:

$$\langle L\xi, \eta \rangle = \langle \xi, L\eta \rangle. \quad (2.39)$$

Eq. (2.38) obeys the following properties:

$$\langle \xi | \eta \rangle = \langle \eta^+ | \xi^+ \rangle^* = -\langle \eta | \xi \rangle. \quad (2.40)$$

The eigenmodes  $\xi_\nu$  and eigenfrequencies  $\Omega_\nu$  of  $L$  satisfy the equation.

$$L\xi_\nu = \Omega_\nu \xi_\nu \quad L\xi_\nu^+ = -\Omega_\nu \xi_\nu^+, \quad \nu = 1, \dots, M_0. \quad (2.41)$$

The eigenmodes come in conjugate pairs: Each vector  $\xi_\nu$  with frequency  $\Omega_\nu$  has a counterpart  $\xi_{-\nu} = \xi_\nu^+$  with frequency  $-\Omega_\nu$ . Since  $L$  is real, the electronic modes can be taken to be real as well. A classical mode picture of the optical response is obtained by constructing the electronic oscillators defined by the coordinate-momentum variables

$$Q_\nu = \frac{\xi_\nu + \xi_\nu^+}{\sqrt{2}}, \quad P_\nu = -i \frac{\xi_\nu - \xi_\nu^+}{\sqrt{2}}. \quad (2.42)$$

---

<sup>1</sup>This estimate is based on a single MIPS R8000 processor on the SGI Power Indigo workstation.

$P$  and  $Q$  satisfy the relation

$$LQ_\nu = \Omega_\nu iP_\nu, \quad LiP_\nu = \Omega_\nu Q_\nu, \quad \nu = 1, \dots, M_0. \quad (2.43)$$

We shall adopt the following normalization of the electronic modes [56]:

$$\langle \xi_\alpha^+ | \xi_\beta \rangle = \delta_{\alpha\beta}, \quad \langle \xi_\alpha^+ | \xi_\beta^+ \rangle = 0; \quad (2.44)$$

$$\langle P_\alpha | Q_\beta \rangle = i\delta_{\alpha\beta}, \quad \langle P_\alpha | P_\beta \rangle = \langle Q_\alpha | Q_\beta \rangle = 0. \quad (2.45)$$

The electronic oscillator is a pair of conjugated electronic modes ( $K \times K$  matrices  $\xi_\nu$  and  $\xi_\nu^+$  or  $P_\nu$  and  $Q_\nu$ ) with the frequency  $\Omega_\nu$ . Any interband  $K \times K$  matrix  $A$  can be expanded in the basis set of electronic oscillators as

$$A = \sum_{\nu=1}^{M_0} \langle \xi_\nu^+ | A \rangle \xi_\nu - \langle \xi_\nu | A \rangle \xi_\nu^+ = \sum_{\nu=1}^{M_0} \langle Q_\nu | A \rangle iP_\nu - \langle iP_\nu | A \rangle Q_\nu. \quad (2.46)$$

## 2.4 The Density–Matrix–Spectral–Moment Algorithm (DSMA)

The Density–Matrix–Spectral–Moments Algorithm (DSMA) [74,73,70] is an approximate scheme for solving the TDHF equations which allows us to calculate  $\xi^{(j)}$  from the source ( $\eta^{(j)}$ ) by solving Eq. (2.36) without a direct diagonalization of  $L$ . This is accomplished by computing the set of electronic oscillators which dominate the expansion of  $\eta^{(j)}$ . One can take  $\eta^{(j)}(t)$  to be real and express it in terms of our momentum variables as [73,70]

$$\eta^{(j)} = \sum_{\nu=1}^{M_0} \langle \xi_\nu^+ | \eta^{(j)} \rangle \xi_\nu - \langle \xi_\nu | \eta^{(j)} \rangle \xi_\nu^+ = \sum_{\nu=1}^{M_0} \langle Q_\nu | \eta^{(j)} \rangle iP_\nu = \sum_{\nu=1}^{M_0} \mu_\nu^{(j)} iP_\nu, \quad (2.47)$$

where  $\eta^{(j)}$  can be viewed either in the frequency or in the time domain, and  $\mu_\nu^{(j)} = \sqrt{2} \langle \xi_\nu | \eta^{(j)} \rangle = \langle Q_\nu | \eta^{(j)} \rangle$  are the real frequency (or time) dependent expansion coefficients. These electronic oscillators provide a convenient procedure for solving Eq. (2.36) [56]. The formal solutions of Eq. (2.36) in the time

and frequency domain are

$$\xi^{(j)}(t) = \int_0^t d\tau e^{-iL(t-\tau)} \eta^{(j)}(\tau), \quad \xi^{(j)}(\omega) = \frac{1}{\omega - L} \eta^{(j)}(\omega). \quad (2.48)$$

Substituting the expansion (2.47) for  $\eta^{(j)}$  in these equations and utilizing the eigenvector properties of the modes

$$\begin{aligned} e^{-iLt} \xi_\nu &= e^{-i\Omega_\nu t} \xi_\nu, & e^{-iLt} \xi_\nu^+ &= e^{i\Omega_\nu t} \xi_\nu^+, \\ \frac{1}{\omega - L} \xi_\nu &= \frac{1}{\omega - \Omega_\nu} \xi_\nu, & \frac{1}{\omega - L} \xi_\nu^+ &= \frac{1}{\omega + \Omega_\nu} \xi_\nu^+ \end{aligned} \quad (2.49)$$

we obtain the solution of Eq. (2.36) in terms of eigenmodes  $\xi_\nu$  and  $\xi_\nu^+$  (or  $P_\nu$  and  $Q_\nu$ ). For example, the  $j$ -th order interband component of the reduced single-electron density matrix in frequency domain is given by

$$\xi^{(j)}(\omega) = \sum_{\nu=1}^{M_0} \mu_\nu^{(j)}(\omega) \left[ \frac{\Omega_\nu}{\Omega_\nu^2 - \omega^2} Q_\nu - \frac{i\omega}{\Omega_\nu^2 - \omega^2} P_\nu \right]. \quad (2.50)$$

Since only few electronic oscillators contribute significantly to the source in the expansion (2.47), the summation can be truncated at some effective number of oscillators  $M \ll M_0$  without sacrificing accuracy.

The family of the density-matrix spectral moments is defined as  $S_n \equiv L^n \eta$  which are the expansion coefficients in the short-time evolution of the density-matrix response function (see Appendix 2.8). These moments are used to construct the main DSMA equations [73,70]

$$S_n^{(j)} = \sum_{\nu=1}^M \Omega_\nu^n \mu_\nu^{(j)} i P_\nu, \quad n = 0, 2, 4, \dots, 2M - 2, \quad (2.51)$$

$$S_n^{(j)} = \sum_{\nu=1}^M \Omega_\nu^n \mu_\nu^{(j)} Q_\nu, \quad n = 1, 3, 5, \dots, 2M - 1, \quad (2.52)$$

where  $S_0^{(j)} = \eta^{(j)}$  and  $S_n^{(j)} = L^n S_0^{(j)}$ ,  $n = 1, 2, \dots$ . In principle, the spectral moments  $S_n$  can be expressed using the electronic normal modes  $\xi_\nu$ , but the choice of momentum-coordinate hermitian variables has two advantages: First,

it allows to separate the total system of equations (2.51, 2.52) into two independent subsystems (2.51) and (2.52), which is computationally preferable. Second, the matrix  $\eta$ , which is the input to the procedure, is hermitian and expressed through momentum variables (Eq. (2.47)). The higher moments  $S_n$  are, therefore, either momentum or coordinate type.

The scalar products  $\mathcal{K}_n^{(j)} \equiv \langle S_n^{(j)} | S_{n+1}^{(j)} \rangle$ ,  $n = 1, 2, \dots, 2M$  provide a set of equations for the frequencies  $\Omega_\nu$  and oscillator strength  $f_\nu^{(j)} = (\mu_\nu^{(j)})^2 \Omega_\nu^{-2}$ :

$$\sum_{\nu=1}^M f_\nu^{(j)} \Omega_\nu^{2n} = \mathcal{K}_n^{(j)} \quad n = 0, 1, 2, \dots, 2M - 1. \quad (2.53)$$

The set of DSMA equations [(2.51)-(2.53)] is now complete. We start our calculations by computing the moments  $S_n^{(j)}$  and  $\mathcal{K}_n^{(j)}$  by acting Liouville operator  $L$  (2.29) on the source  $\eta^{(j)}$  and using definition of the scalar product (2.38). We then solve Eqs. (2.53) for the frequencies  $\Omega_\nu$  and oscillator strengths  $f_\nu^{(j)}$ . These nonlinear equations have a simple analytical solution (Appendix 2.9). Once we have  $\Omega_\nu$  and  $\mu_\nu^{(j)}$ , we solve (2.51) and (2.52) for the modes  $P_\nu$  and  $Q_\nu$ . The most time consuming part of the DSMA is the calculation of commutators. Typically only a small number of modes is required and the DSMA greatly reduces the numerical effort involved in solving the complete TDHF equations.

The procedure starts with a single mode approximation and by successively adding new modes improved approximations for frequencies and oscillator strengths of the dominant modes is obtained, until some convergence criteria are satisfied. The linear response  $j = 1$  is calculated first. The resulting first order modes are used to calculate the relevant modes for the second order response ( $j = 2$ ) and so forth. Because of truncation at  $M$  oscillators, the resulting electronic modes do not coincide with the TDHF modes. Eqs. (2.43)

---

<sup>2</sup>Quantities  $f_\nu^{(j)}$  and  $\mu_\nu^{(j)}$  depend on the external field (Eq. (2.28)). For example, for linear response we have  $f_\nu^{(1)} \equiv -\mathcal{E}(t)f_\nu$  and  $\mu_\nu^{(1)} \equiv -\mathcal{E}(t)\mu_\nu$ . Here  $f_\nu$  and  $\mu_\nu$  are the oscillator strength and the ground state dipole, respectively.

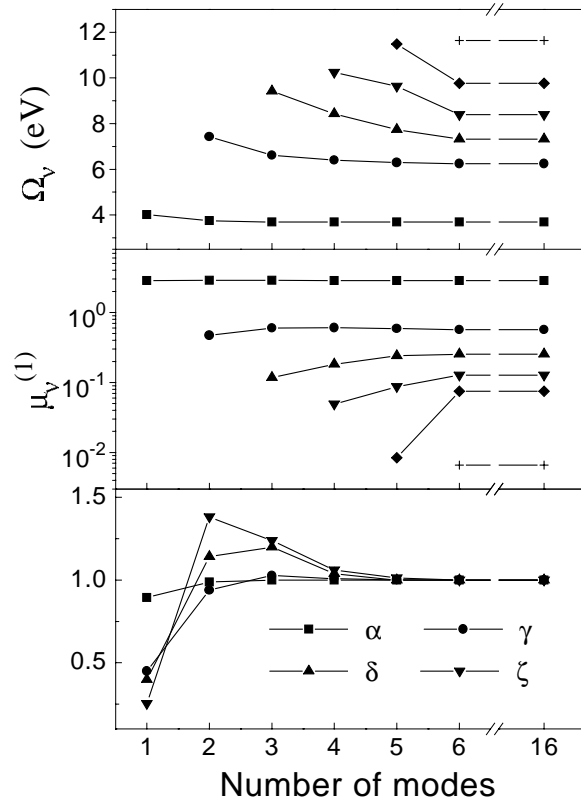


Figure 2.2: Variation of electronic oscillator frequencies  $\Omega_\nu$ , effective dipole moments  $\mu_\nu^{(1)}$ , and first ( $\alpha$ ), third ( $\gamma$ ), fifth ( $\delta$ ), and seventh ( $\zeta$ ) off-resonant polarizabilities with the number of modes used for octatetraene ( $N=8$ ). The polarizabilities will be defined later in this Section. Here convergence of the DSMA to the full TDHF calculation ( $M = 16$ ) is demonstrated. The magnitudes of polarizabilities are normalized at their converged values:  $\alpha = 3.2 \times 10^{-23} \text{ esu}$ ,  $\gamma = 6.6 \times 10^{-35} \text{ esu}$ ,  $\delta = 1.4 \times 10^{-46} \text{ esu}$ ,  $\zeta = 2.3 \times 10^{-59} \text{ esu}$ .

hold approximately, but the normalization relations (2.45) are satisfied exactly. These effective electronic oscillators give the best approximation for the spectrum with a given number of features ( $M$ ).

The following examples show the efficiency of the DSMA for calculations done with the PPP hamiltonian. Convergence as a function of the number of modes  $M$ ,  $M = 1 - 6$  is shown in Fig. 2.2 for octatetraene ( $N = 8$ ). Only few (3-4) modes contribute significantly to the response, but to calculate them accurately we need to include some additional high frequency modes with very small oscillator strengths. Using six modes we reproduce the frequencies and

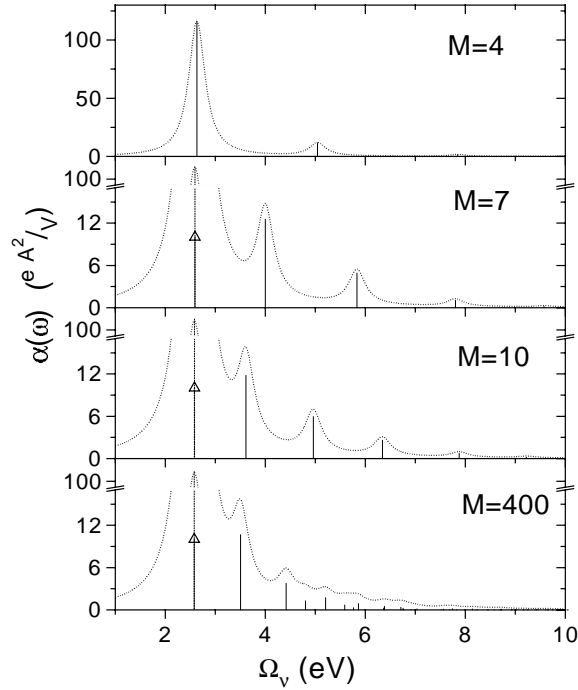


Figure 2.3: Convergence of the linear absorption (the imaginary part of  $\alpha$  (Eq. (1.5))) with the number of modes used for  $N=40$  atom oligomer. The linewidth is  $\epsilon = 0.2eV$ . Note, that the fundamental band at  $2.57 eV$  with strength  $109 e\text{\AA}^2/V$  [ $1.57 \times 10^{-21} esu$ ] remains basically the same in all panels.

the first order effective dipoles  $\mu_v^{(1)}(\omega = 0)$  to  $10^{-8}$  of the values for the full TDHF (16-mode) calculation. The figure also shows that the polarizabilities converge much faster than the frequencies and dipoles of individual modes. The convergence of the linear absorption (the imaginary part of  $\chi^{(1)}$  (Eq. (2.55))) with the number of modes for a  $N=40$  atom oligomers is displayed in Fig. 2.3. Note that the strong band edge transition is reproduced well even at  $M=4$ . The weaker transitions at higher frequencies require more modes. The convergence of the lowest three nonvanishing polarizabilities ( $\alpha$ ,  $\gamma$ , and  $\delta$ ) of polyacetylene chains with up to 40 carbon atoms as a function of the number of modes used is shown on Fig. 2.4. The linear response is well represented by a single mode calculation whereas the 8 modes approximation gives good values for high hyperpolarizabilities. The DSMA computational time (and memory) requirements of scale very favorably with system size:  $\sim N^3$  (and



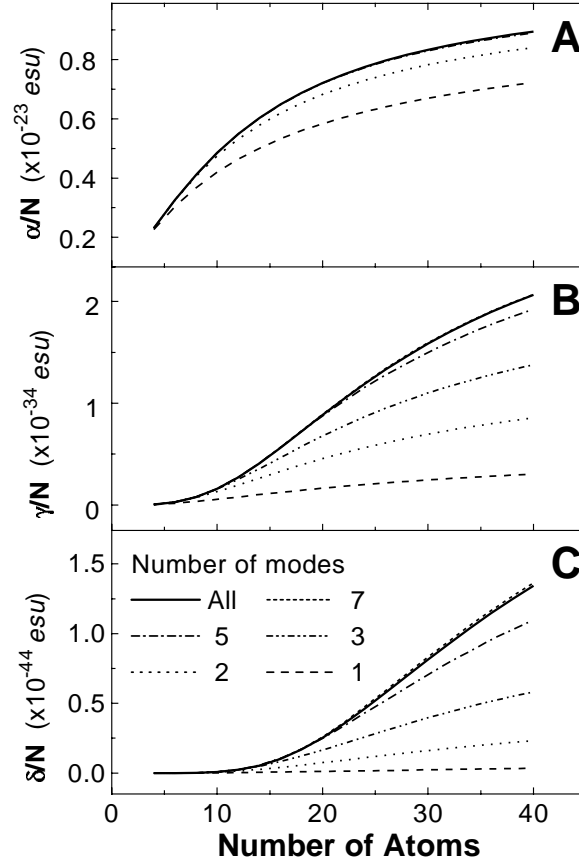


Figure 2.4: **A - C**) convergence of the lowest three nonvanishing polarizabilities ( $\alpha$ ,  $\gamma$ , and  $\delta$ ) of polyacetylene chains (up to 40 carbon atoms) with the number of modes used for calculations. The polarizabilities will be defined later in this Section. Here convergence of the DSMA is demonstrated. The results obtained with the full TDHF calculations (panel **(A)** and **(B)**) and with  $M = 12$  modes (panel **(C)**) are shown by solid lines. Note that  $M = 7$  modes approximation gives good values for hyperpolarizabilities  $\gamma$ , and  $\delta$

$N^2$ ) compared with  $\sim N^6$  (and  $N^4$ ) for the TDHF and  $\sim N^8$  (and  $N^6$ ) for the SOS/CI. Furthermore, the computational time of the  $j$ 'th order polarizability scales only linearly with  $j$ . This makes it possible to calculate high order nonlinearities of very large molecules [3] with modest computational effort.

One advantage of the DSMA is that it immediately gives a global overview of the entire spectrum. However the number of effective oscillators  $M$  cannot be increased at will to improve the accuracy. High moments scale as ( $\mathcal{K}_n \sim \Omega^{2n}$ ) and are dominated by the high frequency tails. Therefore increasing

the number of oscillators does not refine the low and middle frequency range. In practice  $M$  is limited to  $\leq 10 - 14$ . Applications of the DSMA using the PPP hamiltonian which only describes the  $\pi$ -electron system allowed to calculate accurately spectra of polyens dominating by a few lines. The INDO/S hamiltonian includes also the valence electrons, therefore the source is not limited to  $\pi - \pi^*$  molecular excitations but also depends on a manifold of high-frequency atomic transitions. For molecules with many peaks in the spectra, the DSMA does not reproduce delicate spectral features such as excitations with a small oscillator strength.

To improve the accuracy, the DSMA needs to be applied iteratively. The DSMA automatically generates orthonormal effective oscillators (Eqs. (2.45)) which satisfy the eigenvalue equation (2.43) in an optimal way. Therefore, each of the effective DSMA modes is a superposition of the exact TDHF modes with similar frequencies. Thus the entire spectrum is divided into several regions. Each effective oscillator is responsible for part of spectrum and it is dominated by fewer exact oscillators than the initial source. This property allows to use any effective mode  $P_\nu$  as a new fictitious source term  $\eta = iP_\nu$  in the DSMA. The resulting oscillators are much closer to the exact ones. This procedure (i.e. using one of the new oscillators as a new fictitious source for the next DSMA level) can be repeated several times until some convergence criteria are satisfied. In practice this fictitious source is dominated by a single oscillator  $(P_1, Q_1)$  which converges to the exact one. To recover the next mode, the same iterative procedure can be applied with one principal difference: all input sources must be made orthogonal to the lower modes. Thus by using

$$\eta_\perp = \eta - \sum_k^{recovered} \langle Q_k | \eta \rangle P_k, \quad (2.54)$$

all the recovered modes are excluded from the source in the following calculations. We can continue this iterative process utilizing this orthogonalization

procedure to refine several electronic modes. This yields an expansion of the original source and allows us to focus on desirable fine features of the spectrum at high resolution.

Linear absorption can be calculated using Eq. (1.5) recast in the form

$$\alpha(\omega) = \sum_{\nu} \frac{f_{\nu}}{\Omega_{\nu}^2 - (\omega + i\Gamma)^2}, \quad (2.55)$$

where  $f_{\nu} = 2\Omega_{\nu}Tr(\mu\xi_{\nu})^2$  is the oscillator-strength of the  $g$  to  $\nu$  transition.

In principle, the frequency(time)-dependent nonlinear polarizabilities can be calculated by applying the DSMA to the frequency(time)-dependent source [Eq. (2.28)]. This is difficult because hundreds DSMA runs are needed to scan accurately all frequency(time) region. In practice the off-resonant response is calculated first. The expressions for the different orders of static sources  $\eta^{(j)} = \eta^{(j)}(\omega = 0)$  and intraband components of density matrices  $T^{(j)} = T^{(j)}(\omega = 0)$  are given by Eqs. (2.33) and (2.37) for the static electric field  $\mathcal{E}(t) = const$ . We run the iterative DSMA for each order of the optical response. Calculations give the sets of electronic oscillators  $(\Omega_{\nu}, P_{\nu}, Q_{\nu})$  which dominate  $j$ th order of responses ( $j = 1, 2, \dots$ ). The density matrix induced by a static field is given by

$$\xi^{(j)} = \sum_{\nu=1}^{M_0} \frac{Tr(\bar{\rho}[\eta_{\nu}^{(j)}, Q_{\nu}])}{\Omega_{\nu}} Q_{\nu} \quad (2.56)$$

and

$$\delta\rho^{(j)} = \xi^{(j)} + T(\xi^{(j-1)}, \xi^{(j-2)}, \dots). \quad (2.57)$$

The static polarizabilities are readily obtained using Eq. (2.31)

$$\chi^{(j)} = -\frac{1}{\mathcal{E}_o^k} Tr(\mu\delta\rho^{(j)}(\omega = 0)), \quad (2.58)$$

where  $\chi^{(1)} = \alpha(0)$ ,  $\chi^{(2)} = \beta(0)$ ,  $\chi^{(3)} = \gamma(0)$ , *etc.* The resulting electronic oscillators need to be used to construct frequency(time)-dependent optical response. Frequency-dependent response functions with up to the third order response are expressed through the electronic modes in [56] [Eqs. (5.6) and

(E3)]. For example, oscillators dominating the first, second, and third orders off-resonant responses contributes to the three, two, and one-photon resonances in the resonant third order polarizability  $\gamma(-\omega; \omega_1, \omega_2, \omega_3)$ .

The DSMA has a close formal connection with other short-time algorithms widely used in different contexts. These include the Lanczos algorithm for computing the eigenvalues of a hermitian matrix [75–77], the Mori-Zwanzig procedure of reduced dynamics [78–80] and the continued fraction representation of correlation functions [81]. In particular, we note the analogy with the analysis of optical lineshapes in terms of spectral moments [82]. The moments can be easily calculated without going through a complex eigenvalue problem, and often very few moments provide for an adequate representation of the lineshape.

In summary, the DSMA calculates the optical response by solving the TDHF equations for motion of the single-electron density matrix. The algorithm consists of several levels of increasing complexity. First the entire optical response with low resolution is recovered at extremely low computational cost. All strong transitions are fully recovered but the fine structure of spectrum is missing. The iterative DSMA provides more detailed information. The simplest version of this procedure was implemented to calculate the optical response of organic molecules. The band edge transition oscillator was calculated first. The remaining electronic oscillators were recovered sequentially with increasing frequency and were used to compute optical polarizabilities.

<sup>3</sup> This approach allows us to recover accurately the experimentally relevant low-frequency spectral region (up to  $\sim 8$  eV).

---

<sup>3</sup>A more general (and complex) procedure is to focus on a limited frequency region, and pick up physically important modes by analyzing all the effective oscillators obtained at each iteration. The remaining modes are included in the dominant modes and only a few modes are necessary. In such a case the detailed structure of the chosen spectral region is investigated, but the algorithms for sorting out the effective electronic oscillators need to be developed for each particular case.

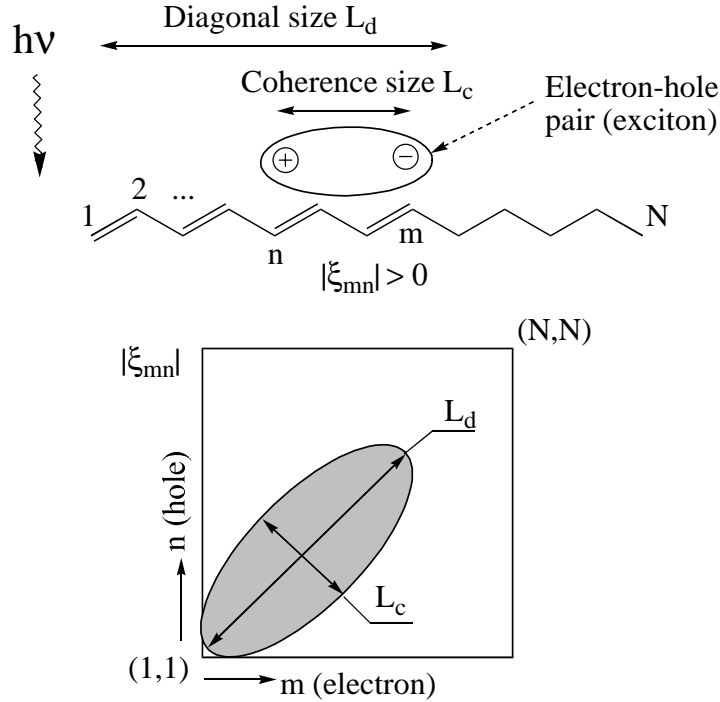
## 2.5 Real-space CEO analysis of electronic response.

Each calculated density matrix  $\rho^{g\nu} \equiv \xi_\nu$  with corresponding frequency  $\Omega_\nu$  enters to the TDHF equation of motion as an electronic oscillator. It can be used as powerful tool to establish the relation between electronic structure and molecular optical response. To introduce the CEO we start with the ground state density matrix  $\bar{\rho}_{mn} \equiv \langle g | c_m^\dagger c_n | g \rangle$ , which has been widely used for the analysis of the ground state properties [46,47,83–85]. The diagonal elements  $\bar{\rho}_{nn}$  are used in various population analyses (Löwdin, Milliken) to prescribe a portion of charge to specific atoms and are commonly visualized using contour charge density maps. The off-diagonal elements,  $m \neq n$ , represent the bonding structure (i.e. bond orders) associated with a pair of atomic orbitals and are useful in interpreting the chemical bonding pattern along the molecule [48–51,83,84].

In complete analogy with the ground state the diagonal elements of  $\xi_\nu$  ( $n = m$ ) represent the net charge induced on the  $n$ 'th atomic orbital by an external field, whereas  $(\xi_\nu)_{mn}$   $n \neq m$  is the dynamical bond-order representing the joint amplitude of finding an electron on orbital  $m$  and a hole on orbital  $n$ . Electronic modes are thus directly related to the motions of optically induced charges and electronic coherences. This is illustrated by Fig. 2.5. The off-diagonal size  $L_c$  of  $(\xi_\nu)$  which measures the degree of coherence between electrons and holes at different sites, control the scaling of molecular properties with size, whereas the diagonal size ( $L_d$ ) reflects the localization of optical excitation within the molecule.

We can draw an analogy with the description of vibrational spectroscopy [86], in which the coherent motion of various atoms with well-defined amplitude and phase relations are represented by collective nuclear coordinates; the normal modes. The normal modes provide a natural coordinate system and

## Delocalization of optical excitation



$$|\xi_{mn}| \sim |\xi_{nm}| \quad \text{no charge transfer}$$

$$|\xi_{mn}| \gg |\xi_{nm}| \quad \text{electron transfer (m} \rightarrow \text{n)}$$

$$|\xi_{mn}| \ll |\xi_{nm}| \quad \text{hole transfer (m} \rightarrow \text{n)}$$

Figure 2.5: Two-dimensional representation and physical interpretation of electronic modes. Each mode  $\xi_\nu$  is an  $N \times N$  matrix,  $N$  being the molecular size. By displaying this matrix in two-dimensions we establish a direct real-space connection between the optical response and motions of charges in the molecule upon optical excitation. The x axis represents an electron on site  $n$ , the y axis describes a hole on site  $m$ . An incident light moves an electron from some occupied to an unoccupied orbitals, creating an electron-hole pair (or exciton). The state of this pair can be characterized by two lengthscales: First, the distance between electron and hole (i.e., how far the electron can travel apart from the hole). This coherence size  $L_c$  is the "width" of the density matrix along the anti-diagonal direction. The second length  $L_d$  describes the exciton center of mass position (i.e., where the optical excitation resides within the molecule).  $L_d$  is the "width" of the density matrix along the diagonal direction. Finally charge transfer processes can be characterized by the asymmetry of mode with respect to the diagonal.  $(\xi_\nu)_{mn} \sim (\xi_\nu)_{nm}$  means that there is no preferable direction of motion for electrons (or holes), whereas  $(\xi_\nu)_{mn} \gg (\xi_\nu)_{nm}$  shows the motion of electron from  $m$  to  $n$ .

allow an alternative classical real-space interpretation of infrared or Raman spectra [87,88], instead of a description in terms of transitions among specific vibrational states. The normal modes of nuclear vibrations are simply superpositions of the  $3N$  nuclear displacements. In complete analogy,  $\xi_\nu$  can be viewed as *collective coordinates* which represent the displacements of the electronic density matrix elements from their equilibrium (ground state) values  $\bar{\rho}_{nm}$ .

## 2.6 Density matrices vs. eigenstates; advantages of the CEO representation.

We will now compare the representation of the molecular optical response in terms of global many-electron states and single-electron density matrices calculated using the TDHF method.

Any spectroscopic process includes an optical excitation which moves an electron from some occupied to unoccupied orbitals, thereby creating an electron-hole pair. The natural description of the optical response should therefore be based on following the simultaneous and coupled dynamics of this pair; the two indices of the density matrix carry precisely this information. Molecular eigenstates, however, use a single-particle basis set. Correlations are incorporated through an extensive CI calculation. By working in a space of higher dimensionality (the pair) the essential physics of the system is captured, and even the simplest (TDHF) factorization yields an adequate description. In a single-particle basis, a much more extensive numerical effort is needed. A real space CEO analysis which pinpoints the origin of each optical transition is obtained by displaying the electronic mode matrices graphically. The fact that only few oscillators typically dominate the response greatly simplifies the theoretical description. The weak anharmonicities which justify the harmonic picture may be attributed to the large delocalization size. In atoms, on the

other hand, collective excitations have been found to converge to local modes rather than to normal modes [89]. In semiconductors, the electron-hole pairs are loosely bound and form Wannier excitons [38]. In molecular aggregates, each pair is tightly bound and can be considered as a single particle (Frenkel exciton) [25,90,91]. Conjugated polymers are intermediate between these two extremes, and the collective oscillators in conjugated polymers can be viewed as charge-transfer excitons. The CEO thus offers a unified description of different materials and allows a direct comparison of their optical properties [92]. Also, one can go beyond the semiempirical Hamiltonians and the TDHF approximation and include additional variables and use a different ansatz for the wave function [93]. Technically the calculation of optical properties using summation over states is also unified and universal. However, very different approximate schemes and terminologies are usually used in the calculation of the eigenstates of various systems; This prohibits a clear comparison and obscures the origin of differences. The electronic oscillator picture applies to all materials by simply changing parameters (such as the electron hole mass, the Coulomb interaction, and the hopping matrix elements) [71].

We next review the computational advantages and limitations of the electronic oscillator approach. The sum-over-states method becomes rapidly more complex with molecular size. Both calculating the eigenstates and performing the necessary summations over them are intractable for large systems. Knowing the complete set of eigenstates allows the calculation of any optical response including to strong fields. This is therefore an "all or nothing" approach. The oscillator approach, carries less information but for considerably less effort. Computational time of CI calculations scales as  $N^6$ ; The CEO/DSMA procedure scales only as  $N^2$ . Our results allow the interpretation of the most interesting crossover region towards the bulk. The CEO approach can be readily applied for very large molecules with thousands of atoms. However, there are



some types of computations to which the CEO/DSMA method may either not be applied or applied with caution. The problems arise when one need to calculate exact eigenvectors of the Liouville operator in the high-frequency region. An iterative DSMA calculates electronic modes one by one starting from low frequency with decreasing accuracy. Some difficulties were found with applying DSMA in the following cases: Calculation of high frequency weak optical excitation as a smooth function of given parameters (e.g. weak changes in molecular geometry along the vibrational normal mode); Computation of fine structure in the spectrum with many lines (e.g. inorganic semiconductors). DSMA successfully recovers up to 20 transitions; The DSMA input parameters for computing nonlinear optical properties in weakly assymmetric molecules have to be carefully chosen. Here the problem arises that a weak perturbation (donor/acceptor or external field) slightly mixes electronic modes with original  $B_u$  and  $A_g$  symmetry. That defines the nonlinear anharmonicities and the magnitudes of hyperpolarizabilities. In this case electronic modes need to be computed accurately. To overcome these difficulties new improved algorithms need to be developed. For example, the lack of long-range electronic coherence allows us to truncate the density matrix and only retain off-diagonal elements of closely lying atoms [94]. This may result in most favorable linear  $N$ -scaling of computational effort with size, resembling similar developments in ground-state calculations [95,96].

The merits of the oscillator picture are more pronounced when nonlinear optical properties are calculated [55,60,73,97]. Interference effects in the sum-over-states approach result in an almost complete cancellation of large positive and negative contributions to optical susceptibilities [72,28,29], which limits the accuracy and makes approximate calculations dangerous (since innocent approximations may lead to huge errors). One consequence of this is that individual terms do not have the correct scaling with size. The latter is only

obtained once all of the terms are carefully combined. In the oscillator picture these cancellations are built-in from the start and each separate contribution to the susceptibility scales properly. The real-space approach has been shown to provide an adequate description of the scaling and saturation of off-resonant linear and nonlinear polarizabilities (see Sections 5, 4, and 10) [55,60,73,98].

We further note that by treating the electronic degrees of freedom as oscillators we can couple them more naturally to nuclear degrees of freedom, which constitute another set of oscillators. The incorporation of nuclear notions thus becomes much more straightforward compared with the eigenstate representation, and lends itself more easily to semiclassical approximations. The time-dependent density-matrix should then allow us to follow the dynamics of coherent intramolecular and intermolecular vibrations, solvent modes, and isomerization and account for vibronic structure and line broadening [99].

The oscillator approach allows us to develop a natural framework for the interpretation and the design of molecules with specific properties. Instead of asking which of the many-electron states are most relevant, we can explore how do different regions of the molecule couple and affect each other. The nonlocal character of the response is intimately connected with the electronic coherence of the induced density matrix. For example, one can then address directly the effects of donor-acceptor substitutions and geometry (see Section 6). A new type of chemical intuition which focuses directly on the electronic charges and coherences and is not based on properties of many-electron eigenstates emerges naturally (see Sections 9 and 7). The present analysis makes it possible to guide the design and synthesis of organic molecules with desired optical properties.

## 2.7 Appendix A. Relations between the Inter- and Intraband Components of the Density Matrix.

The single-electron reduced density matrix in the TDHF approximation satisfies the condition  $\rho^2(t) = \rho(t)$  at all times [55,56,52]. Using Eq. (2.22) then results in

$$\left(\bar{\rho} + \xi(t) + T(\xi(t))\right)^2 = \bar{\rho} + \xi(t) + T(\xi(t)). \quad (2.59)$$

To simplify this expression it is possible to use following relations:  $\bar{\rho}^2 = \bar{\rho}$ ,  $\xi = \bar{\rho}\xi + \xi\bar{\rho}$ , and  $T\bar{\rho} = \bar{\rho}T$ . A simple rule may be applied to separate the remaining terms: product of two inter- (or two intra-) band matrices gives an intraband matrix, whereas product of inter- into intra- (or intra- into inter-) band matrices results in an interband matrix. Finally, the intraband part of equation (2.59) is

$$(T(\xi))^2 + (2\bar{\rho} - I)T(\xi) + \xi^2 = 0. \quad (2.60)$$

The formal solution of this quadratic equation, with the condition  $T(\xi = 0) = 0$  yields

$$T(\xi) = (2\bar{\rho} - 1) \frac{1 - \sqrt{1 - 4\xi^2}}{2}. \quad (2.61)$$

A Taylor series expansion of this expression in  $\xi$  finally gives

$$T(\xi) = (2\bar{\rho} - 1) \sum_{m=1}^{\infty} \frac{2^m (2m - 3)!!}{2m!} \xi^{2m}. \quad (2.62)$$

When  $\xi$  is small,  $T \approx (\bar{\rho} - 1/2)\xi^2$  is quadratic in  $\xi$ .

## 2.8 Appendix B. Short-time Evolution of the density-matrix response function.

The interband component of the reduced single-electron density matrix to  $j$ 'th order in the field  $\xi^{(j)}(\omega)$  in the frequency domain can be represented as

$$\xi^{(j)}(\omega) = \int_0^{+\infty} dt e^{i\omega t} S^{(j)}(t, \omega), \quad (2.63)$$

where we have introduced the matrix  $S^{(j)}(t, \omega)$

$$S^{(j)}(t, \omega) \equiv -ie^{-iLt}\eta^{(j)}(\omega). \quad (2.64)$$

This matrix satisfies the equation

$$i\frac{\partial S^{(j)}(t, \omega)}{\partial t} - LS^{(j)}(t, \omega) = 0, \quad (2.65)$$

with the initial condition

$$S^{(j)}(0, \omega) = -i\eta^{(j)}(\omega). \quad (2.66)$$

In Eqs. (2.64) and (2.66) the  $S^{(j)}$  matrix is viewed as a vector in Liouville space. We next expand the solution of Eq. (2.65) in a Taylor series

$$S^{(j)}(t, \omega) = -i(S_0^{(j)}(\omega) + (-i)\frac{S_1^{(j)}(\omega)}{1!}t + \dots) = -i\sum_{n=0}(-i)^n\frac{S_n^{(j)}(\omega)}{n!}t^n, \quad (2.67)$$

where  $S_0^{(j)}(\omega) = \eta^{(j)}(\omega)$  and  $S_k^{(j)}(\omega) = L^k S_0^{(j)}(\omega)$ ,  $k = 1, 2, \dots$ . This expansion describes the short time evolution of initial vector  $\eta(\omega)$  in the subspace determined by  $-ie^{-iLt}$ .

## 2.9 Appendix C. Solution of Eqs. (2.53)

The system of nonlinear equations (2.53) may be solved as follows. Let us consider the following system of  $2n$  equations with respect to  $n$  “nonlinear” frequency  $\Omega_n$  and  $n$  “linear” oscillator strength  $f_n$  variables.

$$\begin{aligned} \mathcal{K}_0 &= f_1 + f_2 + f_3 + \dots + f_n \\ \mathcal{K}_1 &= f_1\Omega_1^2 + f_2\Omega_2^2 + \dots + f_n\Omega_n^2 \\ \mathcal{K}_2 &= f_1\Omega_1^4 + f_2\Omega_2^4 + \dots + f_n\Omega_n^4 \\ &\dots\dots\dots \\ \mathcal{K}_{n-1} &= f_1\Omega_1^{2(n-1)} + f_2\Omega_2^{2(n-1)} + \dots + f_n\Omega_n^{2(n-1)} \\ \mathcal{K}_n &= f_1\Omega_1^{2n} + f_2\Omega_2^{2n} + \dots + f_n\Omega_n^{2n} \\ &\dots\dots\dots \\ \mathcal{K}_{2n-1} &= f_1\Omega_1^{2(2n-1)} + f_2\Omega_2^{2(2n-1)} + \dots + f_n\Omega_n^{2(2n-1)}. \end{aligned} \quad (2.68)$$

The frequency variables  $\Omega^2 = x$  are the roots of the polynomial

$$x^n - a_1x^{n-1} - a_2x^{n-2} - \dots - a_{n-1}x - a_n, \tag{2.69}$$

where the coefficients  $a_i, i = 1, \dots, n$  are the solution of system of  $n$  linear equations

$$\begin{aligned} \mathcal{K}_n &= \mathcal{K}_{n-1}a_n + \mathcal{K}_{n-2}a_{n-1} + \mathcal{K}_{n-3}a_{n-2} + \dots + \mathcal{K}_1a_2 + \mathcal{K}_0a_1 \\ \mathcal{K}_{n+1} &= \mathcal{K}_na_n + \mathcal{K}_{n-1}a_{n-1} + \mathcal{K}_{n-2}a_{n-2} + \dots + \mathcal{K}_2a_2 + \mathcal{K}_1a_1 \\ \mathcal{K}_{n+2} &= \mathcal{K}_{n+1}a_n + \mathcal{K}_na_{n-1} + \mathcal{K}_{n-1}a_{n-2} + \dots + \mathcal{K}_3a_2 + \mathcal{K}_2a_1 \\ &\dots\dots\dots \\ \mathcal{K}_{2n-1} &= \mathcal{K}_{2n-2}a_n + \mathcal{K}_{2n-3}a_{n-1} + \mathcal{K}_{2n-4}a_{n-2} + \dots + \mathcal{K}_na_2 + \mathcal{K}_{n-1}a_1. \end{aligned} \tag{2.70}$$

To rationalize Eqs. (2.69) and 2.70) we note that Viet's theorem [100] establishes the relationship between the polynomial roots and coefficients

$$\begin{aligned} a_1 &= x_1 + x_2 + \dots + x_n \\ a_2 &= - \sum_{i_1 < i_2} x_{i_1}x_{i_2} \\ &\dots\dots\dots \\ a_k &= (-1)^{(k+1)} \sum_{i_1 < i_2 < \dots < i_k} x_{i_1}x_{i_2} \dots x_{i_k} \\ &\dots\dots\dots \\ a_n &= (-1)^{(n+1)}x_1x_2 \dots x_n. \end{aligned} \tag{2.71}$$

To verify Eqs. (2.70) let simply substitute Eqs. (2.71) in the expression for  $\mathcal{K}_n$  (2.70)

$$\begin{aligned} \mathcal{K}_n &= \left(\sum_i f_i x_i^{n-1}\right)\left(\sum_j x_j\right) - \left(\sum_i f_i x_i^{n-2}\right)\left(\sum_{j_1 < j_2} x_{j_1}x_{j_2}\right) + \dots \\ &= \sum_i f_i x_i^n + \sum_{i \neq j} f_i x_i^{n-1}x_j - \left(\sum_i f_i x_i^{n-2}\right)\left(\sum_{j_1 < j_2} x_{j_1}x_{j_2}\right) + \dots \\ &= \mathcal{K}_n - \sum_{i \neq (j_1 < j_2)} f_i x_i^{n-2}x_{j_1}x_{j_2} + \left(\sum_i f_i x_i^{n-3}\right)\left(\sum_{j_1 < j_2 < j_3} x_{j_1}x_{j_2}x_{j_3}\right) - \dots = \dots \\ &= \mathcal{K}_n + (-1)^n \sum_{i \neq (j_1 < \dots < j_{n-1})} f_i x_i x_{j_1} \dots x_{j_{n-1}} + (-1)^{n+1} \sum_i f_i x_1 x_2 \dots x_n = \mathcal{K}_n. \end{aligned} \tag{2.72}$$

Thus all terms (except  $\mathcal{K}_n$ ) in the r.h.s. of Eq. (2.72) vanish, leaving the identity  $\mathcal{K}_n \equiv \mathcal{K}_n$ .

Eqs. (2.70) is known as the Toeplitz linear system. The inversion of the Toeplitz matrices is straightforward [101] and poses no numerical difficulties.

Once the frequencies are found, the oscillator strengths can be computed by solving the linear system of the first  $n$ -equations of (2.68) for the variables  $f_n$ . Thus the solution of the nonlinear system (2.68) is obtained in three steps: two linear problems, and finding the zeros of a polynomial with real coefficients (the only nonlinear task).

Since  $f_1 \ll f_2 \ll f_3 \ll \dots \ll f_n$ , and  $\Omega_1^n \gg \Omega_2^n \gg \dots \gg \Omega_n^n$ , the lower frequency terms are dominant in the first equations of system (2.68) and the higher frequency terms dominate the higher ones. This allows us to increase the accuracy of the low frequencies by adding new high frequency modes (and the necessary higher moments).

# Chapter 3

## Time-Dependent Density-Matrix-Response-Functions (DMRF) Algorithm for calculating Excited States.

### 3.1 Density matrix response functions and material properties

In this Chapter we develop a semiclassical approach for computing the density matrices  $\rho^{\nu\eta}$  (Eq. (1.2)) out of the electronic modes  $\rho^{g\nu}$ . This procedure extends the TDHF for calculating relevant properties of excited electronic states and connects the CEO to the molecular states representation.

Our approach starts by coupling the molecule to an external field  $\mathcal{E}(t)$  through

$$H_{int} = -\mu\mathcal{E}(t) \equiv \sum_{nm} \mathcal{E}_{nm}(t)c_n^+c_m. \quad (3.1)$$

Where  $\mathcal{E}_{nm}(t) \equiv \mu_{nm}\mathcal{E}(t)$ . The induced density matrix can be then expanded in powers of the incoming field

$$\begin{aligned} \rho_{nm}(t) = & \bar{\rho}_{nm} + \int_{-\infty}^t d\tau \sum_{n'm'} S_{nm,n'm'}^{(1)}(t;\tau)\mathcal{E}_{n'm'}(\tau) + \int_{-\infty}^t \int_{-\infty}^t d\tau_1 d\tau_2 \\ & \sum_{\substack{n'm' \\ n''m''}} S_{nm,n'm',n''m''}^{(2)}(t;\tau_1,\tau_2)\mathcal{E}_{n'm'}(\tau_1)\mathcal{E}_{n''m''}(\tau_2) + \dots \end{aligned} \quad (3.2)$$

The  $j$ -th order density-matrix response functions (DMRF)  $S^{(j)}$  can be calculated using the Time-Dependent Hartree-Fock (TDHF) technique [52,33,34] described in Chapter 2. Since the DMRF can be alternatively expanded in terms of the system energies and matrix elements of the single-electron operators  $c_m^\dagger c_n$ , it constitutes a source of information on these quantities. However, it is not easy to interpret the TDHF response in terms of the global eigenstates since the structure of the TDHF expressions is very different from their standard SOS counterparts.

The present Chapter provides an algorithm for inverting the DMRF to obtain an effective multilevel system which gives the same response functions, resulting in the eigenvalues and all density matrix elements (Eq. (1.2)). Note that the DMRF are more general than the optical response functions since the interaction (Eq. (3.1)) is not limited to the dipole operator. The latter often has selection rules which limit the information to a few dominant states. The freedom to use any external field  $\mathcal{E}_{nm}(t)$  in Eq. (3.1) allows us to calculate all possible states. The effective multilevel system will be constructed in four steps (Fig. 3.1).

(i) Starting with the original quantum fermion model QFM (Eq. 3.4) we build its classical limit by considering the space of single Slater determinants  $\mathbf{M}$  (the space of coherent states as its phase space). The Poisson bracket on  $\mathbf{M}$  and the classical Hamiltonian have been introduced in [56]. We make use of the observation [102] that the TDHF approximation can be considered as a classical limit of the original many-electron system. Hereafter we refer to the classical limit of the QFM as the classical oscillator model (COM). As shown in [102] any classical system can be mapped onto a set of classical coupled oscillators. For example in Section 11 resonant two-pulse four-wave mixing experiments in conjugated polyenes have been modeled using the electronic-oscillator representation.



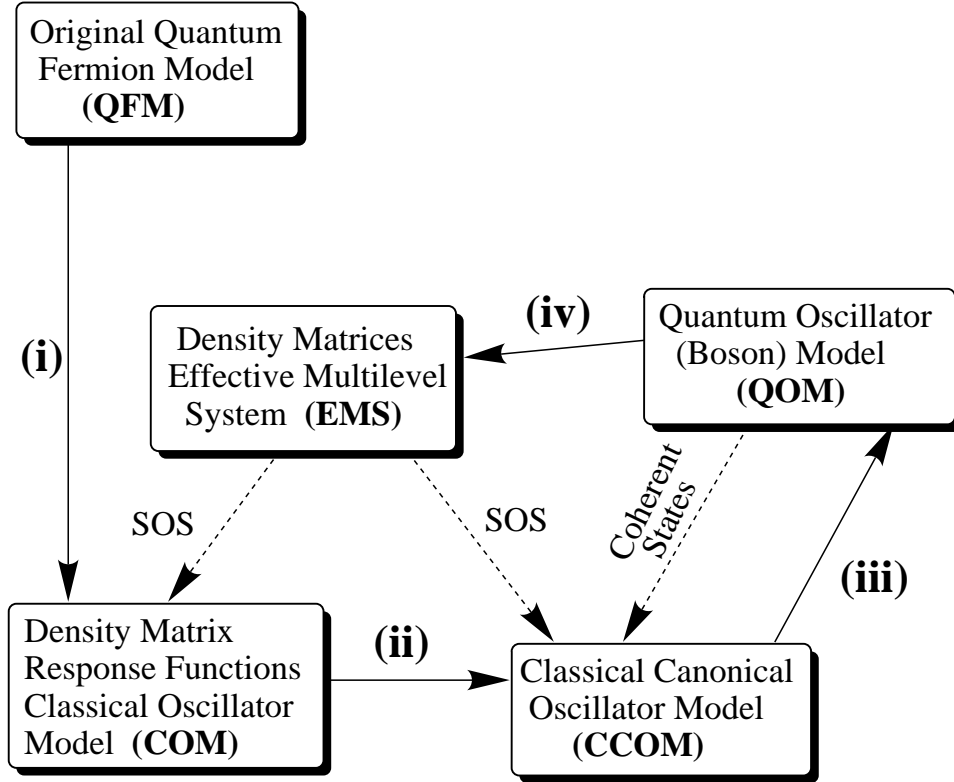


Figure 3.1: The four steps involved in constructing the effective multilevel system (EMS) out of the original quantum Fermion Model (QFM).

(ii) In the vicinity of the stationary solution  $\bar{\rho} \in N$  of the TDHF equations, we transform the local variables on  $\mathbf{M}$  and transform the Poisson bracket into a canonical form. This establishes the oscillator representation of the COM. Stated differently, this shows the equivalence of the COM and a classical canonical oscillator model (CCOM) defined as the COM represented in terms of the canonical variables.

(iii) We build a quantum oscillator model (QOM) by quantizing the CCOM, so that the classical limit of the QOM reproduces the CCOM. The classical system of oscillators can thus be viewed as the classical limit of a system of quantum coupled oscillators. We thus have two quantum models (QFM and QOM) which correspond to the original electronic system and the system of

quantum anharmonic oscillators, respectively. Their classical limits COM and CCOM respectively are equivalent, and the COM describes the QFM within the TDHF approximation.

(iv) Finally, using a perturbative approach we build an effective multilevel system EMS whose exact optical response reproduces the classical approximation of the QOM which is the CCOM and in turn coincides with the TDHF approximation of the original model QFM. In summary the EMS constitutes a quantum model whose optical response reproduces the TDHF approximation of the original model.

In Section 3.2 we carry out steps (i) and (ii) and map the original quantum fermion model onto a classical canonical oscillator model. Steps (iii) and (iv) are made in Section 3.3. Details of the calculations are given in the Appendices 3.5-3.7. In Section 6.4 we apply this algorithm to a family of unsubstituted and acceptor-substituted carotenoids. The induced density matrices  $\rho_{nm}^{\nu\eta}$  for the states which dominate the linear and the quadratic response are investigated. Finally we discuss and summarize these results in Section 3.4.

## 3.2 Classical Electronic Oscillators in the TDHF Approach:

We consider a system described by the molecular electronic Hamiltonian (Eq. (2.1)). The classical oscillator model is constructed using the procedure for approaching the classical limit outlined in [102]. We start by defining the phase space of the single Slater determinants  $\mathbf{M} = G(N, K; C)$ ,  $K$  being the basis set size and  $N$  is the number of electrons.  $\mathbf{M}$  can be alternatively represented as the space of hermitian  $K \times K$  single-electron reduced density-matrices with  $\rho^2 = \rho$  and  $\text{rank}(\rho) = N$ . The classical Hamiltonian is

$$H(\rho) = \langle \Omega(\rho) | \hat{H} | \Omega(\rho) \rangle, \quad (3.3)$$

where  $\Omega(\rho)$  is the Slater determinant corresponding to  $\rho$ . Expressions for  $H(\rho)$  in terms of the original parameters of the molecular electronic Hamiltonian (Eq. (2.1)) and for the Poisson bracket were given in [56]. The TDHF equation adopts the form of the equation of motion of Hamilton's classical dynamics on  $\mathbf{M}$ . The stationary point of the TDHF equations which corresponds to the minimum of the energy function  $H(\rho)$  on  $\mathbf{M}$  constitutes the Hartree-Fock (HF) reduced ground state single-electron density matrix  $\bar{\rho}$  which can be found by solving the Hartree-Fock (HF) equation (2.10) [51]

To construct the classical oscillators (step (ii)), local coordinates on  $\mathbf{M}$  representing deviations from  $\bar{\rho}$  need to be defined. The restricted TDHF scheme [56] allows us to reduce the number of variables from  $K^2$  to particle-hole variables  $N(K - N)$ . To that end we decompose the single-electron density matrix to the particle-hole  $\xi$  and the particle-particle and the hole-hole  $T(\xi)$  parts of the deviation of the reduced single-electron density matrix from the ground state  $\bar{\rho}$  (see Eq. (2.22)).  $\bar{\rho}$ ,  $\xi$ , and  $T(\xi)$  in Eq. (2.22) are  $K \times K$  matrices.<sup>1</sup> Only the particle-hole components of the density matrix ( $\xi$ ) need to be calculated explicitly (see Section 2.2). For computing DMRF not higher than third order it is sufficient to retain only the lowest (second order) term in Eq. (2.26).

A convenient coordinate system can be obtained by parameterizing the electron-hole component ( $\xi$ ) of the density matrix. To introduce variables close to canonical (as will be explained latter) it is convenient to use the TDHF equations for  $\xi(t)$  (Eq. (2.28)). The oscillator variables (Eqs. (2.41)) are computed as the eigenmodes of the linear part of this equation.  $z_\alpha$  and its complex conjugate  $z_{-\alpha} = z_\alpha^*$  constitute the complex oscillator amplitudes (Eqs. (11.1)). Eqs. (11.1) and (2.22) define a local coordinate system  $z_\alpha$  on  $\mathbf{M}$  where  $\bar{\rho}$  is the origin. Substitution of Eqs. (11.1) and (2.22) into Eq. (3.3) yields the classical Hamiltonian for the variables  $z_\alpha$ .  $H(z_\alpha)$  can be calculated

---

<sup>1</sup> $\bar{\rho}$  and  $\xi(t)$  are matrices of rank  $N$ ,  $N < K$ .

in a form of an expansion in powers of  $z_\alpha$ . The expression to fourth-order is presented in [56]. For the current applications the Hamiltonian up to third-order is needed

$$H(z) = \sum_{\alpha>0} \Omega_\alpha z_{-\alpha} z_\alpha + \frac{1}{3} \sum_{\alpha\beta\gamma} V_{\alpha,\beta\gamma} z_\alpha z_\beta z_\gamma - \mathcal{E}(t) \mathcal{P}(z) , \quad (3.4)$$

with the polarization

$$\mathcal{P}(z) = \sum_{\alpha} \mu_\alpha z_\alpha + \frac{1}{2} \sum_{\alpha\beta} \mu_{\alpha\beta} z_\alpha z_\beta , \quad (3.5)$$

where

$$\begin{aligned} \mu_\alpha &= \text{Tr}([\bar{\rho}, \xi_\alpha][\mu, \bar{\rho}]) \\ \mu_{\alpha,\beta} &= \text{Tr}([\bar{\rho}, \xi_\alpha][\mu, \xi_\beta]) \\ V_{\alpha,\beta\gamma} &= \text{Tr}([\bar{\rho}, \xi_\alpha][V(\xi_\beta), \xi_\gamma]) \\ &+ \text{Tr}([\bar{\rho}, \xi_\alpha][V(\frac{1}{2}[[\xi_\beta, \bar{\rho}], \xi_\gamma]), \bar{\rho}]) . \end{aligned} \quad (3.6)$$

Here  $\xi$ ,  $\bar{\rho}$ , and  $\mu$  are  $K \times K$  matrices in the single-electron space, and the trace is defined in this space.

The Poisson bracket for the  $z_\alpha$  variables is calculated in [56] and to first-order in  $z_\alpha$  it has the canonical form

$$\{z_\alpha, z_\beta\} = i\delta_{\alpha,-\beta} . \quad (3.7)$$

It has the following useful properties:

$$\begin{aligned} \{z_\alpha, z_\beta\} &= -\{z_\beta, z_\alpha\} , \\ \{z_\alpha, z_\beta z_\gamma\} &= \{z_\alpha, z_\beta\} z_\gamma + z_\beta \{z_\alpha, z_\gamma\} . \end{aligned} \quad (3.8)$$

The classical Hamilton equation of motion  $\dot{z} = \{H, z\}$  obtained using Eqs. (3.4)-(3.6) can be written as

$$i \frac{\partial}{\partial t} z_\alpha = \Omega_\alpha z_\alpha - \mathcal{E} \mu_{-\alpha} - \mathcal{E} \sum_{\beta} \mu_{-\alpha,\beta} z_\beta + \sum_{\beta\gamma} V_{-\alpha,\beta\gamma} z_\beta z_\gamma . \quad (3.9)$$

These equations are equivalent to Eq. (2.28). The linear and the second order response functions calculated by solving these equations are given in Appendix 3.5.

Eqs. (3.4)-(3.9) define the classical oscillator model. The variable  $z_\alpha$  describes the  $\alpha$ th oscillator, as is clearly seen from the form of the Poisson bracket [Eq. (3.6)]. Higher-order terms of the Hamiltonian can be calculated order-by-order. Similarly the Poisson bracket is not strictly canonical and the r.h.s. of Eq. (3.7) can be expanded in powers of  $z_\alpha$ . Second order corrections have been calculated in [102]. These deviations can however be eliminated (since the Poisson bracket can be always transformed to a canonical form [103]) using a nonlinear transformation of variables

$$z'_\alpha = z_\alpha + \sum_{\alpha\beta\gamma\delta} S_{\alpha,\beta\gamma\delta} z_\beta z_\gamma z_\delta + \dots \quad (3.10)$$

In practice, the canonical variables can be calculated order-by-order in  $z_\alpha$ . Expressing the Hamiltonian in terms of the canonical variable  $z'_\alpha$  allows us to define a CCOM to any given order in  $z_\alpha$ . This accomplishes step (ii) of the procedure.

### 3.3 Intrastate and Transition Electronic Density Matrices for the Effective Multilevel System

Step (iii) involves the construction of a quantum oscillator model QOM whose classical limit reproduces the CCOM. To that end we associate with each classical variable  $z_\alpha$  an annihilation operator  $a_\alpha$  ( $z_\alpha = \langle a_\alpha \rangle$ ,  $\alpha > 0$ ),  $z_{-\alpha} = z_\alpha^*$  is associated with a creation operator  $a_\alpha^+$  ( $z_\alpha^* = \langle a_\alpha \rangle^+$ ). These satisfy the boson commutation relations:

$$[a_\alpha, a_\beta^+] = \delta_{\alpha\beta} . \quad (3.11)$$

The QOM Hamiltonian  $H_1$  is defined by

$$H_1 =: H(a_\alpha, a_\alpha^+) : , \quad (3.12)$$

where  $H(a_\alpha, a_\alpha^+)$  is the classical Hamiltonian of the CCOM, which is given by Eqs. (3.4) and (3.5) up to third order, and  $: \dots :$  stands for normal ordering.

We then have

$$\begin{aligned} H_1 &= \sum_{\alpha} \Omega_{\alpha} a_{\alpha}^{+} a_{\alpha} + \frac{1}{3!} \left( \sum_{\alpha\beta\gamma} V_{\alpha,\beta\gamma} a_{\alpha} a_{\beta} a_{\gamma} + 3 \sum_{\alpha\beta\gamma} V_{-\alpha,\beta\gamma} a_{\alpha}^{+} a_{\beta} a_{\gamma} + h.c. \right) \\ &- \mathcal{EP}(a_{\alpha}^{+}, a_{\alpha}) , \end{aligned} \quad (3.13)$$

with

$$\mathcal{P}(a_{\alpha}^{+}, a_{\alpha}) = \sum_{\alpha} \mu_{\alpha} a_{\alpha} + \frac{1}{2!} \left( \sum_{\alpha\beta} \mu_{\alpha\beta} a_{\alpha} a_{\beta} + \sum_{\alpha\beta} \mu_{-\alpha\beta} a_{\alpha}^{+} a_{\beta} + h.c. \right) , \quad (3.14)$$

and the summation in Eqs. (3.13) and (3.14) runs over  $\alpha, \beta, \gamma > 0$ .

The classical limit of the QOM can be obtained by requiring that each oscillator  $\alpha$  remains in a coherent state parameterized by  $z_{\alpha}$  at all times. This amounts to the following factorizations  $\langle a_{\alpha} a_{\beta} \rangle = z_{\alpha} z_{\beta}$  and  $\langle a_{\alpha}^{+} a_{\beta} \rangle = z_{\alpha}^{*} z_{\beta}$ . Using these factorizations, the Heizenberg equation of motion  $\dot{a}_{\alpha} = \frac{i}{\hbar} [H_1, a_{\alpha}]$  with  $H_1$  given by Eq. (3.13) coincides with the classical equation of motion (Eq. (3.9)). The CCOM is thus the classical limit of the QOM and step (iii) is accomplished.

We now turn to step (iv), namely constructing the effective multilevel system EMS whose response reproduces the classical limit of QOM (which in turn coincides with the TDHF approximation of the QFM). This will be based on the picture established in [102] that the semiclassical expansion is a reexpansion of the optical response in the anharmonicities of the Hamiltonian and nonlinearities of the polarization operator in  $a$  and  $a^{+}$ . This is carried out for the response up to second order in Appendix 3.6. In particular, the linear response in the classical approximation is obtained by setting  $V_{\alpha,\beta\gamma} = 0$  and

$\mu_{\alpha\beta} = 0$  (i.e., using the model of a set of linearly driven uncoupled harmonic oscillators) whereas the second-order response also depends on the terms proportional to  $V_{\alpha,\beta\gamma}$  and  $\mu_{\alpha\beta}$ .

The QOM is improved successively by incorporating higher-order responses. We will concentrate on the lower-energy excited states which can be constructed using the linear and the second-order responses. For the linear response we set  $V_{\alpha,\beta\gamma} = 0$  and  $\mu_{\alpha\beta} = 0$  and obtain a system of harmonic oscillators with the polarization linear in  $a$  and  $a^+$ . Since the polarization is represented by the most general operator given by linear and bilinear combinations  $c_m^+ c_n$  of fermion operators, we can obtain the matrix elements of  $c_m^+ c_n$  between the ground state and single-excited oscillator states involved in the linear response. The second order response depends on the anharmonicities to the first order. This leads to first-order corrections to the oscillator wavefunctions whereas the eigenvalues remain the same (since they only contain higher-order corrections). This implies that in this order of perturbation theory which corresponds to the classical limit, the system remains harmonic and simply attains new matrix elements of  $c_m^+ c_n$ .

It follows from Eqs. (2.1) and (3.13) together with Eqs. (3.6) that the operator  $c_m^+ c_n$  can be represented in terms of the oscillator operators in the following form

$$\begin{aligned}
 c_m^+ c_n &= \bar{\rho}_{mn} + \sum_{\alpha} \{ (\xi_{\alpha}^+)_{mn} a_{\alpha}^+ + (\xi_{\alpha})_{mn} a_{\alpha} \} \\
 &+ \frac{1}{2} \sum_{\alpha\beta} \left\{ ([\xi_{\alpha}^+, \bar{\rho}] \xi_{\beta}^+)_{mn} a_{\alpha}^+ a_{\beta}^+ ([\xi_{\alpha}^+, \bar{\rho}] \xi_{\beta})_{mn} a_{\alpha}^+ a_{\beta} \right. \\
 &\left. + ([\xi_{\alpha}, \bar{\rho}] \xi_{\beta}^+)_{mn} a_{\alpha} a_{\beta}^+ + ([\xi_{\alpha}, \bar{\rho}] \xi_{\beta})_{mn} a_{\alpha} a_{\beta} \right\}. \quad (3.15)
 \end{aligned}$$

The EMS is constructed as a system of harmonic oscillators with the eigenstates  $|k\alpha, l\beta, \dots\rangle$  and eigenenergies  $E = k\Omega_{\alpha} + l\Omega_{\beta} + \dots$ , where the integers  $k, l = 0, 1, 2, \dots$  label the excited states of the various oscillators. The EMS

are calculated to first-order in  $V$  in terms of the oscillator states of QOM in Appendix 3.6. The contributions to the response functions  $S^{(j)}$  can, therefore, be classified according to the matrix elements of the effective oscillator system  $\langle k\alpha, \dots | c_m^+ c_n | l\beta, \dots \rangle$ .

The effective level scheme that reproduces the linear response  $S^{(1)}$  consists of the ground state  $|g\rangle$  and all single excitations  $|1\alpha\rangle$ . The relevant density matrix elements are

$$\langle g | c_m^+ c_n | g \rangle = \bar{\rho}_{mn} , \quad (3.16)$$

$$\langle g | c_m^+ c_n | 1\alpha \rangle = (\xi_\alpha)_{mn} . \quad (3.17)$$

Eqs. (3.16) and Eq. (3.17) simply recover our input i.e. the ground state density matrix and the TDHF electronic modes contributing to the linear response.

The second-order response  $S^{(2)}$  is represented by an effective system consisting of the ground state  $|g\rangle$ , single  $|1\alpha\rangle$ , and double  $|1\alpha 1\beta\rangle$  excited states. These are given by Eqs. (3.39) to first order in  $V$ . The state  $|2\alpha\rangle$  is the special case of  $|1\alpha 1\beta\rangle$  when  $\alpha = \beta$ . The necessary additional matrix elements are obtained by combining Eqs. (3.39) and (3.15):

$$\begin{aligned} \langle g | c_m^+ c_n | 1\alpha 1\beta \rangle &= \frac{([\xi_\alpha, \bar{\rho}] \xi_\beta)_{mn}}{2} \\ &+ 2 \sum_\gamma \left\{ \frac{V_{\alpha\beta-\gamma}(\xi_\gamma)_{mn}}{\Omega_\alpha + \Omega_\beta - \Omega_\gamma} - \frac{V_{\alpha\beta\gamma}(\xi_\gamma^+)_{mn}}{\Omega_\alpha + \Omega_\beta + \Omega_\gamma} \right\}, \end{aligned} \quad (3.18)$$

$$\begin{aligned} \langle 1\alpha | c_m^+ c_n | 1\beta \rangle &= \bar{\rho}_{mn} \delta_{\alpha\beta} + ([\xi_\alpha^+, \bar{\rho}] \xi_\beta)_{mn} \\ &+ \sum_\gamma \left\{ \frac{V_{-\alpha-\beta\gamma}(\xi_\gamma)_{mn}}{-\Omega_\alpha + \Omega_\beta - \Omega_\gamma} + \frac{V_{\alpha\beta-\gamma}(\xi_\gamma^+)_{mn}}{\Omega_\alpha - \Omega_\beta - \Omega_\gamma} \right\}, \end{aligned} \quad (3.19)$$

$$\langle 1\alpha | c_m^+ c_n | 1\beta 1\gamma \rangle = (\xi_\gamma)_{mn} \delta_{\alpha\beta} + (\xi_\beta)_{mn} \delta_{\alpha\gamma}, \quad (3.20)$$

where  $V_{\alpha\beta\gamma}$  is given by Eq. (3.6).

Eq. (3.18) gives transition density matrices involving the ground state. Eq. (3.19) expresses the transition density matrices between singly-excited states obtained from  $S^{(1)}$ , and Eq. (3.20) gives the transitions between singly



and doubly excited states. The first term in Eqs. (3.18) and (3.19) represents the interband (particle-particle and hole-hole) part of the density matrix, and involves only two electronic modes. The second (intraband, particle-hole and hole-particle) term, involves a summation over all electronic modes. These matrices provide an approximation for the density matrices between states contributing to the first- and to the second-order optical responses. The corresponding energies are

$$\Omega_{1\alpha} = \Omega_{\alpha}; \quad \Omega_{1\alpha 1\beta} = \Omega_{\alpha} + \Omega_{\beta} . \quad (3.21)$$

Taking higher order anharmonicities into account will allow us to compute density matrix elements involving new states. For example, the third-order response  $S^{(3)}$  includes higher lying excitations:  $\langle g|c_m^+c_n|1\alpha 1\beta 1\gamma\rangle$ ,  $\langle 1\alpha|c_m^+c_n|1\beta 1\gamma 1\delta\rangle$ ,  $\langle 1\alpha 1\beta|c_m^+c_n|1\gamma 1\delta 1\zeta\rangle$ ,  $\langle 1\alpha 1\beta|c_m^+c_n|1\gamma 1\delta\rangle$ . In general,  $S^{(j)}$  involves all transitions contributing to the lower order responses,  $j$ -transitions from the ground, single, double, ...,  $(j-1)$ th excited states to the  $j$ 'th excited state, and transitions between  $(j-1)$ th excited states.

By using an arbitrary single-particle operator  $\mu_{mn}$  in Eqs. (3.18)-(3.20), we can compute the full density matrix response function, which depends on all electronic modes. When  $\mu_{mn}$  is taken to be the dipole operator, we only obtain those modes that dominate the optical response. The ability to focus on the dominant modes alone has proved to be very useful for calculating the optical response [70,104,74]. However, in order to compute the excited-state density matrices all the modes (optically bright and dark) need to be captured.

When only few modes are known, Eqs. (3.18) and (3.19) are dominated by the interband term ( $[\xi_{\alpha}, \bar{\rho}]\xi_{\beta}$ ). The summation over available modes gives a negligible contribution because, in general,  $V_{\alpha\beta\gamma} \ll 1$ . The resulting transition matrices ( $\langle 1\alpha|c_m^+c_n|1\beta\rangle$ ,  $\langle g|c_m^+c_n|1\alpha 1\beta\rangle$ ) will, therefore, preserve all localization properties of the ground state  $\bar{\rho}$  and electronic modes  $\xi_{\alpha}$  and  $\xi_{\beta}$ . On the other hand, the summation over all TDHF modes significantly increases the

contribution of the second term in Eqs. (3.18) and (3.19) yielding the transition matrices which do not depend on the way the molecule interacts with the optical field (molecular dipole) but represent intrinsic molecular properties.

### 3.4 Merits of the DMRF method.

The TDHF uses the single-electron density matrix  $\langle g|c_m^+c_n|g\rangle$  to calculate the single-electron transition density matrices (electronic modes) between the ground state and the excited electronic states  $\langle g|c_m^+c_n|1\alpha\rangle$  which contribute to the linear response. Here a further step is made: using the ground-state density matrix and the electronic modes we calculated additional density matrices: between the ground state and the excited states  $\langle g|c_m^+c_n|1\alpha1\beta\rangle$  which contribute to the second-order response, transition density matrices between states  $\langle 1\alpha|c_m^+c_n|1\beta\rangle$  as well as the single-electron density matrices of the excited states  $\langle 1\alpha|c_m^+c_n|1\alpha\rangle$  which contribute to the linear response.

The TDHF procedure maps the quantum many-electron system onto a system of classical oscillators. The present approach is based on inverting the optical response function and mapping the original system onto an effective set of quantum states. An algorithm is developed for calculating Density-Matrix-Response-Functions (DMRF) for excited electronic states using the Time-Dependent Hartree-Fock (TDHF) approximation. The DMRF carries additional excited-state information about charge distributions and bonding patterns as well as the dynamical changes induced in these quantities by the external field.

The present analysis has several advantages. First, it connects the TDHF representation to the traditional quantum-mechanical treatment of the optical response in terms of global many-electron eigenstates. The latter may be useful for representing the properties of optically excited molecule. The procedure is further numerically inexpensive. The lack of long range electronic coherence

may be used to reduce the number of density matrix elements from  $\sim K^2$  to  $\sim KK_c$  where  $K_c$  denotes the number of orbital points of closely lying atoms [94] which communicate coherently upon optical excitation. Typically  $K_c \ll K$  results in favorable linear N-scaling of computational effort with size, resembling similar developments in ground state calculations [95]. The present approach can be extended to compute vibronic structure of electronic transitions by including the dependence of the electronic modes on nuclear coordinates.

### 3.5 Appendix A. Response Function for the Classical TDHF approach

To compute the DMRF we recast Eq. (3.9) in the form

$$i \frac{\partial z_\alpha(t)}{\partial t} = \Omega z_\alpha(t) + \sum_{\beta\gamma} \left( V_{-\alpha-\beta-\gamma} z_\beta^*(t) z_\gamma^*(t) + 2V_{-\alpha-\beta\gamma} z_\beta^*(t) z_\gamma(t) + V_{-\alpha\beta\gamma} z_\beta(t) z_\gamma(t) \right) - \mathcal{E}(t) \left[ \mu_{-\alpha} + \sum_{\beta} (\mu_{-\alpha-\beta} z_\beta^*(t) + \mu_{-\alpha\beta} z_\beta(t)) \right], \quad (3.22)$$

where the summation goes over  $\alpha, \beta, \gamma > 0$ . This nonlinear equation may be solved by expanding  $z(t)$  ( $z^*(t)$ ) in powers of the external field  $\mathcal{E}(t)$ :  $z(t) = z^{(1)}(t) + z^{(2)}(t) + \dots$ . Using the time-domain Green function

$$G_\alpha(t) = \exp(-i\Omega_\alpha t), \quad (3.23)$$

the first order solution of Eq. (3.22) is

$$z_\alpha^{(1)}(t) = i \int_{-\infty}^t d\tau \mathcal{E}(\tau) \mu_{-\alpha} G_\alpha(t - \tau). \quad (3.24)$$

To second order we obtain

$$\begin{aligned} z_\alpha^{(2)}(t) &= \int_{-\infty}^t \int_{-\infty}^{\tau_2} d\tau_2 d\tau_1 \mathcal{E}(\tau_2) \mathcal{E}(\tau_1) \sum_{\beta} (\mu_{-\alpha-\beta} \mu_\beta G_\beta^*(\tau_2 - \tau_1) \\ &\quad - \mu_{-\alpha\beta} \mu_{-\beta} G_\beta(\tau_2 - \tau_1)) G_\alpha(t - \tau_2) + i \int_{-\infty}^t \int_{-\infty}^{\tau_2} d\tau_2 d\tau_1 \mathcal{E}(\tau_2) \mathcal{E}(\tau_1) \end{aligned}$$

$$\begin{aligned}
 & \times \int_{\tau_2}^t d\tau \sum_{\beta\gamma} (V_{-\alpha-\beta-\gamma} \mu_\beta \mu_\gamma G_\beta^*(\tau - \tau_2) G_\gamma^*(\tau - \tau_1) \\
 & - 2V_{-\alpha\beta-\gamma} \mu_{-\beta} \mu_\gamma G_\beta(\tau - \tau_2) G_\gamma^*(\tau - \tau_1) \\
 & + V_{-\alpha\beta\gamma} \mu_{-\beta} \mu_{-\gamma} G_\beta(\tau - \tau_2) G_\gamma(\tau - \tau_1)) G_\alpha(t - \tau) . \tag{3.25}
 \end{aligned}$$

The time-dependent linear and second-order polarizabilities are given by

$$\mathcal{P}^{(1)} = \sum_{\alpha} \mu_{-\alpha} z_{\alpha}^{*(1)}(t) + \mu_{\alpha} z_{\alpha}^{(1)}(t) , \tag{3.26}$$

$$\begin{aligned}
 \mathcal{P}^{(2)} &= \sum_{\alpha} \mu_{-\alpha} z_{\alpha}^{*(2)}(t) + \mu_{\alpha} z_{\alpha}^{(2)}(t) + \frac{1}{2!} \sum_{\alpha\beta} \left( \mu_{-\alpha-\beta} z_{\alpha}^{*(1)}(t) z_{\beta}^{*(1)}(t) \right. \\
 & \left. + 2\mu_{\alpha-\beta} z_{\alpha}^{*(1)}(t) z_{\beta}^{(1)}(t) + \mu_{\alpha\beta} z_{\alpha}^{(1)}(t) z_{\beta}^{(1)}(t) \right) , \tag{3.27}
 \end{aligned}$$

where  $z^{(1)}(t)(z^{*(1)}(t))$  and  $z^{(2)}(t)(z^{*(2)}(t))$  are given by Eqs. (3.24) and (3.25) and their hermitian conjugates. Linear and second-order time-domain response functions are defined by

$$\mathcal{P}^{(1)} = \int d\tau \mathcal{E}(\tau) R^{(1)}(t; \tau) , \tag{3.28}$$

$$\mathcal{P}^{(2)} = \int d\tau_2 d\tau_1 \mathcal{E}(\tau_2) \mathcal{E}(\tau_1) R^{(2)}(t; \tau_1, \tau_2) . \tag{3.29}$$

Comparing Eqs. (3.28) and (3.26) (Eqs. (3.29) and (3.27)) and using Eqs. (3.24) and (3.25) we obtain for linear and second-order time-domain response function

$$\begin{aligned}
 R^{(1)}(t; \tau) &= - \sum_{\alpha} \mu_{-\alpha} \mu_{\alpha} (G_{\alpha}(t - \tau) G_{\alpha}^*(t - \tau)) , \tag{3.30} \\
 R^{(2)}(t; \tau_1, \tau_2) &= i \sum_{\alpha\beta\gamma} \int_{\tau_2}^t d\tau (V_{-\alpha-\beta-\gamma} \mu_{\alpha} \mu_{\beta} \mu_{\gamma} \\
 & \times G_{\alpha}^*(\tau - \tau_2) G_{\beta}^*(\tau - \tau_1) G_{\gamma}(t - \tau) \\
 & - 2V_{\alpha-\beta-\gamma} \mu_{-\alpha} \mu_{\beta} \mu_{\gamma} G_{\alpha}(\tau - \tau_2) G_{\beta}^*(\tau - \tau_1) G_{\gamma}(t - \tau) \\
 & + V_{\alpha\beta-\gamma} \mu_{-\alpha} \mu_{-\beta} \mu_{\gamma} G_{\alpha}(\tau - \tau_2) G_{\beta}(\tau - \tau_1) G_{\gamma}(t - \tau)) + h.c. \\
 & + \frac{1}{2!} \sum_{\alpha\beta} (2\mu_{-\alpha-\beta} \mu_{\alpha} \mu_{\beta} G_{\alpha}^*(\tau_2 - \tau_1)
 \end{aligned}$$

$$\begin{aligned}
 & - \mu_{\alpha-\beta}\mu_{-\alpha}\mu_{\beta}G_{\alpha}(\tau_2 - \tau_1)) G_{\beta}(t - \tau_2) + h.c. \\
 & - (\mu_{-\alpha-\beta}\mu_{\alpha}\mu_{\beta}G_{\alpha}^*(t - \tau_1)G_{\beta}^*(t - \tau_2) \\
 & + \mu_{\alpha\beta}\mu_{-\alpha}\mu_{-\beta}G_{\alpha}(t - \tau_1)G_{\beta}(t - \tau_2) \\
 & - 2\mu_{\alpha-\beta}\mu_{-\alpha}\mu_{\beta}G_{\alpha}(t - \tau_1)G_{\beta}^*(t - \tau_2)) . \tag{3.31}
 \end{aligned}$$

Applying the Fourier transform

$$f(\omega) = \int dt f(t) \exp(-i\omega t) ; \quad f(t) = \frac{1}{2\pi} \int d\omega f(\omega) \exp(i\omega t) \tag{3.32}$$

to Eqs. (3.31) and (3.30), we obtain the frequency-dependent linear and second-order polarizabilities

$$P^{(1)}(-\omega_s; \omega) = \int \frac{d\omega}{2\pi} 2\pi \delta(-\omega_s + \omega) \alpha(-\omega_s; \omega) \mathcal{E}(\omega) , \tag{3.33}$$

$$\begin{aligned}
 P^{(2)}(-\omega_s; \omega_1, \omega_2) &= \int \frac{d\omega_1}{2\pi} \frac{d\omega_2}{2\pi} 2\pi \delta(-\omega_s + \omega_1 + \omega_2) \\
 &\times \beta(-\omega_s; \omega_1, \omega_2) \mathcal{E}(\omega_1) \mathcal{E}(\omega_2) . \tag{3.34}
 \end{aligned}$$

The final expressions for the linear and the second order polarizabilities are:

$$\alpha(\omega) = \sum_{\alpha} \frac{2\mu_{-\alpha}\mu_{\alpha}\Omega_{\alpha}}{\Omega_{\alpha}^2 - \omega^2} , \tag{3.35}$$

$$\begin{aligned}
 \beta(-\omega_s = \omega_1 + \omega_2; \omega_1, \omega_2) &= -\frac{1}{4} \sum_{\alpha\beta\gamma} (V_{\alpha\beta\gamma}\mu_{-\alpha}\mu_{-\beta}\mu_{-\gamma} + h.c.) \\
 &\times \left( \frac{1}{(\Omega_{\alpha} - \omega_1)(\Omega_{\beta} - \omega_2)(\Omega_{\gamma} + \omega_1 + \omega_2)} + \frac{1}{(\Omega_{\alpha} + \omega_1)(\Omega_{\beta} + \omega_2)(\Omega_{\gamma} - \omega_1 - \omega_2)} \right) \\
 &+ (2V_{\alpha-\beta-\gamma}\mu_{-\alpha}\mu_{\beta}\mu_{\gamma} + h.c.) \\
 &\times \left( \frac{1}{(\Omega_{\alpha} + \omega_1)(\Omega_{\beta} - \omega_2)(\Omega_{\gamma} + \omega_1 + \omega_2)} + \frac{1}{(\Omega_{\alpha} - \omega_1)(\Omega_{\beta} + \omega_2)(\Omega_{\gamma} + \omega_1 + \omega_2)} \right) \\
 &+ \left( \frac{1}{(\Omega_{\alpha} - \omega_1)(\Omega_{\beta} + \omega_2)(\Omega_{\gamma} - \omega_1 - \omega_2)} + \frac{1}{(\Omega_{\alpha} + \omega_1)(\Omega_{\beta} - \omega_2)(\Omega_{\gamma} - \omega_1 - \omega_2)} \right) \\
 &+ (V_{-\alpha\beta\gamma}\mu_{\alpha}\mu_{-\beta}\mu_{-\gamma} + h.c.) \\
 &\times \left( \frac{1}{(\Omega_{\alpha} + \omega_1)(\Omega_{\beta} + \omega_2)(\Omega_{\gamma} + \omega_1 + \omega_2)} + \frac{1}{(\Omega_{\alpha} - \omega_1)(\Omega_{\beta} - \omega_2)(\Omega_{\gamma} - \omega_1 - \omega_2)} \right) \\
 &+ \frac{1}{4} \frac{1}{2!} \sum_{\alpha\beta} (\mu_{\alpha\beta}\mu_{-\alpha}\mu_{-\beta} + h.c.) \left( \frac{1}{(\Omega_{\alpha} - \omega_1)(\Omega_{\beta} + \omega_1 + \omega_2)} \right)
 \end{aligned}$$

$$\begin{aligned}
 & + \frac{1}{(\Omega_\alpha - \omega_2)(\Omega_\beta + \omega_1 + \omega_2)} + \frac{1}{(\Omega_\alpha - \omega_1)(\Omega_\beta - \omega_2)} + \frac{1}{(\Omega_\alpha + \omega_1)(\Omega_\beta - \omega_1 - \omega_2)} \\
 & + \left. \frac{1}{(\Omega_\alpha + \omega_2)(\Omega_\beta - \omega_1 - \omega_2)} + \frac{1}{(\Omega_\alpha + \omega_1)(\Omega_\beta + \omega_2)} \right) \\
 & + 2\mu_{-\alpha\beta}\mu_\alpha\mu_{-\beta} \left( \frac{1}{(\Omega_\alpha + \omega_1)(\Omega_\beta + \omega_1 + \omega_2)} + \frac{1}{(\Omega_\alpha + \omega_2)(\Omega_\beta + \omega_1 + \omega_2)} \right. \\
 & + \frac{1}{(\Omega_\alpha + \omega_1)(\Omega_\beta - \omega_2)} + \frac{1}{(\Omega_\alpha - \omega_1)(\Omega_\beta - \omega_1 - \omega_2)} \\
 & \left. + \frac{1}{(\Omega_\alpha - \omega_2)(\Omega_\beta - \omega_1 - \omega_2)} + \frac{1}{(\Omega_\alpha + \omega_1)(\Omega_\beta - \omega_2)} \right) \tag{3.36}
 \end{aligned}$$

### 3.6 Appendix B. Sum-over-States Polarizabilities of the Effective Multilevel System

In this Appendix optical polarizabilities for the quantum model QOM are calculated using the standard Sum-over-States expressions [26]. The linear and the quadratic polarizabilities are given by

$$\alpha(\omega) = \sum_n \frac{2\omega_{ng}r_{gn}r_{ng}}{\omega_{ng}^2 - \omega^2} \tag{3.37}$$

$$\begin{aligned}
 \beta(-\omega_s = \omega_1 + \omega_2; \omega_1, \omega_2) & = -\frac{1}{4} \sum_{n, n'} r_{gn}r_{nn'}r_{n'g} \\
 & \times \left( \frac{1}{(\omega_{n'g} + \omega_1 + \omega_2)(\omega_{ng} + \omega_1)} \frac{1}{(\omega_{n'g} - \omega_1 - \omega_2)(\omega_{ng} - \omega_1)} \right. \\
 & + \frac{1}{(\omega_{n'g} + \omega_1 + \omega_2)(\omega_{ng} + \omega_2)} + \frac{1}{(\omega_{n'g} - \omega_1 - \omega_2)(\omega_{ng} - \omega_2)} \\
 & + \frac{1}{(\omega_{n'g} + \omega_1)(\omega_{ng} + \omega_1 + \omega_2)} + \frac{1}{(\omega_{n'g} - \omega_1)(\omega_{ng} - \omega_1 - \omega_2)} \\
 & + \frac{1}{(\omega_{n'g} + \omega_2)(\omega_{ng} + \omega_1 + \omega_2)} + \frac{1}{(\omega_{n'g} - \omega_2)(\omega_{ng} - \omega_1 - \omega_2)} \\
 & + \frac{1}{(\omega_{n'g} - \omega_2)(\omega_{ng} + \omega_1)} + \frac{1}{(\omega_{n'g} + \omega_2)(\omega_{ng} - \omega_1)} \\
 & \left. + \frac{1}{(\omega_{n'g} - \omega_1)(\omega_{ng} + \omega_2)} + \frac{1}{(\omega_{n'g} + \omega_1)(\omega_{ng} - \omega_2)} \right), \tag{3.38}
 \end{aligned}$$

where the sum runs over all excited states  $n$  and  $n'$ , and  $g$  stands for the ground state.  $r_{kl} = \langle k|\mathcal{P}|l\rangle$  ( $r_{lk} = r_{kl}^*$ ) is the transition dipole between  $k$ 'th and  $l$ 'th states.

We start with the Hamiltonian (Eq. (3.13)) representing  $K$  - quantum oscillators with the electronic polarizability operator  $\mathcal{P}(a^+, a)$  (Eq. (3.14)). To calculate the transition dipoles we first compute the wavefunctions of our oscillator system to first order in  $V$ :

$$\begin{aligned}\phi^{(0)} &= |g\rangle_0 - \frac{1}{3!} \sum_{\alpha\beta\gamma} \frac{V_{-\alpha-\beta-\gamma}}{\Omega_\alpha + \Omega_\beta + \Omega_\gamma} a_\alpha^+ a_\beta^+ a_\gamma^+ |g\rangle_0 \\ \phi_\alpha^{(1)} &= a_\alpha^+ |g\rangle_0 + \frac{1}{3!} \sum_{\beta\gamma} \frac{V_{\alpha-\beta-\gamma}}{\Omega_\alpha - \Omega_\beta - \Omega_\gamma} a_\beta^+ a_\gamma^+ |g\rangle_0 \\ \phi_{\beta\gamma}^{(2)} &= a_\beta^+ a_\gamma^+ |g\rangle_0 - \frac{1}{3!} \sum_\alpha \frac{2V_{-\alpha\beta\gamma}}{\Omega_\alpha - \Omega_\beta - \Omega_\gamma} a_\alpha^+ |g\rangle_0 \\ &\quad + \frac{1}{3!} \sum_{\delta\zeta} \left( \frac{V_{-\gamma-\delta\zeta} a_\beta^+}{\Omega_\gamma - \Omega_\delta - \Omega_\zeta} + \frac{V_{-\delta-\zeta\beta} a_\gamma^+}{\Omega_\beta - \Omega_\delta - \Omega_\zeta} \right) a_\delta^+ a_m^+ |g\rangle_0 \quad (3.39)\end{aligned}$$

where  $V_{\alpha\beta\gamma}$  is given by Eq. (3.6) and  $|g\rangle_0$ ,  $a_\alpha^+ |g\rangle_0$ ,  $a_\alpha^+ a_\beta^+ |g\rangle_0$ , and  $a_\alpha^+ a_\beta^+ a_\gamma^+ |g\rangle_0$  denote the ground, single, double and triple excited states of the uncoupled system respectively.

The transition dipoles among the ground and the first two excited states are given by:

$$\langle \phi^{(0)} | \mathcal{P} | \phi^{(0)} \rangle = 0, \quad (3.40)$$

$$\langle \phi^{(0)} | \mathcal{P} | \phi_\alpha^{(1)} \rangle = \mu_\alpha, \quad (3.41)$$

$$\langle \phi^{(0)} | \mathcal{P} | \phi_{\alpha\beta}^{(2)} \rangle = \frac{1}{2!} \mu_{\alpha\beta} + 2 \sum_\gamma \left\{ \frac{V_{\alpha\beta-\gamma} \mu_\gamma}{\Omega_\alpha + \Omega_\beta - \Omega_\gamma} - \frac{V_{\alpha\beta\gamma} \mu_{-\gamma}}{\Omega_\alpha + \Omega_\beta + \Omega_\gamma} \right\}, \quad (3.42)$$

$$\langle \phi_\alpha^{(1)} | \mathcal{P} | \phi_\beta^{(1)} \rangle = \mu_{-\alpha\beta} + \sum_\gamma \left\{ \frac{V_{\alpha\beta-\gamma} \mu_{-\gamma}}{\Omega_\alpha - \Omega_\beta - \Omega_\gamma} + \frac{V_{-\alpha-\beta\gamma} \mu_\gamma}{-\Omega_\alpha + \Omega_\beta - \Omega_\gamma} \right\}, \quad (3.43)$$

$$\langle \phi_\alpha^{(1)} | \mathcal{P} | \phi_{\alpha\beta}^{(2)} \rangle = \mu_\beta. \quad (3.44)$$

Substituting these transitions dipoles in Eqs. (3.37) and (3.38) we obtain expressions for the linear and the second-order polarizabilities which coincide

with Eqs. (3.35) and (3.36). This proves the equivalence of the linear and the second-order polarizabilities of the QOM calculated in the classical limit and using the Sum-over-States expression.

### 3.7 Appendix C. Nonlinear response of systems with Coordinate-dependent anharmonicities

When the anharmonicities in Eqs. (3.13) and (3.14) only depend on coordinates  $q_\alpha = (a_\alpha^+ + a_\alpha)q_{0\alpha}/\sqrt{2}$  (and not on the momenta  $p_\alpha = (a_\alpha^+ - a_\alpha)p_{0\alpha}/\sqrt{2}$ ) the DMRF are simplified considerably. In this case we have

$$V_{\alpha\beta\gamma} = V_{-\alpha-\beta-\gamma} = V_{-\alpha\beta\gamma} = V_{-\alpha-\beta\gamma} \equiv V_{\alpha\beta\gamma}^q \frac{q_{0\alpha}q_{0\beta}q_{0\gamma}}{(\sqrt{2})^3}, \quad (3.45)$$

$$\mu_{-\alpha-\beta} = \mu_{\alpha\beta} = \mu_{-\alpha\beta} \equiv \mu_{\alpha\beta}^q \frac{q_{0\alpha}q_{0\beta}}{(\sqrt{2})^2}, \quad (3.46)$$

$$\mu_\alpha = \mu_\alpha \equiv \mu_\alpha^q \frac{q_{0\alpha}}{\sqrt{2}}. \quad (3.47)$$

The time-domain response (Eq. (3.31)) then becomes

$$\begin{aligned} R(t; \tau_1, \tau_2) &= - \int_{\tau_2}^t d\tau \sum_{\alpha\beta\gamma} V_{\alpha\beta\gamma}^q \mu_\alpha^q \mu_\beta^q \mu_\gamma^q \frac{(q_{0\alpha}q_{0\beta}q_{0\gamma})^2}{8} \\ &\quad \times C_\alpha(\tau - \tau_2) C_\beta(\tau - \tau_1) C_\gamma(t - \tau) \\ &\quad + \sum_{\alpha\beta} \mu_{\alpha\beta}^q \mu_\alpha^q \mu_\beta^q \frac{(q_{0\alpha}q_{0\beta})^2}{4} (2C_\alpha(\tau_2 - \tau_1) C_\beta(t - \tau_2) \\ &\quad + C_\alpha(t - \tau_1) C_\beta(t - \tau_2)), \end{aligned} \quad (3.48)$$

where

$$C_\alpha(t) = i(G_\alpha(t) - G_\alpha^*(t)) = 2\sin(\Omega_\alpha t), \quad (3.49)$$

is the classical linear response of a harmonic oscillator.

Similarly Eq. (3.36) reduces to

$$\beta(-\omega_s = \omega_1 + \omega_2; \omega_1, \omega_2) = - \sum_{\alpha\beta\gamma} \frac{V_{\alpha\beta\gamma}^q \mu_\alpha^q \mu_\beta^q \mu_\gamma^q}{M_\alpha M_\beta M_\gamma}$$



$$\begin{aligned}
 & \times \frac{1}{(\Omega_\alpha^2 - \omega_1^2)(\Omega_\beta^2 - \omega_2^2)(\Omega_\gamma^2 - (\omega_1 + \omega_2)^2)} \\
 & + \sum_{\alpha\beta} \frac{\mu_{\alpha\beta}^q \mu_\alpha^q \mu_\beta^q}{M_\alpha M_\beta} \left( \frac{1}{(\Omega_\alpha^2 - \omega_1^2)(\Omega_\beta^2 - (\omega_1 + \omega_2)^2)} \right. \\
 & \left. + \frac{1}{(\Omega_\alpha^2 - \omega_2^2)(\Omega_\beta^2 - (\omega_1 + \omega_2)^2)} + \frac{1}{(\Omega_\alpha^2 - \omega_1^2)(\Omega_\beta^2 - \omega_2^2)} \right). \quad (3.50)
 \end{aligned}$$

## Chapter 4

# Chemical Bonding and Size-Scaling of Off-Resonant Nonlinear Polarizabilities.

The size-scaling of various optical properties in conjugated polymers has been studied extensively, both theoretically [105–108] and experimentally [109–111,13]. Linear absorption of short oligomers with  $N < 12 - 20$  carbon atoms shows an  $\Omega \sim N^{-\mu}$  scaling of the lowest excitation frequency in linear absorption (optical gap) with  $\mu \sim 0.4 - 0.6$  [109]. The Hückel model (which neglects Coulomb interactions) yields  $\mu = 1$  [108]. An important relation is the scaling of nonlinear susceptibilities with molecular size. The power scaling law  $\gamma \sim N^b$  for the third-order polarizability, where  $N$  is the number of carbon atoms, has been established experimentally in the early 70'th [112], and supported by theoretical calculations using the free electron model [113]. Numerous subsequent studies showed that for short chains, the exponent  $b$  can vary between 3 and 8, depending on the system and model, and eventually approaches 1 (saturates) for long molecules. The crossover between these two behaviors is related to the exciton coherence size [60,74,73,109,111]. Calculations performed using the Hückel model predict saturation at long chains ( $N \sim 50$ ) and  $b \sim 5 - 9$  [108,114,115], whereas calculations based on the Pariser-Parr-Pople (PPP) Hamiltonian which includes electronic correlations

predict a shorter saturation size ( $N \sim 20 - 30$ ) and  $b \sim 4 - 5$  [60,59,28,29]. Sum-over-states calculations of  $\gamma$  in short oligomers yield a scaling exponents  $b \approx 8$  for symmetric linear cyanites and  $b \approx 4$  for linear polyenes [116]. Difficulties with the controlled synthesis and poor solubility of polyenic oligomers restricted early experimental studies to molecules with up to 30-40 carbon atoms [13,112,117] which showed no saturation. These problems have been overcome, and the saturation of  $\gamma$  has been observed experimentally at  $\sim 200$  double bonds [111], which is much larger than early estimates.

Considerable attention has been also paid to the dependencies of nonlinearities on other molecular parameters. It has to be argued that the bond-length alternation parameter  $\Delta$  is related to electron localization [118]. In alternating chains the Hückel model predicts  $\gamma \sim \Delta^{-6}$  divergence at small  $\Delta$  [108]. Flytzanis and co-workers employed the Hückel model to study the scaling of off-resonant  $\gamma$  of large oligomers with the saturated optical gap  $\tilde{\Omega}$  [105,118]. The resulting  $\gamma \sim \tilde{\Omega}^{-6}$  scaling law is in a qualitative good agreement with experimental data collected for both off-resonant and resonant third-order polarizabilities of different conjugated polymers [119]. Recent resonant experiments show the following relation  $\gamma(-3\omega; \omega, \omega, \omega)/\alpha_{max} \sim \tilde{\Omega}^{-10}$  [109,110], where the scaling of both  $\gamma$  and  $\alpha_{max}$  (absorption maximum) depends on the concentration of chromophores in films and the ratio is approximately independent on dilution.

## 4.1 Electronic Normal Modes and Size-Scaling of Optical Polarizabilities of Polyacetylene Oligomers

To investigate the size-scaling in unsubstituted polyenes the off-resonant polarizabilities up to seventh order, for polyacetylene oligomers with up to 300 carbon atoms were calculated using the DSMA combined with the PPP hamil-

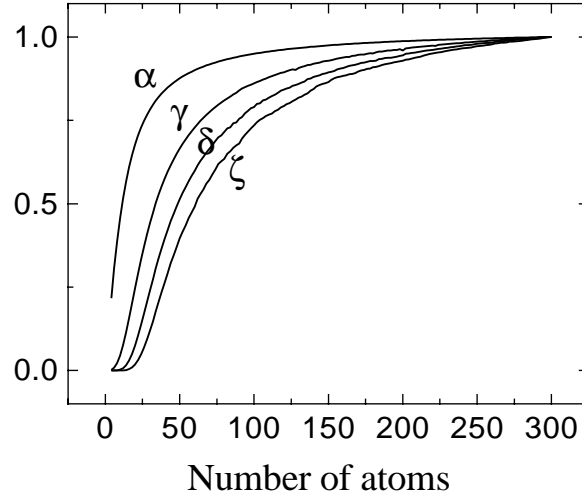


Figure 4.1: Scaling of linear  $\alpha$  third order  $\gamma$ , fifth order  $\delta$ , and seventh order  $\zeta$  polarizabilities with size. Shown are the magnitudes of polarizability normalized at its saturated value  $\frac{\chi^{(j)}(N)}{N\chi_{sat}^{(j)}}$ , where  $\chi_{sat}^{(j)} = \frac{\chi^{(j)}(N)}{N}$  at  $N \rightarrow \infty$ ,  $j=1,3,5,7$ . The magnitudes of saturated polarizabilities are:  $\alpha_{sat} = 1.7 \times 10^{-23}$  esu,  $\gamma_{sat} = 1.1 \times 10^{-33}$  esu,  $\delta_{sat} = 1.9 \times 10^{-43}$  esu,  $\zeta_{sat} = 5.2 \times 10^{-53}$  esu.

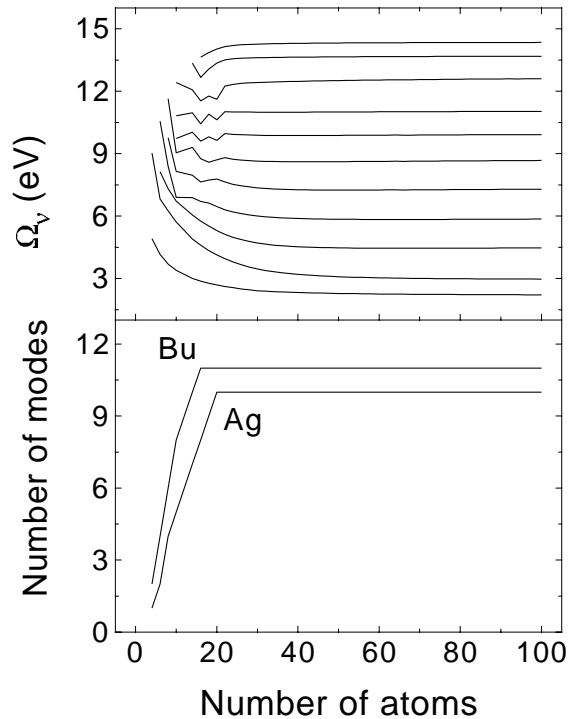


Figure 4.2: Upper panel: size dependence of mode frequencies, lower panel: the number of dominant modes, needed to compute susceptibilities with 0.1% accuracy compared with the full  $N^2/4$  modes TDHF calculations.

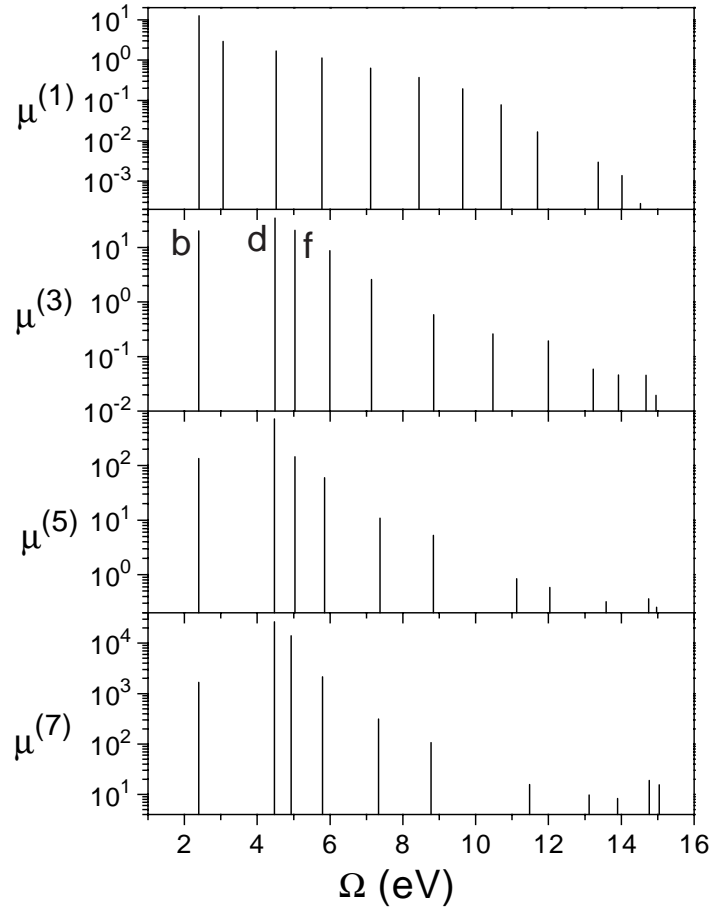


Figure 4.3: The effective dipole moments  $\mu_\nu$  vs. Electronic Oscillator Frequencies  $\Omega_\nu$  for an  $N = 100$  polyacetylene chain. Shown are the dominant modes in first, third, fifth, and seventh orders of nonlinearity.

tonian (see Section 2.1). In all calculations the fixed geometry was used with unit cell size along the backbone  $a = 1.22\text{\AA}$  and bond-length alternation parameter  $l_n = \Delta = 0.07\text{\AA}$ . The variation of the lowest four nonvanishing polarizabilities  $\alpha, \gamma, \delta,$  and  $\zeta$  with the number of carbon atoms  $N$  is displayed in the Fig. 4.1. Since the molecules have an inversion symmetry, antisymmetric ( $B_u$ ) modes contribute to the odd order responses ( $j = 1, 3, 5, 7$ ), whereas the symmetric ( $A_g$ ) oscillators appear only in the even order responses ( $j = 2, 4, 6$ ). Only 11  $B_u$  and 10  $A_g$  modes (see Fig. 4.2) were required to obtain a 0.1% accuracy compared with the full ( $N^2/4$ ) modes TDHF calculations (comparisons were made for chains with up to 40 carbon atoms and up to the third-order

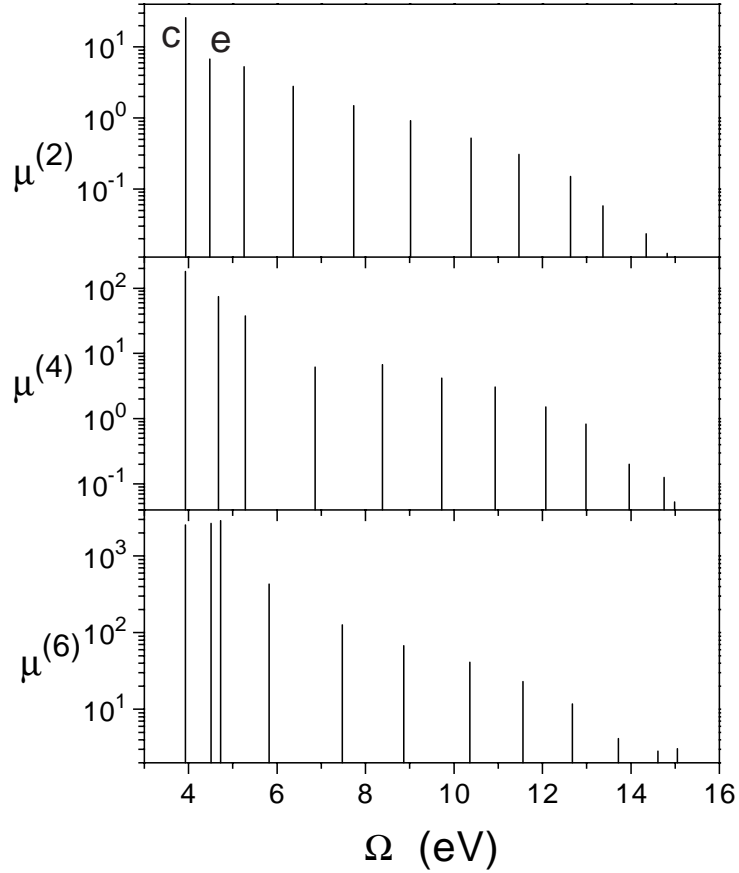


Figure 4.4: The effective dipole moments  $\mu_\nu$  vs. Electronic Oscillator Frequencies  $\Omega_\nu$  for an  $N = 100$  polyacetylene chain. Shown are the dominant modes in second, fourth, and sixth orders of nonlinearity.

response, where the full TDHF calculations were feasible). Comparison of the absolute magnitudes of the calculated polarizabilities with *ab initio* coupled perturbed Hartree-Fock theory [30,31] show an agreement to within a factor of 1.5 for linear and 2.5 for third-order static polarizabilities. This agreement is very encouraging, in particular given that the present calculations did not employ any geometry optimization.

The effective dipole moments,  $\mu_\nu^{(j)}$  (Eq. (2.50)) of antisymmetric ( $B_u$ ) and symmetric ( $A_g$ ) oscillators of a  $N = 100$  polyacetylene chain are displayed vs. mode frequencies  $\Omega_\nu$  in Figs. 4.3 and 4.4 respectively. An important observation is that the same modes dominate at all orders. These modes

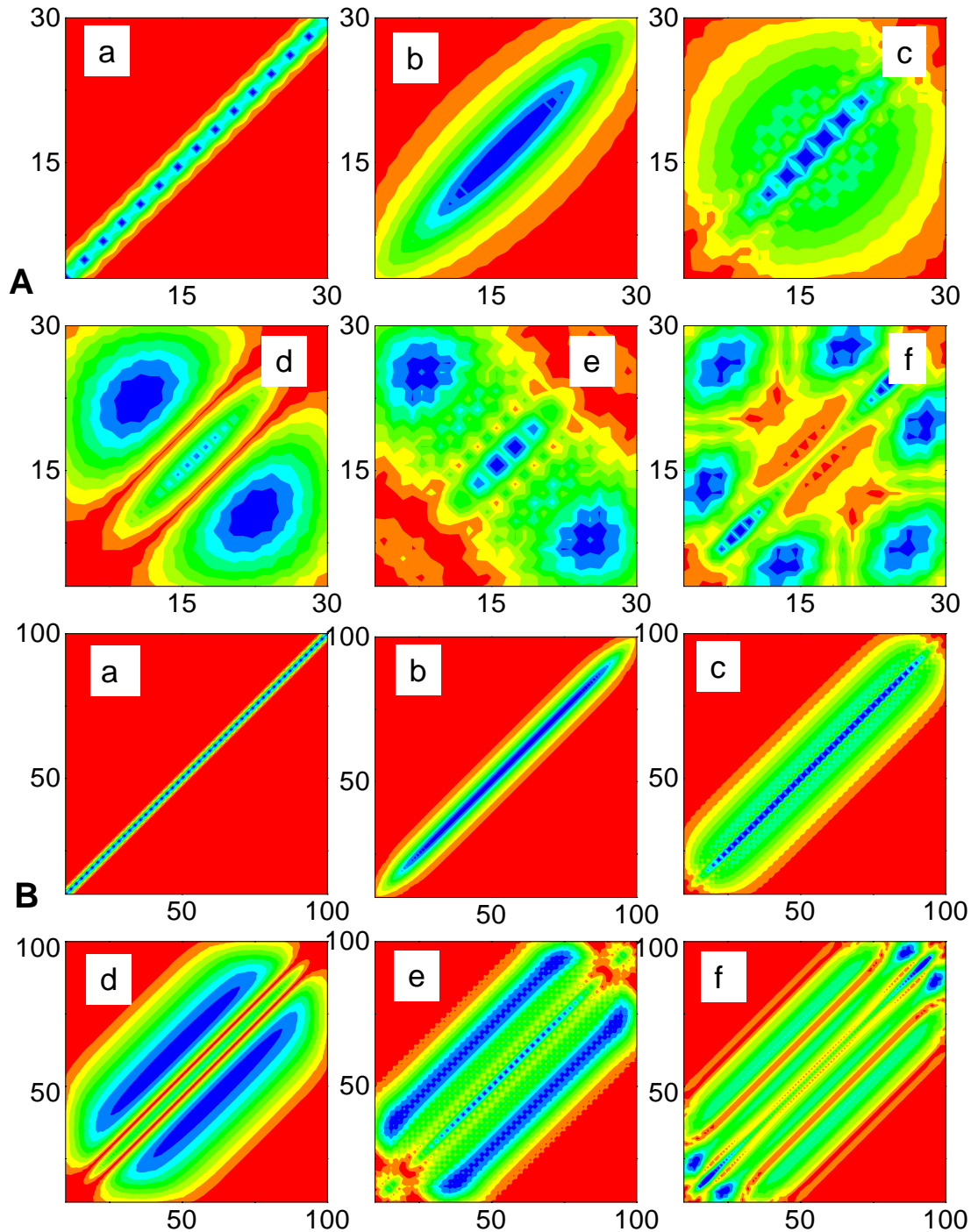


Figure 4.5: **A)** Contour plots of  $\bar{\rho}$  (a) and the dominant modes (b-f) that contribute to the responses up to the seventh order for the system of Figs. 4.3 and 4.4 ( $N = 30$ ). Shown are the absolute values of the density matrices smoothed over four points to eliminate fast oscillations and to highlight the long range behavior. The axes are labeled by the carbon atoms along the chain. Exciton confinement effects are clearly seen in panels c, d, e, f. Frequencies of modes b-f are 2.6, 4.0, 4.8, 5.2, and 5.6 eV, respectively. **B)** Same as **A** but for a longer chain ( $N = 100$ ). Frequencies of b-f modes are 2.4, 3.9, 4.5, 4.7, and 5.1 eV, respectively.

manifest themselves in the response with different effective oscillator strengths at each order. Higher-frequency modes make more significant contributions to the higher order response. Contour plots of the ground state density matrix  $\bar{\rho}(a)$  as well as the five dominant modes labeled b-f in Figs 4.3 and 4.4 is shown in Figure 4.5B for  $N = 100$ . The delocalization of the off diagonal elements represents *electronic coherence* between different atoms. Figure 4.5B clearly shows how electronic coherence which is very limited for the almost diagonal  $\bar{\rho}$ , increases very rapidly for the higher modes. To illustrate finite size effects the same quantities for  $N = 30$  are displayed in Figure 4.5A. We note that modes a and b are hardly affected by reducing the size from 100 to 30. However, the higher modes which are more delocalized, show significant confinement effects. Thus the mode size measured by the off-diagonal electronic coherence grows with its frequency [55,60,74], and, therefore, the coherence size increases for higher orders nonlinearities. This can be seen in Fig. 4.6 where the variation of the scaling exponents  $b \equiv d[\ln\chi]/d[\ln N]$ ,  $\chi = \alpha, \gamma, \delta$ , and  $\zeta$  with size is displayed. The curves shown in Fig. 4.6 attain a maximums  $b_\gamma = 3.5$  at  $N_\gamma = 8$ ;  $b_\delta = 5.7$  at  $N_\delta = 10$ ;  $b_\zeta = 7.9$  at  $N_\zeta = 12$ .<sup>1</sup>  $b$  reaches a maximum and eventually approaches 1 (saturates). This saturation occurs at longer sizes with increased order of nonlinearity. Measurements of  $\gamma$  in solution as a function of chain length in long chains (up to 240 double bonds) were reported in [111]. The experimental  $b$ -curve resembles Fig. 4.6 with a maximum  $b_\gamma = 2.5$  for  $N_\gamma = 60$  double bonds. The size-scaling of optical susceptibilities of donor/acceptor substituted molecules are investigated further using advanced INDO/S hamiltonian in Chapter 10.

The various terms in the effective dipole moment  $\eta^{(i)}$  (Eq. (2.37)) make different contributions to the effective oscillator strengths and to the nonlinear response. This allows us to separate the relative contributions of different pro-

---

<sup>1</sup> $b$  attains a larger maximum value for calculations with geometry optimization.



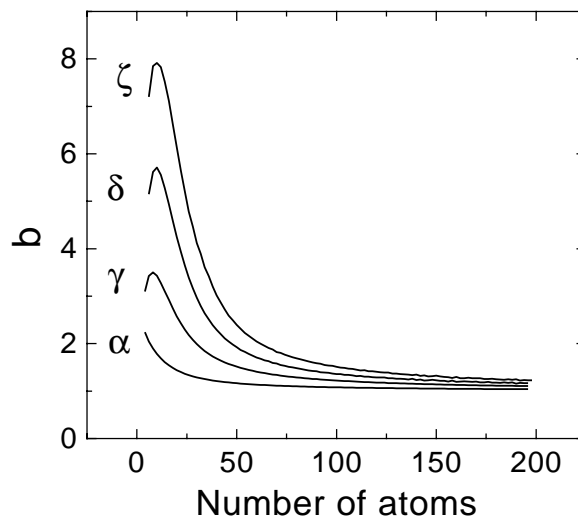


Figure 4.6: Variation of the scaling exponents  $b \equiv d[\ln\chi]/d[\ln N]$ ,  $\chi = \alpha, \gamma, \delta,$  and  $\zeta$  with size. Note that both the maximum value of  $b$  and the size where the maximum is attained increase with the degree of nonlinearity.

cesses to the response. As an example, the ratio ( $a \equiv \chi_{p-h}^{(j)}/\chi^{(j)}$ ) of interband contribution to the total polarizability  $\gamma, \delta,$  and  $\zeta$  for oligomers with up to 150 atoms are depicted in Fig. 4.7. For small chains, the particle-hole contribution is negative in all cases. With increased chain length this contribution changes sign, and for chains longer than the exciton coherence size ( $\sim 30$ ) [60,74,73,98] the ratio saturates to the values  $a_\gamma = 0.4$ ;  $a_\delta = 0.26$ ;  $a_\zeta = 0.19$ .

## 4.2 Single-Oscillator Approximation for Off-Resonant Polarizabilities

In addition to its clear numerical advantages, the oscillator representation may be used to develop simple rules of thumb for the scaling of optical polarizabilities with molecular size and chemical bonding. In this Section a simple analytical expressions for the polyenic off-resonant linear and nonlinear polarizabilities are derived and the parameters which affect the magnitude and the scaling of these optical properties are investigated.

The ground state can be defined through molecular geometry (the average

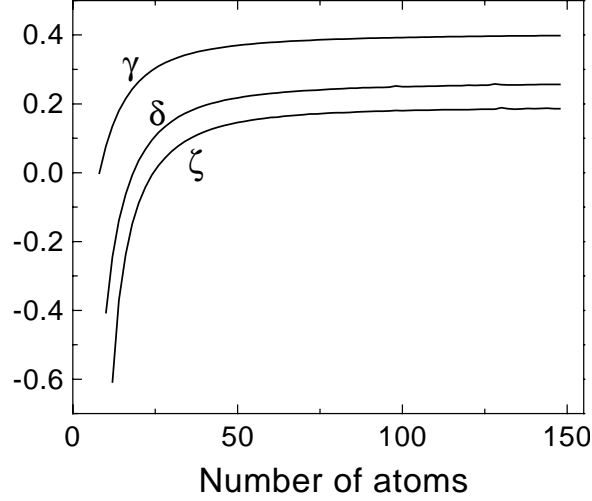


Figure 4.7: The ratio of the interband contribution ( $a = \chi_{p-h}^{(j)} / \chi^{(j)}$ ) to  $\gamma$ ,  $\delta$ , and  $\zeta$  polarizabilities. Note that for small chain lengths the particle-hole contributions to the high order polarizabilities are negative, and the interband contribution decreases with increased degree of nonlinearity. The ratio saturates to the values  $a_\gamma = 0.4$ ;  $a_\delta = 0.26$ ;  $a_\zeta = 0.19$ .

bond length  $a$  and the bond length alternation  $\Delta$  parameters) and ground state density matrix (charges and chemical bonding). The chemical bonding is described by the bond order  $\sigma_n \equiv (\bar{\rho}_{n,n+1} + \bar{\rho}_{n+1,n+2})/2$  and the bond order alternation parameters  $\kappa_n \equiv |\bar{\rho}_{n,n+1} - \bar{\rho}_{n+1,n+2}|$ . Numerical calculations show that the bond order parameter  $\sigma_n$  depends only weakly on the bond length alternation  $\Delta$  in polyacetylene. Since  $\bar{\rho}_{nm}$  is a localized function of  $n - m$ , and edge effects are short range, we thus expect both  $\sigma_n$  and  $\kappa_n$  to depend very weakly on  $n$  (apart from small edge effects). The average values of  $\sigma = \langle \sigma_n \rangle = 0.31$  and  $\kappa = \langle \kappa_n \rangle$  can be therefore safely used as good measures of the chemical bonding.

We start with the linear response and renormalized spectral moments which are independent on the applied static field

$$f^{(2k)} \equiv -\frac{1}{\mathcal{E}_0} \mathcal{K}_k^{(1)}. \quad (4.1)$$

A family of sum rules for the linear response Eq. (2.53) can then be recasted

as

$$\begin{aligned} f^{(n)} &= \sum_{\nu=1}^M (\Omega_{\nu})^n f_{\nu}, \quad n = 0, 2, 4, \dots, \\ f^{(n)} &\equiv 0, \quad n = 1, 3, 5, \dots \end{aligned} \quad (4.2)$$

By taking the simplest (single-mode) approximation ( $M = 1$ ) we obtain closed analytical expressions for the susceptibilities. Making use of sum rule for  $n = 0, 2$  and Eq. (2.55) we obtain for the off-resonant polarizability  $\alpha \equiv \alpha(\omega = 0)$

$$\alpha = [f^{(0)}]^2 / f^{(2)}, \quad \Omega = [f^{(2)} / f^{(0)}]^{1/2} \quad (4.3)$$

The single mode approximation lumps the contributions of all electronic oscillators into a single effective oscillator with frequency  $\Omega$ . This mode may not be identified with any of the original TDHF modes; it is rather a natural collective variable which represents in the best way the contribution of all electronic oscillators to the zero frequency optical response.

Eqs. (4.3) express the linear polarizability  $\alpha$  and the optical gap  $\Omega$  in terms of the parameters of the Hamiltonian and its ground state  $\bar{\rho}_{mn}$ . This provides an important structure-polarizability relationship, which allows to predict the magnitude of the linear response using detailed information regarding the chemical structure and bonding. The moments contain the global relevant information about system and are much easier to model and parameterize compared with individual frequencies  $\Omega_{\nu}$  and oscillator strengths  $f_{\nu}$ .

To proceed further, the dependence of the spectral moments  $f^{(0)}$  and  $f^{(2)}$  on molecular parameters is examined. We expect that for large sizes,  $f^{(n)} \sim N$  for all  $n$ . Numerical results for  $\bar{\rho}_{mn}$  show that boundary effects on  $\bar{\rho}_{mn}$  are short range [60,98], and only affect it when the distance of  $m$  and  $n$  from an edge is one or two atoms. This suggests that boundary effects on the sum rules should also be short range, and that  $f^{(n)}$  can be written in the form  $f^{(n)} = N f_1^{(n)} + f_0^{(n)}$ , where  $f_1^{(n)}$  is related to the  $N \rightarrow \infty$  behavior, and  $f_0^{(n)}$

represent edge effects in the sum rules. Careful examination of the sum rules shows that the largest corrections to this form are  $\sim N^{-1}$  and  $\sim N^{-1} \ln N$ , which can be safely neglected for  $N \geq 10$ . Expressions for  $f_1^{(n)}$  and  $f_0^{(n)}$  can be obtained by inspecting the behavior of  $f^{(n)}$  for large  $N$ :  $f_1^{(n)}$  are expressed in terms of the saturated components of  $\bar{\rho}_{mn}$ , i.e., the values of  $\bar{\rho}_{mn}$  for large  $N$  when  $m$  and  $n$  are far from the edges, while  $f_0^{(n)}$  involves the values of  $\bar{\rho}_{mn}$  near the edges (note that  $\bar{\rho}_{mn}$  is strongly localized in  $m - n$ ). Neglecting edge effects we have  $f^{(0)} = N f_1^{(0)}$ . For  $f^{(2)}$  the  $N$ -independent term  $f_0^{(2)}$  is retained. This will be rationalized below.

Substituting  $f^{(2)}$  and  $f^{(0)}$  in Eq (4.3) we obtain

$$\alpha = \chi^{(1)} = \frac{[f_1^{(0)}]^2}{f_1^{(2)}} \frac{N^2}{N + L} \quad (4.4)$$

where  $L \equiv f_0^{(2)}/f_1^{(2)}$  is the effective coherence length.

Having established the size-scaling of  $\alpha$  with size  $N$ , we turn to its dependence on other molecular parameters. Using the sum rules of [120] for  $f^{(0)}$  we have  $f_1^{(0)} = 4e^2 a^2 \beta_0 \sigma$ . The second moment  $f^{(2)}$  is more complicated. The formal expression for  $f^{(2)}$  [120] implies that it vanishes in a translationally invariant system. There are three mechanisms which break the translational symmetry with respect to the lattice constant and make  $f^{(2)}$  finite: bond order alternation related to symmetry breaking in  $\bar{\rho}$ , bond-length alternation which causes symmetry breaking in the Hamiltonian, and edge effects.<sup>2</sup> The second mechanism does not contribute to  $f_1^{(2)}$ ; this means that  $f_1^{(2)}$  is small when  $\Delta$  is small, that edge effects are important even for large  $N$ , and the term  $f_0^{(2)}$  is needed.

The moments  $f^{(1)}$  and  $f^{(2)}$  using the sum rules [120] for different values of  $\Delta$  and  $N$  were calculated numerically. The results are presented in Fig. 4.8. The left panel shows  $f^{(0)} = f_1^{(0)} N$  with  $f_1^{(0)} = 4.4 e^3 \text{\AA}^2 V$  independent of  $\Delta$

<sup>2</sup>Note that a finite  $\kappa$  in the infinite chain even when  $\Delta = 0$  is a signature to spontaneous symmetry breaking induced by Coulomb interaction.

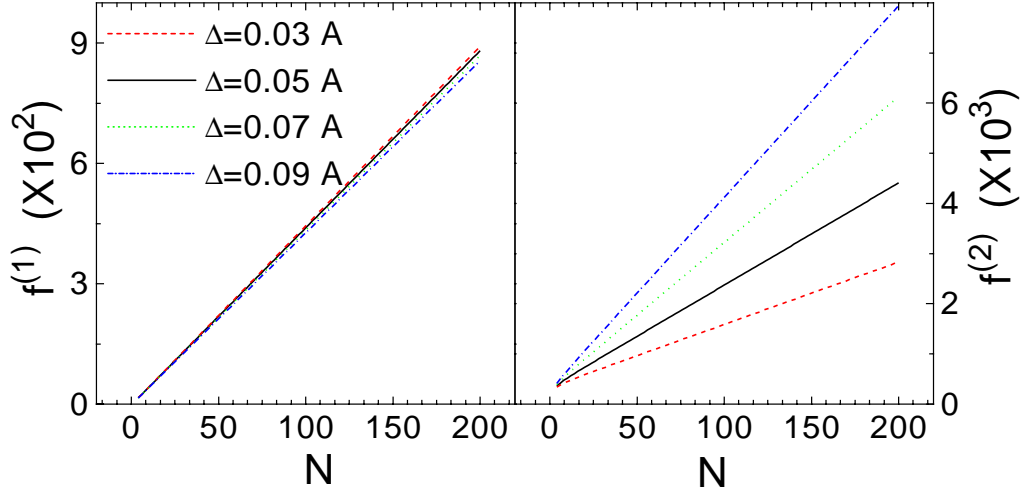


Figure 4.8: Scaling of the first  $f^{(1)}$  [ $e^3 \text{\AA}^2 V$ ] and second  $f^{(2)}$  [ $e^5 \text{\AA}^2 V^3$ ] moments of the linear absorption with number of carbon atoms for different values of bond-length alternation. Calculations were made using the DSMA algorithm.

as expected. The right panel shows  $f^{(2)} = f_1^{(2)}N + f_0^{(2)}$ . The dependence of  $f_1^{(2)}$  and  $f_0^{(2)}$  on  $\Delta$  are displayed in Fig. 4.9 (upper panels). For  $0.02 \text{\AA} \leq \Delta \leq 0.1 \text{\AA}$  they can be approximated by the Taylor expansions  $f_1^{(2)} = a_1 \Delta$ ,  $f_0^{(2)} = b_0 + b_1 \Delta + b_2 \Delta^2$ . Numerical fits give the following coefficients:  $a_1 = 410 e^5 \text{\AA} V^3$ ;  $b_0 = 350 e^5 \text{\AA}^2 V^3$ ;  $b_1 = -140 e^5 \text{\AA} V^3$ ;  $b_2 = -3900 e^5 V^3$ . The  $\Delta$ -dependence of  $\Omega$  and  $L$  is then given by

$$\Omega(N, \Delta) = \left( \frac{N + L(\Delta)}{N} \right)^{\frac{1}{2}} \tilde{\Omega}(\Delta), \quad (4.5)$$

with

$$L(\Delta) = \frac{b_0 + b_1 \Delta + b_2 \Delta^2}{a_1 \Delta}; \quad \tilde{\Omega}(\Delta) = \sqrt{\frac{a_1 \Delta}{f_1^{(0)}}}. \quad (4.6)$$

The coherence length  $L(\Delta)$  and the optical gap for infinite chains  $\tilde{\Omega}(\Delta)$  are displayed in Fig. 4.9 (lower panel). Eq. (4.5) gives the  $\Omega \sim N^{-\nu}$  behavior of the optical gap with  $\nu = 0.5$  for short chains ( $N < L(\Delta)$ ) and its saturation for  $N > L(\Delta)$  (for comparison, the Hückel model [105,108] where Coulomb interactions are neglected predicts  $\nu = 1$ ). Exponents close to 0.5 has been observed experimentally in various oligomers [109,110].

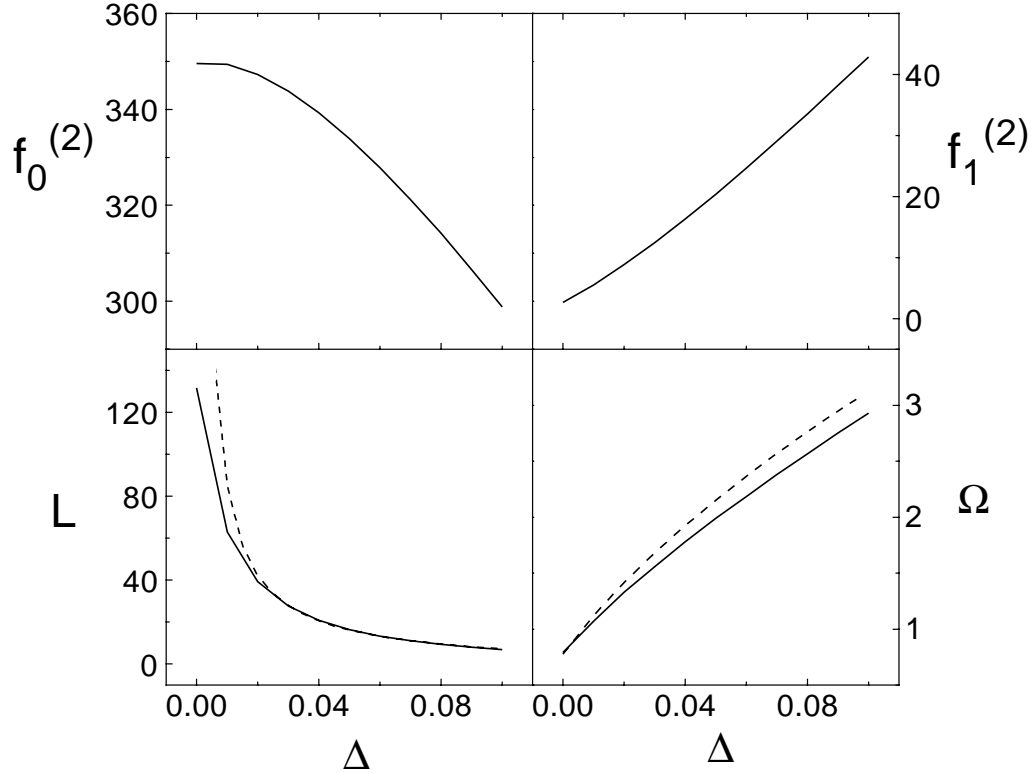


Figure 4.9: Upper panels: variation of the coefficients ( $f_1^{(2)}$  [ $e^5 \text{Å}^2 V^3$ ] and  $f_0^{(2)}$  [ $e^5 \text{Å}^2 V^3$ ]) in the Taylor expansion of the second moment with the bond length alternation  $\Delta$  [ $\text{Å}$ ]. Calculations were made using the DSMA algorithm. Bottom panels: The  $\Delta$  [ $\text{Å}$ ] dependence of the coherence size  $L$  and the optical gap  $\tilde{\Omega}$  [eV]. Solid lines - full TDHF calculations. Dashed line - Eq. (4.6)

The linear scaling of  $f_1^{(2)}$  with  $\Delta$  yields our final expression for the single-mode approximation of the linear response  $\alpha \equiv \chi^{(1)}$

$$\chi^{(1)} = \frac{(ea)^2}{8\beta'\Delta} k_1 \frac{N^2}{N + L(\Delta)}. \quad (4.7)$$

Here  $4\beta'\Delta$  is the Hückel band gap. The dimensionless parameter  $k_1$  defined by Eqs. (4.7) can be estimated using  $\bar{\rho}_{mn}$  in a long chain. Eqs. (4.5) and (4.7) give  $\alpha(N) \sim N/\Omega^2(N)$  in agreement with the result of Silbey [121] who used an “average” frequency  $\bar{\Omega}$  to perform the sum over states in  $\alpha$ . This “average” frequency is identified as the frequency of our collective electronic oscillator.

The sum rule analysis of  $\chi^{(1)}$  can be extended to higher order (nonlinear) polarizabilities. These calculations are more tedious since the number of terms

in the susceptibilities is much larger, which requires the use of additional sum rules, and the introduction of a new effective electronic mode at each order of response. The scaling behavior of all terms contributing to the third order response have been examined. Upon retaining only the dominant ones and applying similar arguments for higher order responses we finally obtained

$$\chi^{(j)} = k_j \frac{j(ea)^{j+1}}{2(4\beta'\Delta)^j} \frac{N^{j+1}}{[N + L(\Delta)]^j}, \quad (4.8)$$

where  $j = 1, 3, 5$  correspond to the polarizabilities  $\alpha, \gamma, \delta$  etc. These expressions are valid only for finite bond-length alternation  $\Delta$ .  $\Delta = 0$  needs to be treated separately.

The solid lines of Fig. 4.10 represent the full TDHF calculations of  $\alpha, \gamma$  and  $\delta$  for polyacetylene chains with up to 200 carbon atoms for various values of  $\Delta$ . The dotted lines were calculated using Eq. (4.8) and show an excellent agreement.  $L(\Delta) \equiv f_0^{(2)}/f_1^{(2)}$  were computed using the expressions given in [120].  $k_j(\Delta)$ ,  $j = 1, 3, 5$  displayed in Fig. 4.11 were the only fitting parameters.  $k_j$  are order 1 and depend only weakly on  $\Delta$ .

Eq. (4.8) predicts the following relation between the saturated third order off-resonant susceptibility  $\gamma$  and optical gap  $\tilde{\Omega}$ :  $\gamma \sim \Delta^{-3} \sim \tilde{\Omega}^{-6}$ . In the Hückel model on the other hand we have  $\gamma \sim \Delta^{-6} \sim \tilde{\Omega}^{-6}$  [105]. This  $\tilde{\Omega}^{-6}$  scaling is in agreement with experiment [119]. Note that these two models predict a different scaling with  $\Delta$ .

To examine the  $\chi^{(j)} \sim N^{b_j}$  power law the scaling exponent  $b_j = d[\ln\chi^{(j)}]/d[\ln N]$  [60,74,73,98] was calculated. This gives  $b_j = (1 + \frac{jL}{N+L})$ . For small sizes it starts as  $b_j = 1 + j$ . The convergence of the scaling exponent  $b$  to 1 allows us to introduce an operational definition of the saturation size, defined as size  $N^*$  whereby  $b_j = 1 + \eta$ ,  $\eta$  being a chosen small parameter. We then get  $N^* = (j/\eta - 1)L$ . For  $\eta = 0.1$  this gives  $(10j - 1)L$ . It is clear from Fig. 4.10 that the effective saturation size increases with  $j$  as predicted by this equation, even though it still depends on a single coherence size. For  $j = 3$ ,

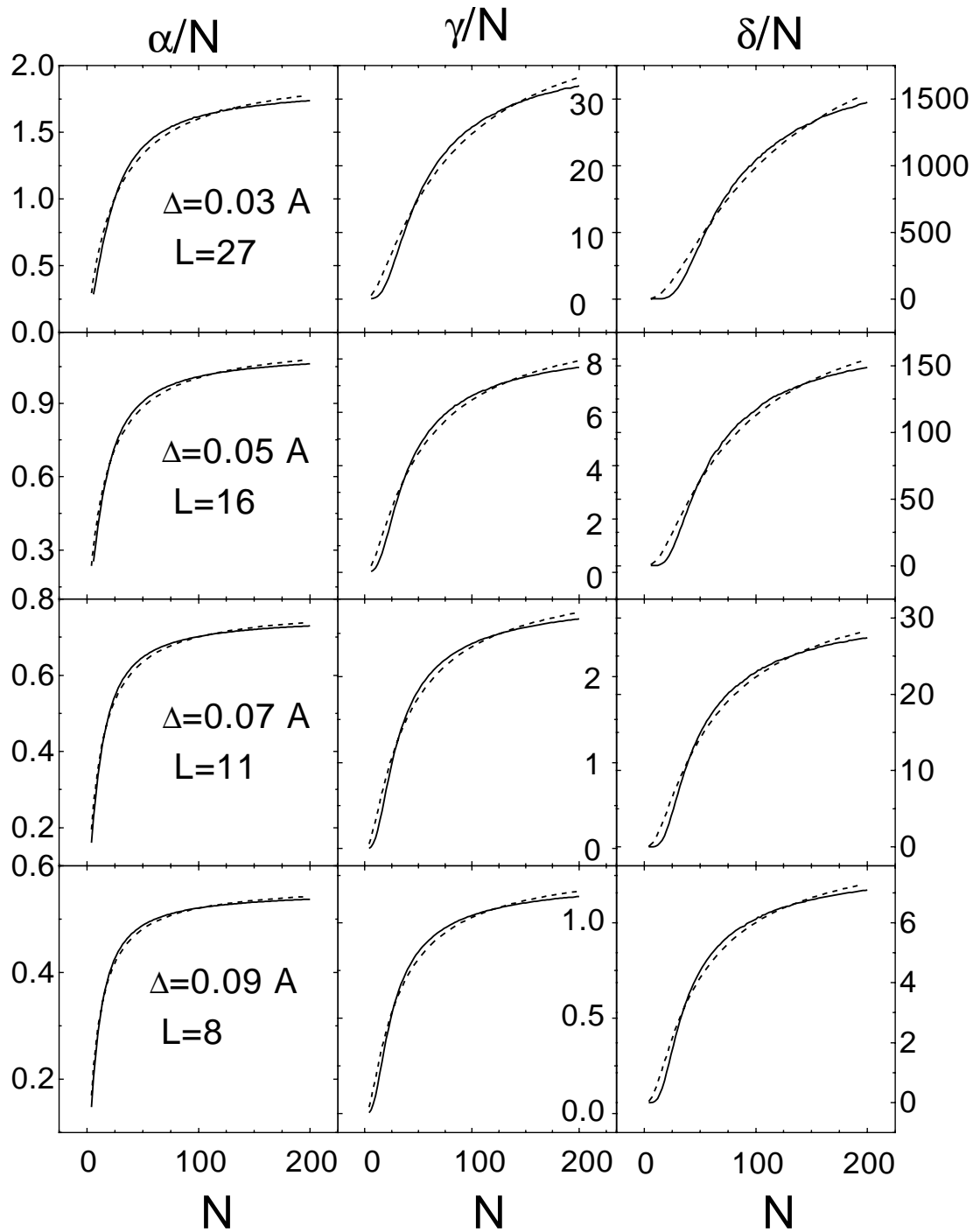


Figure 4.10: Scaling of the first third and fifth order polarizabilities ( $\alpha$ ,  $\gamma$ , and  $\delta$  are in the units of  $e\text{\AA}^2V^{-1}$  [ $1.441 \times 10^{-23}esu$ ],  $e\text{\AA}^4V^{-3}$  [ $1.297 \times 10^{-34}esu$ ], and  $e\text{\AA}^6V^{-5}$  [ $1.167 \times 10^{-45}esu$ ]) of polyacetylene chains with the numbers of carbon atoms for various values of the bond length alternation parameter  $\Delta = 0.03\text{\AA}$ ,  $0.05\text{\AA}$ ,  $0.07\text{\AA}$ , and  $0.09\text{\AA}$ , as indicated, solid line - full TDHF calculation, dashed line - Eq. (4.8)



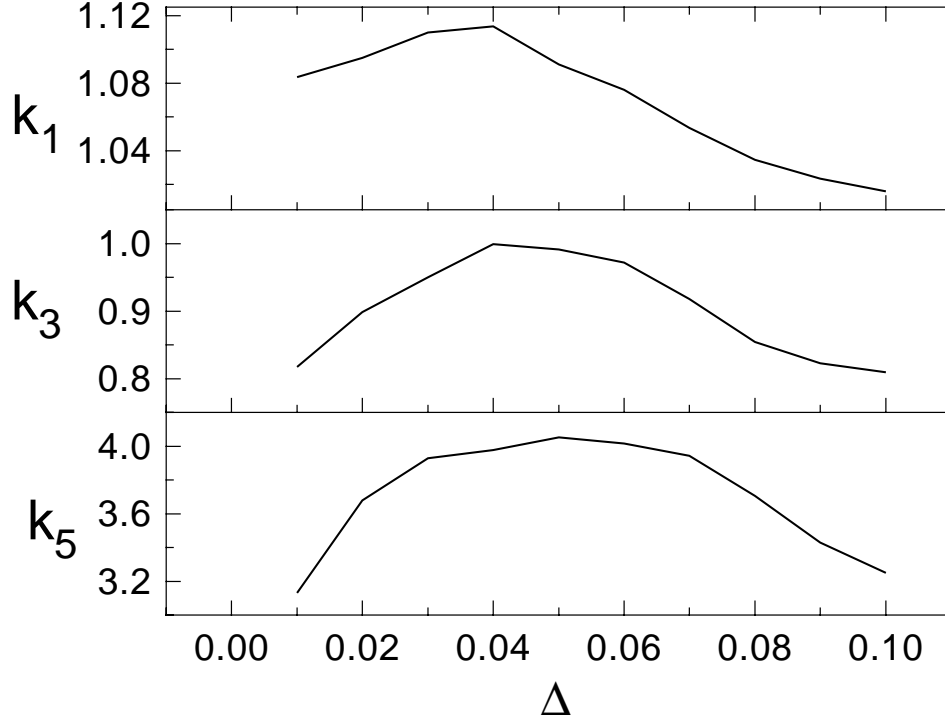


Figure 4.11: Variation of the dimensionless parameters  $k_j$  with the bond length alternation  $\Delta$  [ $\text{\AA}$ ].  $k_j$  were obtained by fitting Eq.(7) to the TDHF (see Fig. 4.10).

$\eta = 0.5$ , and  $\Delta = 0.03\text{\AA}$  which corresponds to  $L = 27$  we obtain  $N^* = 135$ , in good agreement with Fig. 4.9 of [111] where the value of  $\eta = 0.5$  is reached at  $N^* \sim 120$ .

In summary, expressions for size-dependent off-resonant polarizabilities  $\chi^{(j)}$  and the optical gap  $\tilde{\Omega}$  [Eqs. (4.5) - (4.8)] which predict their variation with the bond-length alternation parameter  $\Delta$  have been derived. The saturated ( $N \rightarrow \infty$ ) values of  $\chi^{(1)}$ ,  $\chi^{(3)}$ , and  $\chi^{(5)}$  show strong dependence on bond-length alternation  $\Delta$ :  $\alpha \sim \Delta^{-1}$ ,  $\gamma \sim \Delta^{-3}$ ,  $\delta \sim \Delta^{-5}$ .  $\Delta$  can be varied while keeping  $\beta_0$  fixed (for example by using different solvents or by substitution). Our expressions predict correctly the experimental scaling  $\Omega \sim N^{-0.5}$  [109,110],  $\gamma \sim \tilde{\Omega}^{-6}$  [105,119], and provide a good estimate of the saturation length of  $\gamma$  [111].

## Chapter 5

# Linear Optical Excitations in PPV Oligomers

In this Chapter we investigated the electronic excitations of poly(p-phenylene vinylene) (PPV) oligomers (Fig. 5.1) [61,122–130] and their scaling with size. Recent interest in this photoluminescent polymer is connected with its possible use as a photoconductor [131,132]. The possibility of using it for photonic devices is rapidly becoming reality: High performance photonic devices fabricated from PPV have been made, including light emitting diodes (LEDs), display panels, light emitting electrochemical cells (LECs), photovoltaic cells, photodetectors, and optical switches. These polymer-based devices have reached performance level comparable with their inorganic counterparts. Organic photonic devices rely on the recombination of electrons and holes photogenerated or injected at the contact. To understand, and possibly improve, operation of these devices it is necessary a thorough understanding of the photogeneration and charge transfer processes. Although substantial amount of experimental [125–129] and theoretical [61,122–124,59] work has been reported for PPVs, a consistent picture for the overall electronic excitation processes has yet to emerge.

The  $\pi$  molecular orbitals of PPV have been classified as either localized (*l*) or delocalized (*d*) [131,129]. The former have an electron density on

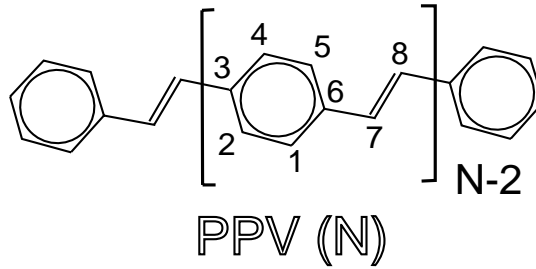


Figure 5.1: Geometry and atom labeling of PPV oligomers. Bond angles are  $120^\circ$ , except  $\alpha(r_{6,7}, r_{7,8}) = 128^\circ$ , and the distances are:  $r_{1,2} = r_{2,3} = r_{3,4} = r_{4,5} = r_{5,6} = r_{6,1} = 1.39\text{\AA}$ ,  $r_{6,7} = 1.44\text{\AA}$ ,  $r_{7,8} = 1.33\text{\AA}$ .

carbon atoms 1,2,4, and 5 (Fig.5.1), while the latter are delocalized over all carbon atoms. The experimental absorption spectrum of PPV thin film [123,124] shown in Fig. 5.2A (dashed line) is typical for other PPV-derivatives [131,123,124,128]. It has a fundamental ( $d \rightarrow d^*$ ) band at 2.5 eV [496 nm] (I), two weak peaks at 3.7 eV [335 nm] ( $d \rightarrow d^*$ ) (II) and 4.8 eV [258 nm] ( $l \rightarrow d^*$  and  $d \rightarrow l^*$ ) (III), and a strong ( $l \rightarrow l^*$ ) band at 6.0 eV [207 nm] (IV). Peak II originates from electron correlations [131,129] and is missed by HF calculations.

## 5.1 Electronic Normal Modes and Optical Absorption (PPP hamiltonian)

Linear absorption of PPV oligomers with up to 50 repeat was calculated using the DSMA combined with the PPP hamiltonian (see Section 2.1). In all calculations the experimental geometry [133] has been used (see Fig. 5.1). The absorption spectra were then calculated using Eq. (2.55). The calculated spectrum of PPV(10) shown in Fig. 5.2A (solid line) closely resembles the experimental spectrum and has similar features at 2.83 (I), 3.3 (II), 4.5 (III), and 5.6 eV (IV) [438, 376, 276, and 221 nm]. In addition, it shows a fifth band centered at 7.0 eV [177 nm] (V). The oscillator strengths  $f_\nu$  of PPV(10) are shown in Fig. 5.2A.

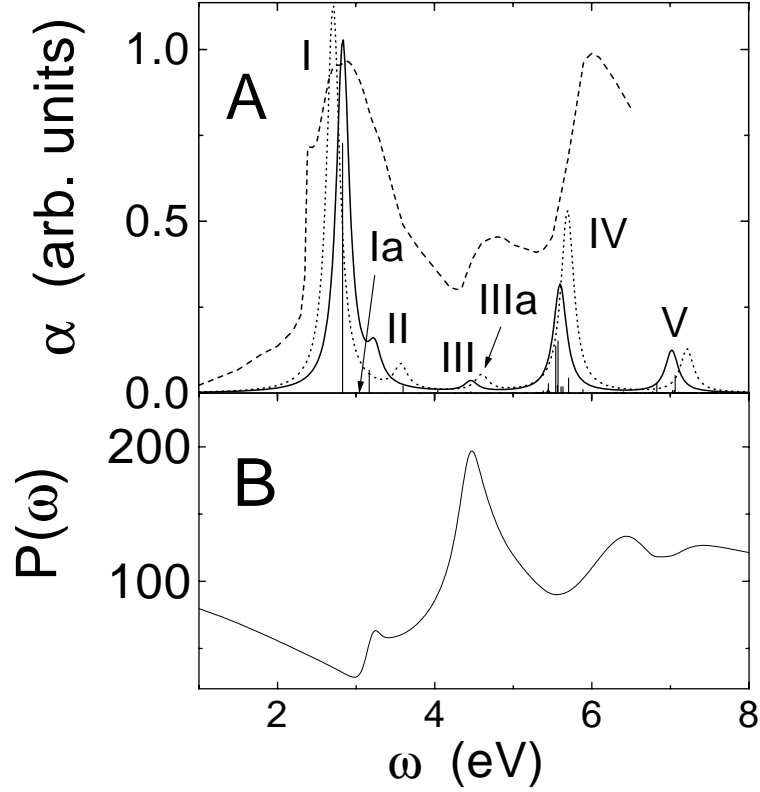


Figure 5.2: (A) Absorption spectrum of PPV(10) (the imaginary part of  $\alpha$  Eq.(1)). Dashed line: experimental absorption of a PPV thin film. Solid and dotted lines: absorption lineshapes of PPV(10) obtained with 12 effective modes calculations and linewidth  $\Gamma_\nu = 0.1\text{eV}$  using PPP and INDO/S hamiltonians, respectively; The sticks represent oscillator strengths  $f_\nu$ ,  $\nu = 1, N^2/4$  of PPV(10) obtained by the full TDHF with PPP hamiltonian. (B) The frequency – dependent participation ratio of the induced density matrix.

By displaying the dominant oscillators in the site representation, a new picture that relates the optical properties directly to motions of charges in the system is obtained, without ever introducing electronic eigenstates. The extent of spatial coherence then provides a view of the underlying coherence sizes. A two-dimensional plot of  $\bar{\rho}$  of PPV(10) is shown in Fig. 5.3A. The coordinate axes represent repeat units along the chain and the absolute values of matrix elements are depicted by different colors.  $\bar{\rho}$  is dominated by the diagonal and near-diagonal elements, reflecting the bonds between nearest neighbors. Figure 5.3B shows a single unit of Fig. 5.3A on an expanded scale using the atom labeling given in Fig. 5.1. It reflects bond strength distribution over the

benzene ring (1-6 elements), strong double bond (7-8), and weaker single bond (6-7) of the vinylene group. This bonding pattern is to be expected from the molecular structure.

The coordinates  $Q_\nu$  and momenta  $P_\nu$  of the dominant electronic oscillators are examined next. Vibrational normal modes represent coherent displacements of various atoms, and these electronic modes represent the displacements of the electronic density matrix with respect to  $\bar{\rho}$ . The diagonal elements reflect induced charges on various atoms, whereas the off-diagonal elements represent dynamical fluctuations of interatomic chemical bonding [60,74,104,70,61]. Our calculations show that the absorption is dominated by five oscillators denoted I-V. The coordinate and momentum eigenvectors of the oscillator responsible for the lowest absorption peak (I) of PPV(10) are shown in Fig. 5.3, C and D. The same quantities for the second oscillator corresponding to peak (II) are shown in Fig. 5.3, F and G. Despite the different structure of these electronic modes, the delocalization pattern of the off-diagonal elements representing electronic coherence between different atoms is similar. Both modes are delocalized and can be viewed as  $d \rightarrow d^*$  transitions.  $Q_\nu$  and  $P_\nu$  clearly show that the weak coherences between the phenylene ring of the  $i$ -th repeat unit, and the vinylene group of the  $i + 1$ -st repeat unit are enhanced by optical excitation. In addition, a weak dynamical coherence develops between the  $i$ -th and the  $i + 2$ -nd repeat units. These figures illustrate that finite size effects are limited to the terminating repeat units and that the momenta are more delocalized than the coordinates for a single unit. The coherence size, that is the 'width' of the momentum density matrix along the coordinate axes, where the coherences decrease to 10% of their maximum values) is 5 repeat units. The same modes for a longer chain [(PPV(20))] displayed in Fig. 5.3, E and H are virtually identical to those of PPV(10). Therefore, 10 repeat units already resembles the infinite chain as far as the optical spectrum is concerned.

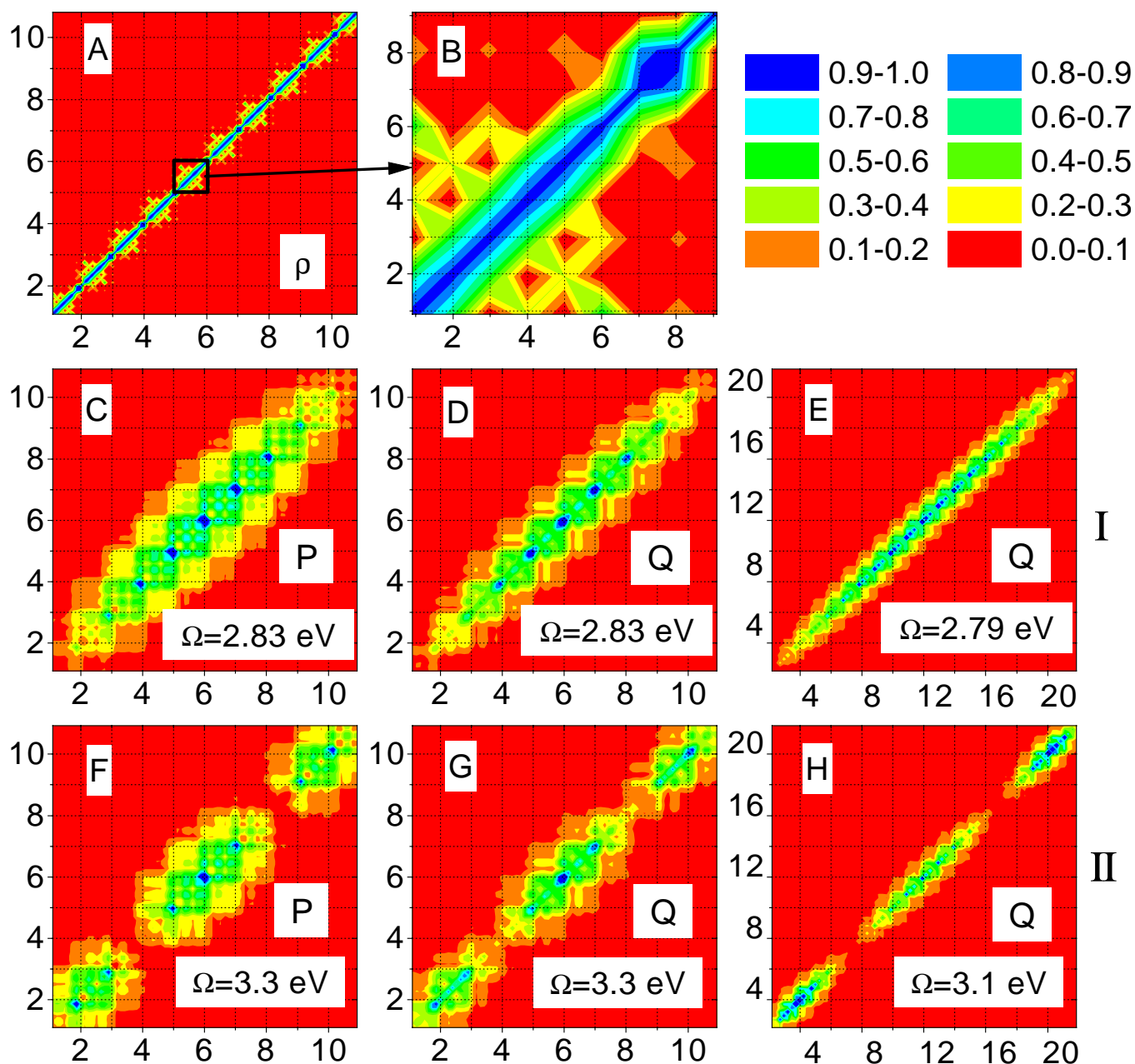


Figure 5.3: Contour plots of density matrices. (A)  $\bar{\rho}$  of PPV(10); (B) magnified region of (A) representing the single unit of polymer chain and the color maps; (C) momentum, and (D) coordinate of PPV(10), and (E) coordinate of PPV(20) of the lowest absorption peak (I); (F), (G), (H) are the same quantities as in C to E but for the second absorption peak (II). The axis labels represent the repeat units, except in (B) where the axes represents the individual carbon atoms as numbered in Fig. 5.1.

The coordinate and momentum of the third peak (III) of PPV(10) are shown in Fig. 5.4, A and B. This mode is delocalized with a coherence-size similar to modes (I) and (II), however, its structure along the oligomer chain is very different: Bonding is weak at the center and strong towards the edges. The electronic modes are most suitable for investigating charge transfer processes and photoconductivity [131,132]. The strong local optical dipoles along the chain can affect charge transfer and electron hopping. Oscillator III, which has the strongest optical coherences induced at the chain ends (see Fig. 5.4, A and 5.3, B), should play an important role in effects involving charge separation.

The coordinates and momenta of the high frequency peaks (IV) and (V) of PPV(10) (Fig. 5.3, D, E, G, and H) are completely localized on a single repeat unit. This behavior is drastically different from polyacetylene, where the electronic coherence-size increases monotonically for the higher frequency modes (see Fig. 5.2) [74]. The coordinates of these modes for a single PPV unit on an expanded scale are shown in Fig. 5.4, F and I. For the fourth peak (IV) the optically induced coherences only involve the phenylene ring carbon atoms 1,2,4, and 5 (Fig. 5.1), in agreement with the results obtained in [131,129]. The oscillator responsible for peak (IV) represents several nearly-degenerate localized oscillators (see Fig. 5.2A). The high-frequency peak (V) predicted by our calculations lies beyond the experimentally studied frequency range. It corresponds to localized and weakly delocalized transitions involving the vinylene group atoms 7 and 8, and the phenylene ring atoms 3 and 6. A weak coherence between the vinylene groups of neighboring repeat units is observed as well.

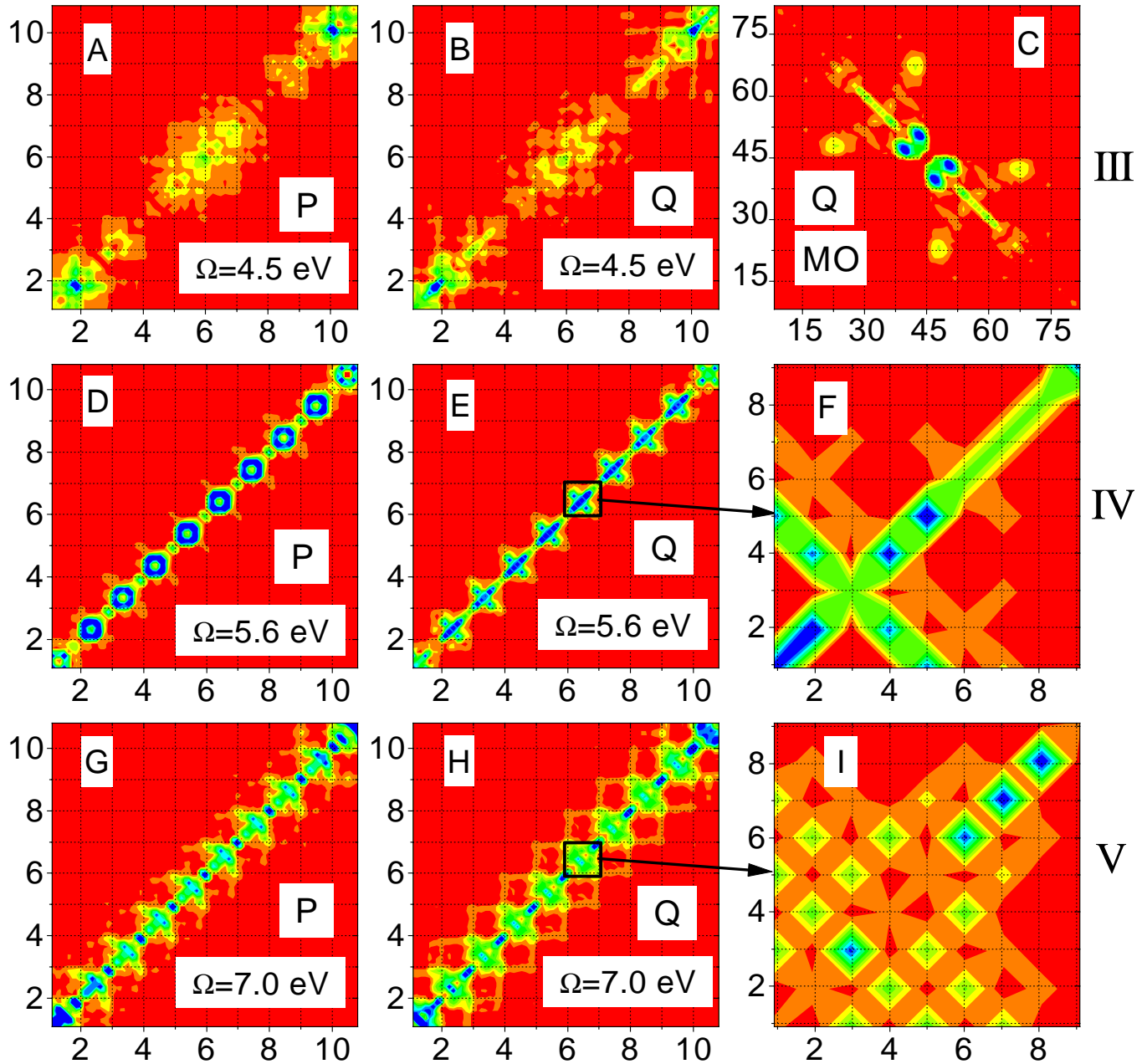


Figure 5.4: Contour plots of density matrices. (A) Momentum, and (B) coordinate in the real space, and (C) coordinate in the molecular orbital representation of the peak (III) of PPV(10). (D) Momentum, and (E) coordinate of PPV(10) for the fourth absorption peak (IV), and (F) magnified area of (E) representing the single unit of polymer chain. (G, H, and I) the same quantities as in B to F but for the fifth absorption peak (V). The axis of (A), (B), (D), (E), (G), and (H) are labeled to the repeat units of polymer chain. The axis of (C) denote the molecular orbitals. Labeling using the number of carbon atoms according to Fig. 5.1 is used for panels (F) and (I)



## 5.2 Electronic Normal Modes and Optical Absorption (INDO/S hamiltonian)

In Section 2.1 two hamiltonians PPP and INDO/S are introduced. To compare how they work calculations of linear absorption in PPV oligomers were repeated using INDO/S hamiltonian. The calculated INDO/S spectrum of PPV(10) shown in Fig. 5.2A (dotted line) better agrees with the experimental spectrum (dashed line) than the PPP spectrum (solid line). It has spectroscopic features at 2.71 (I), 3.08 (Ia), 3.57 (II), 4.6 (IIIa), 5.7 eV (IV) and 7.2 eV (V) (the labeling will be explained latter). Despite on the improvement, the principal structure of the INDO/S spectrum does not change compare to the PPP spectrum: the spectra have the same number of peaks with comparable intensity. On the other side, INDO/S hamiltonian has approximately 5 times larger basis set than PPP's basis set. This increases the computational memory and time requirements by factors 20-30 and 80-120, respectively. Thus these hamiltonians are complimentary to each other.

The INDO/S electronic modes corresponding to the absorption peaks are examined next (see Section 2.5 in Chapter 2). INDO/S hamiltonian assigns a single  $s$ -type basis function to hydrogen atoms and four basis functions ( $s, p_x, p_y, p_z$ ) to all other heavy atoms of these molecules. The orbitals  $s, p_y, p_z$  on the carbons in the chain are  $sp^2$  hybridized and form the molecular  $\sigma$ -bonding skeleton. Qualitatively, only  $p_x$  orbitals perpendicular to the molecular plane participate in the  $\pi$ -bonding network and are responsible for the lowest optical excitations. Assuming that  $\sigma$ -electrons do not contribute to the ground state charge redistribution and to the optical properties, all  $K \times K$  ( $K$  being the total basis set size) density matrices were sorted out, retaining only elements corresponding to  $p_x$  orbitals. The resulting  $k \times k$  matrices (where  $k < K$  is the number of  $p_x$  orbitals of heavy atoms) were displayed as contour plots. The ground state density matrix elements have the following physical significance:

the diagonal elements ( $n = m$ ) represent the  $\pi$ -electron charge at the  $m$ 'th atom, whereas the off-diagonal ( $n \neq m$ ) elements reflect the  $\pi$ -bond-orders between  $n$  and  $m$  atoms <sup>1</sup>. We thus end up with the same interpretation of the density matrices as used previously for the simpler PPP hamiltonian.

The DSMA calculations results in the set of electronic oscillators in the momentum-coordinate ( $P - Q$ ) representation (see Section 2.4). So far, the two-dimensional plots of these hermitian variables have been examined. Now we turn to the equivalent representation of electronic modes in terms of  $\xi$  and  $\xi^+$ . Even though these variables are not hermitian, two advantages are anticipated in analysis of  $\xi$ : First, it is enough to display a single matrix  $\xi_\nu$  instead of two matrices  $Q_\nu$  and  $P_\nu$  ( $\xi_\nu^+$  matrix is simply transpose of  $\xi_\nu$  if the electronic modes are chosen to be real (see Section 2.3)), and second, the asymmetry of  $\xi_\nu$  with respect to the matrix diagonal is a signature of the charge-transfer character of optical transition (Section 2.5), whereas the absolute values of  $Q_\nu$  and  $P_\nu$  matrix elements are symmetric with respect to the diagonal. The latter become, for example, extremely important in analysis of donor/acceptor substitution effects (Chapter 6).

The electronic modes of six transitions appearing in the spectra of PPV(10) are displayed in Fig. 5.5. All electronic modes are almost symmetric with respect to the diagonal ( $\xi_{mn} \approx \xi_{nm}$ ). This means that there is no preferable direction of motion for electron (or holes). Panel A which shows the band-edge transition I is very similar to the coordinate and momentum of mode I calculated with the PPP hamiltonian. It shows the same off-diagonal delocalization of about 4-5 repeat units. Panel B displays the next Ia transition. This mode is forbidden in linear absorption and does not show up in the PPP calculations for a given set of convergence parameters. It has the same off-diagonal

---

<sup>1</sup>This interpretation applies for the conjugated chains but not to the atoms, where other types of hybridizations are formed. Since our goal is to explore the dynamics of the  $\pi$ -electron system, this interpretation will be used throughout this thesis.

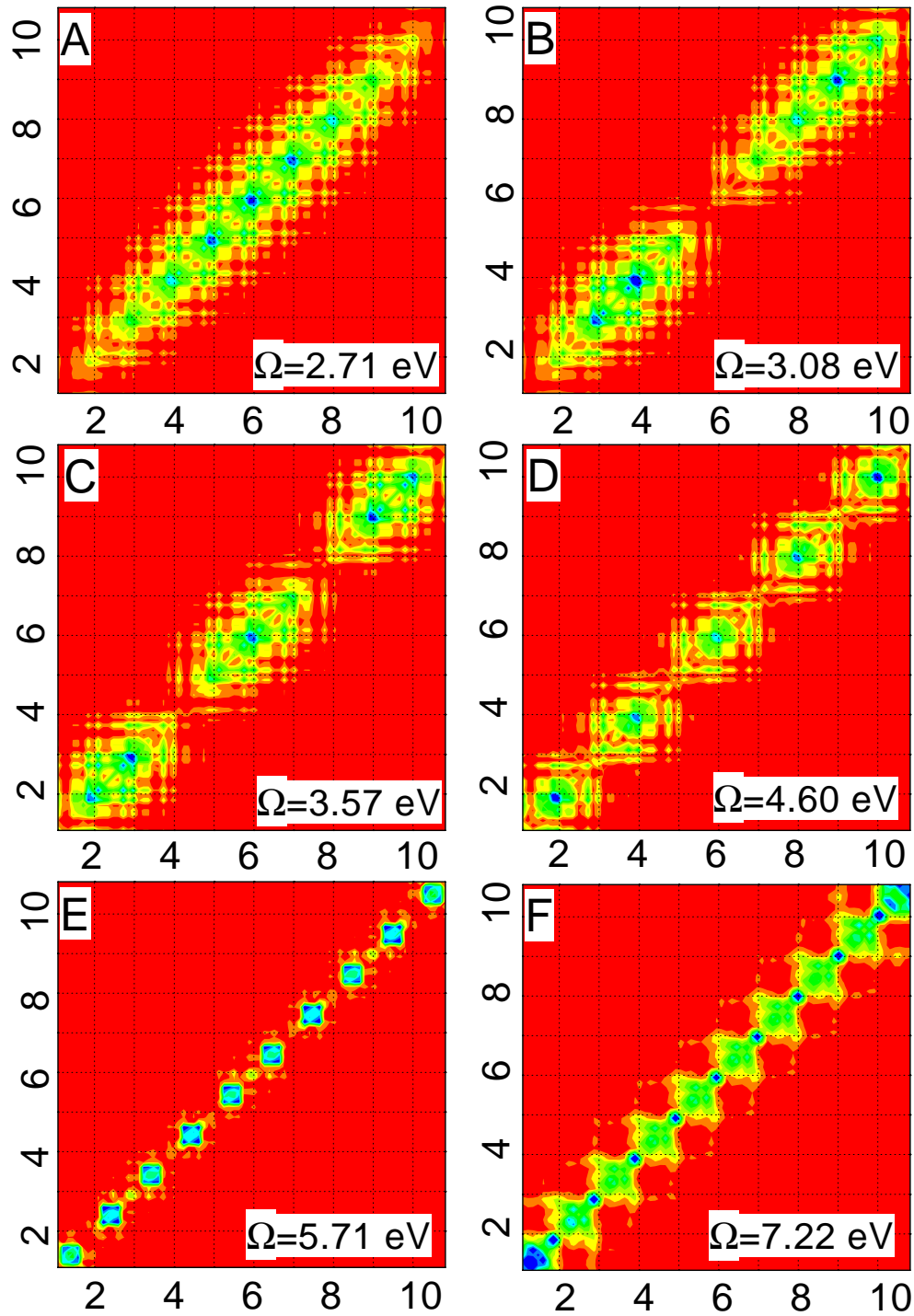


Figure 5.5: Contour plots of electronic modes  $\xi_\nu$  dominating the absorption spectrum of PPV(10). Panels **A**, **B**, **C**, **D**, **E**, **F** represent the modes corresponding to transitions I, Ia, II, IIIa, IV, V, VI in spectrum shown by dotted line in Fig. 5.2. The axis labels represent the repeat units. The ordinate and abscissa label electron and hole respectively.

coherence size as mode I, but a non-uniform diagonal space distribution. The molecule is effectively broken to the two parts with diagonal size of 5 repeat units and a very small electronic coherence between them. Two contributions to the transition dipole cancel each other resulting in vanishing oscillator strength. The next transition II shown in panel C is very similar to mode II in the PPP calculations. As shown in Chapter 6, the total contribution from the ends is approximately zero, and only the middle region contributes to the oscillator strength of this mode. This mode therefore makes only a weak contribution to the linear absorption. The molecule is effectively trimer with weak electronic coherence among monomers. The off-diagonal coherence size is about 3 repeat units and the diagonal sizes are 3, 4, and 3 repeat units. Mode IIIa shown in panel D weakly appears in the absorption spectrum. It has five noninteracting contributions with off-diagonal and diagonal sizes of about 2 repeat units. It is interesting to draw an analogy with mode III in PPP calculations. Even though their diagonal distributions are quite different, these modes both belong to the same spectral frequency region and the strongest contributions to the transition dipoles are localized at the molecular ends. This fact again indicate the charge-transfer and photoconductivity nature of middle-frequency optical transitions in PPV oligomers. The high frequency modes IV and V are localized on the phenyl and vinyl groups, respectively. They are completely analogous to modes IV and V in PPP calculations. Thus the general trend in evolution of electronic modes with frequency is an effective aggregation of molecule to the segments with weak electronic coherence among them. This localization of optical excitations allows to apply the Frenkel exciton model for molecular aggregates, even though the chromophores are not separated spatially (see Chapter 7). The same optical excitations calculated with the INDO/S and PPP hamiltonian have very similar electronic modes. Additional information and modes may be obtained by varying the input set

of convergence parameters.

### 5.3 Molecular Orbital Representation of Electronic Oscillators

Even though the CEO approach is eigenstate-free, it is instructive to establish its connection to the more traditional eigenstate representation. The  $\nu$ 'th oscillator represents the optical transition between the ground state  $\psi_g$  and the  $\nu$ 'th excited state  $\psi_\nu$ . The matrices representing the coordinate  $Q_\nu$  and momentum  $P_\nu$  are given by  $(Q_\nu)_{mn} = \langle \psi_\nu | c_m^\dagger c_n | \psi_g \rangle + \langle \psi_g | c_m^\dagger c_n | \psi_\nu \rangle$ , and  $(P_\nu)_{mn} = \langle \psi_\nu | c_m^\dagger c_n | \psi_g \rangle - \langle \psi_g | c_m^\dagger c_n | \psi_\nu \rangle$ .  $Q_\nu$  and  $P_\nu$  thus carry considerably reduced information about the global eigenstates  $|\psi_\nu\rangle$ . A different perspective on these modes is obtained by expanding them in the molecular orbital representation using a basis set of pairs molecular orbitals. Let us denote the creation (annihilation) operator for  $i$ 'th molecular orbital  $c_i^+(c_i)$ .

We then have

$$Q_\nu = \sum_{i,j}^{N^2/4} \alpha_{i,j}^\nu (c_i^+ c_j + c_j^+ c_i), \quad (5.1)$$

where  $i$  runs over initially unoccupied orbitals (particles) whereas  $j$  denotes occupied orbitals (holes) (see Fig. 5.6A). These coefficients, normalized as  $\sum_{i,j} |\alpha_{i,j}^\nu| = 1$ , represent the contribution of the  $j \rightarrow i$  transition to the  $\nu$ 'th oscillator. Note that the indices  $n, m$  used earlier represent localized atomic orbitals whereas  $i, j$  denote delocalized molecular orbitals. To illustrate how various molecular orbitals contribute to five dominant electronic modes calculated using the PPP model, the following two quantities have been introduced

$$R^\nu(j) = \sum_i [\alpha_{i,j}^\nu]^2, \quad P^\nu = \frac{1}{\sum_{i,j} [\alpha_{i,j}^\nu]^2}, \quad (5.2)$$

where  $i, j = 1, \dots, N/2$ , and  $\nu = I, II, \dots, V$ .  $R^\nu(j)$  represents the total contribution of the  $j$ 'th molecular orbital to all orbital pairs appearing in the

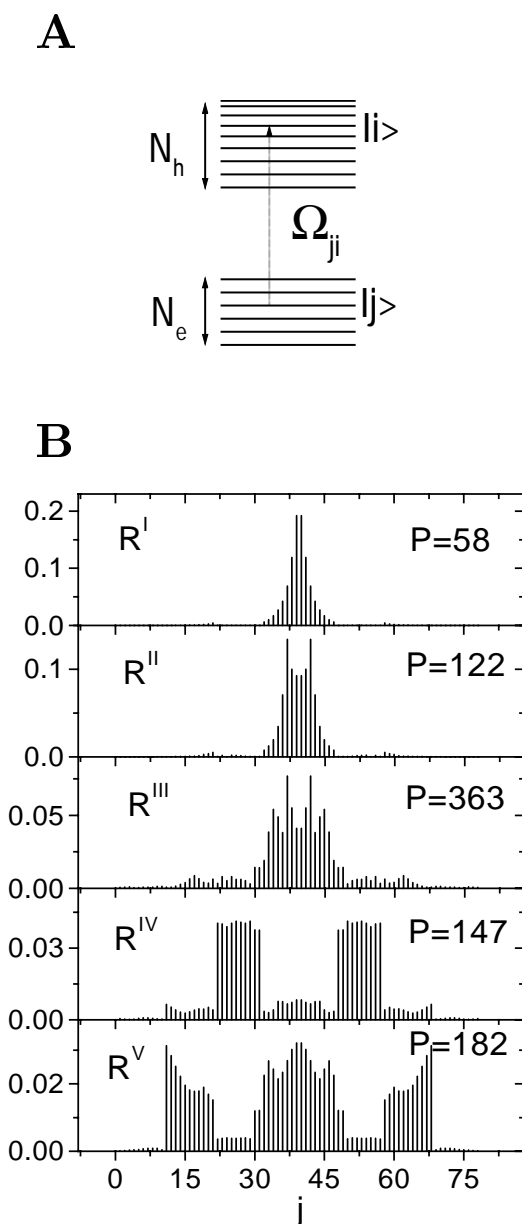


Figure 5.6: **(A)** Origin of the collective electronic oscillators. Each transition between an occupied and an unoccupied orbital represents an electron-hole oscillator. In a molecule with  $N_e$  occupied (electron) and  $N_h$  unoccupied (hole) orbitals we have altogether  $N_e \times N_h$  oscillators. For a system with a filled valence and empty conduction band described by a “minimal basis set”  $N_e = N_h = N/2$  and the number of oscillators is  $N^2/4$ . The collective oscillators  $Q_\nu$  can be represented as superpositions of the electron-hole oscillators (see Eq. (5.2)). The participation ratio  $P^\nu$  measures the effective number of electron-hole pairs contributing to a given collective oscillator. **(B)** The molecular orbital contributions and the inverse participation ratios of orbital pairs corresponding to the five dominant modes of PPV(10) absorption.

$\nu$ 'th oscillator.  $R^\nu(j)$  for the five dominant oscillators in PPV(10) are displayed in Fig. 5.6B.  $R^I(j)$  is relatively localized in the vicinity of the HOMO-LUMO transition (between the highest occupied and lowest unoccupied orbitals), whereas additional pairs of orbitals contribute to the higher modes. The inverse participation ratio  $P^\nu$  measures the number of orbital pairs that contribute significantly to the  $\nu$ 'th oscillator. In the absence of electronic correlations, each oscillator represents a single transition between an occupied and an unoccupied orbitals (in the quantum chemistry terminology) or a single particle-hole pair (in the semiconductor terminology) and  $P^\nu = 1$ . In this case, the oscillator and molecular orbital pair descriptions coincide. In a correlated electronic structure, each mode becomes a linear combination (that is, a wavepacket) of orbital pairs as represented by Eq. (5.1), and  $P^\nu$  increases.  $P^\nu$  is thus a useful measure of electronic correlations. The values of  $P^\nu$  given in Fig. 5.6B show that the higher oscillators are more collective and contain gradually increasing number of electron-hole pair states. The oscillators III and V corresponding to  $d \rightarrow l^*$  transitions have the most collective character. Such strongly correlated excitations require an extensive configuration-interaction calculations in an eigenstates approach. Here they appear naturally through the modes. The CEO is most attractive when  $P^\nu$  is large because in a very efficient way it lumps the important effects of correlations directly into the observables. The collective nature of optical excitations at different frequencies can be analyzed by expanding the induced density matrix in molecular orbitals

$$\delta\rho(\omega) = \sum_{i,j}^{N^2/4} \alpha_{i,j}(\omega)(c_i^+ c_j + c_j^+ c_i). \quad (5.3)$$

A frequency – dependent participation ratio  $P(\omega)$  can be then defined by replacing  $\alpha_{i,j}^\nu$  with  $\alpha_{i,j}(\omega)$  in Eq.(5.2). (A normalization  $\sum_{i,j} |\alpha_{i,j}(\omega)| = 1$  is assumed).  $P(\omega)$  displayed in Fig. 5.2B is a weighted average of the participation ratios  $P^\nu$  of the contributing electronic oscillators.

The molecular orbital representation have been used to analyze the nature of mode III. In Fig. 5.3C its coordinate in the molecular orbital representation is displayed. The Figure clearly shows that only few molecular orbitals close to HOMO-LUMO contribute to this transition. The strongest orbitals can be identified as either delocalized or localized and mode III corresponds to  $l \rightarrow d^*$  and  $d \rightarrow l^*$  transitions. Our calculations further show that the frequencies of modes I, II, III are red-shifted and gradually saturate with increasing chain length, whereas the frequencies of modes IV and V are not affected by size. These findings are consistent with the delocalized and localized nature of the two groups of modes respectively as displayed in Figs. 5.3 and 5.4.



## Chapter 6

# Linear Optical Excitations in Acceptor-substituted Carotenoids.

Carotenoids form one of the most important groups of natural pigments, and are found in all families of vegetables and animal kingdoms [134,135]. Among the innumerable biological molecules, this class attracts a great attention in biophysics, biochemistry, and photophysics. Many practical applications of carotenoids in pharmaceutical and food technology have been reported. The highly polarizable  $\pi$ -electron chain forms the basis for the fundamental photophysical phenomena of biological relevance. In photosynthetic cells these molecules appear in antenna complexes that absorb the light and transfer excitation to the reaction centers [136,137]. In addition they serve as antioxidants by quenching the chlorophyll triplet via energy transfer and preventing the formation of singlet oxygen. The photoisomerization of the closely related retinoids plays a role in various physiological functions (e.g. the primary process of vision) [136,138].

The electronic spectra of a family of acceptor substituted carotenoids [1,2] were calculated using the collective electronic oscillator (CEO) approach [55,74,104,70]. Our analysis shows that it is very difficult to disentangle the effects of donor-acceptor and bridge length on the spectroscopy of molecules

with relatively short bridges. To obtain a clear picture of the optical response of acceptor-substituted molecules it is instructive to study the size-dependence of optical properties starting with very long bridges. In these systems the effects of the acceptor and the bridge regions can be clearly separated. Optical properties of acceptor-substituted molecules with shorter bridges can then be attributed to quantum confinement, which is important when the bridge size becomes comparable to the coherence length  $L_I$ . This analysis is reminiscent of the description of exciton confinement in semiconductor nanostructures [38] where  $L_I$  is given by the Wannier exciton diameter [139–143].

## 6.1 Size-Scaling of the Ground - State Density Matrix.

The six carotenoids listed in order of increasing acceptor-strength in Fig. 6.1 were synthesized and their optical electronic spectra measured in [2]. Betacarotene (1) is a symmetric nonpolar molecule. In the other molecules one end was substituted with an acceptor group.

The Hartree-Fock ground-state density matrices were calculated first. Optimal ground-state geometries were obtained at the AM1 level using Gaussian-94. The ZINDO code was used next to generate the INDO/S hamiltonian (Section 2.1).

The effect of the acceptor on the molecular ground state can be interpreted by using contour plots of the density matrices. The absolute values of the reduced single-electron ground-state density matrix elements  $|\bar{\rho}_{nm}|$  of betacarotene (1) are shown in Fig. 6.2A. The axes represent carbon atoms. (The bridge atoms are labeled 1-18 as indicated in Fig. 6.2). The parts corresponding to the end structures are marked by rectangles in the corners of matrix. The chain's density matrix is dominated by the diagonal and near-diagonal elements, reflecting the bonds between nearest neighbors. The nine bridge

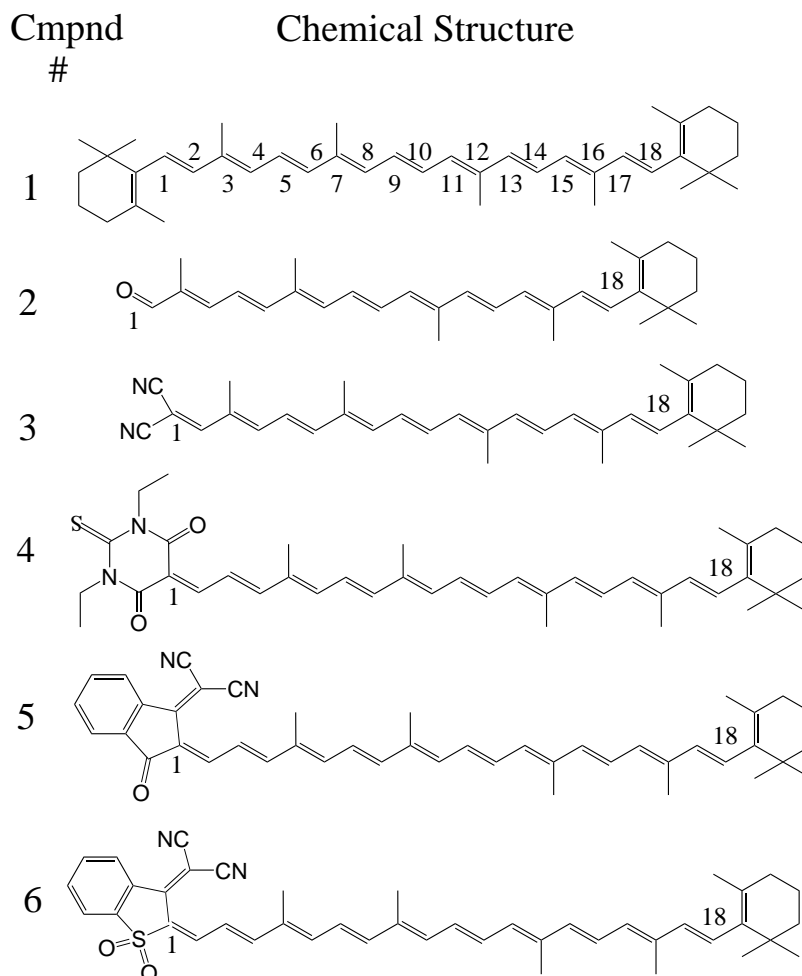


Figure 6.1: Six acceptor-substituted carotenoids [1,2] listed in order increasing acceptor strength. Repeat units numbering used in two-dimensional plots is given for molecule 1.

double bonds and two double bonds located at the ends are clearly identified. The ground-state density matrix of molecule 6 (with the strongest acceptor) is displayed in Fig. 6.2B. The decrease of  $\pi$ -electron density in the bridge (along the diagonal of the matrix) near the acceptor is clearly seen. Other calculated ground-state properties of all molecules are displayed in Fig. 6.3. The growth of ground-state dipole moments (panels A) and the total charge on the acceptor end (panels B) is commensurate with increasing the acceptor strength.

To explore the acceptor effect the size-scaling of the optical response and

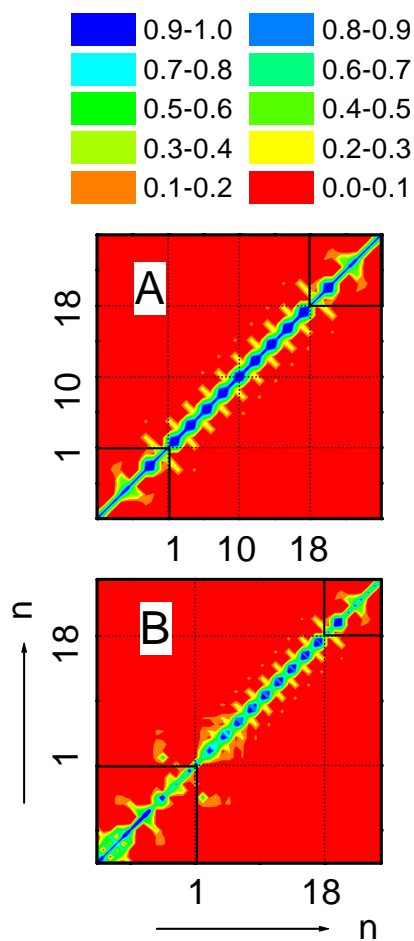


Figure 6.2: Contour plots of ground state density matrices for (A) neutral  $N(10)$  (compound 1) and (B) polar  $P(10)$  (compound 6) molecules. The color code is shown in the upper panel. The structures at the ends of molecules are shown by rectangles.

its saturation to the bulk by increasing the polyenic chain length has been examined.<sup>1</sup> The molecular templates shown in Fig. 6.4 represent two extreme cases: neutral  $N(n)$  and polar  $P(n)$  molecules. Some ground state properties of  $P(40)$  are displayed in Fig. 6.5. We first consider the bond-length alternation parameter  $\delta l_j$  which denotes the difference between the single ( $l_{2j}$ ) and the

<sup>1</sup>During geometry optimization in long molecules, the geometry of the polyenic chain was constrained to be planar.

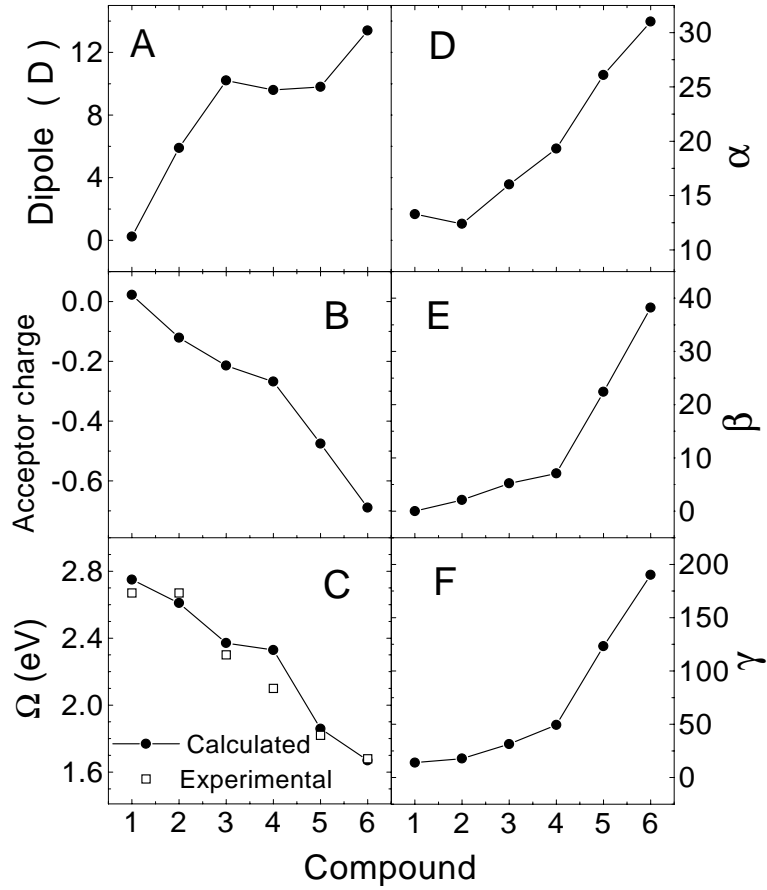


Figure 6.3: Dipole moments (A), total charge on the acceptor (B), frequency of the lowest transition (C), linear  $\alpha(0)$  (D), quadratic  $\beta(0)$  (E), and cubic  $\gamma$  (F) off-resonant polarizabilities for six carotenoids. The ordinate axes are labeled by compound number according to Fig. 6.1.  $\alpha, \beta$ , and  $\gamma$  are in the units of  $e\text{\AA}^2V^{-1}$  [ $1.441 \times 10^{-23}esu$ ],  $e\text{\AA}^3V^{-2}$  [ $4.323 \times 10^{-29}esu$ ], and  $e\text{\AA}^4V^{-3}$  [ $1.297 \times 10^{-34}esu$ ].

double ( $l_{2j-1}$ ) bond lengths in the  $j$ 'th repeat unit along the bridge

$$\delta l_j = l_{2j} - l_{2j-1}, \quad j = 1, \dots, n. \quad (6.1)$$

(Note that the first repeat unit  $j = 1$  is at the acceptor end.) Panel A shows the variation of the bond-length alternation along the bridge. Panel C represents the variation of the total atomic charge  $q_A$  (Eq. (2.18)) along the chain, and

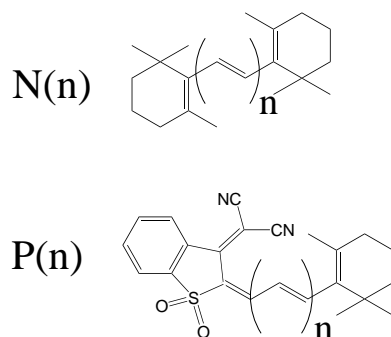


Figure 6.4: Structures of the neutral  $N(n)$  and polar  $P(n)$  (substituted by the strongest acceptor) molecules. Calculations were done for chain lengths of  $n = 10, 15, 20, 30, 40$  double bonds.

panel B shows the integral of this quantity

$$Q_A = Q_{\text{Acceptor}} + \sum_{a=1}^A q_a, \quad (6.2)$$

where  $Q_{\text{Acceptor}} = 0.69e$  is the total electronic charge on the acceptor. These calculations illustrate the interplay of bulk and boundary (end) effects in electronic structure of conjugated molecules. The figures show that the acceptor attracts electronic charge and attempts to invert the chain structure to zwitteronic. The  $\pi$ -electronic system in response screens the acceptor influence by inducing a positive charge at the acceptor end. The electrons completely neutralize the acceptor at an effective length of about 10 double bonds, and the other parts of the molecule are unaffected by the acceptor. This leads to a saturation of the ground - state dipole moment at this molecular size.

The acceptor-strength controls the magnitude of the dipole moment whereas the electronic mobility determines the effective screening length. Our analysis is based on following the charge distribution  $q_A$  and bond-length alternation  $\delta l_n$  along the chain. The bond-order alternation, which is another important characteristic of electronic structure, is usually strongly correlated with the bond-length alternation  $\delta l_n$  [98], and for the sake of brevity  $\delta l_n$  has been used as the measure of both quantities. In the next section the ground-

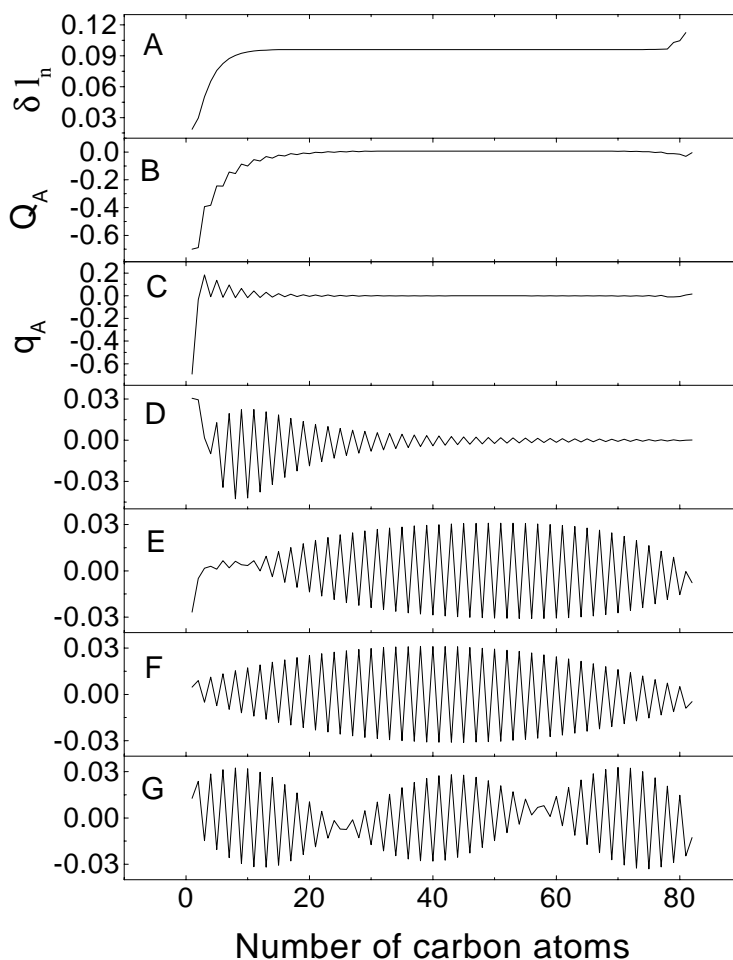


Figure 6.5: Variation of the bond-length alternation (A), total charge  $Q_A$  (B), total atomic charge  $q_A$  (C), diagonal elements of modes  $a$  and  $b$  in polar  $P(n)$  molecule (D and E), and modes  $a'$  and  $b'$  in neutral  $N(n)$  molecule (F and G) along the chain for chain length  $n = 40$  double bonds.

state density matrices will be used to calculate and interpret the optical spectra of these molecules.

## 6.2 Electronic Normal Modes and Optical Absorption

The experimental absorption spectra of the family of substituted carotenoids (Fig. 6.1) are displayed in Fig. 6.6 (dashed lines) [2]. The spectrum of the unsubstituted molecule (1) is dominated by a single peak  $a$ . As the acceptor

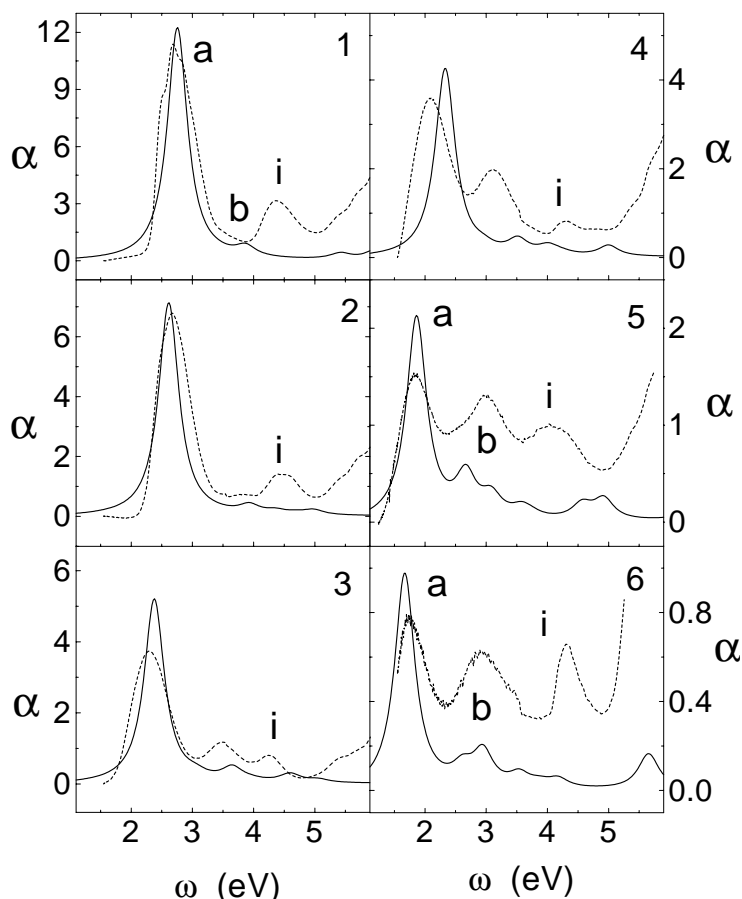


Figure 6.6: Calculated (solid lines) and experimental (dashed lines) linear absorption spectra [1,2] of six carotenoids. Panels are numbered according to Fig. 6.1. The absolute values of linear polarizability are given in arbitrary units. Theoretical spectra were calculated with linewidth  $\Gamma = 0.2$  eV. Peak *i* at 4.5 eV appearing on all experimental spectra originates from the anti-oxidant added to samples.

strength is increased, this peak is red shifted and a second, weaker, peak *b* appears. An additional impurity peak *i*, appearing around 4.5 eV on all experimental spectra (and absent in our calculations), originates from the anti-oxidant added to samples in order to increase their shelf lifetime. Nonlinear polarizabilities of these molecules showed a dramatic growth with increasing acceptor strength.

The absorption spectra were calculated using Eq. (2.55). The TDHF equations were solved using the ground-state density matrices  $\bar{\rho}$  as an input. The



electronic modes  $\xi_\nu$ ) were calculated using the DSMA outlined. The six calculated spectra shown by solid lines in Fig. 6.6 closely resemble the experimental spectra. The red-shift of the band edge transition (*a*) with increasing acceptor strength is completely reproduced: computed frequencies are within 0.07 eV of experiment, except for compound 4 where the difference is 0.23 eV (see panel C in Fig. 6.3). The second peak (*b*) was reproduced in our calculations with a weaker oscillator strength compared with experiment. This discrepancy may be attributed to two factors: First, as will be shown later, an acceptor perturbs the second charge - transfer mode which is dark in the symmetric molecule, and makes it visible in linear absorption. This influence depends not only on the acceptor strength, but also on  $\pi$ -electron mobility, which in turn depends on the bond - length alternation (in non-alternating chains the electrons move more easily). Calculations performed with slightly different geometries (obtained from different levels of semiempirical or *ab initio* geometry optimizations) showed that the relative oscillator-strengths of these peaks in molecules with strong acceptors are much more sensitive to the bond - length alternation than their frequencies (the second peak (*b*) became comparable and even stronger than the first peak (*a*) for some geometries). Therefore, even small differences between experimental and calculated structures can lead to the redistribution of intensity of the linear absorption peaks. Second, the experiments, were carried out in films where intermolecular interactions, which were not taken into account in the present single-molecule calculations, may be significant. For example, intermolecular charge transfer [144–146] is possible between the acceptor and the neutral end of an adjacent molecule.

The right column in Fig. 6.3 shows the variation of the off-resonant first, second, and third order polarizabilities  $\alpha(0)$ ,  $\beta(0)$ , and  $\gamma(0)$  with acceptor strength. We found a steep growth  $\alpha(0)$  and  $\gamma(0)$  by factors 2.5 and 15 respectively from neutral to the most polar case. Experimentally the compound

with the strongest acceptor showed a 45-fold enhancement of resonant  $\gamma$  compare to the neutral betacarotene [1]. To explore this strong acceptor effect on the polarizabilities the size-scaling and saturation to the bulk of the optical response in molecules  $P(n)$  and  $N(n)$  was examined next. We expect the acceptor's influence to decrease with increasing molecular size, and in the infinite chain limit all molecules should have the same linear absorption spectra with the saturated band-edge transition  $\Omega_\infty$  and bulk scaling of linear polarizability  $\alpha \sim n$  [98,60]. Starting with  $N(40)$  and  $P(40)$ , we gradually decreased the chain length and followed the evolution of the optical response up to 10 double bonds which is the bridge length of carotenes 1 and 6. The electronic absorption of  $P(n)$  (solid lines) and  $N(n)$  (dashed lines) are displays in Fig. 6.7 for  $n=40,30,20$ , and 10 double bonds. The figure clearly shows that the oscillator - strength of the lowest frequency peak  $a$  of the polar molecules does not change considerably whereas the second peak  $b$  grows with increasing chain length and gradually attains the bulk limit of the band edge  $a'$  transition of the neutral molecules.

To account for these trends we display in Figures 6.8 and 6.10 the absolute magnitudes of the electronic modes  $\xi_\nu$  corresponding to both peaks using the same format of the ground state calculations (Fig. 6.2). These two-dimensional plots allow us to gain a clear physical insight into the nature of optical excitations. By displaying the matrices representing the modes in the site representation the optical properties are related directly to motions of charges in the system (see Section 2.5 in Chapter 2).

The electronic modes of the two strongest transitions  $\xi_{a'}$  and  $\xi_{b'}$  appearing in the spectra of neutral molecules  $N(40)$  (panels A and B)  $N(20)$  (panels C and D) and  $N(10)$  (panels E and F) are displayed in Fig. 6.8. The electronic modes of the neutral molecule are almost symmetric with respect to the diagonal ( $\xi_{mn} \approx \xi_{nm}$ ). This means that there is no preferable direction of motion for

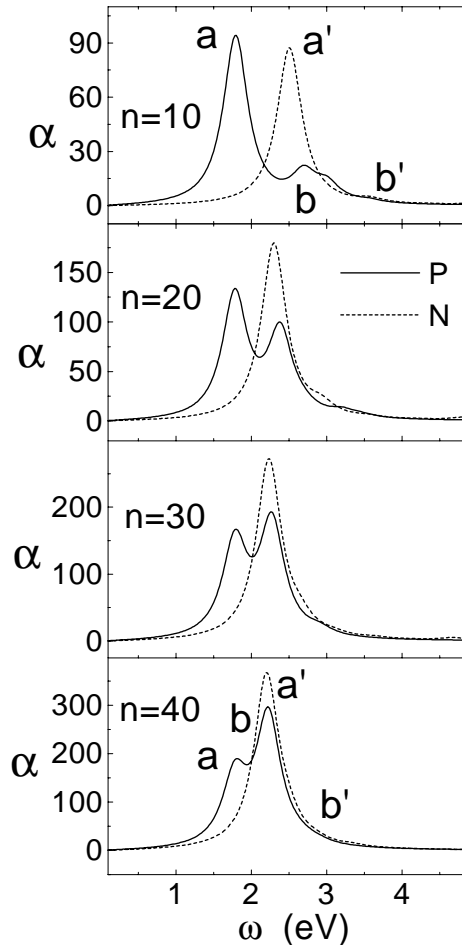


Figure 6.7: Linear absorption spectra calculated with linewidth  $\Gamma = 0.2$  eV of the neutral  $N(n)$  (dashed lines) and polar  $P(n)$  (solid lines) molecules shown in Fig. 6.4. The relative values of linear polarizability are given in arbitrary units.

electron (or holes). The size of the mode along the ‘antidiagonal’ ( $m - n$ ) direction reflects the delocalization of the relative motion of the electron-hole pair (exciton coherence size) whereas the variation along the diagonal reflects their center of mass motion (i.e. where the optical excitation resides within the molecule). These are the off-diagonal and diagonal sizes, respectively (see Section 2.5 in Chapter 2).

A more detailed view of the charge-density-wave i.e. the variation of the diagonal elements for modes  $\xi_{a'}$  and  $\xi_{b'}$  are given in panels F and G of Fig. 6.5

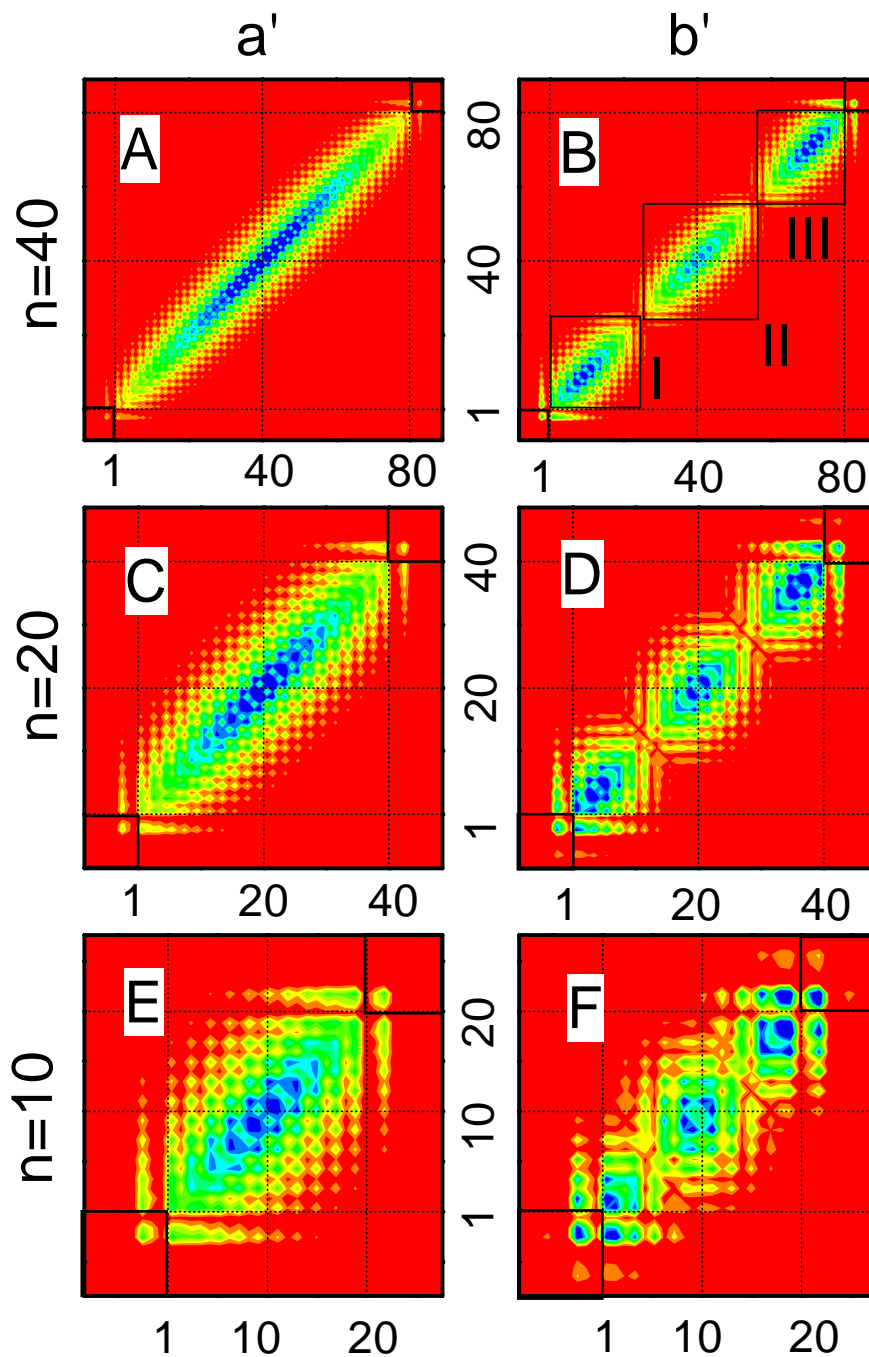


Figure 6.8: Contour plots of density matrices for neutral  $N(n)$  molecule. Top panel: coordinates of the first  $a'$  (A) and second  $b'$  (B) absorption peaks for chain length  $n = 40$  double bonds. Middle and bottom panels display the same quantities but for chain lengths of  $n = 20$  and  $n = 10$  double bonds, respectively. The structures at the ends of molecules are shown by rectangles.

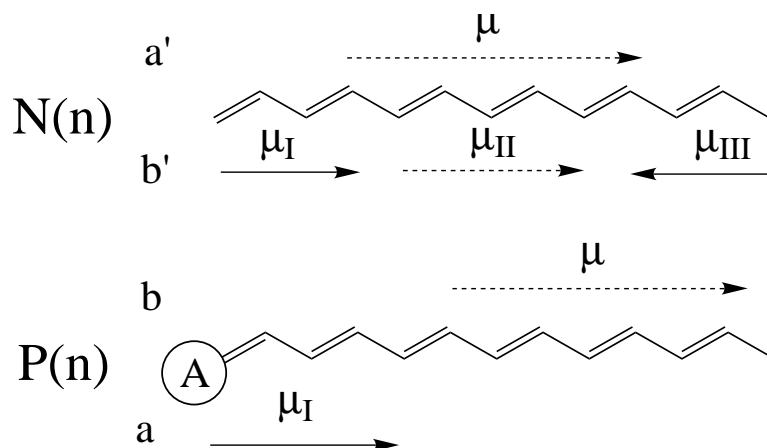


Figure 6.9: Sketch of the dipole moments  $\mu = Tr(\mu Q)$  gain for dominant modes in neutral  $N(n)$  and polar  $P(n)$  molecules with chain length  $n = 40$  double bonds.

(This is a complementary information to Fig. 6.8 which only gives the absolute magnitudes of the density matrix elements and does not show their sign). Optical excitations of a neutral molecule are localized on the polyenic chain, with no significant change in mode structures as the chain-length is increased.  $\xi_{a'}$  is a *bulk mode* with an off-diagonal coherence size (i.e. size, where the amplitudes of coherences decrease to 10% of their maximum values) of about 12 double bonds. The dipole moment  $\mu_{a'} = Tr(\mu \xi_{a'})$  of this mode is uniformly distributed along the chain (see Fig. 6.9). Such bulk features were previously observed in the band-edge transition of polyacetylene oligomers [74,73,98] and Section 4. The second oscillator  $\xi_{b'}$  is very different: It has the same off-diagonal coherence size, but a non-uniform diagonal space distribution. Three contributions to the dipole moment are clearly identified  $\mu_{b'} = Tr(\mu \xi_{b'}) = \mu_I + \mu_{II} + \mu_{III}$ . The distribution of the dipole moment for these three regions is schematically shown in Fig. 6.9. The strongest electronic coherences are created at the end regions of the molecule (*I* and *III*) with diagonal size of about 17 double bonds. Weaker bridge coherences are created in the middle of the chain (*II*). The total contribution from the ends is approximately zero,

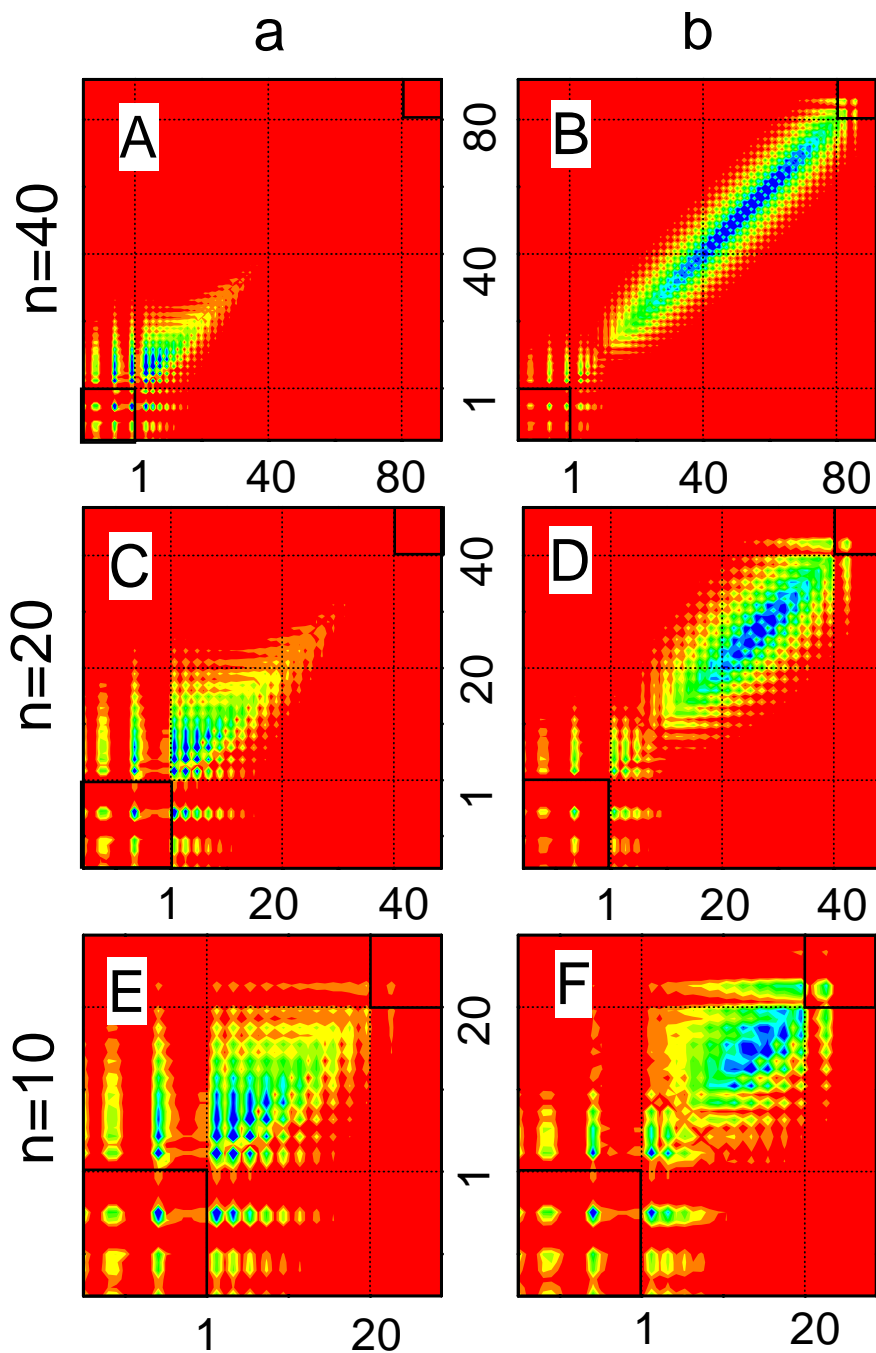


Figure 6.10: Contour plots of density matrices for polar  $P(n)$  molecule. Top panels: coordinates of the first  $a$  (A) and second  $b$  (B) absorption peaks for chain length  $n = 40$  double bonds. Middle and bottom panels display the same quantities but for chain length  $n = 20$  and  $n = 10$  double bonds, respectively. The structures at the ends of molecules are shown by rectangles.

and only the region II contributes to the oscillator strength of this mode. This mode therefore makes only a weak contribution to the linear absorption. However, such *charge transfer* modes have the potential to dominate spectra of nonsymmetric structures.

The electronic modes  $\xi_a$  and  $\xi_b$  of the two oscillators contributing to the linear spectra of the polar molecules P(40), P(20), and P(10) are displayed in Fig. 6.10. The diagonal elements of modes  $\xi_a$  and  $\xi_b$  in P(40) are shown in panels D and C of Fig. 6.5. Fig. 6.10A shows that the lowest peak (a) in P(40) represents a charge-transfer mode, completely localized at the acceptor end with the same off-diagonal and diagonal sizes (12 and 17 double bonds respectively) as for the neutral molecule. The principal difference is the appearance of strong electronic coherences at the acceptor end. The coherences are more pronounced in the electron (ordinate) direction. This implies that the created electron-hole pair involves electron transfer from the acceptor to the chain. The hole resides primarily on the acceptor, whereas the electron can move also in region I of the bridge. This tends to reduce the chain-to-the acceptor electron transfer which takes place in the ground state. The dipole moment of the mode is large and localized (see Fig. 6.9). This mode therefore carries a strong oscillator strength in the optical response of small chains, and saturates (become constant) in larger molecules ( $n > 17$  double bonds). The second bulk mode (b) (Fig. 6.2B) differs only by the part controlled by acceptor from the bulk mode of neutral molecule (compared to Fig. 6.8A). The oscillator - strength of this mode for molecules with  $n > 12$  double bonds grows linearly. The absorption spectra of small chains are therefore controlled by the charge-transfer mode (a) whereas the bulk mode (b) becomes dominant with increasing molecular size. The different character of these modes is lost for chains shorter than effective coherence size of 12 double bonds such as P(10) displayed in Fig. 6.10(E,F). Quantum confinement [141,142] then dra-

matically affects the modes and we can no longer classify them as either end or bridge type. This is clearly evident by starting with large chains and gradually reducing the size.

### 6.3 The Ground-State of Long Polyacetylenes: Solitons

Our study allows us to draw some general conclusions with regard to the ground state of large molecules. Panels A-C of Fig.6.11 display schematically the bond-length alternation pattern of several molecules with increasing acceptor strength. The ground state of an infinitely long molecule is represented by a bond-order wave which gives  $q_A = 0$ ,  $\delta l_n = \pm \delta \bar{l}$ . This means that the ground state is doubly degenerate with either  $\delta l_n = +\delta \bar{l}$  (double-single alternation) or  $\delta l_n = -\delta \bar{l}$  (single-double alternation). In finite molecules, the ground state degeneracy may be broken even if the molecules are very long. In neutral polyenes  $q_A = 0$  at the ends as well as in the bulk, which implies the formation of double bonds at the ends, giving  $\delta l_I > 0$  and  $\delta l_{III} > 0$ . Our calculations show that  $\delta l_I = \delta l_{III} \approx \delta l_{II}$ . The bond alternation in the bulk can assume two values,  $\delta l_{II} = \pm \delta \bar{l}$ . However if  $\delta l_{II} = -\delta \bar{l}$ , two solitons are needed to transform the boundary values  $\delta l_I = \delta l_{III} \approx \delta \bar{l}$  to the bulk values  $\delta l_{II} = -\delta \bar{l}$  (see Fig.6.11A) which means that the energy of the  $\delta l_{II} = -\delta \bar{l}$  configuration is higher than that of the  $\delta l_{II} = \delta \bar{l}$  configuration (Fig.6.11A) by the energy needed to form two solitons. The ground state is no longer degenerate and is represented by a homogeneous solution  $\delta l_{II} = \delta \bar{l}$ . This illustrates that the nondegeneracy of the ground state of linear conjugated molecules may be attributed to boundary effects.

By adding an acceptor to one end of a long molecule, we still have  $q_{III} = 0$ ,  $\delta l_{III} \approx \delta \bar{l}$ , however the charge density at the acceptor end is  $q_I \neq 0$ . This leads to a decrease in the double chemical bond strength at that end, which



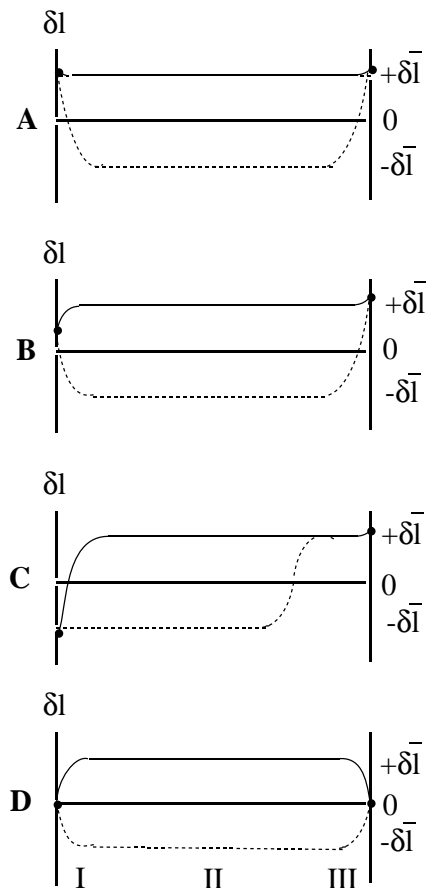


Figure 6.11: Schematic variation of bond - length alternation pattern in the long acceptor substituted molecules with increasing acceptor strength (panels A to C). Two possible configurations corresponding to ground states with  $\delta l_{II} = \delta\bar{l}$  and  $\delta l_{II} = -\delta\bar{l}$  are shown by solid and dashed lines respectively. Panel A. No acceptor, the ground state is non-degenerate and has  $\delta l_{II} = \delta\bar{l}$  (solid line), the state with  $\delta l_{II} = -\delta\bar{l}$  (dashed line) has a higher energy needed to form two solitons. Panel B Intermediate-strength acceptor: the ground state with  $\delta l_{II} = \delta\bar{l}$  is nondegenerate (solid line) and contains a soliton in the acceptor region. A state with  $\delta l_{II} = -\delta\bar{l}$  (dashed line) contains two solitons and has a higher energy. Panel C. Very strong acceptor; The molecule is separated into the acceptor with the charge  $-e$  and anion with the charge  $+e$  and  $(N-1)$  carbon atoms with the ground state representing the charged soliton. The ground state of an anion may become degenerate since a soliton can be formed anywhere (this is represented by the dashed line). However Coulomb interaction between the acceptor and the soliton leads to its localization near the acceptor (solid line). Panel D: Molecule substituted by a donor and an acceptor of intermediate strength. Two ground states with  $\delta l_{II} = \delta\bar{l}$  (solid line) and  $\delta l_{II} = -\delta\bar{l}$  (dashed line) have the same energy (cyanine like).

implies that  $\delta l_I < \delta \bar{l}$ . If the acceptor is not very strong, a soliton is needed to transform  $\delta l = \delta l_I$  to its bulk value,  $\delta l = \delta l_{II} = \delta \bar{l}$ , and no soliton is needed at the other end (solid curve in Fig. 6.11B). This is confirmed by our calculations (see Fig.6.5A). The soliton is located at the acceptor end of the molecule to minimize the length of the region where  $\delta l$  is different from its bulk value. The soliton size represents the length of the region where the boundary value of  $\delta l_I$  transforms to its bulk value. Charge screening occurs in the same region, as is clearly shown in Fig.6.5B and C. A configuration with  $\delta l_{II} = -\delta \bar{l}$  (dashed lines in Fig.6.11B) involves the formation of solitons on both ends and has a higher energy. The strong acceptor case is displayed in Fig.6.11C. In this case we have  $\delta l_I = -\delta \bar{l}$  and the acceptor attracts an additional electron and the molecule is separated into two parts: the edge carbon atom (with charge  $-e$ ) and a polyacetylene anion which contains an odd  $(N - 1)$  number of carbon atoms and charge  $+e$ . The ground state of an anion (known as a charge soliton) [147,148] is needed to change the sign of the bond - length alternation  $\delta l = \pm \delta \bar{l}$  on the ends of the molecule. The charge  $+e$  is concentrated in the region where  $\delta l$  undergoes the change from  $-\delta \bar{l}$  to  $+\delta \bar{l}$ . The center of this region,  $x_0$ , and size of the region,  $\Delta x$ , are usually referred to as the soliton position and size respectively. The ground state is highly degenerate since the soliton can be found anywhere along the molecule ( a typical situation is represented by the dashed line in Fig. 6.11C). This leads to the formation of a soliton band in the ground state. The ground state closely resembles the charged solitons observed in the ground state of anions of degenerate polymers molecules with odd numbers of carbon atoms [147]. However the Coulomb interaction between the charged acceptor and the soliton may lead to localization of the soliton in the vicinity of the edge (solid line in Fig. 6.11D). Decreasing the acceptor strength leads to a reduction of the absolute value,  $q$ , of charge accepted by the edge atom ( $q_A < e$ ) and to

the appearance of bonding between the acceptor and the anion, which leads to  $-\delta\bar{l} < \delta l_I < \delta\bar{l}$ . This situation, which has been considered above, can be qualitatively represented as follows: a charged soliton is located at  $x_0 < \Delta x/2$  and is cut at  $x = 0$  (the acceptor position) since there are no carbon atoms at  $x < 0$ . If  $\delta l(x - x_0)$  is the soliton profile then  $\delta l_I = \delta l(x - x_0)$  and  $q_A < e$  is the charge in the soliton in the region  $-x_0 < x < \infty$ . Note that  $x_0$  can assume negative values as well. The weaker the acceptor, the smaller is  $x_0$ : decreasing  $x_0$  leads to the decrease of  $q_A$  and increase of  $\delta l_I$ . In the case of a very weak acceptor,  $x_0 \rightarrow -\infty$  (i.e.  $q_A \rightarrow 0$ ,  $\delta l_I \rightarrow \delta\bar{l}$ ). An intermediate case represented in Fig.6.11D corresponds to  $x_0 = 0$ .

If we add an acceptor to one end (I) and a donor to the other end (III), the ground state degeneracy should occur at some intermediate donor and acceptor strength corresponding to  $\delta l_I \approx \delta l_{III} \approx 0$ . Two configurations corresponding to ground states with  $\delta l_{II} = \pm\delta\bar{l}$  are shown in Fig.6.11D. However in short molecules ( $L < \Delta x$ ) the ground state will then be non-alternating with  $\delta l = 0$ . This is known as the cyanine limit [149,150].

## 6.4 Excited States Density Matrices of Acceptor-Substituted Carotenoids.

To calculate the excited states density matrices of carotenoids the DMRF algorithm (see Section 3) was then applied to nonpolar ( $N$ ) and polar ( $P$ ) conjugated polyenes whereby one end is substituted with a strong acceptor group (see Fig. 6.4 for  $n = 10$ ). The structures and atom labeling are displayed in Fig. 6.12. Optimal ground-state geometries were obtained at the AM1 level using Gaussian-94. The ZINDO code was utilized to generate INDO/S [66-68,64,65] hamiltonian and the CEO/DSMA procedure was then applied to compute the dominant electronic modes and the corresponding dipole moments  $\mu_{\nu}^{(j)}$  which contribute to the first and to the second order off-resonant

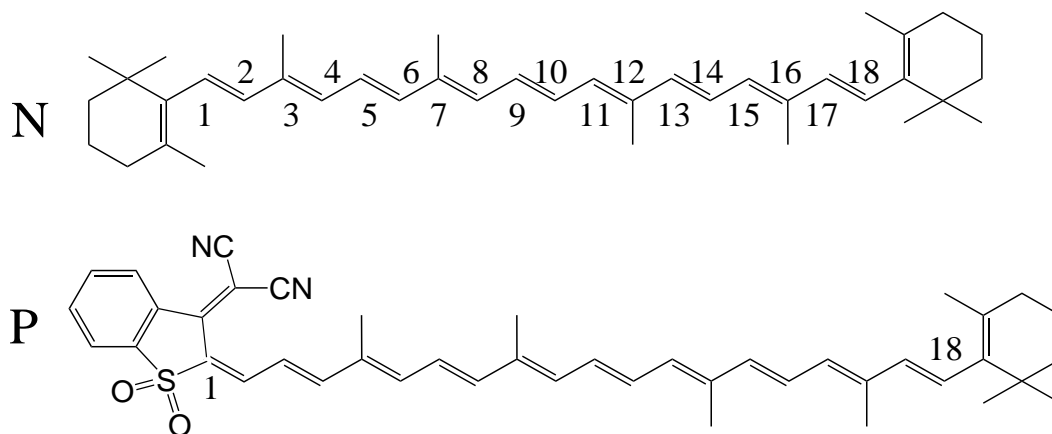


Figure 6.12: Structures and atom labeling of the neutral *N* and polar *P* (substituted by the strong acceptor) molecules.

optical response:

$$\xi^{(j)} = \sum_{\nu} \mu_{\nu}^{(j)} \xi_{\nu} + (\mu_{\nu}^{(j)})^* \xi_{\nu}^+, \quad j = 1, 2. \quad (6.3)$$

Satisfactory convergence of the response to within  $\sim 10^{-3}$  was achieved using 10-15 effective electronic modes.

In Figure 6.13 we display the dipole moments (Eq. (6.3)) of the dominant modes vs. mode frequencies  $\Omega_{\nu}$ , calculated using the first and the second order response. Since the N molecule has an inversion symmetry, the first order response depends only on antisymmetric ( $B_u$ ) oscillators (panel A) whereas the second order response depends on symmetric ( $A_g$ ) oscillators (panel B). The figure shows that the response of the N molecule is dominated by a single electronic mode. In contrast, the P molecule shows four major peaks in each order of the response, and its electronic oscillators do not possess any symmetry. The same modes (a and b) with different dipoles show up in both responses.

The single-electron density matrices  $\rho_{nm}^{\nu\eta}$  for the states corresponding to peaks a, b, and c in N and a' b', c' and d' in P are examined next. These density matrices computed using Eqs. (3.16)-(3.17) and (3.18)-(3.20) represent the projection of the full matrix which contributes to the first and to the

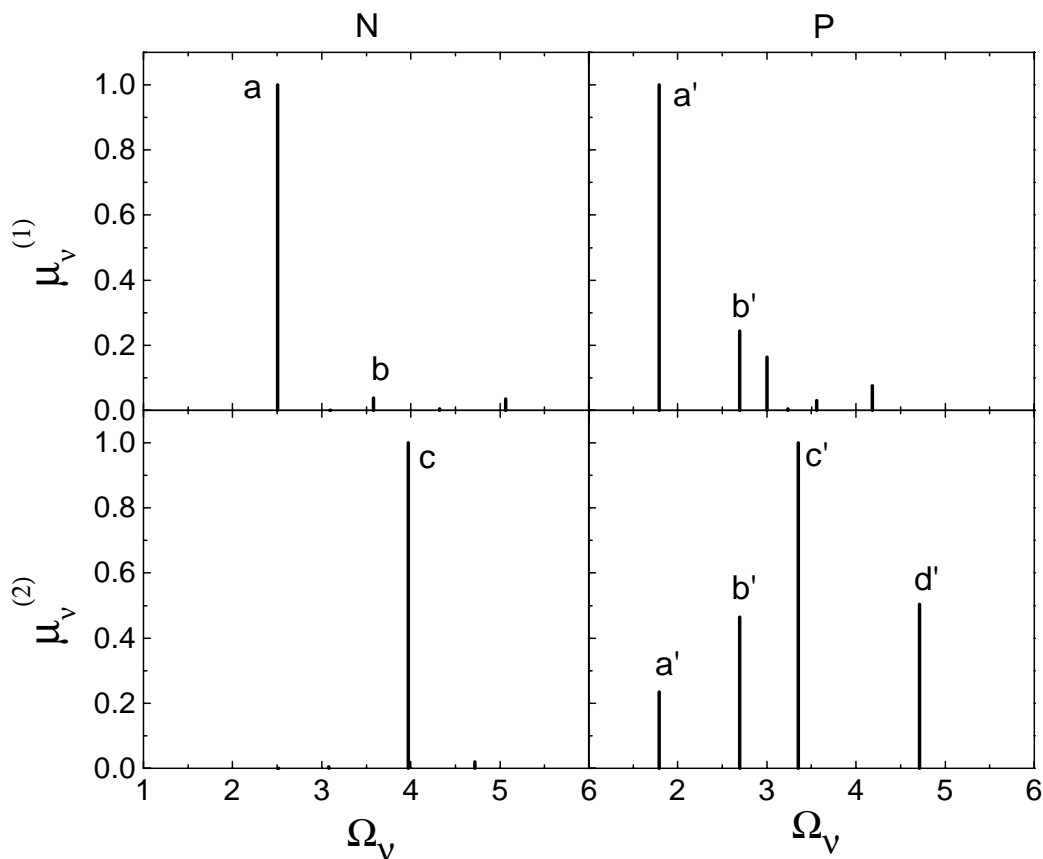


Figure 6.13: The dipole moments  $\mu_\nu$  are displayed vs. electronic mode frequencies  $\Omega_\nu$  for the molecules shown in Fig. 6.12. Shown are the dominant modes in the first two orders of nonlinearity. The dipoles are given in arbitrary units.

second order response, because only the electronic modes which dominate the linear and the quadratic optical responses were used in the calculations. Other components of the matrix do not have a dipole moment and, therefore, do not contribute to the optical response. The effect of the acceptor on the molecular properties can be illustrated using contour plots of the density matrices. The absolute value of the reduced ground state density matrix  $\rho^{gg}$  of N is shown in the upper left panel of Fig. 6.14. The axes represent carbon atoms. The ground state density matrix is dominated by diagonal and near-diagonal elements, reflecting the bonds between nearest neighbors. The (x1) scaling factor indicates that the largest values of the matrix shown by the blue color are

equal to 1. The diagonal elements represent the electronic charges on each carbon atom. The absolute values of the matrix  $\Delta\rho^{aa} \equiv \rho^{aa} - \rho^{gg}$  (panel N  $\Delta\rho^{aa}$ ) is the difference between the density matrix of state a and the ground state density matrix. The matrix is delocalized over the entire molecule. The x10 factor implies that the part of the excited state density matrix which contributes to the second-order optical response only changes slightly compared to the ground state. The difference for the density matrix of state b  $\Delta\rho^{bb}$  (panel N  $\Delta\rho^{bb}$ ) is less delocalized compared with  $\Delta\rho^{aa}$ . In addition it is nonuniform along the diagonal, which leads to diagonal localization sizes.  $\Delta\rho^{cc}$  corresponding to the electronic mode contributing to the second-order optical response possesses a delocalization and magnitude similar to  $\Delta\rho^{aa}$ . For all excited state matrices, the off-diagonal elements are much larger than the diagonal. This means that upon optical excitation of the unsubstituted molecule the changes in the bonding pattern are much more significant compared with the charge redistribution.

The middle and the right columns in Fig. 6.14 show the transition density matrices. Transitions involving the ground state are described by the electronic modes ( $\rho^{ga}$ ,  $\rho^{gb}$ , and  $\rho^{gc}$ )<sup>2</sup>. They have delocalization properties very similar to the corresponding states density matrices, because in the calculations of the latter these modes make the dominant contribution. Similarly, the transition density matrices between excited states shown in the right column of Fig. 6.14 are delocalized over the entire molecule and have a symmetric structure. The strongest coherences appear to be at the center of the matrices because the density matrices of states a, b, and c have the strongest bonding pattern at the center.

Fig. 6.15 displays the absolute values of the calculated density matrices of P. The strong acceptor perturbs the ground state, as shown by the reduction

---

<sup>2</sup> $\rho^{ga}$  and  $\rho^{gb}$  contributing to the linear response have been analyzed in Section 6.2. They correspond to the modes  $a'$  and  $b'$  displayed in Fig. 6.8 (bottom row)

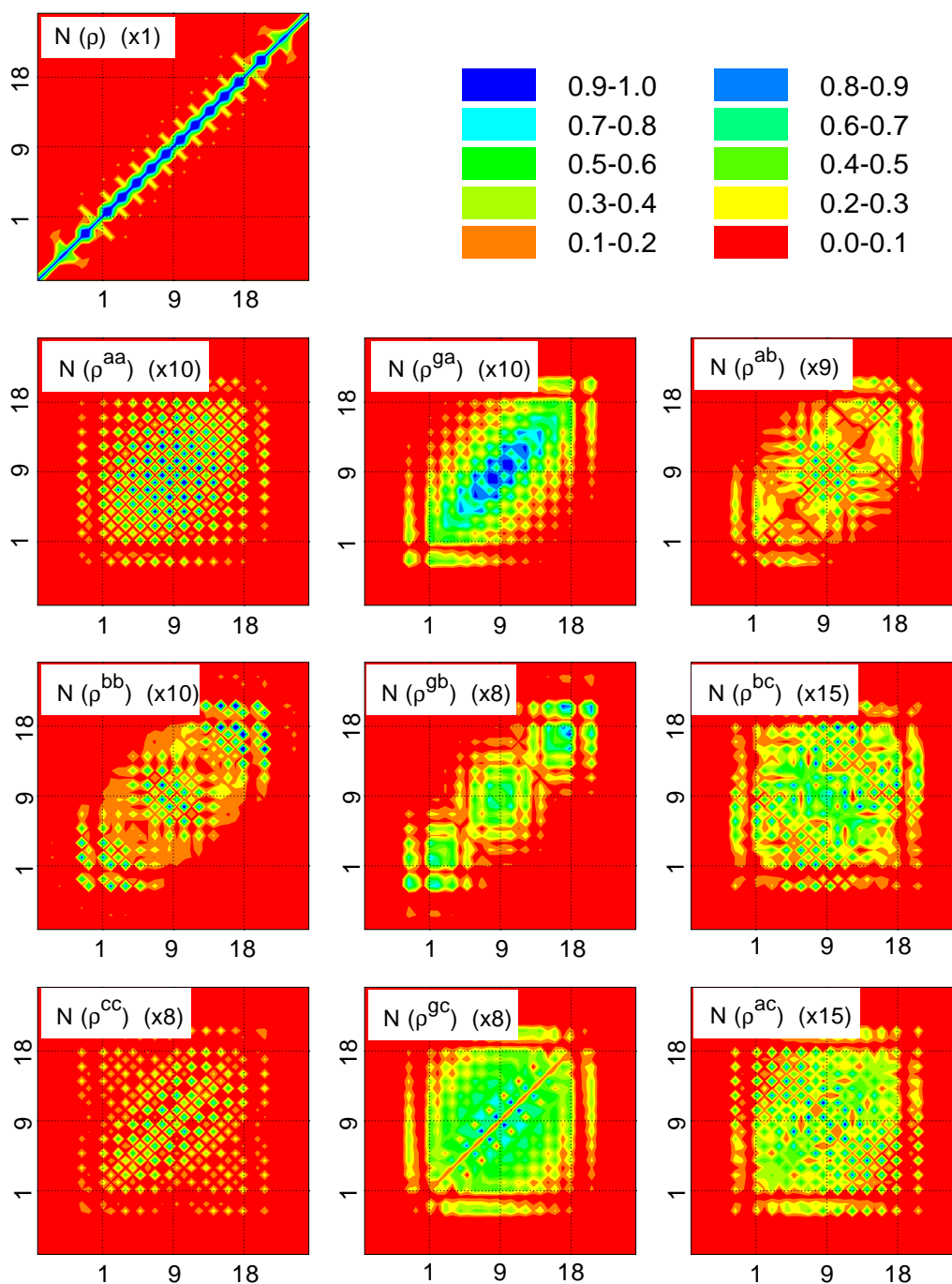


Figure 6.14: Contour plots of ground and excited state density matrices which dominate the linear absorption of molecules N. The axis labels represent the individual carbon atoms as labeled in Fig. 6.12. Panel labels indicate the molecule (Fig. 6.12) and the state corresponding to the peak in Fig. 6.13.  $\rho^{gg}$  ground state density matrix;  $\Delta\rho^{\nu\nu} \equiv \rho^{\nu\nu} - \rho^{gg}$  the difference between the density matrices of state  $\nu$  and the ground state;  $\rho^{\nu\eta}$  the transition density matrices.

of the electronic density towards the acceptor in panel P  $\rho^{gg}$ . The difference  $\Delta\rho^{a'a'}$  for state a' is localized in the acceptor end (panel P  $\Delta\rho^{a'a'}$ ), whereas  $\Delta\rho^{b'b'}$  for state b is localized on the neutral end of the molecule (panel P  $\Delta\rho^{b'b'}$ ). Note that  $\Delta\rho^{a'a'}$  has a very large diagonal and off-diagonal elements implying that excitation to state a changes the charge distribution as well as the bonding pattern compared to the ground state. In contrast,  $\Delta\rho^{b'b'}$  is dominated only by off-diagonal elements which makes it similar to the excited state density matrices of the unsubstituted molecule. This reflects the fundamental difference between states a' and b'.  $\Delta\rho^{c'c'}$  and  $\Delta\rho^{d'd'}$  corresponding to the electronic mode contributing to the second-order optical response are both localized at the acceptor end, and are dominated by a few large diagonal and off-diagonal elements. The former has a stronger bulk contribution.

The transition density matrices between the ground and the excited states (electronic modes  $\rho^{ga'}$  and  $\rho^{gb'}$ ) are highly asymmetric and delocalized, reflecting the motions of charges along the molecule upon optical excitation<sup>3</sup>. The x and the y axis label the electron and the hole respectively. The diagonal elements  $\rho_{nn}$  show induced charges on various atoms whereas the off-diagonal elements  $\rho_{nm}$  represent the probability amplitude of finding an excess electron at the m-th atomic orbital and a hole on the n-th atomic orbital.  $\rho^{gc'}$  and  $\rho^{gd'}$  corresponding to the high frequency excited states and contributing to the second order response are less asymmetric than the former and delocalized over the entire molecule (compared with  $\rho^{c'c'}$  and  $\rho^{d'd'}$ ). The transition density matrices shown in the right column of Fig. 6.15 are delocalized over the entire molecule. The strongest coherences appear where the density matrices of corresponding states have the strongest bonding patterns. Note that these density matrix elements are smaller (x10-12) compared to the other displayed matrices (x4-9), because the states a, b', and c' are localized in different regions.

---

<sup>3</sup> $\rho^{ga'}$  and  $\rho^{gb'}$  contributing to the linear response have been analyzed in Section 6.2. They correspond to the modes *a* and *b* displayed in Fig. 6.10 (bottom row)



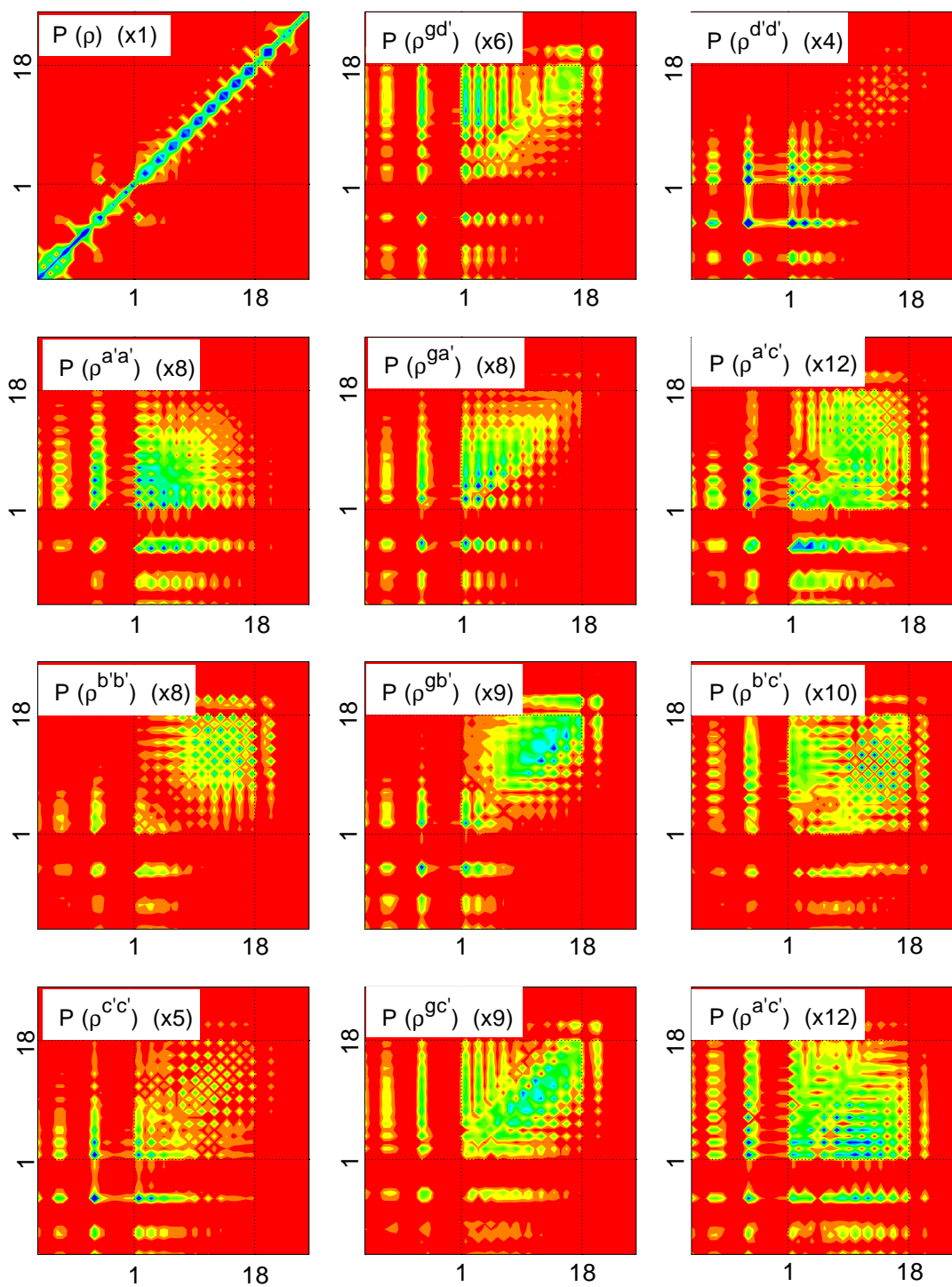


Figure 6.15: Same as in Fig. 6.14 but for the polar molecule P.

## 6.5 Quantum Confinement and Coherence Sizes

The optical response of long acceptor-substituted molecules can be interpreted by dividing them into three effective regions: the acceptor (*I*) and the neutral (*III*) boundary transition regions at the molecular ends, connected by the bridge (middle) region (*II*). (In donor-acceptor substituted molecules, which were not considered here, region *III* will represent the donor end.) There is no charge transfer between these regions, which means that the optical properties are additive and can be interpreted in the same way as those of molecular aggregates [72]. Region *II* has the same properties as the neutral molecule; it has only odd order responses which scale linearly with size whereas regions *I* and *III* have a fixed size. The ground and the excited states are zwitteronic. These effective regions are responsible for even-order optical responses which naturally do not depend on the size of the underlying molecule. They contribute to odd-order response as well, but for long chains these responses are dominated by the region *II* contribution which is proportional to the size. For long chains the influence of the acceptor has a finite range which leads to the creation of several coherence sizes. The first coherence length,  $L_I$ , is related to the size on which the acceptor charge is screened; our calculations show that the bond-length alternation,  $\delta l$ , is different from its bulk value in the same region, hereafter referred to as the transition region. The acceptor may affect the excited states by either modifying an existing delocalized state in the transition region or creating new localized states at that region. Both mechanisms affect optical properties, and in particular they lead to a non-zero second-order polarizability  $\beta$ . We expect that the energy of a delocalized state should not be affected by the acceptor, whereas the energy of a localized state should strongly depend on the acceptor strength. This implies that localized and delocalized states may be readily distinguished by resonant three-wave

mixing spectroscopies.

Optical properties of short molecules can be interpreted in terms of quantum confinement when the molecular size becomes comparable with the sizes  $L_I$  and  $L_{III}$  of the *I* and *III* - regions. These constitute additional coherence diagonal sizes, as opposed to the coherence off-diagonal size of the neutral molecule,  $L_{II}$ , represented by the width of its bulk mode (see Fig.6.2F). In this case the electronic eigenstates of regions *I*, *II*, and *III* are mixed (see Fig.6.8C and D) and for smaller sizes the separation into effective subunits is no longer possible since charge transfer takes place across the entire molecule (see Fig.6.8A and B). The local excitation created by the acceptor drastically increases the polarizabilities of polyenic molecules. The  $\pi$ -electronic system screens the acceptor influence: the acceptor strength controls the magnitude of the dipole moment whereas the electronic mobility determines the effective screening length.

## Chapter 7

# Localized Electronic Excitations in Phenylacetylene Dendrimers

Dendrimeric molecules with branched tree-like structures are drawing considerable attention [151–157]. The dynamics of photophysical (electronic and vibrational energy transfer) as well as photochemical processes has been demonstrated to be strongly affected by geometric confinement. Theoretical interest in these "Cayley trees" arises from their peculiar dimensionality: The connectivity between different sites is one-dimensional (there is only one path to go between two points), however, the number of atoms grows exponentially with generation, as in infinite dimensional systems. This leads to unusual transport and optical properties. Calculating the optical electronic excitations in these systems is a formidable task, and no simple methods exist for analyzing the nature of these excitations and predicting their scaling with molecular size.

A collective electronic oscillator (CEO) approach [104,74,70] was applied for calculating the absorption spectra of two families of dendrimers made up of phenylacetylene repeat unit in a self-similar fashion around the core (see Fig. 7.1). These macromolecules have been suggested as a artificial photonic antenna systems [158,3,159,160]. The spectral frequency profile of family A, which has the same segment (linear unit) length in the various generations, is unchanged across the series of molecules (see bottom two panels in Fig. 7.2).

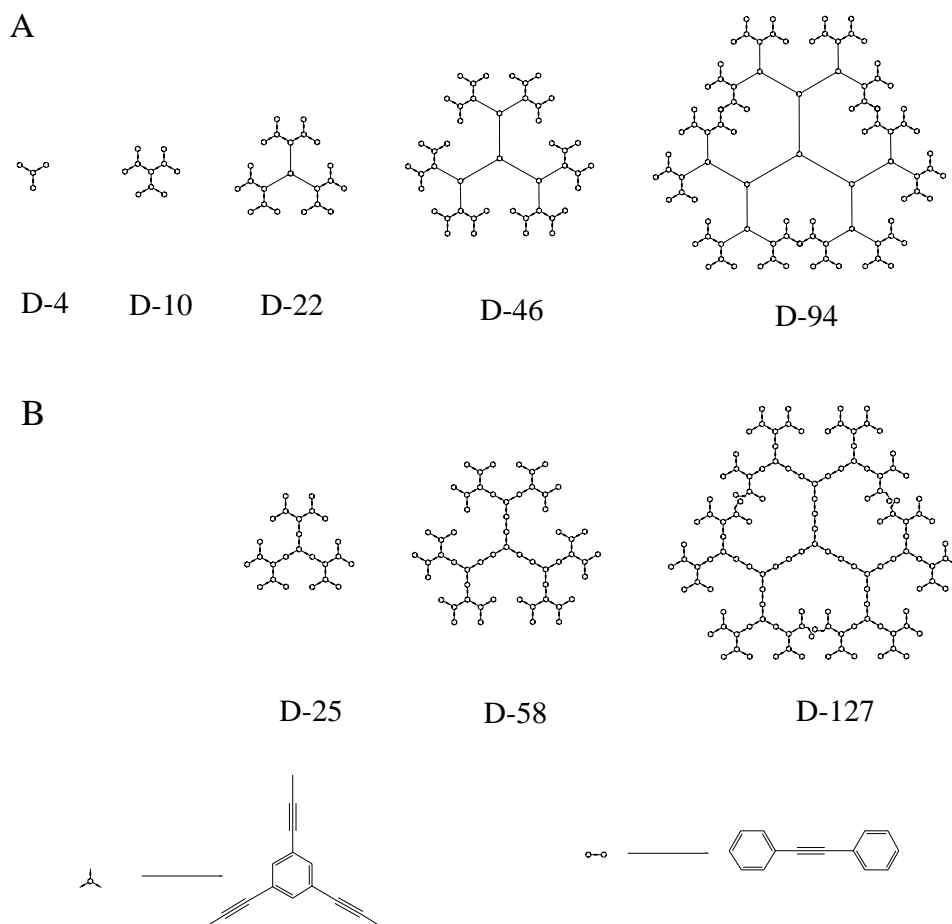


Figure 7.1: Structures of the two families of phenylacetylene dendrimers [3]. The compact dendrimers (A) are made of the same linear building block P1. The extended dendrimers (B) have a varying linear unit length which decreases for higher generations.

Family B has a varying segment length that increase for higher generations. Here the absorption spectra displayed in the dashed lines in Fig. 7.2 show new red-shifted features as the molecular size is increased. This energy hierarchy is shown in Fig. 7.3. Our analysis shows how these trends follow naturally from the localized electronic excitations in these systems. It is difficult to anticipate this localization by inspecting the molecular orbitals: The system is conjugated and the orbitals are delocalized [25,11]. Nevertheless, it is demonstrated that the electron-hole pairs which contribute to the elementary optical collec-

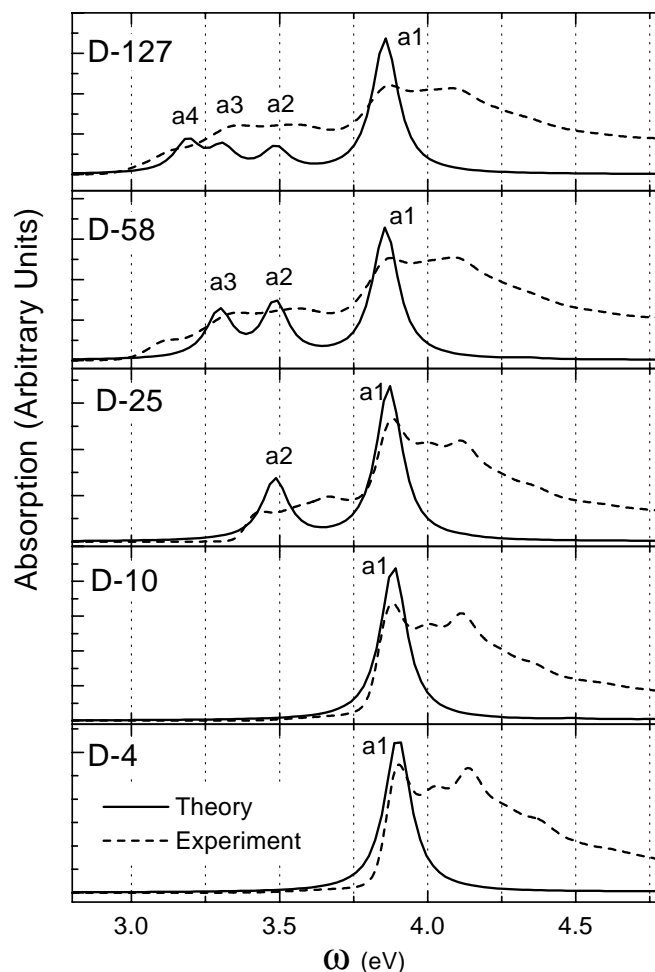


Figure 7.2: Calculated (solid lines) [3] and experimental (dashed lines) absorption spectra of the dendrimers shown in Fig. 7.1

tive excitations are well localized. Our calculations establish the existence of localized optical excitations and show how all the observed trends with dendrimer size and geometry follow directly from this localization. Strategies for the synthesis of antennae with specified energy funneling to a desired active site follow directly from our analysis.

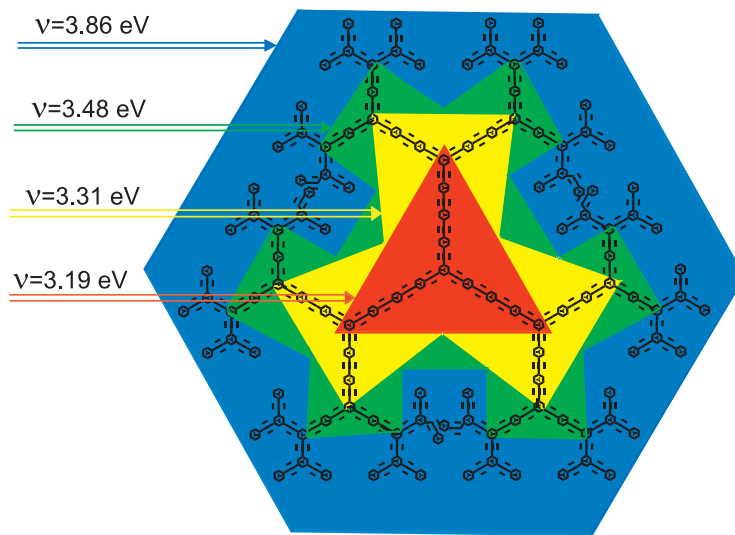


Figure 7.3: The generations (shown by different colors) in the extended dendrimers have a varying linear segment length. Their absorption frequency is blue-shifted for higher generations.

## 7.1 Collective Electronic Excitations in Linear Oligomers

The dendrimers shown in Fig 7.1 are made out of phenylacetylene oligomer segments connected through *para*- or *meta*- substitutions of the benzene rings, leading to linear or zigzag chains respectively [3,159,160]. Understanding the electronic excitations of these segments should be the first step in analyzing the dendrimer spectra. In this section we examine the linear (*para*- substituted) molecules (P-series) with  $n = 1, 2, 3, 7$  repeat units (triple bonds) and the M7 molecule which consists of linear P1, P2, P3 segments connected at the *meta*- position with overall  $n = 7$  repeat units (see Fig 7.4.) Molecules P7 and M7 are made of the same segments, have the same size, and only differ by geometry (*meta*- vs. *para*- substitutions). The notable difference between their spectra turns out to be the key for our analysis.

The Hartree-Fock ground-state density matrices  $\bar{\rho}_{mn}$  were calculated first. Optimal ground-state geometries were obtained at the AM1 level using

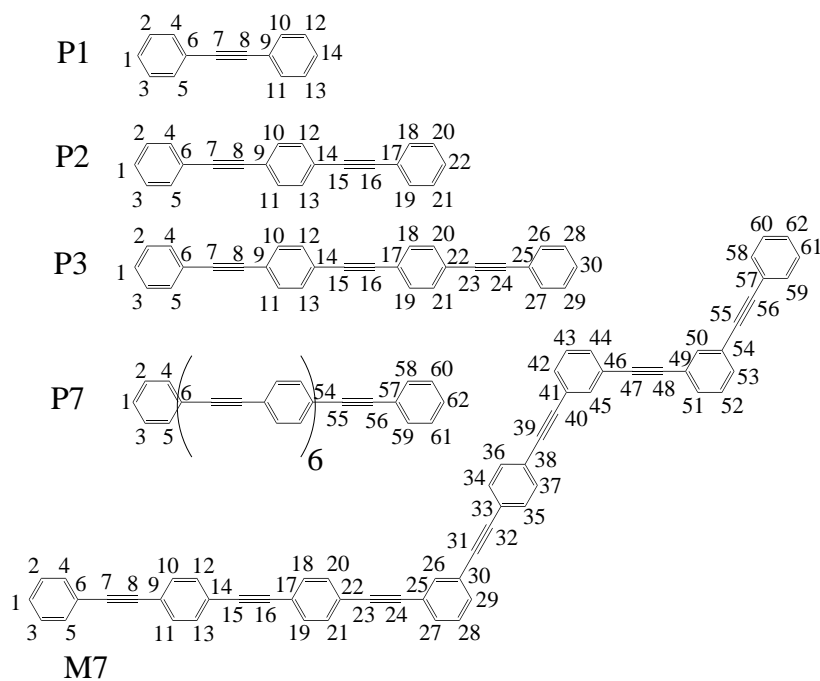


Figure 7.4: Structures and atom labeling of the linear *para*-oligomers  $P_n$  with  $n = 1, 2, 3, 4, 7$  repeat units (triple bonds), and the M7 oligomer made of the P1, P2, P3 units conjugated at *meta*- position.

Gaussian-94. The ZINDO code was used next to generate the INDO/S hamiltonian [64–67] and the CEO/DSMA procedure [74] was finally applied to compute the linear absorption spectra. Satisfactory convergence of the linear absorption was achieved using 10-15 effective electronic modes.

The calculated linear absorption spectra (Eq. (2.55)) are shown in Fig. 7.5. The P-oligomers have two major absorption lines in the 3-6 eV frequency range. The band-edge transition (a) is significantly red-shifted with increasing the chain length, whereas the second peak (b) only shows a small red-shift [104]. The 5.6 eV mode (b) of M7 is similar to P7(b). However, the (a) transition is markedly different; Instead of a single line it has three low-frequency transitions (a1, a2, and a3) at the same frequencies as the band-edge transitions in P1, P2, and P3 oligomers which are the building linear blocks of this molecule.

To explore the nature of the electronic motions underlying the various peaks and to establish a direct real-space link between the optical response



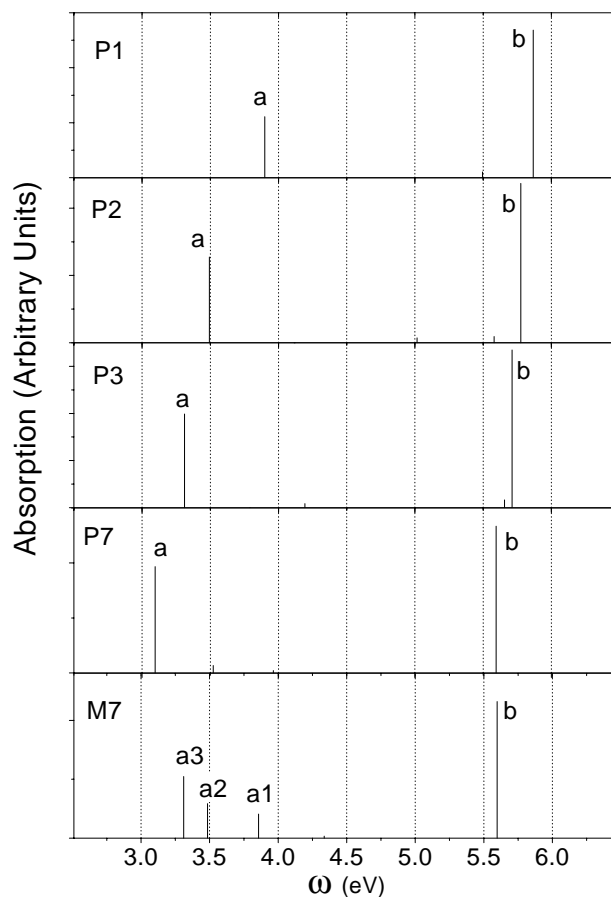


Figure 7.5: Calculated linear absorption (oscillator strengths  $f_\nu$  vs. transition frequencies  $\Omega_\nu$ ) of the molecules shown in Fig. 7.4. Mode frequencies of P1 ( $\Omega_a = 3.90$  eV,  $\Omega_b = 5.87$  eV); P2 ( $\Omega_a = 3.49$  eV,  $\Omega_b = 5.78$  eV); P3 ( $\Omega_a = 3.31$  eV,  $\Omega_b = 5.71$  eV); P7 ( $\Omega_a = 3.11$  eV,  $\Omega_b = 5.60$  eV); M7 ( $\Omega_{a1} = 3.86$  eV,  $\Omega_{a2} = 3.48$  eV,  $\Omega_{a3} = 3.31$  eV,  $\Omega_b = 5.60$  eV).

and the dynamics of charges induced by optical excitation, the collective modes corresponding to these electronic excitations were examined (see Section 2.5 in Chapter 2). Contour plots of the ground state density matrices are shown in Fig 7.6. The size of the matrices is equal to the number of carbon atoms in the molecule, labeled according to Fig. 7.4. Panel P1( $\rho$ ) in Fig. 7.6 displays the ground state density matrix  $\bar{\rho}$  of P1. It is dominated by the diagonal and near-diagonal elements, reflecting the bonds between nearest neighbors. The aromatic rings (corners of the matrix) and the acetylenic triple bond at

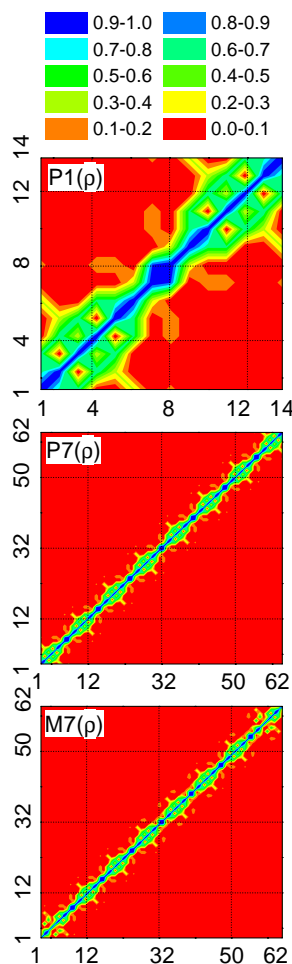


Figure 7.6: Contour plots of the ground state density matrices of oligomers P1, P7, and M7. The axes represent the carbon atoms as labeled in Fig. 7.4. The panels are labeled the molecule (Fig. 7.4) and the electronic mode (Fig. 7.5) (e.g.  $P1(\rho)$  is the ground state density matrix of molecule P1). The aromatic ring units are shown by solid rectangles. The color code is given in the top panel.

the center are clearly visible. Panels  $P7(\rho)$   $M7(\rho)$  in Fig. 7.6 show the ground state density matrices of P7 and M7. The two density matrices are very similar and may be constructed by repeating the P1 density matrix: *para*- and *meta*-conjugation make a very little difference as far as the ground state is concerned. This is, however, not the case for the electronic normal modes  $\xi_\nu$  responsible for optical excitations, displayed in Fig. 7.7. The ordinate and abscissa now represent an electron and a hole, respectively.

The right column displays the high-frequency transition (b) in P-oligomers.

This mode is completely localized on a single repeat unit, and the optically induced coherences (off-diagonal elements) involve only the arene atoms. Its localized nature leads to the similar charge and coherences distributions in M7(b) and P7(b) (and in the high frequency mode in PPV oligomers [104]). This explains the similarity of peak (b) in the absorption spectra of M7 and P7.

The middle column shows the lowest frequency (band edge) mode (a) of the *para*- oligomers. P1(a) centered at the triple bond shows maximum coherences and is delocalized over the entire molecule. Carbons 2, 3, 12, and 13, which are at *meta*- position, have a vanishing electronic coherences with other carbon atoms. This is shown by the 'ring' around the plot with small coherences. Analogous patterns can be seen in mode (a) of longer linear oligomers P2, P3, and P7. The mode saturates with size and is no longer confined by the molecular ends, already in P7. These plots clearly illustrate the two characteristic length scales corresponding to the variation of the density matrix along the 'antidiagonal' and the 'diagonal' directions, respectively. The former reflects the size of electron-hole pair created upon optical excitation, (i.e. the confinements of their relative motion). The latter shows the delocalization size of the pair's center of mass motion and represents energy migration across the molecule. These are the exciton coherence and localization sizes respectively (see Section 2.5 in Chapter 2). The coherence size (where the coherences decrease to 10 % of their maximum values), is 5 repeat units, in agreement with that found in Chapter 5 for PPV oligomers. The boundary *meta*- atoms (2, 3,  $8n+4$ ,  $8n+5$ ) have a vanishing coherences in all P-oligomers.

The left column in Fig. 7.7 displays the electronic modes of M7. Mode (a3) is localized at the P3 linear segment of M7 and is virtually identical to mode (a) of the P3 oligomer. Similarly M7(a2) and M7(a1) resemble P2(a) and P1(a) respectively. Note that a1 is degenerate because M7 has two identical P1

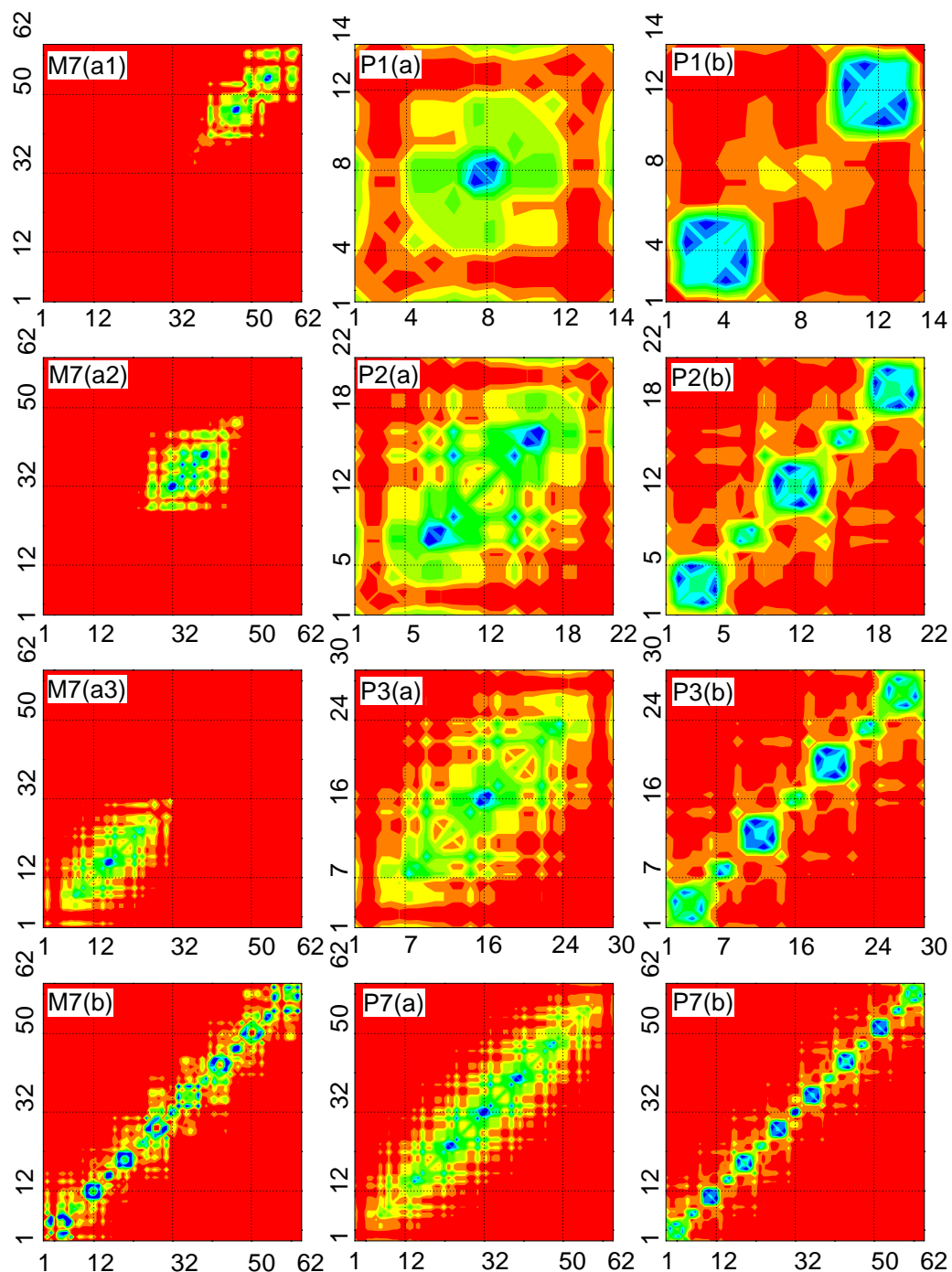


Figure 7.7: Contour plots of the electronic modes which dominate the absorption spectra of the oligomers shown in Fig. 7.4. The axes represent the carbon atoms as labeled in Fig. 7.4. The panels indicate the molecule (Fig. 7.4) and the electronic mode (Fig. 7.5). The linear units in M7 are shown by solid rectangles. The color code is given in Fig. 7.6.

building units. The complete absence of coherence across *meta*- substitution shown in this Figure is remarkable. The optical excitations are clearly confined to the various segments. *Meta*- conjugation makes a clear barrier for excitonic motion whereas *para*- conjugation is transparent to electronic coherences. This difference does not show up in the ground state, which is very similar in both cases (see Fig. (7.6)).

It is well established that *meta*- substituents are much less effective in changing reaction rates compared with their *para*- counterparts [5,6]. This can be understood using resonant structures which show that charges injected into the system by an nucleophilic or an electrophilic substituent are delocalized only at the *ortho*- and *para*- positions. The present study which establishes the same trend for electron-hole pairs created by light provides a direct link between spectroscopy and well-established rules of thumb for chemical reactivity.

## 7.2 Spectra and Energy funneling in Dendrimers

Electronic excitations in molecular aggregates made out of chromophores with nonoverlapping charge distributions may be described as Frenkel excitons [161,162]. In these systems electron exchange is negligible and each chromophore has its own electrons. Frenkel excitons are tightly bound electron-hole pairs that hop coherently or incoherently across the aggregate. At first glance this picture does not apply to dendrimers which have a conjugated electronic structure and their single-electron states (molecular orbitals) are fully delocalized along the entire molecule. However, our analysis shows that while the electron-hole pairs of molecule conjugated at the *para*- position are delocalized, their motions are sharply confined by *meta*- conjugation. Individual molecular orbitals are not partially useful in the interpretation of the spectra which are dominated by the pairs of orbitals. It is the localization of these

pairs as shown in the electronic normal modes that controls the nature of optical excitations. An important and very surprising result of the present study is that the Frenkel exciton picture is not restricted to chromophores with nonoverlapping charge distributions; It can be safely used as long as the electronic modes are spatially separated and the quasiparticles of the system are localized.

The lack of electronic coherence across *meta*-substitutions suggests that the optical excitations of dendrimers can be described by dividing them into weakly-interacting chromophores separated by the *meta*-substitutions. In zero-order the interactions among chromophores can be neglected altogether. The oligomer's optical spectrum is then simply the sum of the spectra of its segments which are separated by *meta*-substitutions. The *meta*-conjugated dendimer behaves as a collection of its linear *para*-conjugated segments which interact with light independently.

To calculate the absorption spectra of dendrimers [3,159,160] family A was modeled as a collection of P1 chromophores. The spectra will thus only show one low frequency peak  $a_1$  whose intensity will increase with growing molecular size. Equation (2.55) with the empirical linewidth  $\Gamma = 0.02 \text{ eV}$  is used to calculate the modeled spectra of dendrimers. The experimental and the modeled spectra of D-4 and D-10 members of family A are displayed in Fig. 7.2. The spectra of other generations of this family are very similar [3].

The absorption spectra of the B family have been calculated by simply adding the spectra of its segments. For example D-58 consist of 3 units of P3, 6 units of P2, and 36 units of P1. We thus multiply the corresponding oscillator strengths  $f_{P3}$ ,  $f_{P2}$ , and  $f_{P1}$  by the number of absorbing units and use Eq. (2.55) to calculate the spectrum. The resulting calculated and experimental spectra of extended dendrimers B are shown in Fig. 7.2. The plots show that this simple procedure can produce the band edge red-shift trend as well as

relative peaks intensities in these macromolecules, in complete agreement with experiment.

The lack of electronic coherence across the *meta*- positions implies that electron (and hole) exchange is blocked, in contrast to the *para*- and *ortho*-positions, which allow a significant charge delocalization. However, Coulomb interactions between segments do allow the transfer of energy through the migration of electron-hole pairs (excitons). This motion may be either coherent or incoherent via the Forster-Dexter mechanism [161,162]. The electrostatic interaction between electronic modes on neighboring segments chemically bonded through the *meta*- positions is estimated to be  $\sim 500 \text{ cm}^{-1}$ . This value is supported by direct calculations of absorption spectra in the compact (family A) dendrimers, which show a weak Davydov-like splitting  $\sim 200 - 600 \text{ cm}^{-1}$  in the band-edge transition. This is typical value for  $J$  aggregates [163], biological antenna complexes [164], and molecular crystals [161,162]. An important consequence of the present study is the ability to break the electronic excitations of dendrimers into several chromophores, despite the delocalized nature of the underlying electronic states. This provides a useful guideline for designing artificial antennae: by adjusting the lengths of the *para*- substituted segments in each generation it should be possible to control the funneling of energy to a desired site. Antennae such as family B have an energy gradient which favors the migration of energy towards the center where a reactive site can be placed.

## Chapter 8

# Charge-Transfer Electronic Excitations in Free-Base ( $H_2P$ ) and Magnesium ( $MgP$ ) Porphins.

Photosynthesis is the process through which the Earth's biosphere harvests the sunlight energy. The primary pigments of photosynthesis are porphyrins [165]. Because of their fundamental and practical importance, these molecules have been the subject of extensive studies [166,167]. Considerable experimental and theoretical effort has been devoted to characterize the electronic structure of porphins (see Fig. 8.1) which are the basic building blocks of porphyrins [168–179]. The excited states of porphins has been observed using UV and photoelectron spectroscopy [170–172]. Their theoretical description was first made using the free-electron model proposed in 1949 [180,181]. The four-orbital model [182,183], and subsequent extensive Pariser-Par-Pople/CI calculations in 1965 reproduced the absorption spectra [168]. Recent semiempirical INDO/CI [169,174,175] and computationally expensive *ab initio* [176,178,179,184] methods were employed to obtain a more accurate calculation of porphin's spectra. However the nature of these optical excitations is still under debate [174,178,179,184].

The linear absorption spectra of porphins (Fig. 8.1 and Tables 8.1 and 8.2)



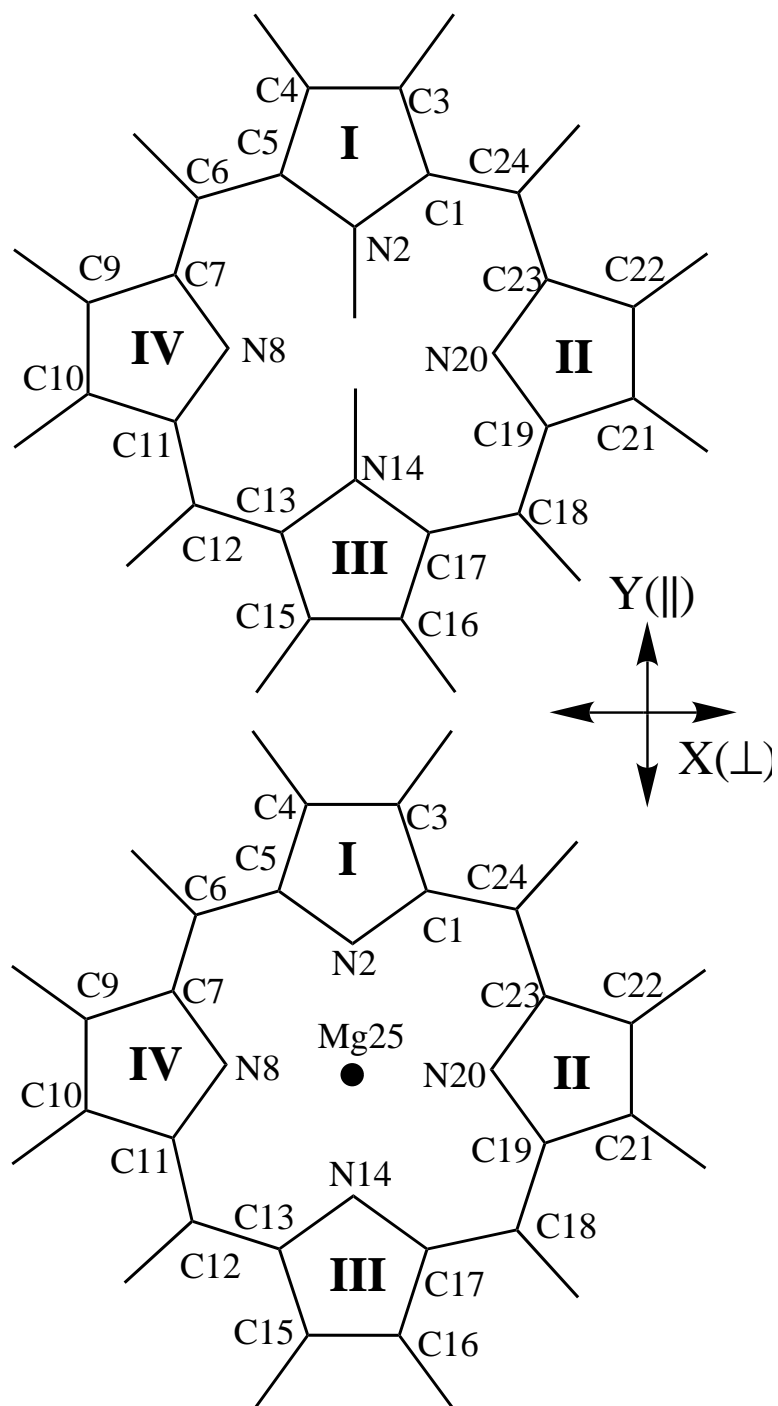


Figure 8.1: Structures and atom labeling of the Free-Base Porphin ( $H_2P$ ) (top) and Magnesium Porphin ( $MgP$ ) (bottom)

can be divided into three distinct spectral regions. The lowest Q band is weak. This transition is degenerate in  $MgP$  and is split into two lines in  $H_2P$  where the  $D_{4h}$  symmetry is broken. The higher frequency very strong Soret (B) band shows up as a sharp peak in both  $MgP$  and  $H_2P$ , whereas the following (N) transition is broad and weak. The proper assignment of these peaks in  $H_2P$  is still controversial [174,178,179]. The traditional interpretation given by Edwards [172] assigns  $B_{\parallel}$  and  $B_{\perp}$  to the two almost degenerate transitions with  $\sim 0.03$  eV splitting at low temperature [170]. The N transition has a different nature, and it cannot be described by the 4 orbital model used for Q and B. The failure of almost all theoretical calculations to predict the weak splitting of the B transitions in  $H_2P$  and the oscillator strength of N requires a different interpretation. The weak splitting in B has been attributed to the vibrational progression in  $B_{\parallel}$ , whereas N has been assigned as  $B_{\perp}$  and its electronic state which is similar to  $B_{\parallel}$ , was described by the 4 orbital model. The weak L and M high frequency transitions are rarely calculated. Theory usually overestimates their oscillator strengths (see Tables 8.1 and 8.2).

In this Chapter the CEO approach is applied for calculating the absorption spectra of Free-Base ( $H_2P$ ) and Magnesium ( $MgP$ ) Porphins. The CEO unambiguously identifies which part of the molecule participates in a given optical excitation, and assess its degree of localization. Our analysis is extended to the high frequency up to 6 eV region, where the origin of the L and M bands is traced. In Section 8.1 the linear absorption spectra of porphins is presented. In Section 8.2 the nature of the relevant electronic modes which dominate the linear absorption is investigated. Finally we discuss the spectroscopic trends and summarize our results in Section 8.3.

## 8.1 The Linear Absorption Spectra.

Optimal ground-state geometries of the free-base and magnesium porphins shown in Fig 8.1, were obtained at the 6-31G\* level using Gaussian-94. *MgP* geometry was optimized with the *Mg* atom moved to 0.4Å out-of-(xy)plane as suggested from the X-ray structure of chlorophyll-a [169,185]. *H<sub>2</sub>P* has *D<sub>2h</sub>* symmetry, whereas *MgP* possesses *D<sub>4h</sub>* symmetry in the xy-plane. The ZINDO code was used first to generate the INDO/S hamiltonian [64–67]. The Hartree-Fock ground-state density matrices [46,47] were calculated next. The CEO/DSMA procedure [70,74] was finally applied to compute the linear absorption spectra and the relevant transition density matrices which constitutes the *electronic normal modes*  $\xi_\nu$ . Transition dipoles are then calculated using the dipole moment operator  $\mu_{mn} = \sum_{mn} \mu_{mn} c_m^+ c_n$

$$\mu_\nu = \text{Tr}(\mu \xi_\nu), \quad (8.1)$$

and the oscillator strengths are given

$$f_\nu = \frac{2}{3} \Omega_\nu \mu_\nu^2. \quad (8.2)$$

Satisfactory convergence of the linear absorption was achieved using 10-15 effective electronic modes. The CEO focuses only on the optically active transitions. All calculated electronic excitations appearing in the absorption spectra of both molecules are of  $\pi - \pi^*$  type.

The calculated linear absorption spectra of free-base porphin are presented and compared with experiment [172] in Table 8.1. The calculated linear spectrum of magnesium porphin and the experimental spectra of magnesium etioporphin (MgEtio) and magnesium tetraphenylporphin (MgTPP) [173] are given in Table 8.2. For comparison, spectra computed with semiempirical (CIS) [174,169] and *ab initio* (SAC-CI, STEOM-CCSD) [184,178,179] methods are presented as well for both molecules. The TDHF coincides with the

Table 8.1: Calculated and experimental excitation energies of the free base porphrin. Energies are in  $eV$ . Oscillator strengths are given in parentheses.

Transition	CEO	RPA <sup>a</sup>	Exp. <sup>b</sup>	CIS <sup>a</sup>	SAC-CI <sup>c</sup>	STEOM-CCSD <sup>d</sup>
$Q_{\parallel}$	1.54 (0.025)	1.46 (0.020)	1.98 (0.01)	1.70 (0.022)	1.75 (0.0001)	1.75 (0.0007)
$Q_{\perp}$	1.98 (0.028)	1.97 (0.033)	2.42 (0.06)	2.06 (0.033)	2.23 (0.0006)	2.40 (0.013)
$B_{\parallel}$	2.966 (1.122)	2.986 (1.146)	3.33 (1.15)	3.37 (1.616)	3.56 (1.03)	3.47 (0.693)
$B_{\perp}$	3.011 (1.272)	3.030 (1.228)		3.52 (2.411)	3.75 (1.73)	3.62 (1.20)
$N_{\parallel}$	4.03 (0.441)	4.00 (0.424)	3.65 (<0.1)	4.09 (1.478)	4.24 (0.976)	4.06 (0.931)
$L1_{\perp}$	4.53 (0.140)	4.41 (0.115)	4.25 ( $\sim$ 0.1)	4.42 (0.366)	4.52 (0.350)	4.35 (0.422)
$L2_{\perp}$	4.95 (0.236)		4.67 ( $\sim$ 0.1)		5.31 (0.280)	5.00 (0.153)
$M_{\parallel}$	5.41 (0.323)		5.50 ( $\sim$ 0.1)		5.45 (0.351)	5.17 (0.272)

<sup>a</sup> Reference [174]<sup>b</sup> Reference [172]<sup>c</sup> Reference [178]<sup>d</sup> Reference [179]

Table 8.2: Calculated excitation energies of the magnesium porphin. Experimental energies are given for Mg etioporphin (MgEtio) and Mg tetraphenylporphin (MgTTP). Energies are in  $eV$ . Oscillator strengths are given in parentheses.

Trans.	CEO	MgEtio Exp. <sup>a</sup>	MgTTP Exp. <sup>a</sup>	CIS <sup>b</sup>	SAC-CI <sup>c</sup>
<i>Q</i>	1.79 (0.058y)	2.14	2.07	2.02 (0.07xy)	2.01 (0.00152)
<i>B</i>	3.09 (1.223y)	3.18	3.04	3.63 (5.13xy)	3.63 (1.99)
<i>TX</i>	3.93 ) (0.037z)			3.93 (0.04z)	
<i>N</i>	4.36 (0.032y)	3.82	3.96	4.28 (0.08xy)	4.15 (0.069)
<i>L</i>	5.14 (0.282y)	4.7	5.16	4.97 (0.95xy)	4.75 (0.00446)
<i>M</i>		5.23	6.20		4.89 (0.590)

<sup>a</sup> Reference [173]

<sup>b</sup> Reference [169]

<sup>c</sup> Reference [184]

Random Phase Approximation (RPA) for the linear optical response of many-electron systems.<sup>1</sup> Zerner and co-workers applied the RPA to calculate the linear absorption of  $H_2P$  up to 4.5  $eV$ . Our low-frequency calculated spectrum is, therefore, very close to that of given in Ref. [174]<sup>2</sup> (see Table 8.1) and supports all conclusions of its authors. The calculations of  $MgP$  at RPA (or TDHF) level has not been reported yet.

<sup>1</sup>See, for example, Chapter 8.5 in Ref. [52]. The electronic modes are identical to the transition densities of the RPA eigenvalue equation.

<sup>2</sup>Our input geometry is different from that of [174]

The CEO underestimates the lowest (Q band) excitation energies compared with experiment and other calculations for both  $H_2P$  and  $MgP$ . However, it predicts well the Q-band experimental splitting [172] (0.44 eV versus 0.447 eV) and the oscillator strengths of  $Q_{\parallel}$  and  $Q_{\perp}$  transitions (0.025 and 0.028 versus 0.01 and 0.06) in  $H_2P$ . The CIS procedure reproduces these values correctly as well (0.355 eV, 0.022 and 0.033) [174] whereas *ab initio* methods failed to predict the oscillator strengths (see Table 8.1). Both the RPA calculations [174] and our CEO results slightly underestimate the excitation energies of the Soret (B) band compare with experiment and *ab initio* calculations, however, they reproduce the correct intensities and B splitting. The electronic-oscillator analysis presented in Sec. 8.2 shows that  $B_{\parallel}$  and  $B_{\perp}$  have the same electronic nature whereas N transitions in both  $MgP$  and  $H_2P$  have the same origin, which is completely different from B. This agrees with recent *ab initio* results of Gwaltney and Bartlett [179] and contradicts the calculations of Nakatsuji *et al.* [178,184] who suggested that the N peaks in  $MgP$  and  $H_2P$  have a completely different nature. The CEO frequencies of the  $N$ ,  $L$  and  $M$  bands are in fair agreement with experiment for both molecules. In addition, the predicted CEO intensities of high frequency (4-6 eV) transitions in  $H_2P$  are much better compared with *ab initio* calculations.

The spectrum of  $MgP$  shows an additional charge transfer peak TX. Its transition dipole lies along the z-axis perpendicular to the molecular plane. This transition is forbidden for planar geometry and its intensity grows fast as the  $Mg$  atom is displaced out of the molecular plane. CIS level calculations performed by Zerner and co-workers [169] show that the TX frequency is extremely sensitive to the Mg position off the molecular plane. Our calculations (not shown) support this observation.

## 8.2 Collective Electronic Excitations.

To explore the nature of the electronic motions underlying the absorption peaks and to establish a direct real-space link between the optical response and the underlying dynamics of charges, relevant electronic modes are examined next (see Section 2.5 in Chapter 2).

Because all the optically allowed transitions in the linear absorption of  $MgP$  and  $H_2P$  are of  $\pi - \pi^*$  type, we focused our analysis on the  $\pi$ -electronic parts of the density matrices. Contour plots of the ground state density matrices are shown in Fig 8.2. The size of the matrices is equal to the number of carbon atoms in the molecule, labeled according to Fig. 8.1. The ground state density matrix  $\bar{\rho}$  of  $H_2P$  (panel  $H_2P(\rho)$  in Fig. 8.2) is dominated by diagonal and near-diagonal elements, reflecting the bonds between nearest neighbors. The blue dots on the diagonal show that the nitrogen atoms 2, 8, 14, and 20 possess an excess electronic charge, this effect is stronger for atoms 2 and 14 which do not possess a lone electronic pair. The ground state density matrix of  $MgP$  (panel  $MgP(\rho)$ ) is somewhat different since all nitrogens have the same electronic charge. The magnesium atom (upper right corner of the panel) lacks electronic density. This is usually represented as  $Mg^{2+}$  ion in the formal structures of this molecule. (For a more detailed Milliken analysis [50,51] see, for example, [169]).

We next turn to the transition density matrices (electronic modes)  $\xi_\nu$ . Like  $\bar{\rho}$ , these are also  $N \times N$  matrices, however, unlike  $\bar{\rho}$ , these matrices are not symmetric. The off-diagonal elements  $(\xi_\nu)_{mn}$  show the amplitude of having an excess a hole at  $n$  and an electron at  $m$ . Hole and electron dynamics is thus shown along the x and y axes, respectively. Panel  $MgP(TX)$  in Fig. 8.2 shows the charge transfer TX mode. The figure shows that the electron is transferred from the porphin ring to the  $Mg(25)$  upon excitation. This transition mostly involves the pyrrole carbon atoms (e.g. 1,3,4,5 in the ring I).

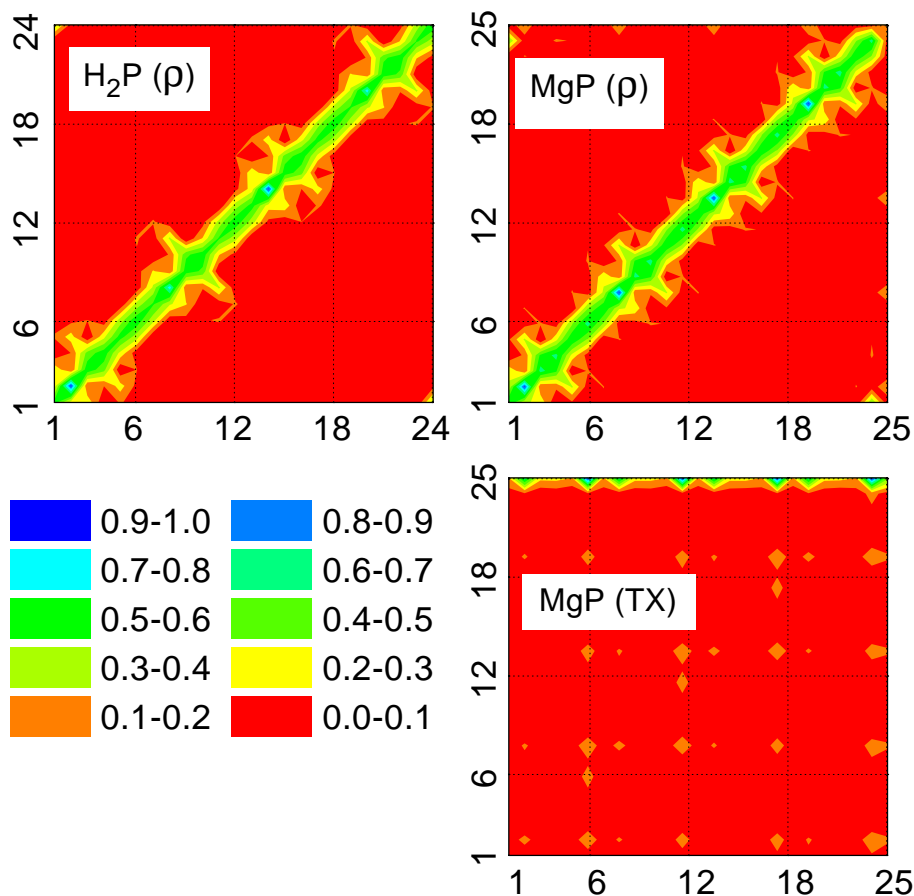


Figure 8.2: Contour plots of the ground state density matrices of Free-Base Porphin ( $H_2P(\rho)$ ), Magnesium Porphin ( $MgP(\rho)$ ), and charge transfer electronic mode TX (panel  $MgP(TX)$ ). The axes represent the carbon atoms as labeled in Fig. 8.1. The ordinate and abscissa label electron and hole respectively. The color code is given in the bottom left panel.

Panel  $H_2P(Q_{\parallel})$  in Fig. 8.3 displays the lowest electronic mode of free base porphyrin. The mode is delocalized over the entire molecule and is dominated by the off-diagonal coherences between neighboring bridge carbons 5-7,11-13,17-19,23-1. The structure of  $Q_{\perp}$  shown in  $H_2P(Q_{\perp})$  is similar to  $Q_{\parallel}$  except that the largest elements are on the diagonal at the bridge carbons. The Q mode of  $MgP$  shares the features of both  $Q_{\parallel}$  and  $Q_{\perp}$  and is dominated by the diagonal as well as near-diagonal elements of the bridge carbons. Note that all Q electronic modes are almost symmetric with respect to the diagonal. This reflects the absence of preferable direction of motion for holes or electrons.



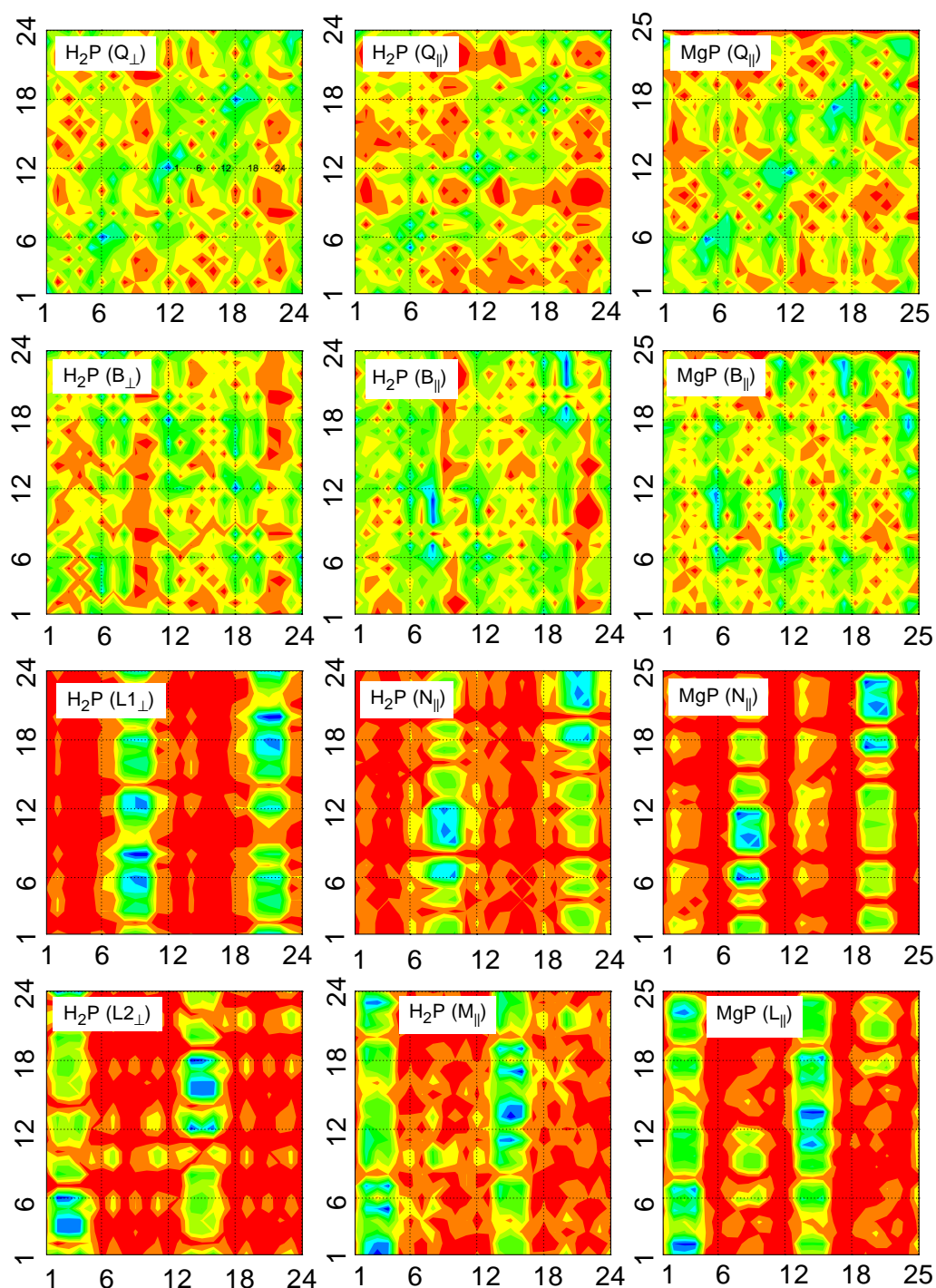


Figure 8.3: Contour plots of the electronic modes which dominate the absorption spectra of Free-Base and Magnesium Porphin shown in Fig. 8.1. The axes represent the carbon atoms as labeled in Fig. 8.1. The ordinate and abscissa label electron and hole respectively. Each panel indicates the molecule (Fig. 8.1) and the electronic mode (Tables 8.1 and 8.2). The color code is given in Fig. 8.2.

This is no longer the case for the Soret transition whose electronic modes are shown in the second row in Fig. 8.3. Here all modes have the same structure: they are delocalized over the entire molecule and stretched along the  $y$  (electron) direction, reflecting the charge-transfer character of the Soret band. In addition, each B-transition is dominated by a specific charge transfer process (blue elements). The preferable process in  $B_{\perp} H_2P$  is electron transfer among bridge carbons:  $6 \rightarrow 12, 12 \rightarrow 18, 18 \rightarrow 24,$  and  $24 \rightarrow 6$ .  $B_{\parallel}$  in  $H_2P$  describes electron transfer from the nitrogens to the neighboring pyrrole carbons in the II and IV rings:  $8 \rightarrow 7, 9, 10, 11$  and  $20 \rightarrow 19, 21, 22, 23$ .  $B_{\parallel}$  in  $MgP$  is dominated by electron transfer from the bridge carbons 6,12,18,24 to other parts of the molecule.

The N-transitions (panels  $H_2P (N_{\parallel})$  and  $MgP (N_{\parallel})$  in Fig. 8.3) in both  $H_2P$  and  $MgP$  are virtually the same and completely different from the low frequency transitions. The modes are localized on the two vertical "strips" and describe electron transfer from the pyrrole rings IV (left strip) and II (right strip) to the entire molecule. Despite the similarity of these electronic modes, the oscillator strength of  $H_2P (N_{\parallel})$  is much larger than that of  $MgP (N_{\parallel})$ . To explain this we display in Fig. 8.4 the diagonal elements of these modes. It is reasonable to assume that they are primarily responsible for the transition dipole. The figure shows that the diagonal elements are the same at the pyrroles II and IV, and differ for I and III. Thus the minor diagonal delocalization of mode  $H_2P (N_{\parallel})$  to pyrroles I and III leads to a considerable contribution to the transition dipole. The dotted line in Fig. 8.4) displays the difference  $\mu_n^{MgP} - \mu_n^{H_2P}$  of atomic contributions to the  $\mu_N$  for these molecules. It clearly shows that the transition dipole of  $H_2P (N_{\parallel})$  is constructive on the I and III and destructive on the II and IV rings. Therefore, the internal hydrogens of  $H_2P$  which make rings I and III 'special' compared to  $MgP$ , provide a 12-fold increase of oscillator strength of N transition. Possible reason for the

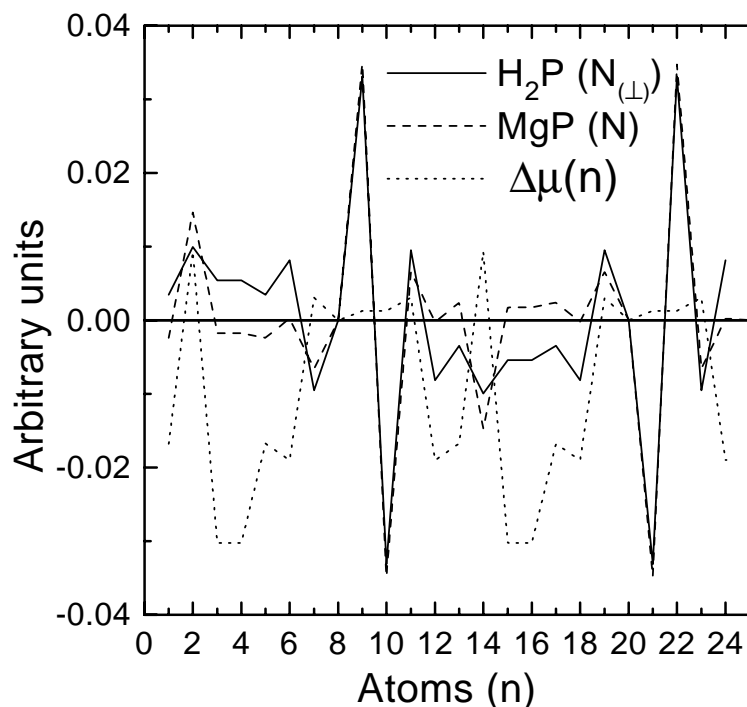


Figure 8.4: Variation of the diagonal elements of modes  $H_2P (N_{\perp})$  (solid line) and  $MgP (N_{\parallel})$  (dashed line). The X axis represents the carbon atoms as labeled in Fig. 8.1. The dotted line represents the difference of atomic contributions to the transition dipole of mode N in molecules  $H_2P$  and  $MgP$ :  $\mu_n^{MgP} - \mu_n^{H_2P}$ ,  $n = 1 \dots 24$ .

overestimated theoretical intensity of N transition in free-base porphin is that molecular vibrations restrict the delocalization of  $H_2P (N_{\parallel})$  to the pyrroles I and III, resulting in a dramatic reduction of the transition dipole.

The higher frequency excitations in porphins have the same charge transfer character similar to the N-transition.  $H_2P (L1_{\perp})$  is virtually the same as  $H_2P (N_{\parallel})$ . It has smaller delocalization to pyrroles I and III and, therefore, a weaker oscillator strength. Modes  $H_2P (L2_{\perp})$ ,  $H_2P (M_{\perp})$ , and  $MgP (L_{\parallel})$  displayed at the bottom row of Fig. 8.3) are similar to the modes shown at the previous (third) row of this figure. However, they describe electron delocalization from pyrroles I and III to the entire molecule with a small participation of II and IV rings which provide the intensities of these transitions.

Since the modes of  $MgP$  are degenerate, we only display the  $\parallel$  modes. The

$\perp$  modes are obtained by simply rotating the  $\parallel$  modes. For example  $MgP$  ( $N_{\perp}$ ) will describe the electron transfer from pyrroles I and III (as opposed to II and IV in  $MgP$  ( $N_{\parallel}$ )).  $MgP$  ( $L_{\perp}$ ) describes electron transfer from pyrroles II and IV (rather than I and III in  $L_{\parallel}$ ). The high frequency modes of free base porphin may be divided into pairs ( $N_{\parallel}$ ,  $L2_{\perp}$ ) and ( $M_{\parallel}$ ,  $L1_{\perp}$ ) similar to the Q and B pairs.

### 8.3 Conclusions.

The absorption spectra of  $H_2P$  and  $MgP$  computed using the CEO method are in good agreement with experiment. Our calculations support the traditional interpretation of these spectra [172]. Coupling to vibrations is not necessary for reproducing the gross features of these spectra. The frequencies and peak intensities in the UV region up to 6 eV are accounted for as well. The computational cost is minimal - seconds<sup>3</sup> compared to days of extensive *ab initio* calculations [179]. In addition the real space electronic modes analysis presented in Section 8.2 reveals the nature of the corresponding optical excitations in a direct and unambiguous way. The low frequency Q bands are delocalized over the entire molecule. The intense Soret (B) transitions are also delocalized but start to show an electronic transfer character. All high-frequency excitations have specific electron transfer nature from the pyrroles to the entire molecule. They are very similar in both  $MgP$  and  $H_2P$ . However, internal hydrogens in the latter break the symmetry and finally lead to 12-fold increase of intensity of the N-band. Our real-space analysis also shows that all high-frequency transitions are degenerate in  $MgP$  and may be divided into pairs similar to the Q and B pairs in  $H_2P$ .

The CEO analysis presented in this paper does not account for Rydberg states of the molecule. They are not predicted because diffuse functions are

---

<sup>3</sup>A single MIPS R10000 175 MHz processor on the SGI Octane workstation has been used.

not included in the INDO/S basis set. It has been suggested that low Rydberg states could participate in photosynthesis [171], and considerable *ab initio* effort has been devoted to address their spectroscopic signatures [176,177,179]. Most *ab initio* calculations find the lowest Rydberg state at  $\sim 1$  eV above the Soret band. The CEO is not limited to INDO/S parameterization and could be combined with any hamiltonian which includes diffuse functions. This should allow to address Rydberg and ionized states.

## Chapter 9

# Linear Electronic Excitations in Stilbenoid Aggregates

The optical response of chromophore aggregates provides an important tool in the studies of intermolecular interactions and bonding. Extensive experimental and theoretical attention has been devoted to studies of clusters in supersonic beams [186–190], J-aggregates of cyanine dyes [24], supramolecular structures [191–193], and biological complexes (photosynthetic antennae and reaction centers) [194,195]. It is possible to treat the aggregates as giant molecules and employ methods of quantum chemistry to calculate their electronic structure. These approaches are limited to small aggregates [196–200]. An important challenging goal is to relate the electronic states and spectra of aggregates to those of their basic building blocks - the monomers. By doing so it should become possible to get a better microscopic insight into the nature of their electronic excitations and to predict qualitative features of complex large systems using simple, readily available information.

The problem is simplified considerably when the chromophores are well separated in space, and their interactions are purely Coulombic (electron exchange is negligible). Each chromophore then retains its own electrons and the system may be described using the Frenkel exciton hamiltonian [161,162]. This allows the perturbative treatment of intermolecular interactions. The

situation is much more complex when electronic states are delocalized among the chromophores. No obvious perturbative theory exists in this case. The calculations of optical excitations are tedious and provide no simple rules of thumb for predicting spectroscopic trends.

The CEO approach can be effectively used to calculate and analyze the electronic spectra of molecular aggregates. The present study is focused on a family of stilbenoid chromophore dimers with well defined geometry synthesized recently [201,202]. In Section 9.1 the electronic modes of the monomers and the paracyclophane unit of these aggregates are analyzed. In Section 9.2 we investigate the linear absorption and relevant electronic modes of the dimers, and link their properties to the corresponding modes of the monomers and to aggregate geometry. Finally we discuss the trends in fluorescence spectra and radiative rates and summarize our results in Section 9.3.

## 9.1 Electronic modes of the monomeric building blocks

The molecules studied in the present article along with their atomic labeling are displayed in the Fig. 9.1. We considered the dimer structures 1a, 1b, 2a, 2b, the monomer units 1c, 2c, as well as [2,2]paracyclophane Pc, which is the central piece of all dimers studied. Ground state geometries were obtained using the crystal X-ray diffraction data given in [202]<sup>1</sup>. The ZINDO code was utilized to generate INDO/S [66,67] hamiltonian and the CEO/DSMA procedure was then applied to compute the linear absorption spectra. In all calculations the empirical linewidth  $\Gamma = 0.2 eV$  was used, and satisfactory convergence of the linear absorption was achieved using 10-15 effective electronic modes.

---

<sup>1</sup>The geometries were experimentally measured for molecules 1a and 1b; The geometries of Pc and 1c were extracted from 1a X-ray data; The geometries of 2a, 2b, and 2c were assembled from 1a and 1b X-ray data by elongating the stilbene units.

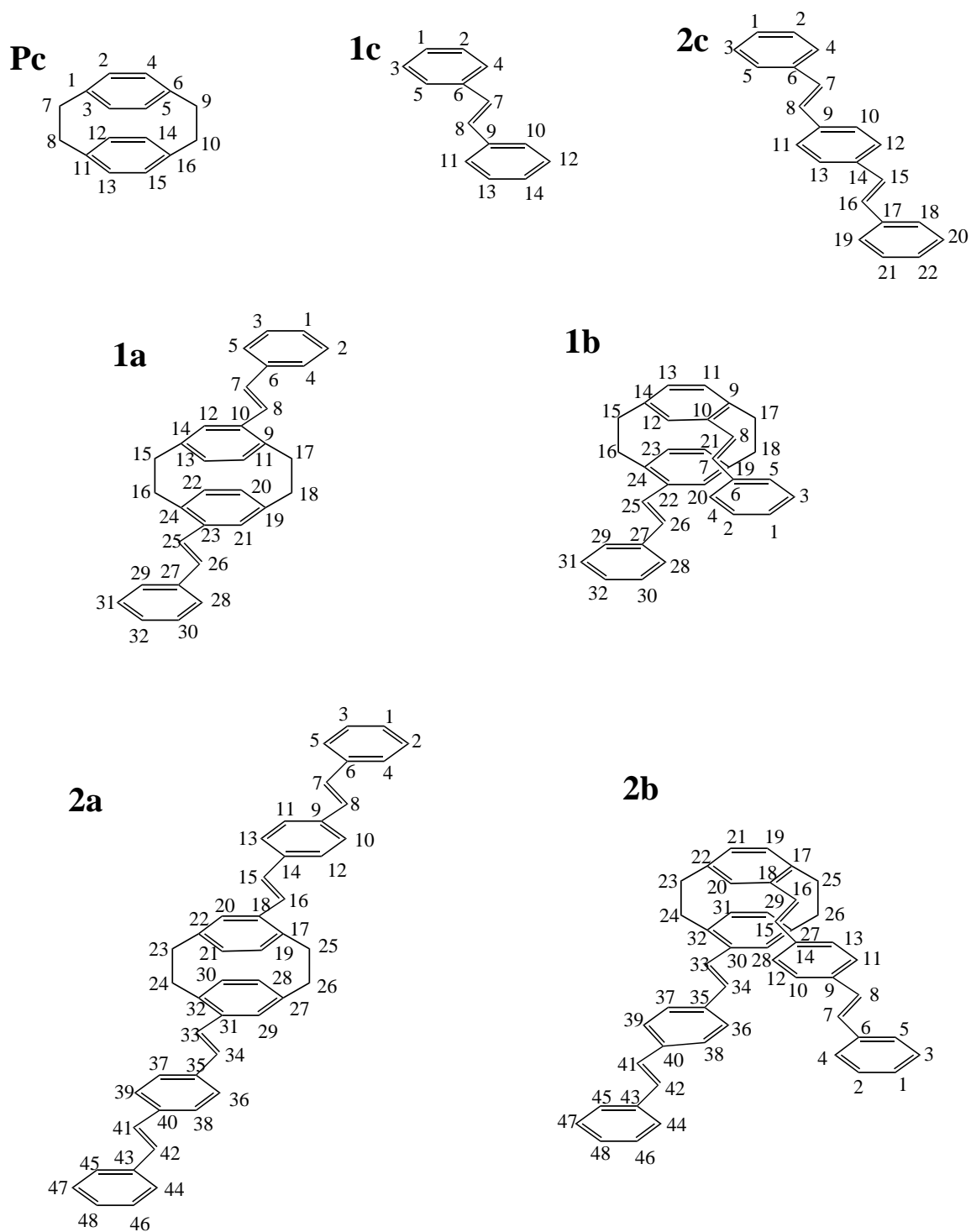


Figure 9.1: Structures and atom labeling of [2,2]paracyclophane (Pc), stilbenoid monomers (1c, 2c) and dimers (1a, 2a, 1b, 2b).



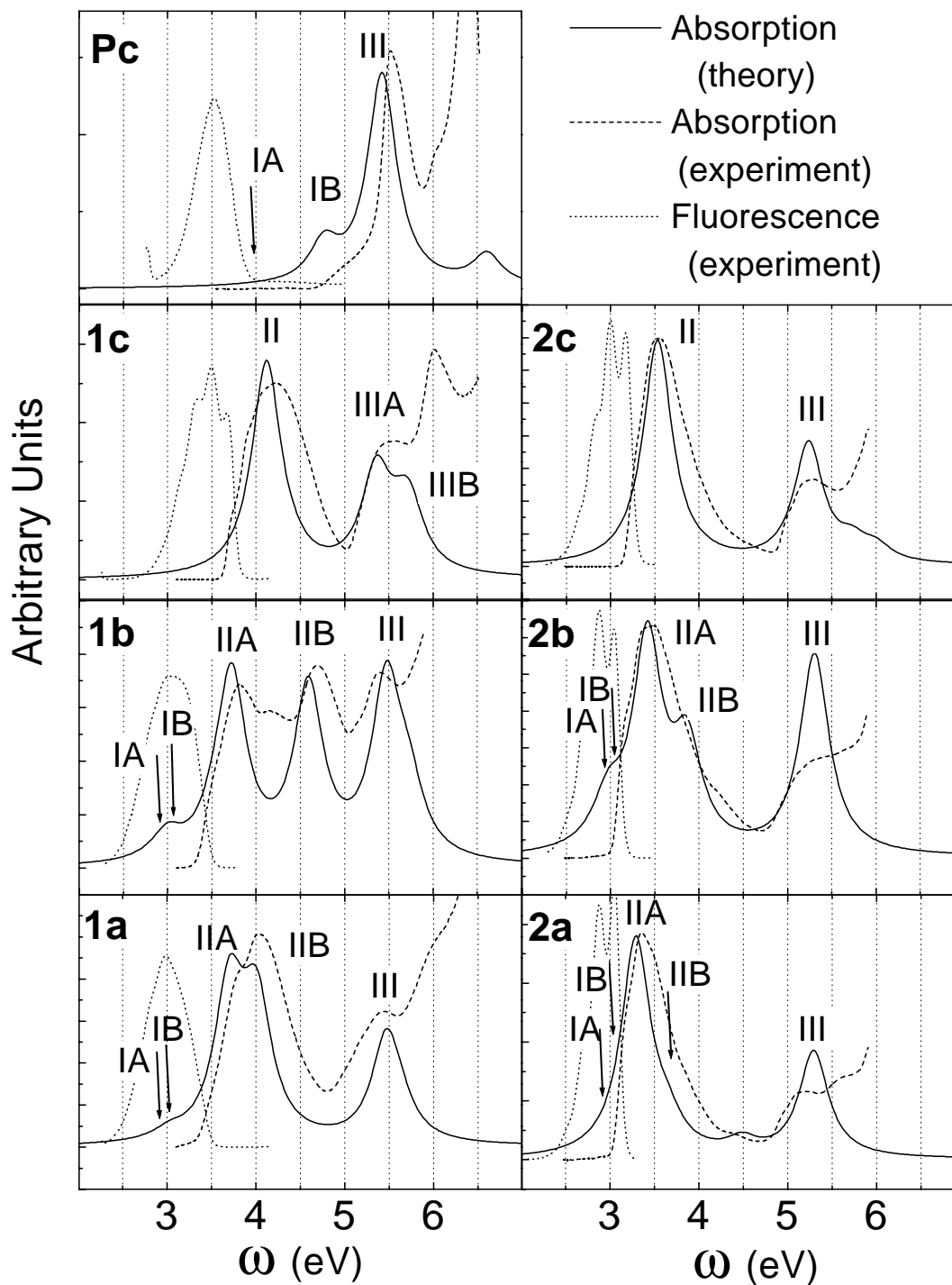


Figure 9.2: Calculated (solid lines) and experimental (dashed lines) absorption spectra and experimental (dotted lines) fluorescence spectra of the molecules presented in Fig. 9.1.

The calculated spectra of the monomers 1c and 2c are displayed in Fig. 9.2 (solid lines). Experimental absorption and fluorescence spectra [201] are shown by dashed and dotted lines respectively. The lowest strong absorption peak of 1c and 2c is denoted as II (The reason of this notation will become clear in the next section where the dimers spectra are considered). No geometry optimization was carried out and no parameters were tuned or rescaled. Nevertheless the theoretical spectra are in excellent agreement with experiment <sup>2</sup>.

To explore the origin of the various peaks the collective modes corresponding to these electronic excitations were examined. The size of the matrix is equal to the number of carbon atoms in the molecule, labeled according to Fig. 9.1; the ordinate and abscissa represent an electron and a hole respectively (see Section 2.5 in Chapter 2).

Panel 1c( $\rho$ ) in Fig. 9.3 displays the ground state density matrix  $\bar{\rho}$  of molecule 1c. The density matrix is dominated by the diagonal and near-diagonal elements, reflecting the bonds between nearest neighbors. The aromatic rings (corners of the matrix) and the vinylic double bond (center of the matrix) are clearly identified. 1c(II) shows the electronic mode of peak II in 1c. This mode is completely delocalized over the entire molecule with the strongest coherences (off-diagonal elements) in the double bond of the vinylic group. The following two modes of stilbene (1c(IIIA) and 1c(IIIB)) are localized on the first and the second arene rings respectively.

The second column in Fig. 9.3 shows the dominant electronic modes of 2c. They have basically the same properties as the corresponding modes of the shorter molecule 1c. The delocalized mode II is significantly red shifted. Our calculations lumped all localized transitions III to a single effective mode localized at the phenyls.

---

<sup>2</sup>In experimental measurements 1c and 2c were substituted at 2, 5 by methyl groups; 2c was substituted at 22 by tert-butyl group; 2a and 2b were substituted at 1, 48 by tert-butyl groups.

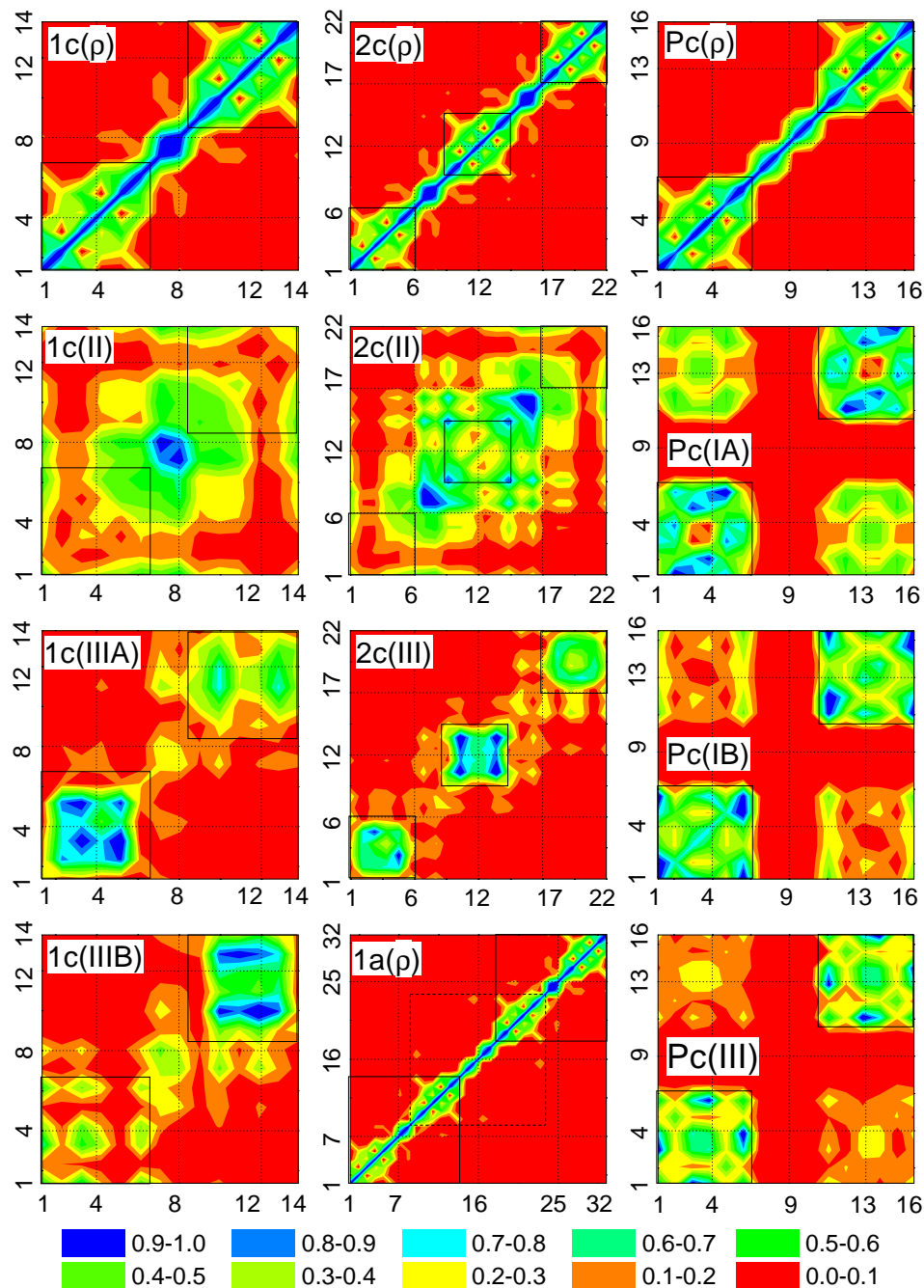


Figure 9.3: Contour plots of ground state density matrices and the electronic modes which dominate the optical absorption of monomers 1c and 2c. The axis labels represent the individual carbon atoms as labeled in Fig. 9.1. The panels indicate the molecule (Fig. 9.1) and the electronic mode (Fig. 9.2) (e.g. 1c( $\rho$ ) is the ground state density matrix of molecule 1c; Pc(III) is mode III of [2,2]paracyclophane Pc). The aromatic ring units are shown by solid rectangles. The color code is given in the bottom row. Mode frequencies of 1c ( $\Omega_{II} = 4.12$  eV,  $\Omega_{IIIA} = 5.36$  eV,  $\Omega_{IIIB} = 5.73$  eV); 2c ( $\Omega_{II} = 3.53$  eV,  $\Omega_{III} = 5.25$  eV); Pc ( $\Omega_{IA} = 3.95$  eV,  $\Omega_{IB} = 4.77$  eV,  $\Omega_{III} = 5.5$  eV)

Before turning to the dimer spectra we shall examine the calculated absorption spectrum of [2,2]paracyclophane (Pc) which in an important common unit of all dimers studied. The electronic properties of Pc has been extensively studied [203,204]. The calculated and experimental spectra of Pc is displayed in the top panel in Fig. 9.2. Three electronic excitations are considered. The lowest transition IA with frequency  $\Omega_{IA} = 3.95 \text{ eV}$  is forbidden in linear absorption <sup>3</sup>. IB is the first peak in absorption ( $\Omega_{IB} = 4.77 \text{ eV}$ ) with a weak dipole along the benzene long axis. Peak III ( $\Omega_{III} = 5.5 \text{ eV}$ ) dominates the absorption. Our calculated frequencies compare well with experiment (4.06 eV, 5.12 eV and 5.42 eV [204]). Pc( $\rho$ ) shown in Fig. 9.3 represents the ground state density matrix  $\bar{\rho}$  of Pc. The aromatic rings at the corners and two bridge shoulders in the center are clearly identified. Pc(IA) shows the lowest electronic modes in Pc. The excitation is localized on the aromatic rings and shows the strong electronic coherence (which is a signature of charge delocalization) between them. Pc(IB) is also delocalized over the entire molecule but with a weaker coherences between aromatic rings than Pc(IA). In contrast, the Pc(III) mode shows very small charge delocalization between arene rings. Modes IA and IB are delocalized and are therefore red-shifted compared to mode III which is localized on the arene rings. Due to its localized nature, mode III has roughly the same structure and transition frequency (5.3-5.4 eV) for all three molecules Pc, 1c, and 2c.

## 9.2 Electronic modes of dimers

Panel 1a( $\rho$ ) in Fig. 9.3 displays the ground state density matrix  $\bar{\rho}$  of 1a. The plot shows that dimerization hardly affects the ground state; The density matrices of the Pc( $\rho$ ) and 1c( $\rho$ ) units can be easily identified in the density

---

<sup>3</sup>Experimentally this transition is weakly vibronically allowed by borrowing intensity from IB [203]. It can be seen by plotting the experimental absorption in logarithmic scale. The fluorescence of Pc originates primarily from IA [203]

matrices of 1a. The ground state density matrices of other dimers (not shown) behave similarly.

We next turn to the optical excitations of the dimers. Panel 1a(I) of Fig. 9.4 shows the lowest frequency electronic mode IA of 1a. This mode is virtually the same as Pc(IA): It is essentially localized on the paracyclophane, has a vanishing oscillator strength, and represents the charge delocalization between monomers. The following mode 1a(II) corresponds to Pc(II) and similarly has a weak oscillator strength. However, the small delocalization to neighboring vinylic groups leads to dramatic red shift in frequency from 3.95 to 2.91 eV for IA and from 4.77 to 3.04 eV for II.

Mode 1a(III) resembles mode III of the monomer 1c (diagonal blocks), but shows some electronic coherences between chromophores (off-diagonal blocks). The structure of 1a(IV) is similar to 1a(III) but it shows a slightly different distribution of coherences and stronger charge delocalization between monomers. The coupling of the monomeric modes 1c(III) leads to a Davydov-like splitting resulting in modes IIIA and IIIB in the dimers [205]. The frequency splitting reflects the interaction strength between monomers. The high frequency mode 1a(V) is localized mostly on the aromatic rings at the edge, and weakly penetrates to the central Pc unit, with a small trace of optical coherences between the monomers. This mode shows about the same localization properties as 1c(III). We thus conclude that the electronic excitations of the dimer 1a can be constructed from the excitations of its Pc and 1c units, perturbed by interaction between monomers.

Electronic modes of different dimers are compared next in order to investigate how geometry and monomer-size affect charge delocalization. The second column in Fig. 9.4 shows the electronic modes of 1b (for atom labeling see Fig. 9.2). The dominant optical excitations of the larger dimers 2a and 2b are displayed in the third and fourth columns.

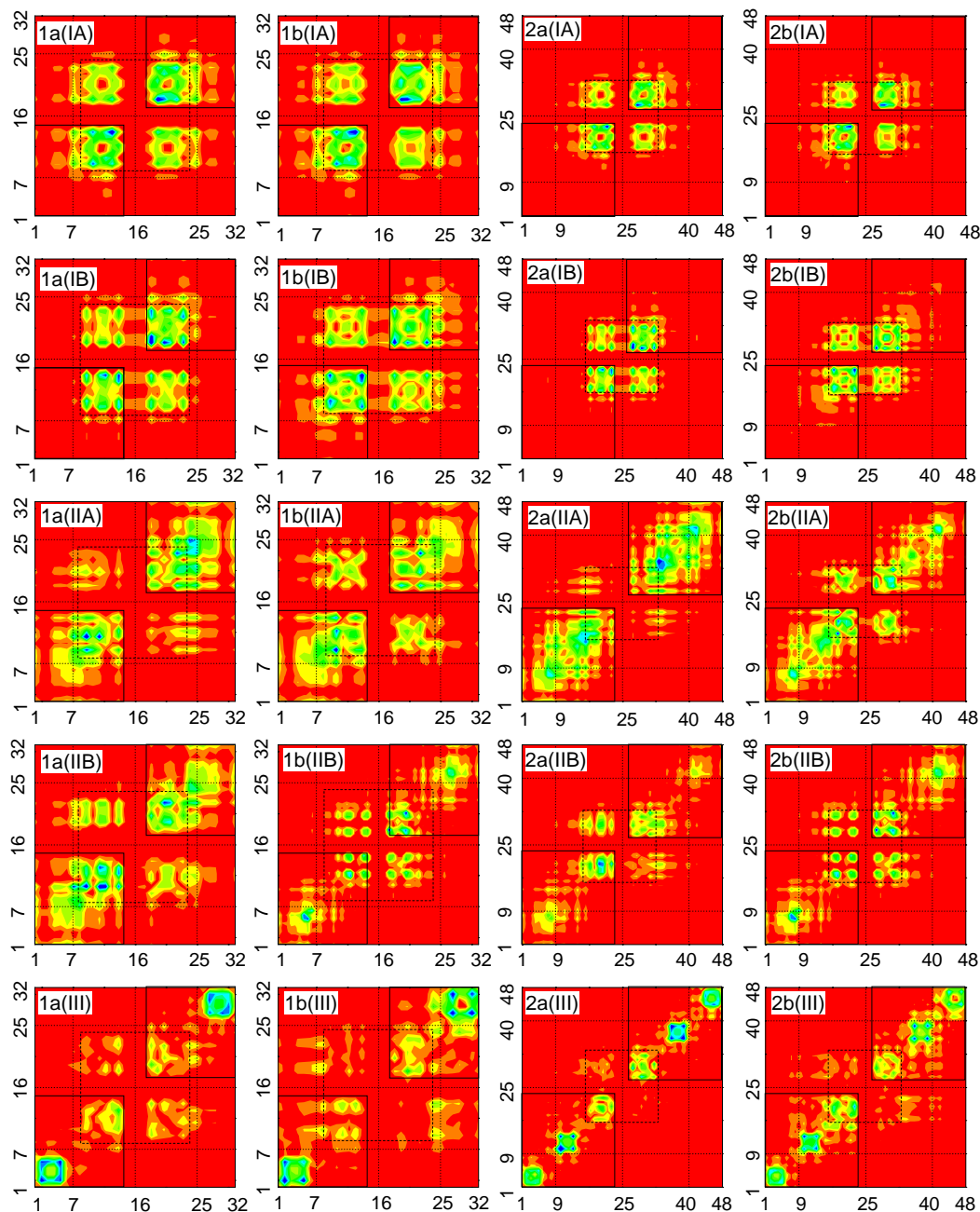


Figure 9.4: Contour plots of electronic modes which dominate the absorption dimers. The axis labels represent the individual carbon atoms as labeled in Fig. 9.1. The panels indicate the molecule (Fig. 9.1) and the electronic mode (Fig. 9.2). The monomers 1c and 2c units are shown by solid rectangles. The paracyclophane Pc unit is shown by dashed rectangle. The color code is given in Fig. 9.3. Mode frequencies of 1a ( $\Omega_{IA} = 2.91$  eV,  $\Omega_{IB} = 3.03$  eV,  $\Omega_{IIA} = 3.69$  eV,  $\Omega_{IIB} = 4.02$  eV,  $\Omega_{III} = 5.46$  eV); 1b ( $\Omega_{IA} = 2.92$  eV,  $\Omega_{IB} = 3.01$  eV,  $\Omega_{IIA} = 3.72$  eV,  $\Omega_{IIB} = 4.59$  eV,  $\Omega_{III} = 5.47$  eV); 2a ( $\Omega_{IA} = 2.91$  eV,  $\Omega_{IB} = 3.03$  eV,  $\Omega_{IIA} = 3.29$  eV,  $\Omega_{IIB} = 3.61$  eV,  $\Omega_{III} = 5.29$  eV); 2b ( $\Omega_{IA} = 2.92$  eV,  $\Omega_{IB} = 3.01$  eV,  $\Omega_{IIA} = 3.41$  eV,  $\Omega_{IIB} = 3.86$  eV,  $\Omega_{III} = 5.30$  eV)

The lowest-frequency modes IA and IB and the high frequency mode III are localized and hardly change upon dimerization. Modes IA with frequency 2.9 eV and mode IB with frequency 3 eV originating from Pc(IA) and Pc(IB) respectively are virtually the same for all four dimers. Mode III which can be attributed to 1c(III) and 2c(III) is localized on the arene rings and shows a weak charge delocalization between monomers for all four molecules. However, it has a quite different diagonal distribution of optical coherences for short (1a, 1b) and long (2a, 2b) dimers. The localized nature of mode III explains the invariance of its transition frequency (5.3-5.5 eV).

The bulk (delocalized) mode II appearing in the spectra as peaks IIA and IIB changes significantly upon dimerization and shows charge delocalization which depends on the molecule. Comparison of IIA and IIB leads to the following observations: (i) charge delocalization is much stronger for molecules with *ortho*- (1b and 2b) than with *para*- (1a and 2a) orientation because the vinylic groups where the monomer bulk mode II is concentrated in b are geometrically closer with separation of about 4 Å, and strongly interact with each other; (ii) charge delocalization is stronger for the shorter molecules (1a and 1b) compared with 2a and 2b because in the former the electron - hole pair 'spends more time' on the Pc unit which promotes charge delocalization; (iii) The stronger the charge delocalization between monomers, the less IIA and IIB resemble the original 1c(II) and 2c(II) modes. The splitting depends on the optical coherences between monomers in the mode. For example 1b exhibits the strongest coherences in mode II and shows the largest splitting  $\sim 0.9$  eV between IIA and IIB peaks. 2a has the weakest coherences in mode II, showing a much smaller splitting  $\sim 0.3$  eV. IIA is much stronger in absorption compared to IIB, which leads to a single peak spectrum of type II.

### 9.3 Emission Spectra and Radiative Decay Rates

In the present study the emission spectra were not calculated explicitly. Nevertheless, our computed electronic modes may be used to analyze the qualitative trends of the experimental fluorescence spectra displayed in Fig. 9.2 (dotted curves). Fluorescence spectra of the monomers, 1c and 2c, both show distinct vibronic structure and have the similar Stokes shifts of 0.7 eV and 0.5 eV respectively (defined as the shift between the strongest peaks in absorption and emission). The fluorescence spectra of dimers 2a and 2b have virtually identical shapes to the monomer (2c) and show Stokes shifts 0.4 eV, 0.5 eV, and 0.5 eV, respectively. The spectra of dimers, 1a and 1b, are markedly different: They are broad and featureless, show no vibronic structures, and their shapes resemble the fluorescence of Pc. The Stokes shifts of 1a and 1b are large compared to 1c (0.8 eV, 0.9 eV, and 0.7 eV, respectively). These observations can be explained by assuming that in the short dimers 1a and 1b the optically excited IIA state relaxes to the lower lying IA and IB states. The fluorescence originates from the states IA and IB which are red-shifted by 0.93 eV and 0.8 eV with respect to IIA. The large Stokes shift is thus electronic in origin.

In contrast, in longer dimers 2a and 2b, the state IIA is significantly red-shifted since it is delocalized, whereas the states IA and IB do not shift. Consequently the separation between II and IA(IB) in long dimers is only about 0.33 eV (0.2 eV). In fact, the states IA and IB lay within the linewidth of optically active transition IIA. Consequently, the relaxation of population to states IA and IB upon excitation of state IIA is less important and the emission originates primarily from the initially excited state.

This picture is supported by a close examination of the radiative decay rate



$\gamma_\nu^r$ , calculated using the expression [72]

$$\gamma_\nu^r = \frac{2}{3}f_\nu\Omega_\nu^2. \quad (9.1)$$

Here  $f_\nu$  and  $\Omega_\nu$  are the oscillator strength and the frequency of mode  $\nu$  (see Eq. (2.55)).

Assuming that only the delocalized mode IIA participates in the fluorescence of long molecules, we obtain  $0.7 \text{ ns}^{-1}$  and  $0.67 \text{ ns}^{-1}$  for the monomer (2c) and the dimer (2a) decay rates. These compare well with experimental values of  $0.55 \text{ ns}^{-1}$  and  $0.5 \text{ ns}^{-1}$  [202], respectively. The calculated rate is somewhat larger because molecular vibrations and solvent effects which reduce electronic coherence were not taken into account. The calculated radiative lifetime of stilbene 1c ( $0.52 \text{ ns}^{-1}$ ) is consistent with the experimental value  $0.62\text{-}0.67 \text{ ns}^{-1}$  [206]. The radiative rates of the short dimers behave markedly different. The experimental radiative rate of 1a is significantly slower and the quantum yield is lower than 2a. Assuming that only the localized mode IB participates in fluorescence of the short dimer 1a, we obtained  $0.05 \text{ ns}^{-1}$  for the radiative rate compared with the experimental value of  $0.06 \text{ ns}^{-1}$  [202]. The calculated rate is underestimated because the fluorescence depends also on states IA and II of 1a. Thus the weak oscillator strengths of IA and IB in 1a and 1b and the fast relaxation to these states lead to the strong fluorescence quenching in the short dimers. This is interesting for the design of optical and luminescent materials.

In summary the optical excitations of a family stilbenoid dimers have been calculated and analyzed using a two-dimensional representation of electronic normal modes in real space. These plots reveal an off-diagonal (diagonal) size associated with relative (center of mass) motion of electron - hole pairs created upon optical excitation. The lowest frequency electronic mode is localized on the paracyclophane group of the dimer, makes a small contribution in absorption of all aggregates, but dominates the emission spectra of small dimers 1a and 1b, leading to a large electronic Stokes shift. The two lower energy

electronic modes, localized on the monomeric units, dominate the linear absorption of all aggregates and the fluorescence of long dimers 2a and 2b. Their electronic coherences reflect the charge delocalization between monomers and strongly depend on the relative chromophore orientation. Our calculations account for all observed trends in absorption spectra, fluorescence Stokes shift, and radiative lifetimes, and establish a rigorous connection between the optical response of aggregates and the properties of the monomers.

## Chapter 10

# Scaling and Saturation of Second Order Off-Resonant Polarizabilities in Donor/Acceptor Polyenes.

Polyenic oligomers are of particular interest as model systems of one-dimensional conjugated chromophores [207]. These molecules possess large optical polarizabilities due to delocalized  $\pi$ -electron excitations [25,11,10,1]. Adding an electron-withdrawing and an electron-donating group enhances the optical response even further [10,12,9,8,13,208–210]. The mechanisms leading to dramatic changes in optical polarizabilities with increasing chain length and donor/acceptor strength and the limiting factors of these enhancements are still not fully understood. Exploring the interplay between these two factors is a key for a rational design strategy of molecules possessing large optical polarizabilities [211]. Experimental investigations are complicated by sample-quality, controlled synthesis and poor solubility of large molecules. On the theoretical side, different approaches are used for small molecules and bulk materials, making it hard to investigate the intermediate crossover regime.

The variation of off-resonant optical polarizabilities with molecular size may be described by the scaling law  $\sim n^b$ ,  $n$  being the number of repeat units. In odd order responses ( $\alpha, \gamma$ ) the scaling exponents  $b$  vary considerably

for short molecules:  $1 < b_\alpha < 2$  and  $2 < b_\gamma < 8$  depending on the system and model [11,28,29,118,98]. For elongated chains we expect the polarizability per repeat-unit  $\alpha/n$  and  $\gamma/n$  to saturate and become size independent; The exponents  $b$  should thus attain the value 1, indicating that the polarizabilities become extensive properties. The saturation of  $\gamma/n$  was first predicted by Flytzanis and co-workers [118]. Recent theoretical studies indicate that it sets in at about 30-50 repeat units. A saturation length of  $\sim 200$  was observed experimentally in one case [111].

Donor/acceptor substituted molecules possess even-order nonlinear polarizabilities. A comprehensive review of the current status of second order polarizability studies was given in [10]. Optical polarizabilities can be calculated using a perturbative expansion involving a summation over all molecular states. By restricting the summation to a single excited state and assuming that the charge-transfer transition is unidirectional, we obtain the two-level expression commonly used to estimate the second order polarizability

$$\beta \propto (\mu_{ee} - \mu_{gg}) \frac{\mu_{ge}^2}{E_{ge}^2}, \quad (10.1)$$

where  $\mu_{gg}$  and  $\mu_{ee}$  are the ground and excited state dipole moments,  $\mu_{ge}$  is the transition dipole, and  $E_{ge}$  is the transition frequency. It is not clear from Eq. (10.1) how should  $\beta$  scale with molecular size. Existing experimental and theoretical studies have not established the precise scaling law of  $\beta$  and its the crossover to the bulk. Experimental studies restricted by synthetic considerations to chain length of 11 repeat units show  $1.4 < b_\beta < 3.2$  [10,12,9,8,13] whereas calculations performed with up to 22 repeat units yield  $1.5 < b_\beta < 2$  [10,212]. Semiempirical calculations made by Morley suggest that for polyenes  $b_\beta = 1$  [208,209] whereas for polyarenes  $b_\beta = 0$  [210]. Using ( $\beta/\text{molecular volume}$ ) as the figure of merit of different materials, he predicted that the optimal values in polyenic and polyarenic chromophores should be about 20 and 3 repeat units respectively [208–210].

In this Chapter the CEO technique [74,104] is used to explore the variation of  $\beta$  over a broad size range, all the way to the bulk. Our calculations show that in marked contrast to  $\alpha$  and  $\gamma$ ,  $\beta$  itself (and not  $\beta/n$ ) saturates for large sizes. A real-space theoretical analysis readily account for this behavior, pinpoint the origin of  $\beta$ , and provide useful guideline for the synthesis of molecules with desirable nonlinear optical properties. Although the calculations presented here are for polyene bridges, this approach can be readily applied to a broad range of optical materials.

## 10.1 Real-space Two-Dimensional analysis of Substitution Effects

The optimal ground-state geometries of the donor/acceptor substituted polyenes shown in Fig. 10.1 were calculated at the AM1 level using Gaussian-94<sup>1</sup>. The ZINDO code was then used to generate the INDO/S hamiltonian [64–67] and calculate Hartree-Fock ground-state density matrices  $\bar{\rho}_{ij}$ .

The effect of donor/acceptor substitutions on the chemical bonding pattern and charge distributions in the ground state can be visualized using contour plots of the density matrices in real-space [104,70]. Absolute values of the reduced single-electron ground-state density matrices elements  $|\bar{\rho}_{ij}|$  of donor/acceptor substituted molecule DA(15) (n=15 is the number of double bonds) are shown in Fig. 10.2A. The axes represent carbon atoms of the bridge labeled 1-30 (In Figures 10.2 and 10.3 the donor end is labeled 1 and the acceptor end is  $2n$ ). The density matrix is dominated by the diagonal and near-diagonal elements, reflecting the bonds between nearest neighbor atoms. The double bonds are clearly identified.

To show the effect of substitution on the ground state we consider the difference matrix  $\Delta\bar{\rho} \equiv |\bar{\rho}_{DA} - \bar{\rho}_N|$  between the density matrices of the substi-

---

<sup>1</sup>During geometry optimization in long molecules, the geometry of the polyenic chain was constrained to be planar.

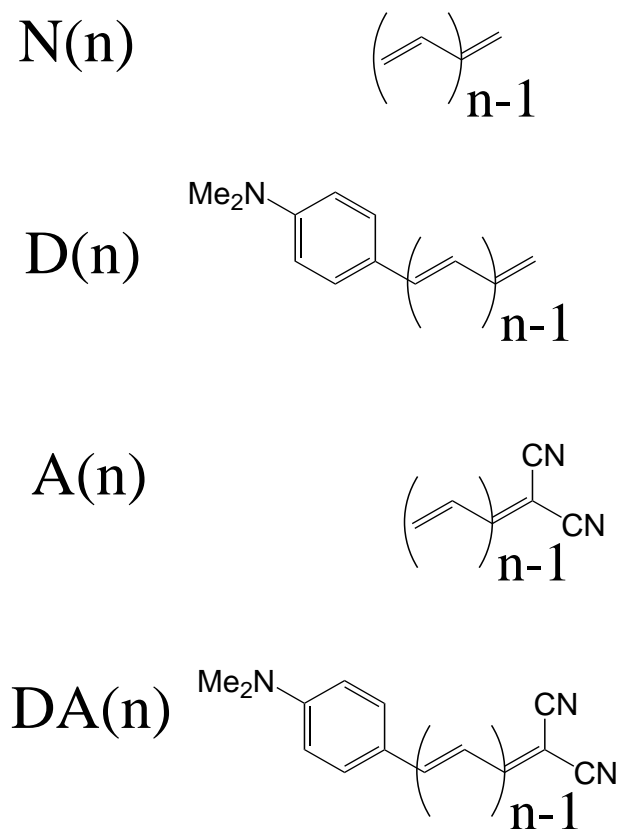


Figure 10.1: Structures of the neutral  $N(n)$ , Donor  $D(n)$ , Acceptor  $A(n)$ , and Donor/Acceptor  $DA(n)$  substituted molecules. Calculations were performed for bridges with  $n = 5, 10, 15, 20, 30, 40$  double bonds.

tuted ( $\bar{\rho}_{DA}$ ) and neutral (unsubstituted) ( $\bar{\rho}_N$ ) molecules for various molecular sizes (see Fig. 10.1). The difference matrices for molecules with  $n=9, 15$  and  $30$  are displayed in Fig. 10.3 A, B, and C respectively. These plots only show the polyenic bridge; The donor and the acceptor regions has been removed. For clarity  $\Delta\rho$  was magnified as indicated in each panel and used the same color code. The plots show that for large sizes ( $n=30$  and  $15$ ) the donor and acceptor do not communicate directly and their effects are well confined to their respective vicinities; Consequently, the donor and the acceptor contributions to the dipole become additive. This is clearly illustrated in the top panel in Fig. 10.4 which shows that the ground-state dipole moment  $\mu_{gg}$  of the

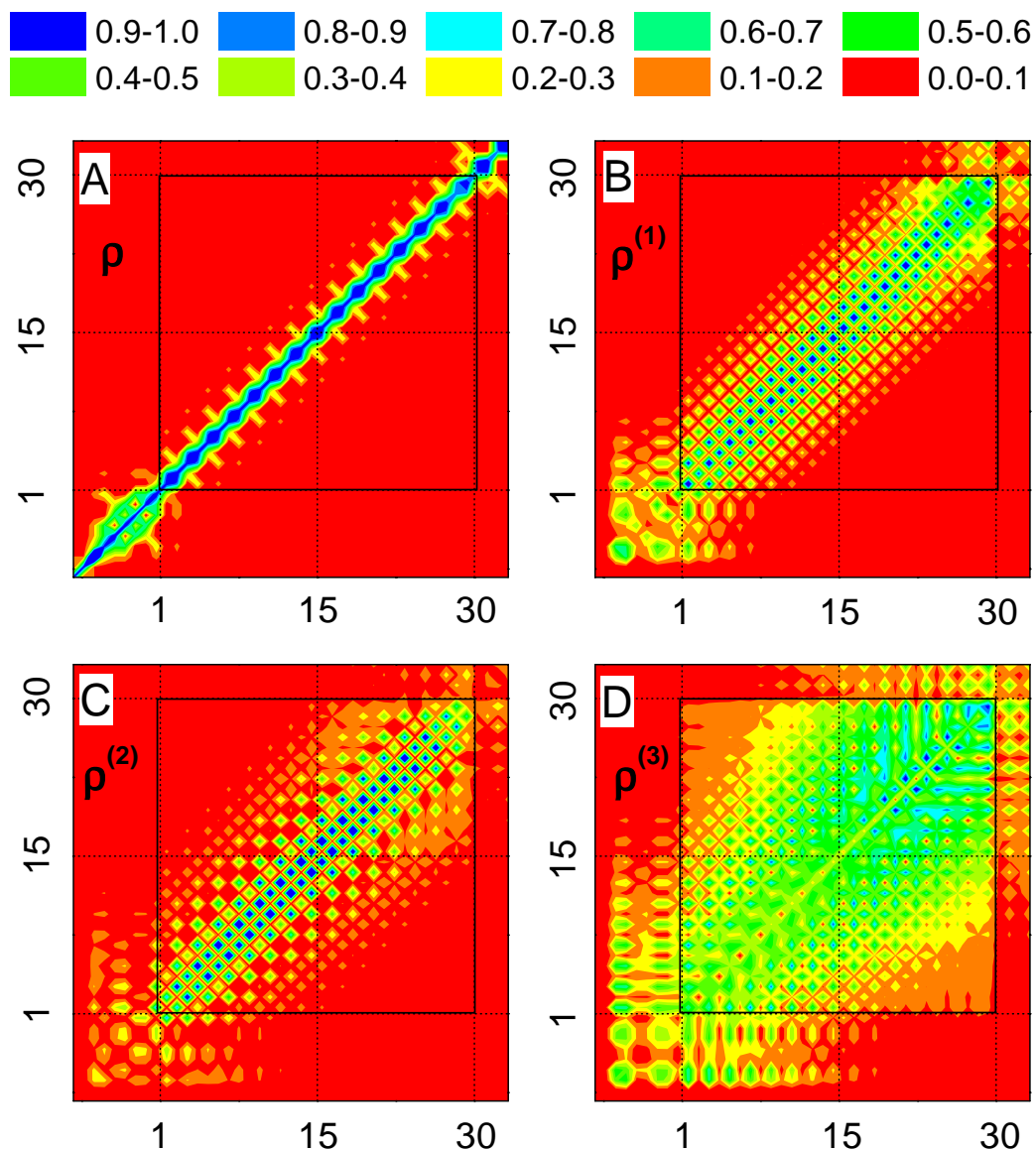


Figure 10.2: Contour plots of the ground state density matrix  $\bar{\rho}$  (A), and the density matrices induced by a static electric field  $\delta\rho^{(1)}$  (B),  $\delta\rho^{(2)}$  (C), and  $\delta\rho^{(3)}$  (D) of molecule DA(15). The part of the density matrix corresponding to the bridge is marked by a rectangle. The axes are labeled by the bridge carbon atoms. Atom 1 (30) correspond to the donor (acceptor) ends.

donor/acceptor molecule is equal to the sum of dipole moments of molecules with donor only (D) and with acceptor only (A) substitutions. For shorter chains (e.g.  $n = 9$  Fig. 10.3A)  $\Delta\bar{\rho}$  is finite all across the chain, indicating a weak coupling of the donor and acceptor. The leveling off the ground-state dipole moments  $\mu_{gg}$  of the donor/acceptor molecules with increasing of chain length (Fig. 10.4A) reflects the absence of long range electronic coherence in large polyenes and is crucial for predicting the scaling of optical properties with size, as will be shown below.

## 10.2 Size-scaling of optical polarizabilities

When the molecule is driven by an external field, its density matrix acquires a time-dependent part  $\rho(t) = \bar{\rho} + \delta\rho(t)$ . In the frequency domain we have [73,104,70]

$$\delta\rho_{ij}(\omega) = \delta\rho_{ij}^{(1)}(\omega) + \delta\rho_{ij}^{(2)}(\omega) + \delta\rho_{ij}^{(3)}(\omega) + \dots \quad (10.2)$$

where  $\delta\rho_{ij}^{(k)}(\omega)$ , the  $k$ 'th order contribution in the incoming optical field, may be calculated by solving the time-dependent Hartree Fock(TDHF) equation of motion using the ground state density matrices as an input [56,70,104]. The  $k$ 'th order polarizability is calculated by taking the expectation value of the dipole operator with respect to  $\delta\rho^{(k)}(\omega)$ .  $\alpha$ ,  $\beta$ , and  $\gamma$  are then calculated using  $\delta\rho^{(1)}$ ,  $\delta\rho^{(2)}$ , and  $\delta\rho^{(3)}$  induced by a static external field.

The resulting size-scaling of the off-resonant polarizabilities  $\alpha/n$ ,  $\beta$  and  $\gamma/n$  is depicted in Fig. 10.4, and the scaling exponents  $b_\alpha$ ,  $b_\beta$  and  $b_\gamma$  are displayed in Fig. 10.5. The behavior of  $b_\alpha$  and  $b_\gamma$  which reach the value 1 at large sizes is consistent with the thermodynamic (bulk) limit.  $b_\beta$ , however is very different and vanishes at large sizes.

To visualize the optical response in real-space and analyze this markedly different behavior of  $\beta$  we examine the induced density matrices  $\delta\rho^{(k)} = \delta\rho^{(k)}(\omega = 0)$  contributing to the optical response. In Fig. 10.2 we display the



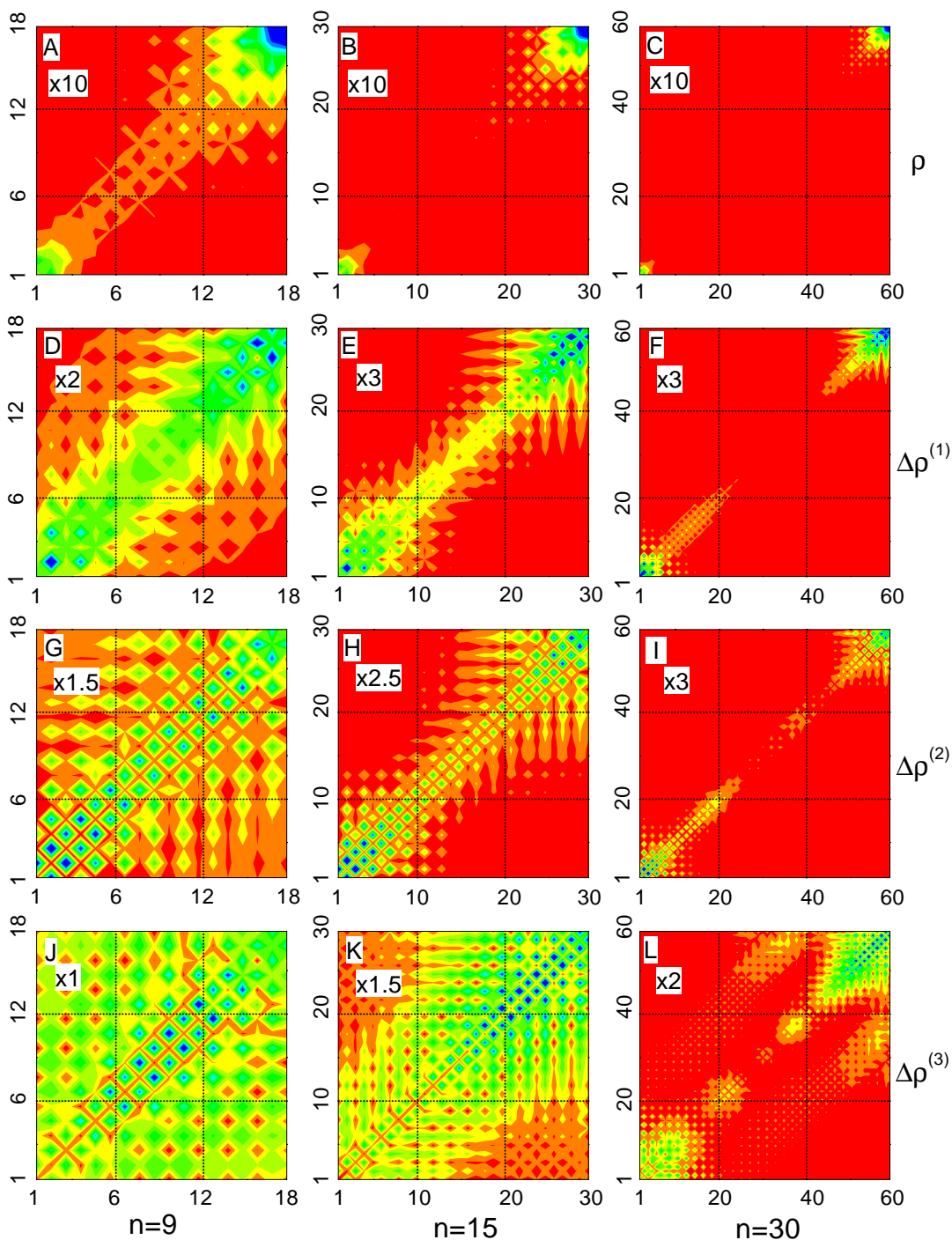


Figure 10.3: Top row: Contour plots of the ground state difference matrices  $\Delta\bar{\rho} = \bar{\rho}_{DA} - \bar{\rho}_N$  for  $n=9$  (A),  $n=15$  (B), and  $n=30$  (C) shown for the bridge part of the matrix. Axes are labeled by the bridge carbon atoms with atom 1 on the donor side and atom  $2n$  on the acceptor side. The second, the third, and the fourth rows display the difference matrices to various orders in the field  $\Delta\rho^{(1)}$ ,  $\Delta\rho^{(2)}$ , and  $\Delta\rho^{(3)}$  respectively.

induced density matrix to first  $\delta\rho^{(1)}$  (B), second  $\delta\rho^{(2)}$  (C) and third  $\delta\rho^{(3)}$  (D) order in the external field. Shown are the absolute magnitudes of these density matrices in the site representation, using the same format of the ground state calculations (Fig. 10.2A). These plots relate the optical properties directly to motions of charges in the system. The diagonal elements  $\delta\rho_{jj}^{(k)}$  reflect induced charges on various atoms whereas the off-diagonal elements  $\delta\rho_{ij}^{(k)}$  show the optically-induced coherences between  $i$ -th and  $j$ -th atomic orbitals. They may be viewed as dynamical bond-orders representing the joint amplitude of finding an electron on atom  $i$  and a hole on atom  $j$ . We note that the coherence size of the induced density matrix (given by its anti-diagonal section) increases as we move from panels B to D, indicating that higher nonlinearities induce a coherence between atoms farther and farther apart.

The effect of substitutions on the optical response can best be visualized by plotting the differences  $\Delta\rho^{(k)} \equiv \delta\rho_{DA}^{(k)} - \delta\rho_N^{(k)}$  between the induced density matrices in the substituted and the neutral molecules. Because the neutral molecule does not possess quadratic polarizability, only the difference  $\Delta\rho^{(2)}$  contributes to  $\beta$ .  $\Delta\rho^{(1)}$ ,  $\Delta\rho^{(2)}$ , and  $\Delta\rho^{(3)}$  are displayed at the second, third, and fourth rows of Fig. 10.3 using the same format of the ground state calculations (top row). The most striking observation from these two-dimensional plots is that the donor/acceptor influence is screened by the  $\pi$  electrons and is confined to a finite section of the bridge with about 15-17 double bonds. For short chains (left column) the donor and acceptor communicate directly since their influence regions overlap spatially and significant electronic coherence develops between them. At large chains ( $n=30$ , right column) their effects are clearly separable. This is the reason why  $\beta$  levels off to a constant with  $b_\beta = 0$ : only the ends of the molecule contribute to  $\beta$  whereas the middle part is identical to that of neutral molecule with vanishing second order polarizability! This scaling is completely different from the behavior of  $\alpha$  and  $\gamma$ ; The entire molecule

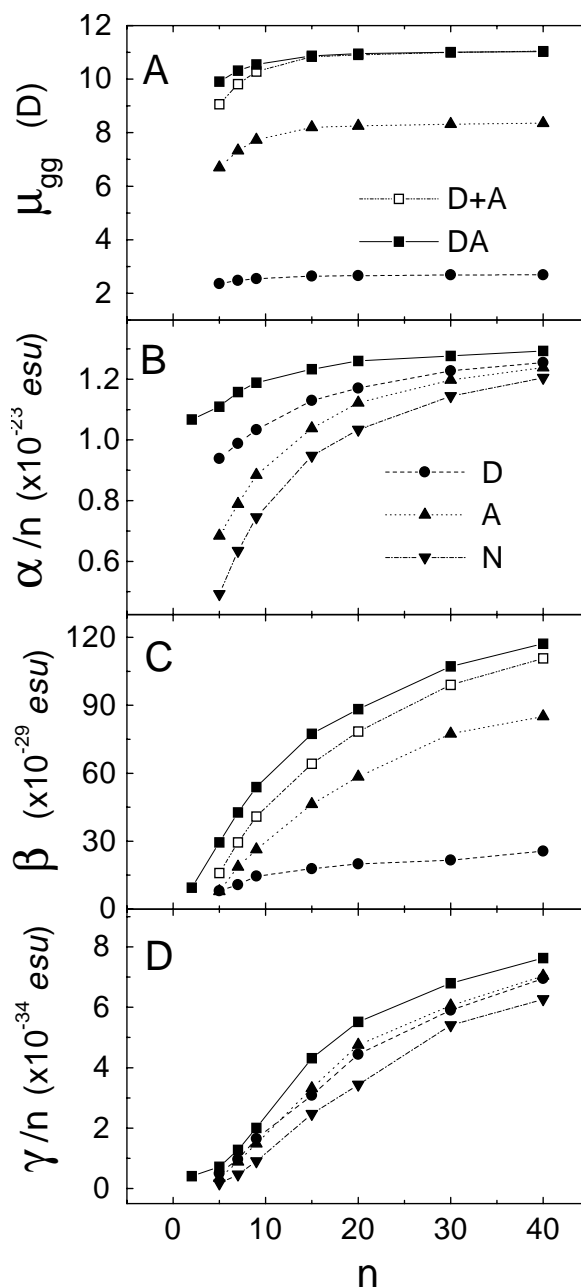


Figure 10.4: Scaling with size and saturation of the ground state dipole moment  $\mu_{gg}$  (A), the first (B), second (C), and third (D) orders off-resonant polarizabilities of the molecules displayed in Fig. 10.1.  $\blacktriangle$  Neutral (no substitutions) N;  $\blacktriangledown$  acceptor substituted (A);  $\bullet$  donor substituted (D);  $\square$  in panels A and C show the sum of molecules (A) and (D). The additivity of  $\mu_{gg}$  and  $\beta$  at large sizes reflects the independent effect of the donor and acceptor. Note the similar saturation behavior of  $\alpha/n$ ,  $\gamma/n$  and  $\beta$ .

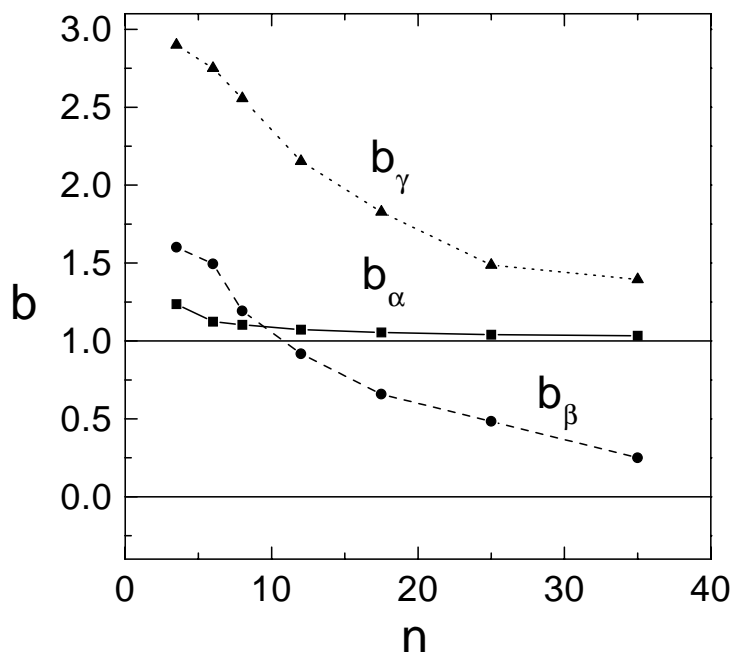


Figure 10.5: Variation of the scaling exponents  $b_\chi \equiv d[\ln \chi]/d[\ln n]$ ,  $\chi = \alpha, \gamma, \delta$  with size for the curves shown in Fig. 10.4. At large sizes  $b_\alpha$  and  $b_\gamma$  tend to 1 whereas  $b_\beta$  approaches 0. These reflect the saturation of  $\alpha/n, \gamma/n$ , and  $\beta$  shown in Fig. 10.4.

contributes to these odd order responses resulting in the fixed polarizability per unit molecular length at large sizes (Fig. 10.4B and D).

We can draw close analogy between size-scaling of the ground state dipole and the second order polarizability by comparing Fig. 10.3 with panels A and C of Fig. 10.4. Only limited coherence regions of the ground state density matrix and the induced density matrices at the molecular ends are affected by the donor and the acceptor. The size of these coherence regions depends on the donor and the acceptor strength. Both the ground state dipole moment and  $\beta$  saturate when the molecular size becomes larger than the size of these regions. For large chains the donor/acceptor contributions to the second order polarizability are additive, as illustrated in Fig. 10.4C:  $\beta$  of the donor/acceptor molecule (DA) becomes equal to the sum of  $\beta$ 's of a molecule with only donor (D) and a molecule with only acceptor (A) substitutions. This additivity is

similar to that displayed earlier for the permanent ground state dipole  $\mu_{gg}$  (Fig. 10.4A).

Unlike the present real-space analysis, the mechanism of saturation of  $\beta$  at large sizes is highly nontrivial when examined using the molecular eigenstates (Eq. (10.1)). Since excited states are delocalized, it can be argued that  $\mu_{ge}^2 \sim n$  at large  $n$  in the two-level model [98,73]. This is necessary to guarantee that the linear scaling of the linear off-resonant polarizability with  $n$ :  $\alpha \sim \frac{f_{ge}}{E_{ge}^2} = \frac{2\mu_{ge}^2}{E_{ge}} \sim n$ , where  $f_{ge}$  is the oscillator strength.  $\mu_{gg}$ ,  $\mu_{ee}$  and  $E_{ge}$  saturate with molecular size [12,9,208,209]. At first glance we thus expect  $\beta \sim n$ . This is however not the case, for the following reason: The difference  $(\mu_{ee} - \mu_{gg})$  originates from charge redistribution upon electronic excitation. Fig. 10.3 clearly shows that charge transfer which affects the permanent dipole only occurs in confined regions at the ends. Since the excited states are delocalized over the entire molecule, the difference  $(\mu_{ee} - \mu_{gg})$  should scale as  $n^{-1}$ , which cancels the  $\sim n$  scaling of  $\mu_{ge}^2$ , resulting in an overall constant  $\beta$ , independent of  $n$ . Another way to state this is that the ground state ( $\mu_{gg}$ ) and the excited state ( $\mu_{ee}$ ) contributions to  $\beta$  both scale as  $n$ , and the saturation of  $\beta$  originates from a delicate cancellation of these two  $\sim n$  terms. It is interesting to note that similar cancellations have been observed in  $\gamma$  as well; Individual contributions which scale as  $n^2$  interfere and almost cancel, resulting in the overall  $\sim n$  scaling [72].

Defining and predicting the saturation size of optical properties has been the main focus of extensive theoretical effort [11,10]. This is a key factor in developing synthetic strategies for novel materials. The interference effects discussed above make it very difficult to predict trends using the molecular eigenstates. In contrast, our two-dimensional plots provide a highly intuitive yet quantitative tool for addressing this longstanding problem: the density matrix shows that the influence of the donor is limited to a few double bonds in its

vicinity, and the same is true for the acceptor. The size of the influence region (along the diagonal and off-diagonal elements) in a large polyene defines the intrinsic coherence size of the system. When the molecular size is larger than the coherence size, the effects of the donor and the acceptor are totally decoupled and additive; both  $\beta$  and  $\mu_{gg}$  then become size-independent. This is reminiscent of the description of quantum confinement in semiconductor nanoparticles [38,139–142]. Our analysis shows that the donor and acceptor are decoupled even in an ideal chain when the purely-electronic response is calculated. Other factors such as vibrations and chain dislocations may contribute further to the decoupling of the donor and the acceptor, and the saturation may show up at shorter sizes.

The picture of electron transfer from donor to acceptor, accompanied by a giant dipole (and  $\beta$ ) is therefore highly misleading in large polyenes. While direct donor-to-acceptor charge transfer does occur at short chains, this is no longer the case for elongated molecules, as is evident from the lack of long-range electronic coherence between the donor and the acceptor.

# Chapter 11

## Electronic-oscillator analysis of femtosecond four-wave mixing in conjugated polyenes.

Resonant time domain nonlinear spectroscopy provides direct information on the creation of carriers and excitons and their subsequent dynamics [213,214,144–146,215–220]. Femtosecond time-resolved absorption spectroscopy revealed the strong coupling between electronic and vibrational states in excited state dynamics of the singlet exciton of polydiacetylene [213,214]. Time-resolved gain and absorption measurements have been performed to study the quantum yield of poly(paraphenylenevinylene) for films, dilute blends and solutions, the defect quenching of luminescence, the formation and decay of excitons [144–146], and the energy relaxation and field-induced exciton dissociation [215–217]. Degenerate four-wave mixing measurements have been performed in perylenes [219]. Recently, the dephasing dynamics of vibronic states in polydiacetylene films has been investigated [220]. These experiments are usually interpreted by simply applying kinetic equations for excited state populations using phenomenological decay rates.

## 11.1 The CEO Representation of Resonant Response

In this Chapter we investigate how ultrafast resonant four-wave mixing (FWM) can be used to provide some alternative, dynamical, signatures of electronic correlations. Our analysis is based on the recently developed coupled electronic oscillator representation of the optical response, obtained by following the dynamics of the reduced single electron density matrix [56]. The equations of motion for the density matrix are expanded in terms of amplitudes of the various electron-hole oscillators. With these equations the optical response is mapped onto a set nonlinear equations; optical nonlinearities are attributed to anharmonicities and scattering of oscillators [56,55,60,74,73,104,70]. The equations of motion derived here hold for the optical response up to the third order in the incoming field. However, extending the present framework to higher order nonlinearities is straightforward.

This technique have been applied to the calculation of a specific resonant time-domain experiment, namely degenerate FWM in the two-pulse self diffraction set-up. We consider the signal generated in the  $2\mathbf{k}_2 - \mathbf{k}_1$  direction, where  $\mathbf{k}_2$  and  $\mathbf{k}_1$  are the incoming wavevectors. We assume resonant excitation of the lowest  $1B_u$  oscillator and identify the oscillators which contribute to this signal. Electronic correlations, which manifest themselves as nonlinear couplings between oscillators, lead to distinct signatures in the FWM signal. Our analysis shows that for the signal considered here, only 2 oscillators have to be considered explicitly, which allows for a very clear and intuitive description of the various nonlinearities [221]. We shall refer to these as the primary oscillators. All other oscillators are excited off-resonance. Their dynamics follows adiabatically the excitation and therefore they can be eliminated from the equations, which results in new anharmonic couplings as well as renormalizations of the existing anharmonicities of the primary oscillators.



To analyze the time-domain signatures of correlations we compare calculations made using the simple Hückel (SSH) model [222], which includes no correlations in the optical response, with the Pariser-Parr-Pople (PPP) model, where Coulomb interactions are included. Some unique signatures of correlations in the ultrafast signals are found: First, due to correlations the shape of the FWM amplitude is changed from a free-induction decay, which has a maximum immediately after the excitation, to one which displays a delayed maximum as function of time. The results are compared with inorganic semiconductor nanostructures, where such effects have been predicted [223–225] and observed [226,227]. Second, the correlations also strongly affect the dynamics of the phase of the FWM signal. The relative phase of the FWM signal with respect to the exciting pulses changes from  $\frac{\pi}{2}$  for the Hückel model to about 0 or  $\pi$ , depending on the signs of the anharmonic coupling coefficients. Third, for the PPP model strong signals for negative delays (pulse  $\mathbf{k}_2$  comes first), which are absent in a simple two-level model are found. Such signals reflect the contributions of a third level which could either be a two-photon  $A_g$  oscillator or a many body effect of two  $B_u$  oscillators [228–230]. Our calculations show, that anharmonicities due to many-particle interactions dominate these signals in conjugated polyenes. This state of affairs is reminiscent of molecular aggregates and was recently analyzed for photosynthetic antenna complexes [231].

### 11.1.1 Equations of motion for electron-hole oscillators

A system of many  $\pi$ -electrons described by the tight-binding PPP Hamiltonian (Section 2.1) [62] is considered with following parameters:  $U_0 = 11.13eV$ ,  $\beta_0 = -2.4eV$ ,  $\beta_1 = -3.5eV\text{\AA}^{-1}$ ,  $\epsilon = 1.5$ ,  $a_0 = 1.2935\text{\AA}$  [55]. For comparison calculations using the Hückel model where the Coulomb interaction is neglected  $U_0 = 0$  were also performed. In this case  $\beta_1 = -5eV\text{\AA}^{-1}$  was used in order to

reproduce the PPP band edge.

The CEO (Chapter 2) maps the calculation of the optical response onto the dynamics of coupled electronic oscillators representing the electron-hole pair components of the reduced single electron density matrix [56]. The particle-hole part of the density matrix can be expanded on terms of these modes  $\xi_\alpha$  (see Eq. (2.46))

$$\xi(t) = \sum_{\alpha>0} (\xi_\alpha z_\alpha(t) + \xi_\alpha^+ z_\alpha^*(t)) \quad . \quad (11.1)$$

Each oscillator  $\alpha$  is described by two operators  $\xi_\alpha$  and  $\xi_\alpha^+$ . Following Ref. [56] we define  $\xi_{-\alpha} = \xi_\alpha^+$ .  $z_\alpha$  and its complex conjugate  $z_{-\alpha} = z_\alpha^*$  will be denoted complex oscillator amplitudes. The oscillator variables, are the eigenmodes of the linear part of Eq. (2.36) and satisfy:

$$L(\xi_\alpha) = \Omega_\alpha \xi_\alpha, \quad L(\xi_{-\alpha}) = -\Omega_\alpha \xi_{-\alpha} \quad . \quad (11.2)$$

They are normalized using the condition (Eq. (2.44)):

$$Tr(\bar{\rho}[\xi_{-\alpha}, \xi_\beta]) = \delta_{\alpha,\beta} \quad . \quad (11.3)$$

Inserting the expansion Eq. (11.1) into Eq. (2.36) gives the following equations of motion for the complex amplitude  $z_\alpha(t)$  of the oscillator variable  $\xi_\alpha$  in the external field  $E(t)$ :

$$\begin{aligned} i \frac{\partial}{\partial t} z_\alpha &= \Omega_\alpha z_\alpha - E \mu_\alpha - E \sum_{\beta} \mu_{\alpha,\beta} z_\beta - E \sum_{\beta\gamma} \mu_{\alpha,\beta\gamma} z_\beta z_\gamma \\ &+ \sum_{\beta\gamma} V_{\alpha,\beta\gamma} z_\beta z_\gamma + \sum_{\beta\gamma\delta} V_{\alpha,\beta\gamma\delta} z_\beta z_\gamma z_\delta \quad , \end{aligned} \quad (11.4)$$

with

$$\begin{aligned} \mu_\alpha &= Tr([\bar{\rho}, \xi_{-\alpha}][\mu, \bar{\rho}]) \\ \mu_{\alpha,\beta} &= Tr([\bar{\rho}, \xi_{-\alpha}][\mu, \xi_\beta]) \\ \mu_{\alpha,\beta\gamma} &= Tr([\bar{\rho}, \xi_{-\alpha}][\mu, \frac{1}{2}[[\xi_\beta, \bar{\rho}], \xi_\gamma]]) \end{aligned} \quad (11.5)$$

$$\begin{aligned}
V_{\alpha,\beta\gamma} &= Tr([\bar{\rho}, \xi_{-\alpha}] [V(\xi_\beta), \xi_\gamma]) + Tr([\bar{\rho}, \xi_{-\alpha}] [V(\frac{1}{2}[[\xi_\beta, \bar{\rho}], \xi_\gamma]), \bar{\rho}]) \\
V_{\alpha,\beta\gamma\delta} &= Tr([\bar{\rho}, \xi_{-\alpha}] [V(\frac{1}{2}[[\xi_\beta, \bar{\rho}], \xi_\gamma]), \xi_\delta]) + Tr([\bar{\rho}, \xi_{-\alpha}] [V(\xi_\beta), \frac{1}{2}[[\xi_\beta, \bar{\rho}], \xi_\gamma]]) \ .
\end{aligned}$$

Eq. (11.4) constitutes the equations of motion for  $z_\alpha$  with  $\alpha > 0$ . The amplitudes for the adjoint (negative frequency) variables are simply the complex conjugates, see Eq. (11.1). The summation indices  $\beta$ ,  $\gamma$ , and  $\delta$  on the right hand side of Eq. (11.4) run over all (positive and negative frequency) oscillator variables.

The first two term in the right hand side of Eq. (11.4) represent a linearly driven harmonic oscillator. The other terms are anharmonicities describing coupling among electronic oscillators. Field-induced and purely material anharmonic coefficients are labeled by  $\mu$  and  $V$ , respectively. Note that the summations on the right hand side include terms where the summation indices are equal ( $\beta = \gamma = \delta$ ) (diagonal anharmonicities). It is important to note that, as is evident from Eq. (11.5), all the anharmonic coefficients can be calculated using the ground state density matrix  $\bar{\rho}$  as well as the eigenmodes  $\xi_\alpha$  of the linearized TDHF equation.

The optical polarization is given by (Eq. (2.34)):

$$P(t) = \sum_{\beta} \tilde{\mu}_{\beta} z_{\beta}(t) + \sum_{\beta\gamma} \tilde{\mu}_{\beta\gamma} z_{\beta}(t) z_{\gamma}(t) \ , \quad (11.6)$$

with

$$\begin{aligned}
\tilde{\mu}_{\beta} &= Tr(\mu \xi_{\beta}) \\
\tilde{\mu}_{\beta\gamma} &= Tr(\mu \frac{1}{2} [[\xi_{\beta}, \bar{\rho}], \xi_{\gamma}]) \ .
\end{aligned} \quad (11.7)$$

Like in Eq. (11.4) also in Eq. (11.6) the summation indices  $\beta$  and  $\gamma$  run over all oscillator variables. Eqs. (11.4) and (11.6) may be used to compute the optical response of our many-electron system. This task has therefore been mapped onto finding the oscillators and the nonlinear couplings  $\mu$  and  $V$ .  $\mu$

describes optical transitions between the oscillators whereas  $V$  describes scattering between oscillators, induced by the many-body Coulomb-interaction.

For a polyacetylene chain with  $N$  carbon atoms and  $N$   $\pi$ -electrons there are  $\frac{N^2}{4}$  particle-hole oscillators. Eq. (11.4) therefore represents the equations of motion for the  $\frac{N^2}{4}$  complex amplitudes of oscillator variables associated with positive frequencies. In Ref. [56] equivalent equations of motion have been given for the coordinate  $Q_\alpha$  and the momentum  $P_\alpha$  of the oscillators. In the analysis of resonant optical nonlinearities it is more convenient to use the complex amplitudes, rather than coordinates and momenta. The expansion of the density matrix in the wave-vectors of the exciting fields, which corresponds to an expansion with respect to the central excitation frequencies, is simpler in this case. The equations used in Ref. [232] contain also particle-particle and hole-hole oscillators to a total number of  $N^2$ . These equations are also equivalent to the present ones, since within the TDHF the additional oscillators carry no information and can be eliminated rigorously [56].

### 11.1.2 Two-oscillator representation of resonant four-wave mixing

In Appendices 11.3 and 11.4 we show how our equations of motion can be applied to compute optical nonlinearities induced by a multiple-pulse excitation. A major advantage of the oscillator representation is that in practical applications it is usually necessary to include only very few oscillators. For off-resonant susceptibilities these are the oscillators that couple most strongly to the ground state density matrix. A tree diagram scheme for identifying the dominant oscillators for the nonlinear response, order by order, has been developed in Ref. [232]. In this Chapter resonant response is considered, and the most natural way to select the relevant oscillators is by including those oscillators whose frequencies are close to various combinations of the incoming

field frequencies. The selectivity is expected to be more pronounced in the resonant case, which enables us to discuss the response using very few parameters (frequencies and anharmonic coefficients) connected to the relevant oscillators.

The exciting field is given by:

$$E(t) = \sum_{j=1,2} \hat{E}_j e^{-((t-\tau_j)/\bar{t}_j)^2} (e^{i\mathbf{k}_j \cdot \mathbf{r} - i\omega_j t} + e^{-i\mathbf{k}_j \cdot \mathbf{r} + i\omega_j t}) \quad . \quad (11.8)$$

Here  $\hat{E}_j$  is the real amplitude,  $\tau_j$  the time delay and  $\omega_j$  the central frequency of pulse  $j$ . In our numerical calculations we have assumed that the central frequencies of both exciting pulses coincide with that of the  $1B_u$  oscillator, which has the largest oscillator strength, i.e.:  $\omega_L = \omega_1 = \omega_2 = \Omega(1B_u) = \Omega_1$ , and a duration of  $\bar{t}_1 = \bar{t}_2 = 20fs$  for the Gaussian pulse envelopes is used. Since the spectral width of even these very short laser pulses (about  $0.1eV$ ) is small compared to the frequency spacing between the oscillators, only a few oscillators will be excited resonantly. Our calculations show that the first and third order response is to very good accuracy dominated by the  $1B_u$  oscillator. In second order there may be one  $A_g$  oscillator which appears as resonantly excited two-photon transition. This will be discussed later using Figs. 11.1 and 11.7.

In Appendix 11.5 we have developed equations which retain only two resonantly excited primary oscillators, the  $1B_u$  and one  $A_g$  oscillator, explicitly. The off-resonant contributions from all other virtual  $A_g$  oscillators in second order, were adiabatically eliminated from the equations of motion, which results in renormalization of anharmonicities and scattering constants. The following equations of motion for the complex amplitudes of the two primary oscillators were obtained.

$$\begin{aligned} i\frac{\partial}{\partial t} z_1 &= (\Omega_1 - \omega_L - i\frac{1}{T_2})z_1 - \mu_1 E - E^2(Y_1 + X_1)z_1 - E^2 X_{-1} z_{-1} \\ &- E\mu_{12} z_2 - E(s_2 + Y_3 + X_3)z_1 z_1 - E(s_1 + Y_2 + X_2)z_{-1} z_1 \\ &+ 2V_{12} z_2 z_{-1} + (V_1 + Y_4 + X_4)z_{-1} z_1 z_1 \end{aligned} \quad (11.9)$$

$$\begin{aligned}
z_{-1} &= z_1^* \\
i\frac{\partial}{\partial t}z_2 &= (\Omega_2 - 2\omega_L - i\frac{1}{T_2'})z_2 - E\mu_{12}z_1 + V_{12}z_1z_1
\end{aligned} \tag{11.10}$$

Here we have added phenomenological dephasing times  $T_2$  and  $T_2'$  for the two-oscillators and  $z_{-1}$  denotes the amplitude of the negative frequency variable  $\xi_{-1}$  of the  $1B_u$  oscillator, see Appendix 11.3. We assume that the relaxation times for the populations, i.e. particle-particle and hole-hole components of the density matrix, are given by  $T_1 = T_2/2$ . We thus do not include pure dephasing processes. To investigate pure dephasing one needs to consider additional dynamic variables [72]; This goes beyond the present treatment. In principle the inclusion of dephasing times for the off-resonant oscillators results in imaginary contributions to the renormalization terms  $X_i, Y_i$ . Since in our case the detuning for the off-resonant terms is very large compared to the dephasing rate, those imaginary parts can be neglected.

All parameters appearing in Eqs. (11.9) and (11.10) have been defined in Eqs. (11.34-11.39). In Appendix 11.5 we also present the equations in more detail, including indices denoting the propagation directions. To obtain the FWM signal we solve Eqs. (11.9) and (11.10) order by order. In first order one has to solve the equation for  $z_1$  keeping just the  $\mu_1 E$  terms on the right hand side. This represents a linearly driven harmonic oscillator with frequency  $\Omega_1$  and transition dipole  $\mu_1$ . The solution of this equation yields  $z_1$  for the propagation directions  $\mathbf{k}_1$  and  $\mathbf{k}_2$ .  $z_{-1}$  is then the complex conjugate of  $z_1$  with the inverse directions  $-\mathbf{k}_1$  and  $-\mathbf{k}_2$  (see Appendices 11.3-11.5). Then we solve the equation for  $z_2$  in second order, keeping inhomogenities representing two-photon resonances, which correspond to the direction  $2\mathbf{k}_2$ . In the equation for  $z_2$  the first term represents an oscillator with frequency  $\Omega_2$ . The other terms are nonlinear sources.  $\mu_{12}$  is a transition dipole coupling the two oscillators and  $V_{12}$  a many-body induced nonlinear coupling. Finally, the first and second order terms are inserted again into the equation for  $z_1$  to calculate the third

order  $\mathbf{k}_S = 2\mathbf{k}_2 - \mathbf{k}_1$  component. The induced polarization in this direction is given by:

$$P_S(t) = e^{-i\omega_L t} \left( \mu_1 z_1 + \sum_{\beta} \mu_{-1\beta} z_{-1} z_{\beta} + \sum_{\beta} \mu_{1\beta} z_1 z_{\beta} \right) . \quad (11.11)$$

As shown in Appendix 11.5 the amplitudes for the virtual  $A_g$  oscillators be evaluated analytically. Inserting these expressions, Eqs. (11.30)-(11.33), into Eq. (11.11) simplifies the expression for the polarization.

$$\begin{aligned} P_S(t) &= e^{-i\omega_L t} (\mu_1 z_1 + \mu_{12} z_{-1} z_2 + (A_1 + B_1) z_{-1} (z_1)^2 \\ &+ (A_2 + B_2) E z_{-1} z_1 + A_3 E (z_1)^2) = e^{-i\omega_L t} |P_S(t)| e^{-i\varphi'(t)}. \end{aligned} \quad (11.12)$$

The anharmonic constants  $A_1$ ,  $A_2$ ,  $A_3$ ,  $B_1$ , and  $B_2$  arise from the elimination of the virtual oscillators, see Eq. (11.40).  $|P_S(t)|$  is the time-resolved amplitude and  $\varphi'(t)$  the slowly varying part of the phase. The total phase of the signal is given by  $\varphi_S(t) = -(\omega_L t + \varphi'(t)) = -\varphi_L(t) - \varphi'(t)$ , where  $\varphi_L(t)$  is exactly the phase of the exciting laser pulses, see Eq. (11.8). We later examine the relative phase of the signal with respect to the exciting pulses [233]

$$\Delta\varphi(t) = \varphi_L(t) - \varphi_S(t) = \varphi'(t) . \quad (11.13)$$

This phase can be measured using heterodyne detection. The time-integrated FWM signal is given by

$$S_{INT}(\tau) = \int |P_S(t)|^2 dt , \quad (11.14)$$

where  $\tau$  is the time delay between the two-pulses.

The interpretation of the various terms in Eq. (11.9), which generate the FWM signal are as follows. First we discuss the terms which only involve the  $1B_u$  oscillator.  $s_1$  is the only nonlinearity which is also present in a simple two level system [234]. It represents the creation of a FWM signal by scattering of the field off a transient grating ( $\mathbf{k}_2 - \mathbf{k}_1$ ). It has its origin in the fact that

electrons are Fermions and is usually referred to as Pauli blocking or phase-space filling nonlinearity [223,224,226].  $s_2$  describes a similar process, where now the field is scattered off a term rotating with twice the transition frequency of the  $1B_u$  oscillator ( $-2\omega_2$ ), instead of a transient grating term ( $\omega_1 - \omega_2$ ), which has no optical rotation frequency, since  $\omega_1 = \omega_2$ .  $V_1$  formally appears as a local-field like nonlinearity [223,72]. It describes self-scattering of the excitation of the  $1B_u$  oscillator induced by the many-particle Coulomb-interaction. Next we discuss the terms resulting from the  $A_g$  oscillator, which is excited resonantly in second order.  $\mu_{12}$  is the transition dipole which couples the  $A_g$  and  $1B_u$  oscillators. It describes the creation of a third order polarization associated with the  $1B_u$  oscillator, created from the excitation of the  $A_g$  oscillator times a field.  $\mu_{12}$  also appears in the definition of the polarization. This term comes from the particle-particle part of the density matrix.  $V_{12}$  describes the many-particle induced coupling between the  $A_g$  and the  $1B_u$  oscillator, which gives rise to nonlinear signals. All other terms ( $X_i$  and  $Y_i$ ) come from the elimination of off-resonant second order contributions.  $X_1, Y_1, X_{-1}$  describe the creation of a FWM signal by scattering of a linear term by two-fields. In the definition of these coefficients it follows that they are determined only by dipole moments between oscillators. All other terms resulting from the elimination process involve many-particle interactions between oscillators, which means that they are zero for the Hückel model. By inspection of the equations of motion one finds that all these terms lead to renormalizations of already existing nonlinear coupling coefficients  $s_1, s_2, V_1$ . Finally, the particle-particle part of the density matrix leads to the quadratic terms in the polarization, Eq. (11.11).

Depending on the time delay, the FWM technique considered here yields information about different anharmonic couplings. For positive delay (pulse  $\mathbf{k}_1$  comes first) this technique is known as photon echo, since in an inhomogeneously broadened system the amplitude of the signal will have an echo-like



envelope [234,235]. As can be analyzed using Eq. (11.36), for a positive delay larger than the pulse duration, when the overlap between the two pulses can be neglected, only few of the inhomogeneities in Eq. (11.9) contribute to the signal. Like in a two-level system, the phase-space filling  $s_1$  and its renormalizations  $Y_2$  and  $X_2$ , only contribute for positive delay [234,235]. Also the small renormalization term  $X_{-1}$  only contributes for positive delay. All of these inhomogeneities explicitly contain pulse  $\mathbf{k}_2$  multiplying a term which is present after both pulses have excited the system, see Eq. (11.36). This only leads to a nonvanishing results, if pulse  $\mathbf{k}_2$  comes after pulse  $\mathbf{k}_1$ . For positive delays also the many-particle induced terms represented by the nonlinear scattering potentials  $V_{12}$  and  $V_1$ , as well as its renormalizations  $Y_4$  and  $X_4$  contribute [223,224]. The sources of these terms do not contain an electric field, but are given by products of complex amplitudes. These amplitudes do not vanish as fast as the exciting pulses, but decay slowly as determined by the dephasing times. Therefore these many-particle terms will contribute to the signal for any time delay [223–225].

For large negative delay the two-photon resonances induce FWM signals even if many-particle interactions are neglected [228–230]. (Note that for a linearly driven harmonic three-level system, i.e. equal energy spacing and dipole moments scaling like  $\sqrt{2}$ , all nonlinear terms cancel identically, and the optical response is purely linear.) This is represented by  $\mu_{12}$  and  $s_2$ , as well as its renormalizations  $Y_3$  and  $X_3$ . These inhomogeneities contain pulse  $\mathbf{k}_1$  multiplying a term which is present after pulse  $\mathbf{k}_2$  has excited the system, see Eq. (11.36). Such terms are nonvanishing only if pulse  $\mathbf{k}_1$  comes after  $\mathbf{k}_2$ . For a small (positive or negative) delay, when the two pulses temporarily overlap, all of the inhomogeneities in Eq. (11.9) contribute. In addition to the ones discussed before, also the small source terms  $Y_1$  and  $X_1$ , may contribute to the signal. Since they contain explicitly both pulse  $\mathbf{k}_1$  and  $\mathbf{k}_2$  they vanish unless

both pulses overlap.

## 11.2 Numerical results

In this section we compare the calculated FWM signals for the Hückel and the PPP models for a 30 carbon atom polyacetylene chain. The signal will be analyzed in terms of the anharmonicities and scattering of the oscillators as described in the previous section. We tabulate all relevant coupling constants and show how many virtual oscillators are needed for calculating the renormalized anharmonicities.

### 11.2.1 The Hückel model

We first discuss the properties of the geometry optimized ground state for the Hückel model [55,236]. The ground state is characterized by a uniform charge density  $\bar{\rho}_{nn} = 0.5$  at each carbon atom. The second quantity, which is closely related to the stabilization mechanism of the ground state, is the bond order defined by

$$p_n = \bar{\rho}_{n,n+1} + \bar{\rho}_{n+1,n} \quad . \quad (11.15)$$

We further introduce the bond order alternation parameter  $p'_n$

$$p'_n = \langle p_n \rangle - (-1)^n p_n \quad (11.16)$$

where  $\langle p_n \rangle$  is the average bond order, which is 0.64 in our calculation. The geometry optimized ground state is a bond order wave, where  $p_n$  alternates between every two bonds [55,60]. Except for boundary effects near the chain ends it has an almost uniform bond order alternation parameter of  $p'_n = 0.21$ . The average bond length is  $1.06 \pm 0.11 \text{ \AA}$ . Thus the transfer integral can be approximated by  $t_{n,n\pm 1} = \bar{\beta}(1 - (-1)^n \delta)$ , with  $\bar{\beta} = -3.9 eV$  and  $\delta = 0.13$ .

For the Hückel model most of the coupling constants appearing in the equations of motion, Eqs. (11.9) and (11.10), are zero, since the Coulomb

Table 11.1: Mode frequencies and anharmonic coupling constants for the Hückel and the PPP models.

	Hückel	PPP
$\Omega(1B_u)$	$2.28eV$	$2.28eV$
$\Omega(5B_u)$	$3.99eV$	$4.52eV$
$\mu_1$	$3.86e\text{\AA}$	$4.80e\text{\AA}$
$s_1$	$-3.86e\text{\AA}$	$-2.81e\text{\AA}$
$s_2$	$0.0e\text{\AA}$	$0.017e\text{\AA}$
$V_1$	$0.0eV$	$0.063eV$
$\mu_{12}$	$0.0eV$	$0.66e\text{\AA}$
$V_{12}$	$0.0eV$	$-0.021eV$
$X_1$	$21.99e\text{\AA}^2V^{-1}$	$5.36e\text{\AA}^2V^{-1}$
$X_{-1}$	$0.0e\text{\AA}^2V^{-1}$	$0.078e\text{\AA}^2V^{-1}$
$X_2$	$0.0e\text{\AA}$	$0.26e\text{\AA}$
$X_3$	$0.0e\text{\AA}$	$0.13e\text{\AA}$
$X_4$	$0.0eV$	$-0.082eV$
$Y_1$	$-36.16e\text{\AA}^2V^{-1}$	$-23.0e\text{\AA}^2V^{-1}$
$Y_2$	$0.0e\text{\AA}$	$-1.33e\text{\AA}$
$Y_3$	$0.0e\text{\AA}$	$-0.67e\text{\AA}$
$Y_4$	$0.0eV$	$0.035eV$

matrix vanishes, see Table 11.1. The surviving terms  $\mu_1, s_1, s_2, \mu_{1n}$  do not include the Coulomb interaction. As can be seen in Appendix 11.5, most of the terms arising from the elimination of the off-resonant  $A_g$  oscillators involve the Coulomb interaction. Therefore only  $X_1, X_{-1}, Y_1$  are finite. Additionally, for the Hückel model we find no  $A_g$  oscillator which can be resonantly excited as a two-photon resonance. This can be seen from Fig. 11.1, which displays the frequencies of all oscillators. The frequency of the lowest  $1B_u$  oscillator is  $2.28eV$ . The  $A_g$  oscillators which are closest in frequency to twice the frequency of the  $1B_u$  are the  $6A_g$  and  $7A_g$  oscillators at  $4.13eV$ . The frequency difference  $2\Omega(1B_u) - \Omega(6A_g) = 0.43eV$  is already larger than the spectral width of the

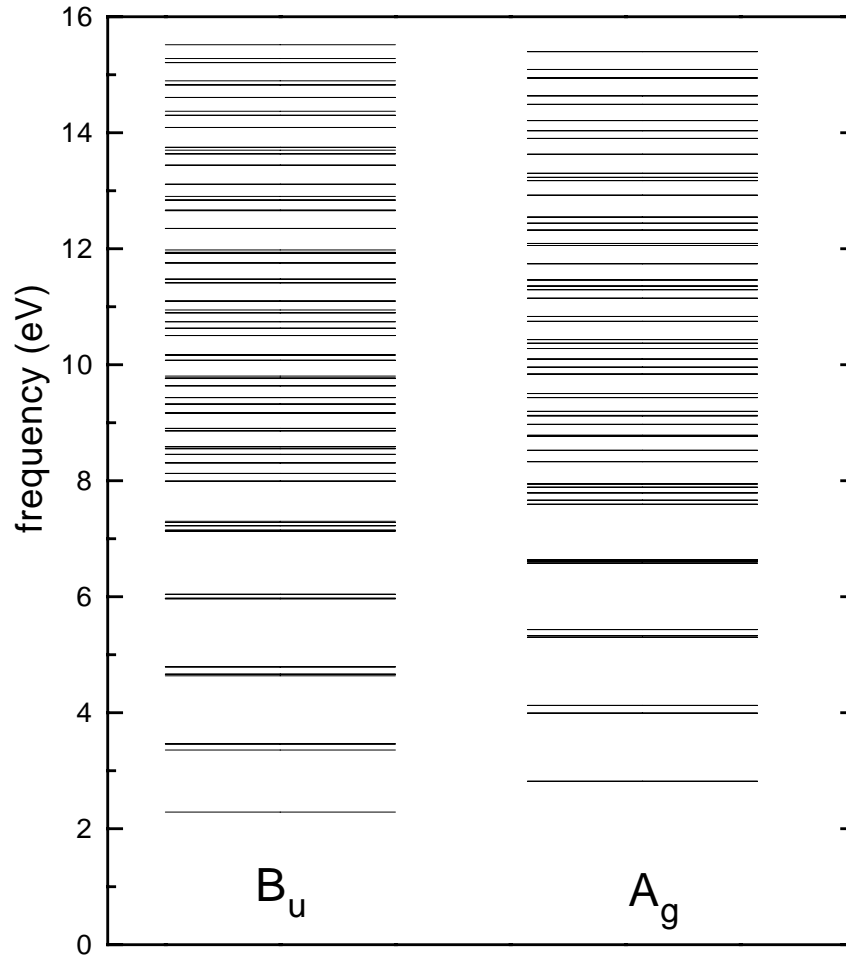


Figure 11.1: Frequencies of all  $B_u$  and  $A_g$  oscillators for the Hückel model of a 30 carbon atom polyacetylene chain. There are 113  $B_u$  and 112  $A_g$  oscillators. The frequencies of the first eight  $B_u$  ( $A_g$ ) oscillators are: 2.28, 3.35, 3.46, 3.46, 4.63, 4.66, 4.66, and 4.79 eV (2.82, 2.82, 3.99, 3.99, 4.13, 4.13, 5.30, and 5.30 eV).

exciting 20 fs laser pulses, which is about 0.1 eV. Therefore all contributions from  $A_g$  oscillators can be assumed to be off-resonant and the only primary oscillator is the  $1B_u$ . In the numerical calculations of the FWM signal we have included the phenomenological relaxation times  $T_2 = 80$  fs for the  $B_u$  and  $T'_2 = 40$  fs for the  $A_g$  oscillators.

In Fig. 11.2 we show the density matrices of the ground-state and of the  $1B_u$  oscillator using the  $\pi$  orbital (real-space) basis. The diagonals of these plots represent the charge density  $\rho_{nn}$ , the off diagonal elements shows the

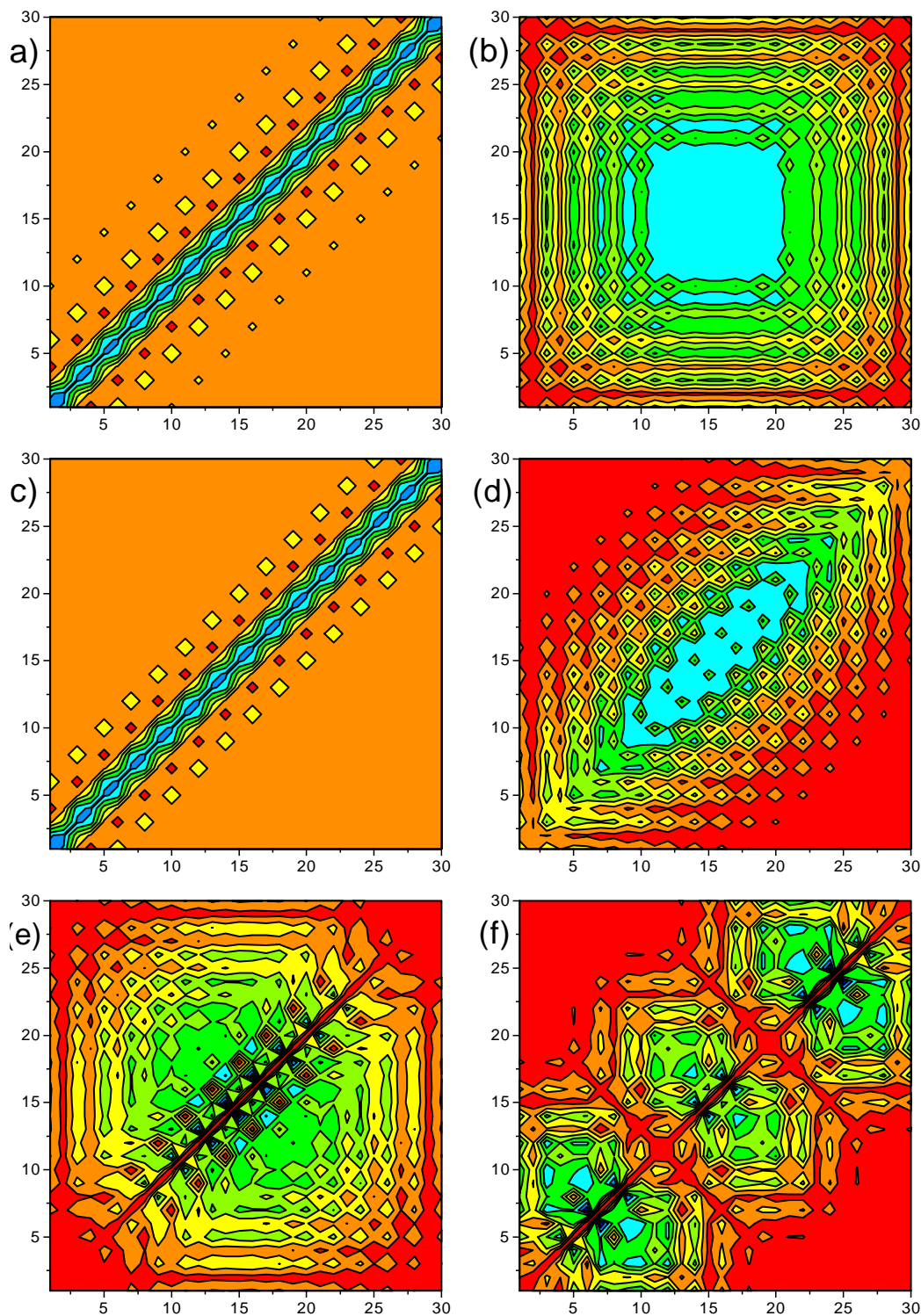


Figure 11.2: (a) Ground state density matrix and (b) absolute value of density matrix representing the  $1B_u$  oscillator for the Hückel model. (c) Ground state density matrix and absolute value of density matrix representing the  $1B_u$  (d),  $3A_g$  (e), and  $5A_g$  (f) oscillators for the PPP model. (Large=blue, green, yellow, red=small)

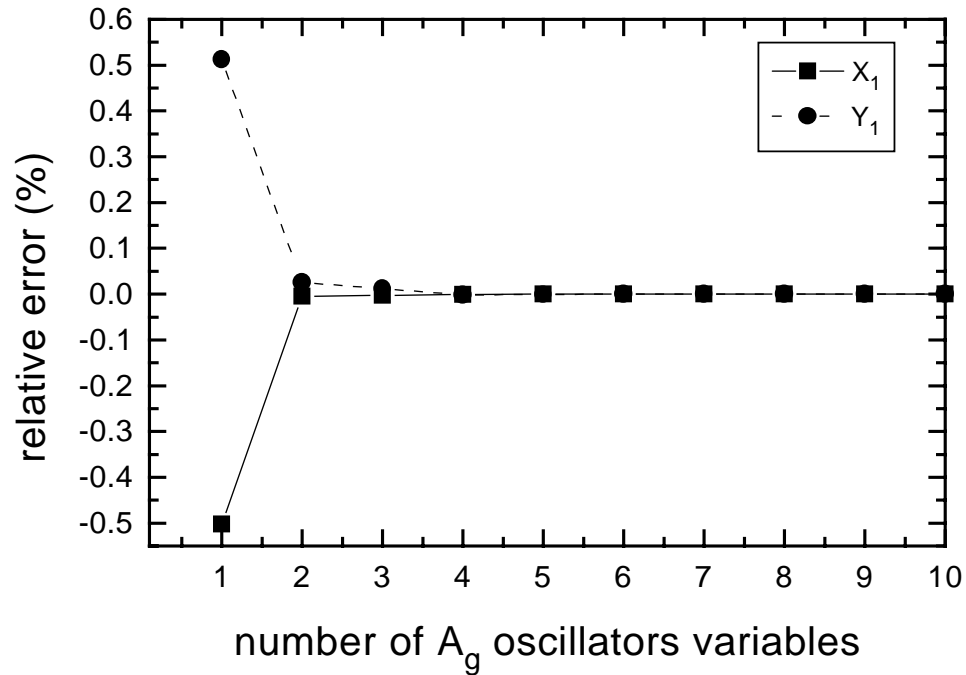


Figure 11.3: Convergence of anharmonicities for the Hückel model as function of number of virtual  $A_g$  oscillator variables. Shown is the relative percent difference of the quantity to its converged value.

electronic coherences in the system. The ground state is more localized along the diagonal than the oscillator, which shows that the optical excitation creates electronic coherence in the system.

In Table 11.1 we give the relevant coupling constants for the Hückel model. It turns out that  $\mu_1 = -s_1$ ; this resembles a simple two-level model, where the inhomogeneity of the optical Bloch equation for the polarization reads  $\mu E(1-n)$  (here  $n$  is the population) [234]. We also find that  $s_2$  is zero, indicating that no two-photon resonance involving solely the  $1B_u$  oscillator contributes to the signal, which again mimics a simple two-level system. Therefore the only nonlinearity, involving just the  $1B_u$  oscillator, is given by  $s_1$ , which represents a scattering of the field off a transient grating.

Looking at the coupling coefficients arising from the elimination of the  $A_g$  oscillators, it turns out that  $X_{-1}$  vanishes, and  $X_1$  and  $Y_1$  are finite. Both of these coefficients represent the scattering of two fields of the linear excitation.

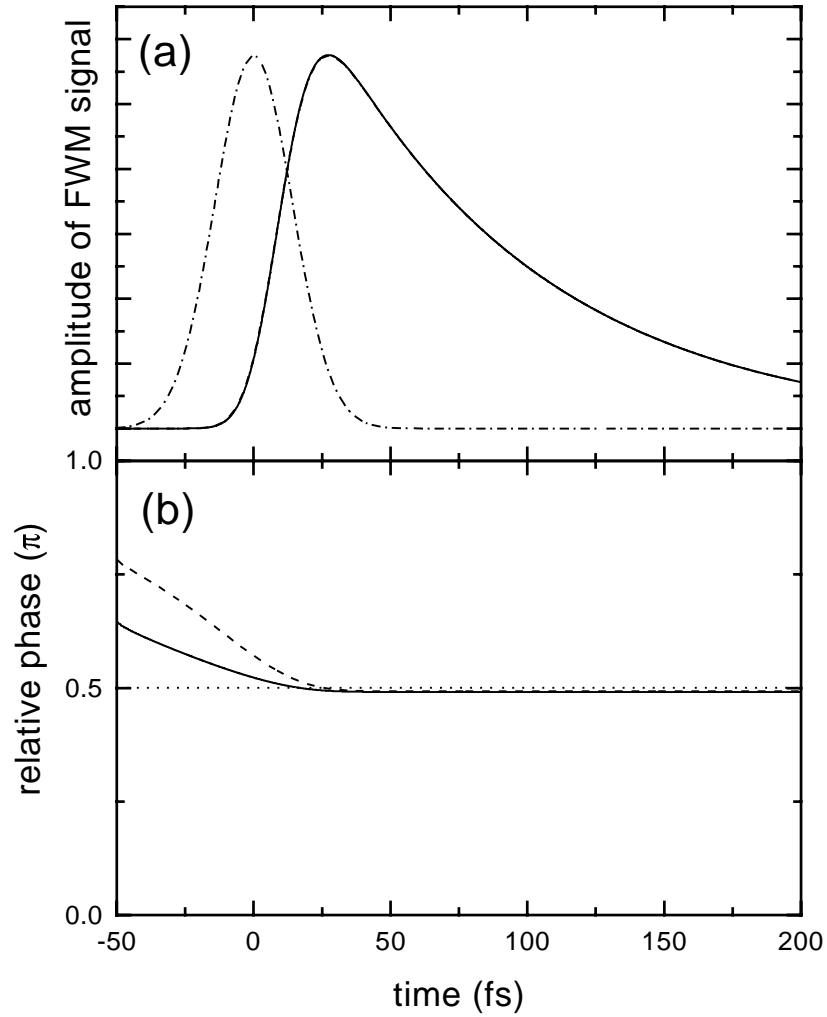


Figure 11.4: (a) Time-resolved amplitude and (b) phase of the FWM signal for time-delay  $\tau = 0\text{fs}$  for the Hückel model. Solid line: model IH, dashed: model IHH, dotted: model IIIH, and dashed-dotted: laser pulse envelope.

These terms result in small contributions to the FWM signal and, as can be seen from Eq. (11.36), they only contribute when the two pulses overlap in time.

To find out how many virtual oscillators contribute to these two terms, we show in Fig. 11.3 the convergence of  $X_1$  and  $Y_1$  with the number of virtual  $A_g$  oscillator variables taken into account. The summations over the  $A_g$  oscillators, see Eq. (11.39), have been made in such a way that we start with the largest term and then one by one include the smaller coupling terms. We see that by

taking just 2 (out of 224)  $A_g$  oscillator variables into account to obtain a 0.5% accuracy for  $X_1$  and 2.5% for  $Y_1$ . The two oscillators most strongly coupled to the  $1B_u$  oscillator are the  $2A_g$  and  $3A_g$  oscillators; both have a frequency of  $2.82eV$ .

In Fig. 11.4 we display the amplitude and the relative phase of the time-resolved FWM signal for time-delay  $\tau = 0fs$  for three different models. Model IH is a full calculation which includes all oscillators explicitly, according to Appendix 11.4. In models IIH and IIIH only the  $1B_u$  oscillator has been considered explicitly. The off resonant  $A_g$  oscillators enter via renormalizations of the anharmonic couplings in model IIH (see Appendix 11.5), while in model IIIH they are neglected. We find that all three calculations are very similar. Only during the excitation process, when the signal is still small, there are slight differences in the phase of the signals. This analysis shows that the resonant FWM signal for the Hückel model is well described by the  $1B_u$  oscillator alone, which can also be described using a simple two-level model. The shape of the amplitude of the FWM signal represents a free-induction decay, which means that the signal reaches its maximum immediately after the excitation by the pulses, and subsequently decays [234]. We also compute the relative phase  $\Delta\varphi$  of the FWM signal, which is given in Fig. 11.4(b), is after the excitation process ( $t > 20fs$ ) equal to  $\frac{\pi}{2}$ . This means that, like in a resonantly excited classical oscillator, the optically excited polarization follows the laser pulse with a phase shift of  $\frac{\pi}{2}$ , which is in agreement with analytical solution of optical Bloch equations performed for ultrashort pulses [223,234]. It has been shown that in this limit the FWM signal caused by phase-space filling has a negative imaginary prefactor, which gives a relative phase of  $\frac{\pi}{2}$ .

The second order density matrix has a  $\mathbf{k}_2 - \mathbf{k}_1$  (transient-grating) and a  $2\mathbf{k}_2$  (two-photon) component. The latter is negligible in the present calculation. Fig. 11.5(a) shows the second order density matrix representing a transient-



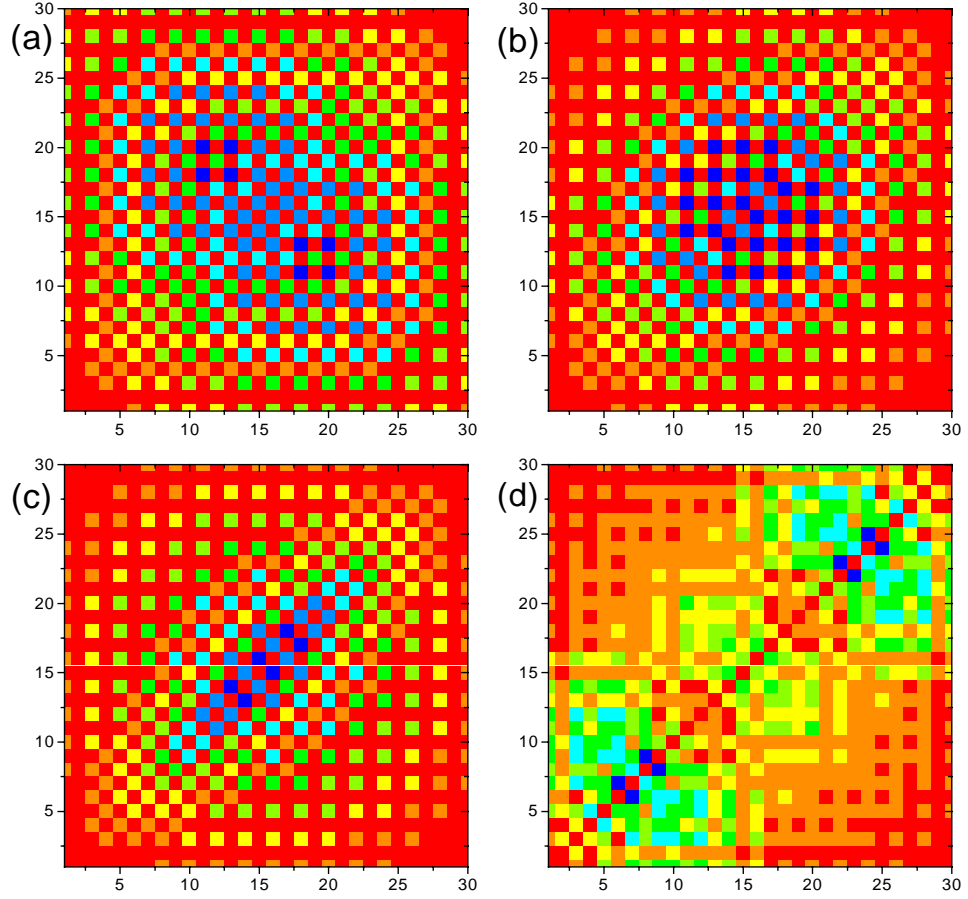


Figure 11.5: Absolute value of second-order density matrix  $\rho^{(2)}(t)$  at  $t = 20fs$  representing transient-grating ( $\mathbf{k}_2 - \mathbf{k}_1$ ) for (a) model IH, Eq. (27), (b) model IP, Eq. (28), (c) model IIP, Eq. (27), and (d) two-photon resonances ( $2\mathbf{k}_2$ ) for model IIP, Eq. (29).

grating in real space

$$\begin{aligned} \rho^{(-1|1)}(t) &= e^{i(\omega_1 - \omega_2)t} \left( \frac{1}{2} ([[\xi_1, \bar{\rho}], \xi_{-1}] + [[\xi_{-1}, \bar{\rho}], \xi_1]) z_{-1}^{(-1|0)}(t) z_1^{(0|1)}(t) \right. \\ &\quad \left. + \sum_{\beta} \xi_{\beta} z_{\beta}^{(-1|1)}(t) \right) , \end{aligned} \quad (11.17)$$

here the upper indices refer to the propagation directions, see Appendix 11.3. Due to the symmetry of this expression the density matrix  $\rho_{ij}$  representing this term is zero if  $i + j$  is even (this is indicated by the red squares in Fig. 11.5(a), where we have used a different plot style but the same color code as in Fig. 11.2). The  $A_g$  oscillator amplitudes ( $z_{\beta}^{(-1|1)}$ ) are small, and the odd index

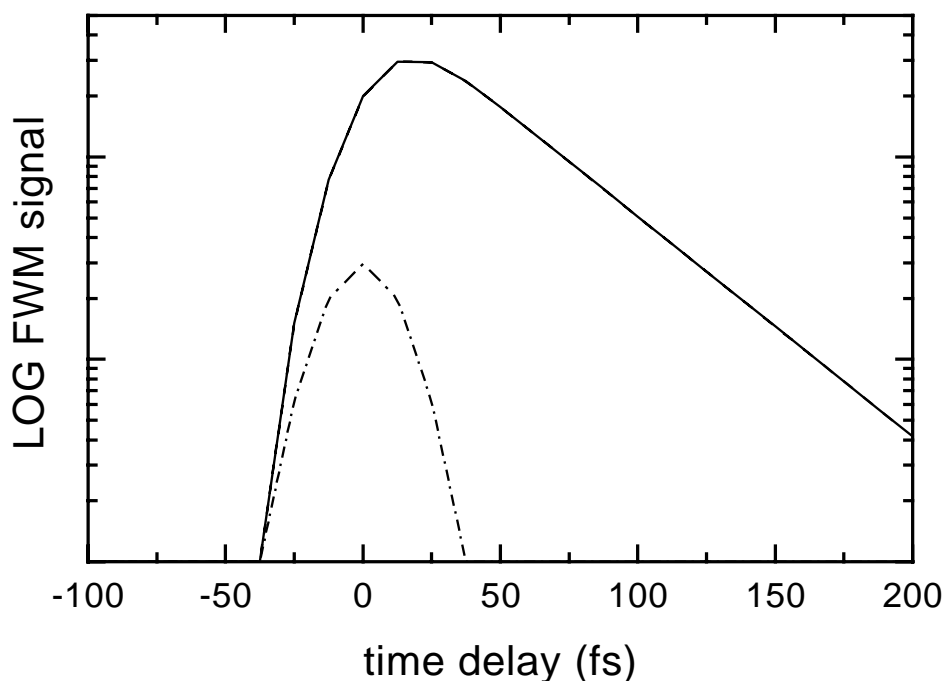


Figure 11.6: Time-integrated FWM for the Hückel model. Solid line: model IH, dashed: model IIIH, and dashed-dotted: laser pulse envelope.

combinations show therefore a profile similar to the  $1B_u$  oscillator shown in Fig. 11.2(b).

Since we have shown that the Hückel model behaves like a simple two-level system, we expect no time-integrated FWM signal for negative delays. This is verified by Fig. 11.6, where we compare model IH and IIIH. While the signal for positive delays decays with  $T_2/2$ , as expected for a homogeneously broadened two-level system, the signal decays much faster for negative delays. The small signals for negative delays solely originate from the finite pulse width. The dashed line in Fig. 11.6 represents the time-integrated signal for model IIIH, it lies almost exactly on the solid line representing model IH.

We should however point out, that the absence of the second primary oscillator, appearing as a two-photon resonance is not an intrinsic property of the Hückel model. For other sizes or bond alternation parameters there may be  $A_g$  oscillators with frequencies in the vicinity of twice the frequency of the  $1B_u$  oscillator, which may then also contribute to the nonlinear response. For

the same parameters used here, we find that for a chain containing 22 carbon atoms the  $6A_g$  and  $7A_g$  oscillators can be resonantly excited as two-photon resonances ( $\Omega(1B_u) = 2.56eV$ ,  $\Omega(6A_g) = \Omega(7A_g) = 5.11eV$ ). Our calculations show, that compared to the  $1B_u$  oscillators, even for this case, the  $A_g$  oscillators contribute only weakly for the signal. For zero delay they are responsible for only 0.8% of the signal (for the 30 carbon atom chain this value is 0.2%). However, for large negative delays, when the contributions from the  $1B_u$  oscillator vanish, the two-photon resonances induce a finite FWM signal. For the chain of 22 carbon atoms these signals for negative delays are very weak. The time-integrated FWM signal for  $\tau = -100fs$  is five orders of magnitude smaller than the one for zero delay. We therefore believe that our conclusions drawn for the resonant response of Hückel model, regarding the weak coupling of the  $1B_u$  to the  $A_g$  oscillators, are of general nature.

### 11.2.2 The PPP model

We shall now explore the role of electronic correlations by repeating the previous calculations for the PPP model. Similar to the Hückel model, the geometry optimized HF ground state is characterized by a bond order wave with a uniform charge density [55,236]. This structure is stabilized by the electron-phonon and the Coulomb exchange interactions. The calculated ground state has an average bond order  $\langle p_n \rangle = 0.63$  and alternation parameter  $p'_n = 0.24$ . The average bond order alternation is a little larger than in the Hückel model. The average bond length is  $1.31 \pm 0.05\text{\AA}$ , where the alternation is due to the larger force constant smaller than in the Hückel model [236]. The average transfer integral can be approximated by  $t_{n,n\pm 1} = \bar{\beta}(1 - (-1)^n\delta)$ , with  $\bar{\beta} = -2.7eV$  and  $\delta = 0.07$ .

All of the coupling constants in Eqs. (11.9) and (11.10) can contribute once the Coulomb interaction is incorporated, see Table 11.1. The frequency

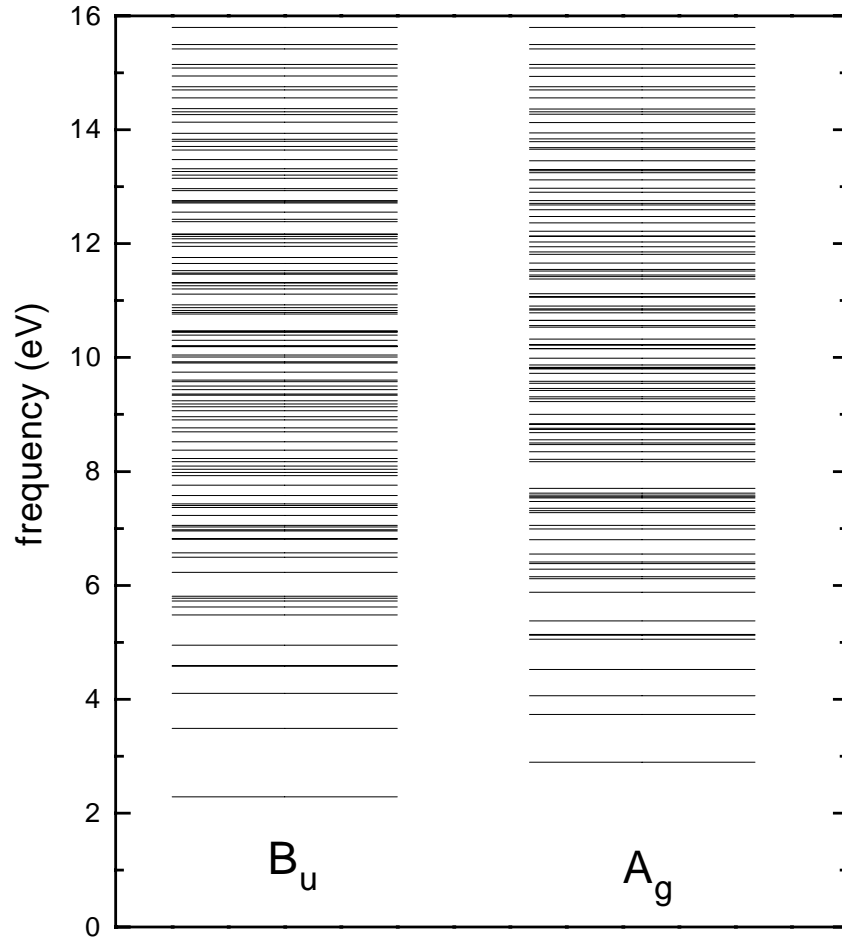


Figure 11.7:  $B_u$  and  $A_g$  oscillator frequencies for the PPP model for a 30 carbon atom polyacetylene chain. There are 113  $B_u$  and 112  $A_g$  oscillators. The frequencies of the first eight  $B_u$  ( $A_g$ ) oscillators are: 2.28, 3.49, 4.10, 4.57, 4.59, 4.95, 5.48, and 5.62 eV (2.89, 3.73, 4.06, 4.52, 5.05, 5.12, 5.13, and 5.37 eV).

of the lowest  $1B_u$  oscillator is again 2.28 eV. The  $A_g$  oscillator which is closest in frequency to twice the frequency of the  $1B_u$  is the  $5A_g$  at 4.52 eV, see Fig. 11.7. The frequency difference  $2\Omega(1B_u) - \Omega(5A_g) = 0.049$  eV is smaller than the spectral width of the exciting 20 fs laser pulses. All other contributions from  $A_g$  oscillators can be assumed to be off-resonant. So the two primary oscillators, which are considered explicitly, are  $1B_u$  and  $5A_g$ .

In Fig. 11.2(c) and (d) we show the density matrices of the HF ground-state and of the  $1B_u$  oscillator. Compared to the  $1B_u$  oscillator, see Fig.

11.2, calculated for the Hückel model, which is strongly delocalized in the off-diagonal direction, the many-particle Coulomb-interaction leads to localization of the oscillator towards the diagonal. Still the ground state is again more localized along the diagonal than the oscillator, which shows that the optical excitation creates electronic coherence in the system. Also shown in Fig. 11.2 are the most strongly contributing  $A_g$  oscillators, (e) the  $3A_g$ , which gives the strongest off resonant contribution, and (f) the  $5A_g$ , which appears as a two-photon resonance.

In Table 11.1 we give the relevant coupling constants for the PPP model. To simplify the analysis of these numerous term, we split the discussion into three parts. In model IP, like in model IIIH for the Hückel model, we neglect all contributions except for the ones involving only the  $1B_u$  oscillator. In addition to these contributions we include in model IIP the renormalization originating from the elimination of the  $A_g$  oscillators appearing as transient-gratings ( $X_i$ ). Finally, in model IIIP we also add the explicitly considered  $5A_g$  oscillator, as well as all renormalizations induced by  $A_g$  oscillators appearing as two-photon resonances ( $Y_i$ ).

In model IP only the following terms contribute:  $\mu_1, s_1, s_2, V_1$ .  $s_1$  describes the phase space filling, unlike the Hückel model, due to correlations its magnitude is not equal to the magnitude of the dipole  $\mu_1$  but is somewhat smaller.  $s_2$  describes a similar process, where now the field is scattered off a term rotating with twice the transition frequency of the  $1B_u$  oscillator, instead of a transient grating term like in  $s_1$ , which basically has no rotation. In the absence of correlation (the Hückel model)  $s_2$  was zero, here  $s_2$  is finite, but still very small, only 0.6% of  $s_1$ , and can therefore be neglected.  $V_1$  represents a many-particle induced scattering potential, which formally appears like a local field correction [223–225]. Actually it includes all many-particle contributions involving only the  $1B_u$  oscillator. Neglecting the small  $s_2$  contribution, the equation

is equivalent to a nonlinear wave-equation, which has been extensively used for the description of nonlinear optical properties of inorganic semiconductors [223,224,226,233]. In this sense the nonlinear wave-equation appears as a special case of the present oscillator equations, obtained when some terms are neglected. This nonlinear wave equations can be derived by expanding the semiconductor Bloch equation [237–239,38] in an excitonic basis, keeping only the  $1s$  exciton. In the language of the semiconductor Bloch equations the nonlinear scattering potential includes energy and field renormalization terms, which are induced by the many-particle Coulomb interaction [225,233].

The FWM signal for model IP is given by the solid lines in Fig. 11.8, where both the amplitude of the FWM signal and its relative phase are plotted. Compared to the Hückel model calculations, the amplitude changes its shape. It is no longer a free-induction decay, but has a maximum at later times, which are determined by the dephasing times. This is the same signature that has been observed in time-resolved FWM experiments on inorganic semiconductor nanostructures [226,227,240]. In semiconductors these signal shapes have been interpreted by a nonlinear Ginzburg-Landau like wave equation for the  $1s$  exciton amplitude [223,224,226,233]. If we only consider the  $1B_u$  oscillator and further neglect the small  $s_2$  term, we obtain an identical wave equation as a special case of the oscillator equations. Besides the phase-space filling ( $s_1$ ) induced by the many particle Coulomb interaction it has an additional nonlinearity ( $V_1$ ), which formally appears like a local field correction. This nonlinear scattering potential describes scattering of the induced polarizations, resulting in a FWM signal. According to analytical solutions of optical Bloch equations including a local field, this contribution has a real positive prefactor [223,233]. Since  $V_1$  itself is positive and since the many-particle induced FWM signal is like in inorganic semiconductors larger than the phase-space filling, the relative phase of the FWM signal, solid line in Fig. 11.8, is about 0, i.e.

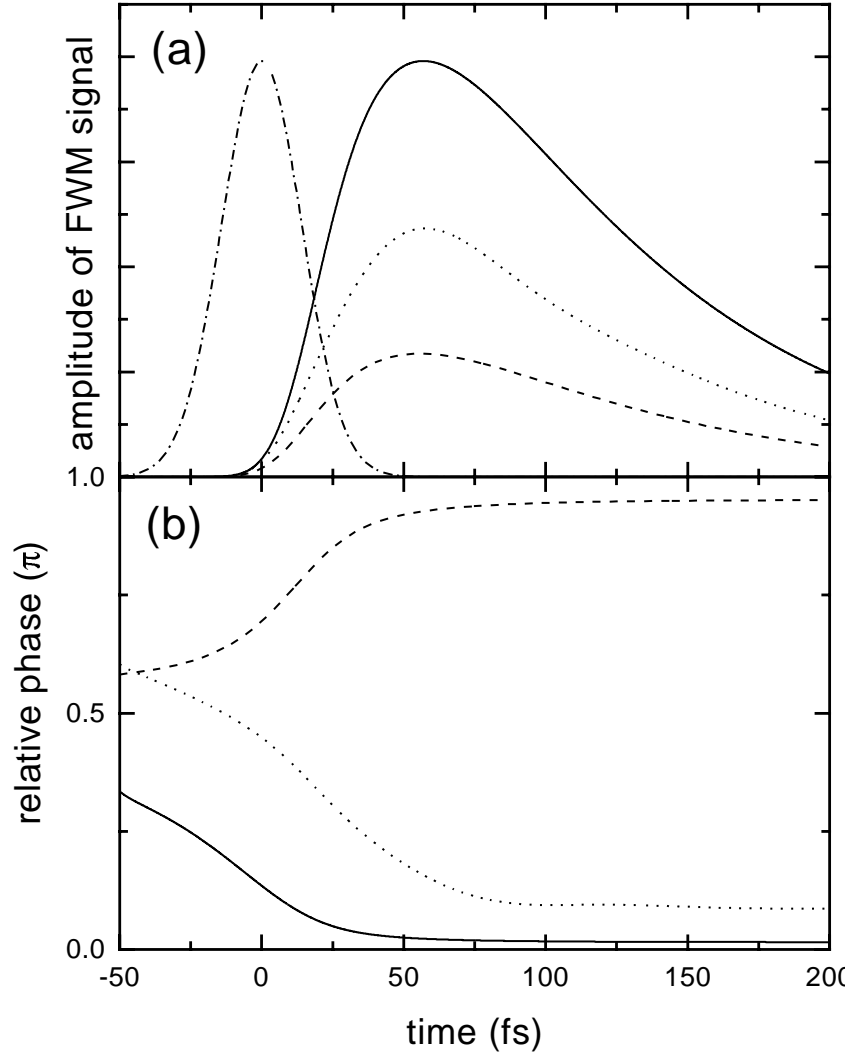


Figure 11.8: (a) Time-resolved amplitude and (b) phase of the FWM signal for time-delay  $\tau = 0$  fs for the PPP model: Solid line: model IP, dashed: model IIP, dotted: model IIIP, and dashed-dotted: laser pulse envelope.

the induced polarization is in phase with the exciting pulse.

Fig. 11.5(b) shows the second-order density matrix in real space, representing a transient-grating ( $\mathbf{k}_2 - \mathbf{k}_1$ ) formed by the  $1B_u$  oscillator

$$\rho^{(-1|1)}(t) = e^{i(\omega_1 - \omega_2)t} \frac{1}{2} ([[\xi_1, \bar{\rho}], \xi_{-1}] + [[\xi_{-1}, \bar{\rho}], \xi_1]) z_{-1}^{(-1|0)}(t) z_1^{(0|1)}(t) \quad . \quad (11.18)$$

Due to the symmetry of this expression, like in the Hückel model, the density matrix  $\rho_{ij}$  representing this term is zero if  $i + j$  is even (this is indicated by the red squares). The odd index combinations show a profile similar to the

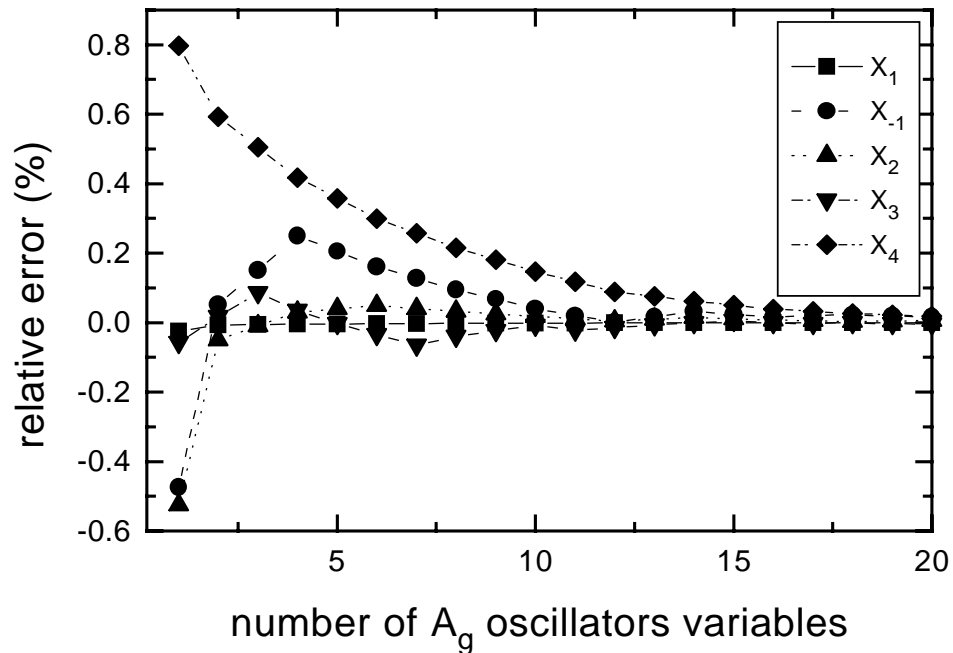


Figure 11.9: Convergence of the  $X$  anharmonicities for the PPP model as function of number of virtual  $A_g$  oscillator variables. Shown is the relative percent difference of the quantity to its converged value.

$1B_u$  oscillator shown in Fig. 11.2(f). Accordingly, like the  $1B_u$  oscillator, also the corresponding transient-grating is more localized in the PPP than in the Hückel model.

In model IIP the off resonant transient grating contributions  $X_1$ - $X_4$  are included. The convergence of these parameters with the number of oscillator variables is shown in Fig. 11.9. The value for  $X_1$ , which is a small contribution, since it describes scattering of a linear term off two-fields, is to 2.7% accuracy given by the coupling to the  $3A_g$  oscillator. For  $X_{-1}$ , we have to keep five  $A_g$  oscillator variables to get 5% accuracy.  $X_2$ , which acts as renormalizations of  $s_1$  is to within 5% given by the coupling to the  $3A_g$  oscillator alone. For  $X_3$ , which acts as renormalizations of  $s_2$  we have to keep contributions from three  $A_g$  oscillator variables to get it to 3% accuracy. To get  $X_4$ , the renormalization of the nonlinear scattering potential  $V_1$  also within 5%, we have to keep 16 oscillator variables. The expression for  $X_4$  it is entirely determined by the Coulomb-interaction between different oscillators. Its slow convergence as



function of the number of oscillators variables compared to the other quantities indicates, that the Coulomb-interaction couples the oscillators much less selectively than the dipole coupling, which is present in the expressions for the other terms.

The FWM signal for model IIP is given in Fig. 11.8 (dashed lines), where the absolute value as well as the relative phase of the FWM signal are plotted. The most notable changes between the signal involving only the  $1B_u$  oscillator and the present one are the decrease in amplitude and the change in phase. These features can be simply explained by considering the values of  $V_1$  and its renormalization  $X_4$ . While  $V_1$  is positive  $+0.063eV$ ,  $X_4$  is calculated to be negative and larger in absolute value  $-0.082eV$ . Therefore the effective nonlinear scattering potential  $V_1 + X_4 = -0.019eV$  is negative and about a factor 3 smaller than  $V_1$ . This reduces the amplitude of the interaction-induced contribution to the signal and changes its phase, which in turn explains the observed differences. This change of phase has strong influence on the spectrally resolved FWM signal. While the Fourier transform (FT) of the signal originating from the  $1B_u$  oscillator is, like in inorganic semiconductors [233,241], slightly asymmetric with respect to detuning with a tail towards lower frequencies, the FT of the signal for model IIP, is asymmetric with tails towards higher frequencies. These spectral features can also be nicely analyzed using a Wigner spectrogram [242,243] as discussed in Ref. [221].

Fig. 11.5(c) shows the transient-grating ( $\mathbf{k}_2 - \mathbf{k}_1$ ) part of the second order density matrix in real space. It is formed by the  $1B_u$  oscillator and some  $A_g$  oscillators and given by Eq. (11.17). The density matrix contains contributions from the  $1B_u$  and about eight  $A_g$  oscillators, which contribute most strongly to  $X_4$ .  $\rho_{ij}$  is again zero if  $i + j$  is even (this is indicated by the red squares). Due to the contributing  $A_g$  oscillators, the resulting density matrix extends further to the off-diagonal than the one originating from the  $1B_u$  oscillator alone.

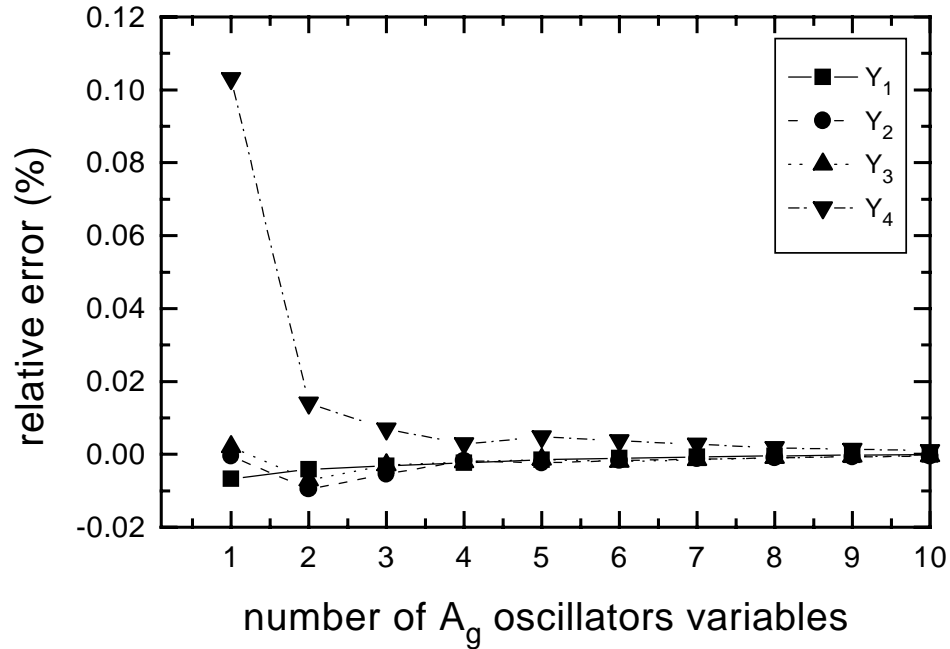


Figure 11.10: Same as Fig. 11.9 but for the  $Y$  anharmonicities.

So far, our analysis demonstrated that the off-resonant terms involving transient gratings contribute significantly. In addition to the previous terms we include in model IIIP all renormalizations arising from terms representing two-photon resonances  $Y_1$ - $Y_4$ . Their convergence with the number of virtual oscillators variables is shown in Fig. 11.10. The value for  $Y_1$  (which is a small contribution, since it describes scattering of a linear term off two-fields) is to 0.7% given by the coupling to the  $3A_g$  oscillator. The value for  $Y_2$  ( $Y_3$ ), which act as renormalizations of  $s_1$  ( $s_2$ ) is to 0.1% (0.2%) given by the coupling to the  $3A_g$  oscillator. The reason that we essentially only need the  $3A_g$  oscillator to determine  $Y_1$ - $Y_3$  is that in addition to its strong dipole coupling to the  $1B_u$  oscillator, it is not too much off resonant compared to most other oscillators. To get  $Y_4$ , the renormalization of the nonlinear scattering potential  $V_1$  also within 5%, we have to keep two oscillators the  $3A_g$  and the  $8A_g$ . As a two-photon resonance we also keep the  $5A_g$  explicitly. It is dipole and Coulomb coupled to the  $1B_u$  oscillator by  $\mu_{12}$  and  $V_{12}$ .

The FWM signal for model IIIP is given in Fig. 11.8 (dotted line). Com-

pared to the model IIP, the amplitude increases again and the phase is close to 0. In order to explain these changes we have to consider two effects. First, like before, the renormalization of  $V_1$ . The effective nonlinear scattering potential is now given by  $V_1 + X_4 + Y_4$  which is  $0.016eV$ , a positive but quite small value. Second, the increase in amplitude is caused by the contribution from the two-photon resonance represented by  $V_{12}$ , which describes the Coulomb coupling between the  $1B_u$  and the  $5A_g$  oscillator.

This change of phase will again influence the spectrally resolved FWM signal, which is now again be asymmetric with respect to the detuning with tails towards negative detuning. This is the same signature which appears when we keep only the  $1B_u$  oscillator, and is also the typical signature in the FT FWM signal of inorganic semiconductors [233,241].

Fig. 11.5(d) shows the two-photon resonance ( $2\mathbf{k}_2$ ) part of the density matrix in real space, which is formed by the  $1B_u$  oscillator and some  $A_g$  oscillators, and given by

$$\rho^{(0|2)}(t) = e^{-2i\omega_2 t} \left( \frac{1}{2} ([[\xi_1, \bar{\rho}], \xi_1] + [[\xi_1, \bar{\rho}], \xi_1]) (z_1^{(0|1)}(t))^2 + \sum_{\beta} \xi_{\beta} z_{\beta}^{(0|2)}(t) \right) . \quad (11.19)$$

The density matrix consists of small contribution from the  $1B_u$  and about mainly two  $A_g$  oscillators, namely  $3A_g$  and  $5A_g$ . Its shape is essentially a superposition of the density matrices representing the  $3A_g$  and the  $5A_g$  oscillators, shown in Fig. 11.2.

Having analyzed the different contributions to the nonlinear optical response within the PPP model, we propose a simplified two-oscillator model [221], which to a good accuracy reproduces the signal. Compared to the model resulting from the elimination of off-resonant contributions, we further neglect small contributions like  $X_1$ ,  $X_{-1}$  and  $Y_1$ , and also  $s_2$  and its renormalization  $X_3$ , and  $Y_3$ . We further neglect the anharmonic constants  $A_1$ ,  $A_2$ ,  $A_3$ ,  $B_1$ , and

$B_2$  that appear in the definition of the polarization. So now the off-resonant oscillators only enter in renormalizations of  $s_1$  and  $V_1$ . The equations considered within this reduced model are [221]

$$\begin{aligned} i\frac{\partial}{\partial t}z_1 &= (\Omega_1 - \omega_L - i\frac{1}{T_2})z_1 - \mu_1 E \\ &- E\mu_{12}z_2 - E(s_1 + Y_2 + X_2)z_1z_{-1} \\ &+ 2V_{12}z_2z_{-1} + (V_1 + Y_4 + X_4)z_{-1}z_1z_1 \end{aligned} \quad (11.20)$$

$$\begin{aligned} z_{-1} &= z_1^* \\ i\frac{\partial}{\partial t}z_2 &= (\Omega_2 - 2\omega_L - i\frac{1}{T_2'})z_2 - E\mu_{12}z_1 + V_{12}z_1z_1 \end{aligned} \quad (11.21)$$

The induced polarization is given by:

$$P_S(t) = e^{-i\omega_L t} (\mu_1 z_1 + \mu_{12} z_2 z_{-1}) \quad . \quad (11.22)$$

We compare the results obtained for this model (IVP) with results obtained by a full calculation (VP), where we have kept all oscillators explicitly (in practice these results were obtained by a real-space calculation), see Appendix 11.4. The good agreement between the two calculations shown in Fig. 11.11, confirms the validity of this simplified description. There are only slight differences in the amplitude and the phase of the FWM signal mainly during the initial excitation process.

Another important effect is the existence of strong FWM signals for negative delays, which may be induced by either two-photon  $A_g$  oscillator variables, or by many-body anharmonicities of the  $B_u$  oscillators. Our calculations show that, as for positive delay, the many-body anharmonicities contribute most strongly to the signal for negative delays. The time-integrated signals in Fig. 11.12 decay for positive delays with  $T_2/2$ , and for negative delays with about  $T_2/4$  [223,224]. The very weak modulations, which can be seen for negative delays, are due to quantum beats with a frequency determined by  $2\Omega(1B_u) - \Omega(5A_g)$ . The results for the full model VP (solid line) and the reduced model IVP (dashed line) are again in very good agreement.

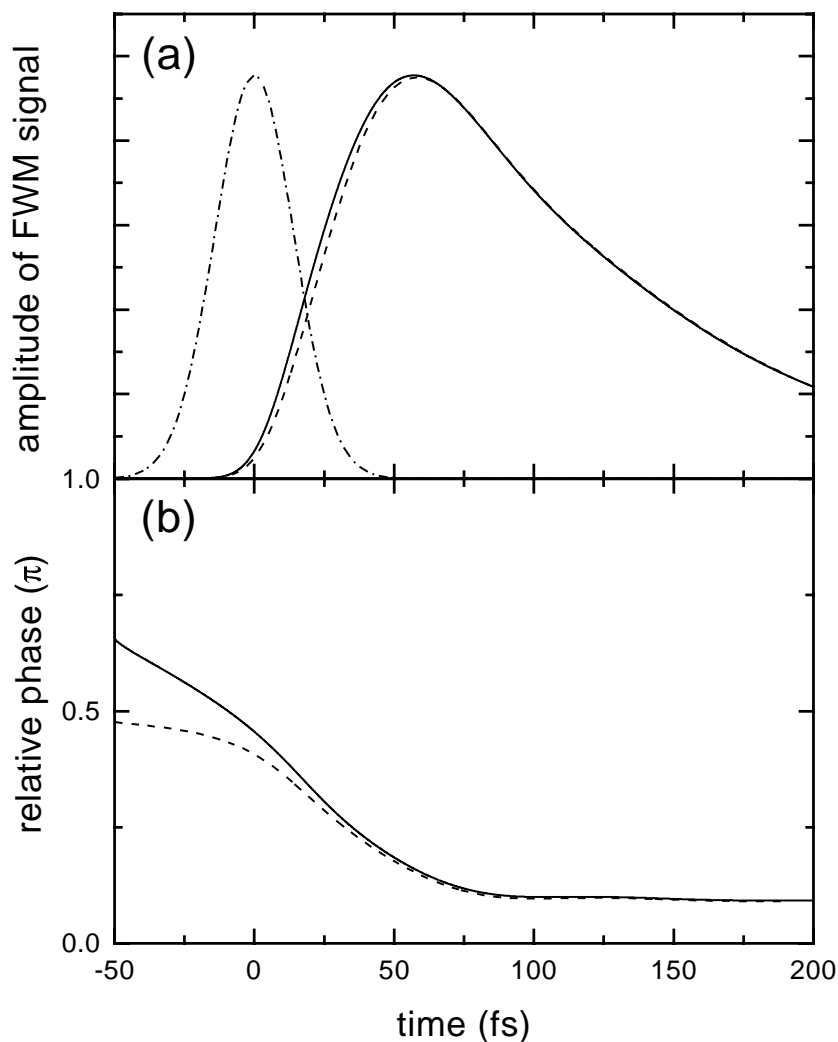


Figure 11.11: (a) Time-resolved amplitude and (b) phase of the FWM signal for time-delay  $\tau = 0 \text{ fs}$  for the PPP model. Solid line: model VP, dashed: model IVP, and dashed-dotted: laser pulse envelope.

In summary, resonant two-pulse four-wave mixing experiments in conjugated polyenes have been modeled using the electronic-oscillator representation. We found that it is only required to consider two electronic oscillators explicitly. The role of electronic correlations has been clarified by comparing calculations done in the absence of electronic correlations (Hückel model) and with strong electronic correlations (PPP model). While both models have similar linear optical properties, i.e. a strong lowest transition at the same spectral position, their nonlinear optical properties are very different. For

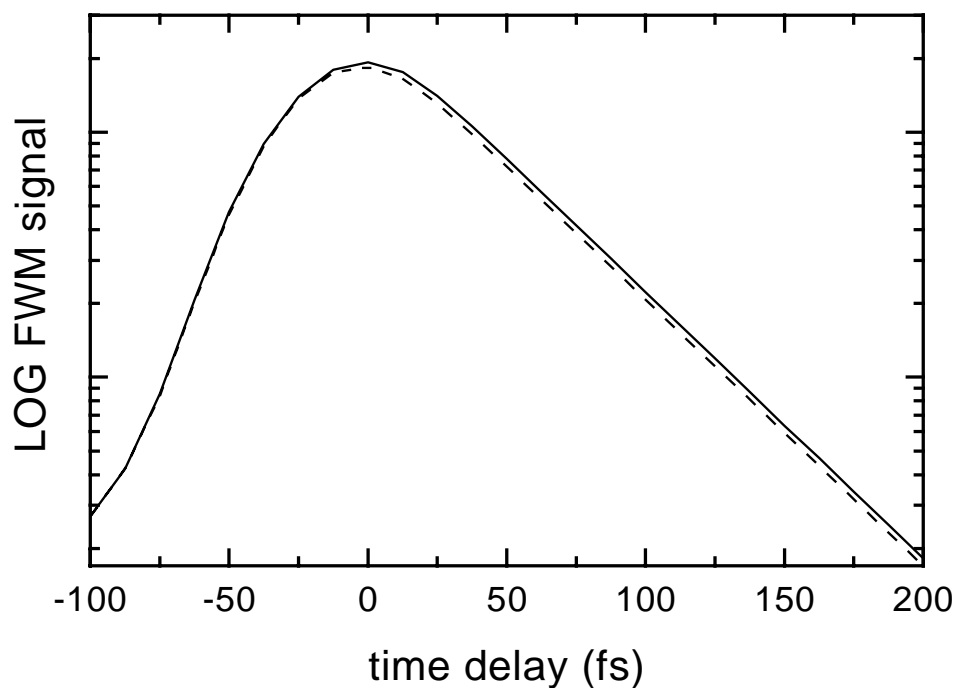


Figure 11.12: Time-integrated FWM for the PPP model. Solid line: model VP, dashed: model IVP.

the PPP model we predict signatures of electronic correlations, which should be observable in ultrafast optical spectroscopy, in both the phase and the amplitude of the signal. We expect analogous effects to be observable using frequency-domain resonant four-wave mixing techniques [244–247]. The coupling coefficients leading to the nonlinear optical response as well as the calculated signals have been compared to theoretical and experimental treatments for inorganic semiconductors. The present approach provides a unified theoretical analysis of resonant nonlinear experiments in organic and inorganic materials.

### 11.3 Appendix A. Equations of motion for two-pulse nonlinear optical response

In this Appendix, we show how the oscillator equations of motion can be used to describe multiple-pulse optical experiments. We consider a two-pulse

nonlinear optical experiment, where the exciting field is given by

$$\begin{aligned} E(t) &= E_1(t)(e^{i\mathbf{k}_1 \cdot \mathbf{r} - i\omega_1 t} + e^{-i\mathbf{k}_1 \cdot \mathbf{r} + i\omega_1 t}) + E_2(t)(e^{i\mathbf{k}_2 \cdot \mathbf{r} - i\omega_2 t} + e^{-i\mathbf{k}_2 \cdot \mathbf{r} + i\omega_2 t}) \\ &= E_1^+(t)e^{-i\omega_1 t} + E_1^-(t)e^{i\omega_1 t} + E_2^+(t)e^{-i\omega_2 t} + E_2^-(t)e^{i\omega_2 t}. \end{aligned} \quad (11.23)$$

$E_{1,2}(t)$  are the pulse envelopes. The term  $E_i^+$  ( $E_i^-$ ) refer to the components of  $E$  with direction  $+\mathbf{k}_i$  ( $-\mathbf{k}_i$ ). Such an exciting field will create excitations associated with different directions  $e^{i\mathbf{K} \cdot \mathbf{r}}$ ,  $\mathbf{K} = n\mathbf{k}_1 + m\mathbf{k}_2$ , where  $n, m$  can be any integers [225,248]. We label these different directional components by  $(n|m)$ , which refers to the excitation associated with the direction  $n\mathbf{k}_1 + m\mathbf{k}_2$ . Inserting this decomposition into the equations of motion Eq. (11.4) and transforming to the rotating frame, leads to

$$\begin{aligned} i\frac{\partial}{\partial t}z_\alpha^{(n|m)} &= (\Omega_\alpha - n\omega_1 - m\omega_2)z_\alpha^{(n|m)} \\ &- \mu_\alpha(\delta_{n=1}\delta_{m=0}E_1^+ + \delta_{n=-1}\delta_{m=0}E_1^- + \delta_{n=0}\delta_{m=1}E_2^+ + \delta_{n=0}\delta_{m=-1}E_2^-) \\ &- E_1^+ \sum_\beta \mu_{\alpha,\beta}z_\beta^{(n-1|m)} - E_1^- \sum_\beta \mu_{\alpha,\beta}z_\beta^{(n+1|m)} \\ &- E_2^+ \sum_\beta \mu_{\alpha,\beta}z_\beta^{(n|m-1)} - E_2^- \sum_\beta \mu_{\alpha,\beta}z_\beta^{(n|m+1)} \\ &- E_1^+ \sum_{n'm'\beta\gamma} \mu_{\alpha,\beta\gamma}z_\beta^{(n-n'-1|m-m')}z_\gamma^{(n'|m')} - E_1^- \sum_{n'm'\beta\gamma} \mu_{\alpha,\beta\gamma}z_\beta^{(n-n'+1|m-m')}z_\gamma^{(n'|m')} \\ &- E_2^+ \sum_{n'm'\beta\gamma} \mu_{\alpha,\beta\gamma}z_\beta^{(n-n'|m-m'-1)}z_\gamma^{(n'|m')} - E_2^- \sum_{n'm'\beta\gamma} \mu_{\alpha,\beta\gamma}z_\beta^{(n-n'|m-m'+1)}z_\gamma^{(n'|m')} \\ &+ \sum_{n'm'\beta\gamma} V_{\alpha,\beta\gamma}z_\beta^{(n-n'|m-m')}z_\gamma^{(n'|m')} \\ &+ \sum_{n'm'n''m''\beta\gamma\delta} V_{\alpha,\beta\gamma\delta}z_\beta^{(n-n'-n''|m-m'-m'')}z_\gamma^{(n'|m')}z_\delta^{(n''|m'')} \end{aligned} \quad (11.24)$$

The polarization is given by:

$$\begin{aligned} P^{(n|m)}(t) &= e^{i(n\mathbf{k}_1+m\mathbf{k}_2) \cdot \mathbf{r} - i(n\omega_1+m\omega_2)t} \\ &\times \left( \sum_\beta \tilde{\mu}_{\beta}z_\beta^{(n|m)} + \sum_{n',m',\beta\gamma} \tilde{\mu}_{\beta\gamma}z_\beta^{(n-n'|m-m')}z_\gamma^{(n'|m')} \right), \end{aligned} \quad (11.25)$$

These equations can be used to describe two pulse experiments; the generalization to experiments with more than two exciting pulses is straightforward.

In Eq. (11.24) we have only to solve explicitly for the complex amplitudes of the oscillator variables associated with positive frequency ( $\alpha > 0$ ). The amplitudes for the corresponding modes with negative frequencies are determined by:  $z_{-\alpha}^{(n|m)} = (z_{\alpha}^{(-n|-m)})^*$ , here  $-\alpha$  refers to the adjoint mode of  $\alpha$ . All oscillator variables and amplitudes have to be included in the summations appearing in right hand sides of Eqs. (11.24) and (11.25).

## 11.4 Appendix B. Iterative calculation of the four-wave mixing signal

In the following we perform a detailed analysis of FWM in self-diffraction geometry, where the third-order signal is monitored in the direction  $2\mathbf{k}_2 - \mathbf{k}_1$ . Only  $B_u$  oscillators can be excited in the linear response.

$$\begin{aligned}
i\frac{\partial}{\partial t}z_{\alpha}^{(1|0)} &= (\Omega_{\alpha} - \omega_1)z_{\alpha}^{(1|0)} - \mu_{\alpha}E_1^+ \\
i\frac{\partial}{\partial t}z_{\alpha}^{(-1|0)} &= (\Omega_{\alpha} + \omega_1)z_{\alpha}^{(-1|0)} - \mu_{\alpha}E_1^- \\
i\frac{\partial}{\partial t}z_{\alpha}^{(0|1)} &= (\Omega_{\alpha} - \omega_2)z_{\alpha}^{(0|1)} - \mu_{\alpha}E_2^+ \\
i\frac{\partial}{\partial t}z_{\alpha}^{(0|-1)} &= (\Omega_{\alpha} + \omega_2)z_{\alpha}^{(0|-1)} - \mu_{\alpha}E_2^- \\
z_{-\alpha}^{(1|0)} &= (z_{\alpha}^{(-1|0)})^* \\
z_{-\alpha}^{(-1|0)} &= (z_{\alpha}^{(1|0)})^* \\
z_{-\alpha}^{(0|1)} &= (z_{\alpha}^{(0|-1)})^* \\
z_{-\alpha}^{(0|-1)} &= (z_{\alpha}^{(0|1)})^*
\end{aligned} \tag{11.26}$$

The second order response consists of different contributions. The particle-particle part is given by  $T(\xi)$  and has not to be calculated separately, but is completely determined by the linear response [56]. Additionally  $A_g$  oscillators can be excited in second order, representing the particle-hole part of the response. To calculate the FWM signal in the direction  $2\mathbf{k}_2 - \mathbf{k}_1$  in third order,



we have to consider a transient-grating ( $\mathbf{k}_2 - \mathbf{k}_1; \omega_1 - \omega_2$ ) and a two-photon ( $2\mathbf{k}_2; -2\omega_2$ ) response.

$$\begin{aligned}
i\frac{\partial}{\partial t}z_{\alpha}^{(-1|1)} &= (\Omega_{\alpha} + \omega_1 - \omega_2)z_{\alpha}^{(-1|1)} - E_1^{-} \sum_{\beta} \mu_{\alpha,\beta} z_{\beta}^{(0|1)} - E_2^{+} \sum_{\beta} \mu_{\alpha,\beta} z_{\beta}^{(-1|0)} \\
&+ \sum_{\beta\gamma} (V_{\alpha,\beta\gamma} + V_{\alpha,\gamma\beta}) z_{\beta}^{(-1|0)} z_{\gamma}^{(0|1)} \\
i\frac{\partial}{\partial t}z_{\alpha}^{(1|-1)} &= (\Omega_{\alpha} - \omega_1 + \omega_2)z_{\alpha}^{(1|-1)} - E_1^{+} \sum_{\beta} \mu_{\alpha,\beta} z_{\beta}^{(0|-1)} - E_2^{-} \sum_{\beta} \mu_{\alpha,\beta} z_{\beta}^{(1|0)} \\
&+ \sum_{\beta\gamma} (V_{\alpha,\beta\gamma} + V_{\alpha,\gamma\beta}) z_{\beta}^{(1|0)} z_{\gamma}^{(0|-1)} \\
i\frac{\partial}{\partial t}z_{\alpha}^{(0|2)} &= (\Omega_{\alpha} - 2\omega_2)z_{\alpha}^{(0|2)} - E_2^{+} \sum_{\beta} \mu_{\alpha,\beta} z_{\beta}^{(0|1)} \\
&+ \sum_{\beta\gamma} V_{\alpha,\beta\gamma} z_{\beta}^{(0|1)} z_{\gamma}^{(0|1)} \\
i\frac{\partial}{\partial t}z_{\alpha}^{(0|-2)} &= (\Omega_{\alpha} + 2\omega_2)z_{\alpha}^{(0|-2)} - E_2^{-} \sum_{\beta} \mu_{\alpha,\beta} z_{\beta}^{(0|-1)} \\
&+ \sum_{\beta\gamma} V_{\alpha,\beta\gamma} z_{\beta}^{(0|-1)} z_{\gamma}^{(0|-1)} \\
z_{-\alpha}^{(-1|1)} &= (z_{\alpha}^{(1|-1)})^* \\
z_{-\alpha}^{(1|-1)} &= (z_{\alpha}^{(-1|1)})^* \\
z_{-\alpha}^{(0|2)} &= (z_{\alpha}^{(0|-2)})^* \\
z_{-\alpha}^{(0|-2)} &= (z_{\alpha}^{(0|2)})^*
\end{aligned} \tag{11.27}$$

In third order again only  $B_u$  oscillators can be excited:

$$\begin{aligned}
i\frac{\partial}{\partial t}z_{\alpha}^{(-1|2)} &= (\Omega_{\alpha} + \omega_1 - 2\omega_2)z_{\alpha}^{(-1|2)} - E_1^{-} \sum_{\beta} \mu_{\alpha,\beta} z_{\beta}^{(0|2)} - E_2^{+} \sum_{\beta} \mu_{\alpha,\beta} z_{\beta}^{(-1|1)} \\
&- E_1^{-} \sum_{\beta\gamma} \mu_{\alpha,\beta\gamma} z_{\beta}^{(0|1)} z_{\gamma}^{(0|1)} - E_2^{+} \sum_{\beta\gamma} (\mu_{\alpha,\beta\gamma} + \mu_{\alpha,\gamma\beta}) z_{\beta}^{(-1|0)} z_{\gamma}^{(0|1)} \\
&+ \sum_{\beta\gamma} (V_{\alpha,\beta\gamma} + V_{\alpha,\gamma\beta}) z_{\beta}^{(0|2)} z_{\gamma}^{(-1|0)} + \sum_{\beta\gamma} (V_{\alpha,\beta\gamma} + V_{\alpha,\gamma\beta}) z_{\beta}^{(-1|1)} z_{\gamma}^{(0|1)} \\
&+ \sum_{\beta\gamma\delta} (V_{\alpha,\beta\gamma\delta} + V_{\alpha,\gamma\beta\delta} + V_{\alpha,\gamma\delta\beta}) z_{\beta}^{(-1|0)} z_{\gamma}^{(0|1)} z_{\delta}^{(0|1)} \\
i\frac{\partial}{\partial t}z_{\alpha}^{(1|-2)} &= (\Omega_{\alpha} - \omega_1 + 2\omega_2)z_{\alpha}^{(1|-2)} - E_1^{+} \sum_{\beta} \mu_{\alpha,\beta} z_{\beta}^{(0|-2)} - E_2^{-} \sum_{\beta} \mu_{\alpha,\beta} z_{\beta}^{(1|-1)}
\end{aligned}$$

$$\begin{aligned}
& - E_1^+ \sum_{\beta\gamma} \mu_{\alpha,\beta\gamma} z_\beta^{(0|-1)} z_\gamma^{(0|-1)} - E_2^- \sum_{\beta\gamma} (\mu_{\alpha,\beta\gamma} + \mu_{\alpha,\gamma\beta}) z_\beta^{(1|0)} z_\gamma^{(0|-1)} \\
& + \sum_{\beta\gamma} (V_{\alpha,\beta\gamma} + V_{\alpha,\gamma\beta}) z_\beta^{(0|-2)} z_\gamma^{(1|0)} + \sum_{\beta\gamma} (V_{\alpha,\beta\gamma} + V_{\alpha,\gamma\beta}) z_\beta^{(1|-1)} z_\gamma^{(0|-1)} \\
& + \sum_{\beta\gamma\delta} (V_{\alpha,\beta\gamma\delta} + V_{\alpha,\gamma\beta\delta} + V_{\alpha,\gamma\delta\beta}) z_\beta^{(1|0)} z_\gamma^{(0|-1)} z_\delta^{(0|-1)} \\
z_{-\alpha}^{(-1|2)} & = (z_\alpha^{(1|-2)})^* \\
z_{-\alpha}^{(1|-2)} & = (z_\alpha^{(-1|2)})^*
\end{aligned} \tag{11.28}$$

The polarization in the  $2\mathbf{k}_2 - \mathbf{k}_1$  direction is finally given by:

$$\begin{aligned}
P^{(-1|2)}(t) & = e^{i(-\mathbf{k}_1+2\mathbf{k}_2)\cdot\mathbf{r}-i(-\omega_1+2\omega_2)t} \left( \sum_{\beta} \tilde{\mu}_\beta z_\beta^{(-1|2)} \right. \\
& \left. + \sum_{\beta\gamma} (\tilde{\mu}_{\beta\gamma} + \tilde{\mu}_{\gamma\beta}) (z_\beta^{(-1|0)} z_\gamma^{(0|2)} + z_\beta^{(0|1)} z_\gamma^{(-1|1)}) \right). \tag{11.29}
\end{aligned}$$

Eqs. (11.28) and (11.29) include all resonant and nonresonant pathways that can contribute to the two-pulse FWM experiment considered here.

## 11.5 Appendix C. Elimination of off-resonant oscillators

Below we describe how the general equations of motion of Appendix 11.4 can be reduced to include only the relevant oscillators, which are needed for the description of resonant FWM. In our numerical calculations we have assumed that the central frequency of both exciting pulses is in resonance with the transition to the  $1B_u$  oscillator, i.e.:  $\omega_L = \omega_1 = \omega_2 = \Omega(1B_u)$ . The pulse envelopes are assumed to be Gaussian,  $E(t) \propto e^{-((t-\hat{t})/\bar{t})^2}$ , with a width of  $\bar{t} = 20fs$ . Since the spectral width of even these very short laser pulses (about  $0.1eV$ ) is small compared to the frequency spacing between the dominant oscillators, only a few oscillators will be excited resonantly. Our calculations show that the first and third order response is to very good accuracy dominated by only the  $1B_u$  oscillator. In second order there may be one  $A_g$  oscillator which appears

as resonantly excited two-photon transition. We now develop equations which only retain two primary oscillators, the  $1B_u$  and one  $A_g$  oscillator explicitly. The off-resonant contributions from all other  $A_g$  oscillators in second order, can be eliminated from the equations of motion and will result in renormalization of anharmonicities and scattering constants.

The elimination of the off-resonant oscillators goes as follows: In the equation of motion for the two-photon resonances  $z_\alpha^{(0|2)}$  we assume that the amplitude adiabatically follows its inhomogeneity on the right hand side of the equation. So we can set  $\frac{\partial}{\partial t} z_\alpha^{(0|2)} = 0$  and then solve the equation, which gives:

$$z_\alpha^{(0|2)} = \frac{1}{\Omega_\alpha - 2\omega_L} (E_2^+ \mu_{\alpha,1} z_1^{(0|1)} - V_{\alpha,11} z_1^{(0|1)} z_1^{(0|1)}) \quad . \quad (11.30)$$

The contributions of  $A_g$  oscillator variables associated with negative frequency are given by:

$$z_{-\alpha}^{(0|2)} = \frac{1}{\Omega_\alpha + 2\omega_L} (E_2^+ \mu_{\alpha,-1} z_1^{(0|1)} - V_{\alpha,-1-1} z_1^{(0|1)} z_1^{(0|1)}) \quad . \quad (11.31)$$

Here the index 1 refers to the positive frequency oscillator variable of  $1B_u$  oscillator and  $-1$  to its adjoint, i.e. the negative frequency variable.

The similar elimination can be done for the transient-grating like terms. Here all oscillators can be assumed to be off resonant, since there is no particle-hole oscillator with zero frequency.

$$z_\alpha^{(-1|1)} = \frac{1}{\Omega_\alpha} (E_1^- \mu_{\alpha,1} z_1^{(0|1)} + E_2^+ \mu_{\alpha,-1} z_{-1}^{(-1|0)} - (V_{\alpha,1-1} + V_{\alpha,-11}) z_{-1}^{(-1|0)} z_1^{(0|1)}) \quad (11.32)$$

and

$$z_{-\alpha}^{(-1|1)} = \frac{1}{\Omega_\alpha} (E_1^- \mu_{\alpha,-1} z_1^{(0|1)} + E_2^+ \mu_{\alpha,1} z_{-1}^{(-1|0)} - (V_{\alpha,-11} + V_{\alpha,1-1}) z_{-1}^{(-1|0)} z_1^{(0|1)}) \quad (11.33)$$

These expressions for the off-resonant second order quantities can be inserted into the equation for the third order amplitude, which leads to the renormalization of some nonlinear coupling constants and a few additional terms. After this elimination, keeping just two oscillators explicitly (1 refers

to the  $1B_u$  oscillator and 2 the  $A_g$  considered as a two-photon resonance), the FWM signal is determined by the following set of equations. In first order:

$$\begin{aligned}
i \frac{\partial}{\partial t} z_1^{(1|0)} &= (\Omega_1 - \omega_L) z_1^{(1|0)} - \mu_1 E_1^+ \\
z_{-1}^{(-1|0)} &= (z_1^{(1|0)})^* \\
i \frac{\partial}{\partial t} z_1^{(0|1)} &= (\Omega_1 - \omega_L) z_1^{(0|1)} - \mu_1 E_2^+ \\
z_{-1}^{(0|-1)} &= (z_1^{(0|1)})^*
\end{aligned} \tag{11.34}$$

In second order:

$$i \frac{\partial}{\partial t} z_2^{(0|2)} = (\Omega_2 - 2\omega_L) z_2^{(0|2)} - E_2^+ \mu_{12} z_1^{(0|1)} + V_{12} z_1^{(0|1)} z_1^{(0|1)}. \tag{11.35}$$

And in third order:

$$\begin{aligned}
i \frac{\partial}{\partial t} z_1^{(-1|2)} &= (\Omega_1 - \omega_L) z_1^{(-1|2)} - E_1^- E_2^+ (Y_1 + X_1) z_1^{(0|1)} - (E_2^+)^2 (X_{-1}) z_{-1}^{(-1|0)} \\
&- E_1^- \mu_{12} z_2^{(0|2)} - E_1^- (s_2 + Y_3 + X_3) z_1^{(0|1)} z_1^{(0|1)} - E_2^+ (s_1 + Y_2 + X_2) z_{-1}^{(-1|0)} z_1^{(0|1)} \\
&+ 2V_{12} z_2^{(0|2)} z_{-1}^{(-1|0)} + (V_1 + Y_4 + X_4) z_{-1}^{(-1|0)} z_1^{(0|1)} z_1^{(0|1)}
\end{aligned} \tag{11.36}$$

The polarization in the direction is given by:

$$\begin{aligned}
P^{(-1|2)}(t) &= e^{i(-\mathbf{k}_1 + 2\mathbf{k}_2) \cdot \mathbf{r} - i(-\omega_1 + 2\omega_2)t} \left( \mu_1 z_1^{(-1|2)} + \sum_{\beta} \mu_{1\beta} z_{-1}^{(-1|0)} z_{\beta}^{(0|2)} \right. \\
&\left. + \sum_{\beta} \mu_{-1\beta} z_1^{(0|1)} z_{\beta}^{(-1|1)} \right).
\end{aligned} \tag{11.37}$$

In these equations we have used some abbreviations:

$$\begin{aligned}
\mu_1 &= \tilde{\mu}_1 \\
\mu_{1n} &= \mu_{1,n} = \mu_{n,1} = (\tilde{\mu}_{-1n} + \tilde{\mu}_{n-1}) \\
s_1 &= (\mu_{1,-11} + \mu_{1,1-1}) \\
s_2 &= \mu_{1,11} \\
V_1 &= (V_{1,11-1} + V_{1,1-11} + V_{1,-111}) \\
V_{12} &= V_{2,11} = \frac{1}{2}(V_{1,-12} + V_{1,2-1}).
\end{aligned} \tag{11.38}$$

The quantities  $X_i$  and  $Y_i$  result from the elimination of the transient grating and two-photon resonances, respectively. They are given by the following summations over the  $A_q$  oscillator variables  $\beta$ :

$$\begin{aligned}
X_1 &= \sum_{\beta} \frac{\mu_{1,\beta}\mu_{\beta,1} + \mu_{1,-\beta}\mu_{\beta,-1}}{\Omega_{\beta}} \\
X_{-1} &= \sum_{\beta} \frac{\mu_{1,\beta}\mu_{\beta,-1} + \mu_{1,-\beta}\mu_{\beta,1}}{\Omega_{\beta}} \\
X_2 &= \sum_{\beta} \frac{-1}{\Omega_{\beta}} (\mu_{1,\beta}(V_{\beta,-11} + V_{\beta,1-1}) + \mu_{\beta,-1}(V_{1,\beta 1} + V_{1,1\beta})) \\
&\quad + \mu_{1,-\beta}(V_{\beta,1-1} + V_{\beta,-11}) + \mu_{\beta,1}(V_{1,-\beta 1} + V_{1,1-\beta}) \\
X_3 &= \sum_{\beta} \frac{-1}{\Omega_{\beta}} (\mu_{\beta,1}(V_{1,\beta 1} + V_{1,1\beta}) + \mu_{\beta,-1}(V_{1,-\beta 1} + V_{1,1-\beta})) \\
X_4 &= \sum_{\beta} \frac{-1}{\Omega_{\beta}} ((V_{\beta,-11} + V_{\beta,1-1})(V_{1,\beta 1} + V_{1,1\beta}) \\
&\quad + (V_{\beta,1-1} + V_{\beta,-11})(V_{1,-\beta 1} + V_{1,1-\beta})) \\
Y_1 &= \sum'_{\beta} \frac{1}{\Omega_{\beta} - 2\omega_L} \mu_{1,\beta}\mu_{\beta,1} \\
&\quad + \sum'_{\beta} \frac{1}{\Omega_{\beta} + 2\omega_L} \mu_{1,-\beta}\mu_{\beta,-1} \\
Y_2 &= \sum'_{\beta} \frac{-1}{\Omega_{\beta} - 2\omega_L} \mu_{\beta,1}(V_{1,\beta-1} + V_{1,-1\beta}) \\
&\quad + \sum'_{\beta} \frac{-1}{\Omega_{\beta} + 2\omega_L} \mu_{\beta,-1}(V_{1,-\beta-1} + V_{1,-1-\beta}) \\
Y_3 &= \sum'_{\beta} \frac{-1}{\Omega_{\beta} - 2\omega_L} \mu_{1,\beta}V_{\beta,11} \\
&\quad + \sum'_{\beta} \frac{-1}{\Omega_{\beta} + 2\omega_L} \mu_{1,-\beta}V_{\beta,-1-1} \\
Y_4 &= \sum'_{\beta} \frac{-1}{\Omega_{\beta} - 2\omega_L} (V_{1,\beta-1} + V_{1,-1\beta})V_{\beta,11} \\
&\quad + \sum'_{\beta} \frac{-1}{\Omega_{\beta} + 2\omega_L} (V_{1,-\beta-1} + V_{1,-1-\beta})V_{\beta,-1-1} . \tag{11.39}
\end{aligned}$$

The primes over the sum symbols for  $Y_i$  indicate, that the summations exclude

the positive frequency variable of the one  $A_g$  oscillator, which is explicitly considered as a two-photon resonance. In Section 11.2 we show, that to a very good accuracy the approximate equations derived in this Appendix reproduce the full results calculated using Eqs. (11.26-11.29).

Inserting the expressions for the amplitudes of the virtual oscillators Eqs. (11.30)-(11.33) into Eq. (11.38) allows to perform the summations over  $\beta$  and simplifies the expression for the polarization. Like in the equations of motion this procedure results in some new anharmonic couplings.

$$\begin{aligned}
P^{(-1|2)}(t) &= e^{i(-\mathbf{k}_1+2\mathbf{k}_2)\cdot\mathbf{r}-i(-\omega_1+2\omega_2)t} [\mu_1 z_1^{(-1|2)} \\
&+ \mu_{12} z_{-1}^{(-1|0)} z_2^{(0|2)} + (A_1 + B_1) z_{-1}^{(-1|0)} (z_1^{(0|1)})^2 \\
&+ (A_2 + B_2) E_2^+ z_{-1}^{(-1|0)} z_1^{(0|1)} + A_3 E_1^- (z_1^{(0|1)})^2] \quad . \quad (11.40)
\end{aligned}$$

Here  $A_1$ ,  $A_2$ , and  $A_3$  are obtained via elimination of the transient-grating terms involving virtual oscillators, and  $B_1$ , as well as  $B_2$  from the corresponding two-photon terms.

# Chapter 12

## Conclusions

A theoretical approach for calculating electronic structure of organic molecules has been developed. The method is based on the collective electronic oscillators (CEO) which represent the dynamics of the optically-driven reduced single-electron density matrix and relate the electronic properties of molecules directly to the motions of electron-hole pairs in real space.

The iterative DSMA procedure has been applied for computing efficiently the electronic oscillators dominating optical response. The computational time (and memory) requirements of this algorithm scale very favorably with system size:  $\sim N^3$  (and  $N^2$ ). A Fortran 77 code was developed which implements the DSMA to calculate molecular electronic spectra. It interfaces with standard quantum chemistry programs and employs the ZINDO package to generate the INDO/S hamiltonian using *ab-initio* optimized molecular geometry, experimental X-ray diffraction, or NMR data. This code makes it possible to compute optical spectra of very large molecules with hundreds of heavy atoms with minimal computational effort. A simple single-oscillator approximation for the off-resonant optical polarizabilities of polyene chains, which reproduce their magnitude and scaling with molecular size and allows a quick prediction of trends, was derived. The CEO was further extended for calculating relevant properties of excited electronic states.

To analyze the calculated spectra, a real-space representation of computed electronic oscillators has been developed. By displaying the electronic mode matrices using two-dimensional plots, a direct connection is established between the optical response and motions of charges in the molecule upon optical excitation. The CEO was applied to the wide variety of conjugated and aggregated organic molecules. The results pinpoint the origin of optical response in these molecules, predict the trends, and may be useful in the design of the new optical materials. Semiconductor, metallic and molecular materials are treated by physicists and chemists using completely different approaches. Application the CEO to systems of various sizes, ranging from small molecules and nanostructures all the way to the bulk, cuts across these disciplines, and should allow a unified treatment of these various materials.



# Bibliography

- [1] S. R. Marder, W. E. Torruellas, V. R. M. Blanchard Desce, G. I. Stegeman, S. Gilmour, J. L. Brédas, J. Li, G. U. Bublitz, and S. G. Boxer, *Science* **276**, 1233 (1997).
- [2] V. Ricci, Master's thesis, Department of Electrical Engineering, University of Central Florida, 1995.
- [3] R. Kopelman, M. Shortreed, Z.-Y. Shi, W. Tan, Z. Xu, J. S. Moore, A. Bar-Haim, and Y. Klafter, *Phys. Rev. Lett.* **78**, 1239 (1997).
- [4] J. B. Birks, *Photophysics of Aromatic Molecules* (Wiley, New York, 1970).
- [5] J. Michl and V. Bonacic-Koutecky, *Photophysics of Aromatic Molecules* (Wiley, New York, 1990).
- [6] M. Klessinger and J. Michl, *Excited States and Photochemistry of Organic Molecules* (VCH, New York, 1995).
- [7] G. U. Bublitz, R. Ortiz, S. R. Marder, and S. G. Boxer, *J. Am. Chem. Soc.* **119**, 3365 (1997).
- [8] M. Blanchard-Desce, J.-M. Lehn, M. Barzoukas, C. Runser, A. Fort, G. Puccetti, I. Ledoux, and J. Zyss, *Nonlinear Optics* **10**, 23 (1995).
- [9] M. Blanchard-Desce, R. Woltmann, J.-M. L. S. Lebus, and P. Kramer, *Chem. Phys. Lett.* **243**, 526 (1995).

- [10] D. R. Kanis, M. A. Ratner, and T. J. Marks, *Chem. Rev.* **94**, 195 (1994).
- [11] J. L. Brédas, C. Adant, P. Tackyx, A. Persoons, and B. M. Pierce, *Chem. Rev.* **94**, 243 (1994).
- [12] M. Blanchard-Desce, C. Runser, A. Fort, M. Barzoukas, J.-M. Lehn, V. Bloy, and V. Alain, *Chem. Phys.* **199**, 253 (1995).
- [13] M. Blanchard-Desce, J.-M. Lehn, M. Barzoukas, I. Ledoux, and J. Zyss, *Chem. Phys.* **181**, 281 (1994).
- [14] M. C. Zerner, K. K. Stavrev, and T. J. Meyer, *J. Am. Chem. Soc.* **117**, 8684 (1995).
- [15] A. Broo and M. C. Zerner, *Chem. Phys.* **196**, 407,423 (1995).
- [16] G. Gustafson, Y. Gao, G. M. Treacy, F. Klauetter, N. Colaneri, and A. Heeger, *Nature* **357**, 477 (1992).
- [17] N. C. Greenham, S. C. Maratti, D. D. C. Bradley, A. B. Holmes, and R. H. Friend, *Nature* **65**, 628 (1993).
- [18] N. Tessler, D. J. Denton, and R. H. Friend, *Nature* **382**, 695 (1996).
- [19] D. D. C. Bradley, *Nature* **382**, 671 (1996).
- [20] S. V. Frolov, W. Gellerman, M. Ozaki, K. Yoshino, and Z. V. Vardeny, *Phys. Rev. Lett.* **78**, 729 (1997).
- [21] Proceedings of the International Conference on Synthetic Metals ICSM 96, *Synthetic Metals*, **84**, 1997.
- [22] R. Pachter, R. Crane, and W. W. Adams, *Materials Research Society Symposia Proceedings* **374**, 39 (1995).

- [23] P. of the NATO Advanced Research Workshop, in *Conjugated Polymeric Materials: Opportunities in Electronics, Optoelectronics, and Molecular Electronics*, Vol. 182 of *NATO ASI, Series E: Applied Sciences*, edited by J. Bredás and R. Chance (Kluwer, Dordrecht, 1990).
- [24] Special Issue "Confined Excitations in Molecular and Semiconductor Nanostructures", edited by S. Mukamel and D. S. Chemla, *Chem. Phys.*, **210**, 1996.
- [25] *Nonlinear Optical Properties of Organic Molecules and Crystals*, edited by J. Zyss and D. S. Chemla (Academic Press, Florida, 1987), Vol. 1 and 2.
- [26] J. F. Ward, *Rev. Mod. Phys.* **37**, 1 (1965).
- [27] B. J. Orr and J. F. Ward, *Mol. Phys.* **20**, 513 (1971).
- [28] J. F. Heflin, K. Y. Wong, Q. Zamani-Khamini, and A. F. Garito, *Phys. Rev. B* **38**, 1573 (1988).
- [29] D. C. Rodenberger, J. F. Heflin, and A. F. Garito, *Nature* **359**, 309 (1992).
- [30] B. Kirtman, J. L. Toto, K. A. Robins, and M. Hasan, *J. Chem. Phys.* **102**, 13 (1995).
- [31] T. T. Toto, J. L. Toto, C. P. de Melo, M. Hasan, and B. Kirtman, *Chem. Phys. Lett* **244**, 59 (1995).
- [32] S. A. Kicharski and R. J. Bartlett, *J. Chem. Phys.* **97**, 4282 (1992).
- [33] H. Sekino and R. J. Bartlett, *J. Chem. Phys.* **95**, 8227 (1991).
- [34] H. Sekino and R. J. Bartlett, *J. Chem. Phys.* **94**, 3665 (1991).

- [35] Z. G. Soos, D. S. Galvao, and S. Etemad, *Phys. Rev. B* **47**, 1742 (1993).
- [36] Z. G. Soos, S. Ramasesha, D. Galvao, R. Kepler, and S. Etemad, *Synth. Metals* **54**, 35 (1993).
- [37] D. Mukhopadhyay, G. W. Hayden, and Z. G. Soos, *Phys. Rev. B* **51**, 15 (1995).
- [38] H. Haug and S. W. Koch, *Quantum Theory of the Optical and Electronic Properties of Semiconductors*, 3rd ed. (World Scientific, Singapore, 1994).
- [39] J. A. Pople, P. M. W. Gill, and B. J. Johnson, *Chem. Phys. Lett.* **199**, 557 (1992).
- [40] A. D. Becke, *Phys. Rev. A* **38**, 3098 (1988).
- [41] E. K. U. Gross, J. F. Dobson, and M. Petersilka, in *Density Functional Theory*, edited by R. F. Nalewajski (Springer, Berlin, 1996), Vol. 181.
- [42] M. E. Casida, in *Recent Advances in Density-Functional Methods*, Vol. 3 of *Part I*, edited by D. A. Chong (World Scientific, Singapore, 1995).
- [43] C. Jamorski, M. E. Casida, and D. R. Salahub, *J. Chem. Phys.* **104**, 5134 (1996).
- [44] P. Hohenberg and W. Kohn, *Phys. Rev.* **136**, B864 (1964).
- [45] W. Kohn and L. J. Sham, *Phys. Rev.* **140**, A1133 (1965).
- [46] R. McWeeny and B. T. Sutcliffe, *Methods of Molecular Quantum Mechanics* (Academic Press, New York, 1976).
- [47] E. R. Davidson, *Reduced Density Matrices in Quantum Chemistry* (Academic Press, New York, 1976).

- [48] P. O. Lowdin, *Phys. Rev.* **97**, 1474 (1955).
- [49] P. O. Lowdin, *Adv. in Phys.* **5**, 1 (1956).
- [50] R. S. Milliken, *J. Chem. Phys.* **23**, 1833, 1841, 2338, 2343 (1955).
- [51] A. Szabo and N. S. Ostlund, *Modern Quantum Chemistry: Introduction to Advanced Electronic Structure Theory* (McGraw-Hill, New York, 1989).
- [52] P. Ring and P. Schuck, *The Nuclear Many-Body Problem* (Springer-Verlag, New York, 1980).
- [53] J.-P. Blaizot and G. Ripka, *Quantum Theory of Finite Systems* (The MIT Press, Cambridge Massachusetts, 1986).
- [54] H. Sekino and R. J. Bartlett, *J. Chem. Phys.* **85**, 976 (1986).
- [55] A. Takahashi and S. Mukamel, *J. Chem. Phys.* **100**, 2366 (1994).
- [56] V. Chernyak and S. Mukamel, *J. Chem. Phys.* **104**, 444 (1996).
- [57] P. A. Dirac, *Proc. Camb. Phil. Soc.* **26**, 376 (1930).
- [58] R. A. Ferrel, *Phys. Rev.* **107**, 1631 (1957).
- [59] S. Mukamel and H. X. Wang, *Phys. Rev. Lett.* **69**, 65 (1992).
- [60] S. Mukamel, A. Takahashi, H. X. Wang, and G. Chen, *Science* **266**, 251 (1994).
- [61] T. Wagersreiter and S. Mukamel, *J. Chem. Phys.* **104**, 7086 (1996).
- [62] H. Fukutome, *J. Mol. Struct. (Theochem)* **188**, 337 (1989).
- [63] M. Hartmann, V. Chernyak, and S. Mukamel, *Phys. Rev. B* **52**, 2528 (1995).

- [64] J. A. Pople and G. A. Segal, *J. Chem. Phys.* **43**, S136 (1965).
- [65] J. A. Pople, D. L. Beveridge, and P. Dobosh, *J. Chem. Phys.* **47**, 2026 (1967).
- [66] J. Ridley and M. C. Zerner, *Theor. Chim. Acta* **32**, 111 (1973).
- [67] M. C. Zerner, G. H. Loew, R. F. Kirchner, and U. T. Mueller-Westerhoff, *J. Am. Chem. Soc.* **102**, 589 (1980).
- [68] J. E. Ridley and M. C. Zerner, *Theoret. Chim. Acta* **42**, 223 (1976).
- [69] A. D. Bacon and M. C. Zerner, *Theoret. Chim. Acta* **53**, 21 (1979).
- [70] S. Tretiak, V. Chernyak, and S. Mukamel, *J. Am. Chem. Soc.* **119**, 11408 (1997).
- [71] S. Yokojima, T. Meier, and S. Mukamel, *J. Chem. Phys.* **106**, 3837 (1997).
- [72] S. Mukamel, *Principles of Nonlinear Optical Spectroscopy* (Oxford, New York, 1995).
- [73] S. Tretiak, V. Chernyak, and S. Mukamel, *J. Chem. Phys.* **105**, 8914 (1996).
- [74] S. Tretiak, V. Chernyak, and S. Mukamel, *Chem. Phys. Lett.* **259**, 55 (1996).
- [75] J. K. Cullum and R. A. Willoughby, *J. Comp. Phys.* **44**, 329 (1981).
- [76] T. J. Park and J. C. Light, *J. Chem. Phys.* **85**, 10 (1986).
- [77] C. Leforestier *et al.*, *J. Comp. Phys.* **94**, 59 (1991).
- [78] H. Mori, *Prog. Theoret. Phys.* **33**, 423 (1965).

- [79] H. Mori, *Prog. Theoret. Phys.* **34**, 399 (1965).
- [80] R. Zwanzig, *Lect. Theoret. Phys.* **3**, 106 (1961).
- [81] G. Brosso and G. P. Parravicini, *Adv. Chem. Phys.* **62**, 81,133 (1985).
- [82] R. R. Ernst, G. Bodenhausen, and A. Wokaun, *Principles of Nuclear Magnetic Resonance in One and Two Dimensions* (Clarendon Press, London, 1987).
- [83] A. E. Reed, L. A. Curtiss, and F. Weinhold, *Chem. Rev.* **88**, 899 (1988).
- [84] A. E. Reed, R. B. Weinstock, and F. Weinhold, *J. Chem. Phys.* **83**, 735 (1985).
- [85] H. White, *Phys. Rev. B* **48**, 10335 (1993).
- [86] E. B. Wilson, J. C. Decius, and P. C. Cross, *Molecular Vibrations* (McGraw-Hill, New York, 1955).
- [87] R. W. Hellwarth, *Progr. Quant. Electron.* **5**, 2 (1977).
- [88] G. Placzek, *The Rayleigh and Raman Scattering*, Vol. 256(L) of *UCRL Transl.* (U.S. Department of Commerce, Washington, D.C., 1962).
- [89] R. S. Berry, in *Structure and Dynamics of Atoms and Molecules: Conceptual Trends*, pp. 155-181, edited by J. L. Calais and E. S. Kryachko (Kluwer, Dordrecht, Netherlands, 1995).
- [90] R. van Grondelle, J. P. Dekker, T. Gillboro, and V. Sundström, *Biochim. Biophys. Acta* **1187**, 1 (1994).
- [91] S. E. Bradforth, R. Jimenez, F. von Mourik, R. van Grondelle, and G. R. Fleming, *J. Phys. Chem.* **99**, 16179 (1995).
- [92] B. I. Greene and J. O. S. Schmitt-Rink, *Science* **247**, 679 (1990).

- [93] V. M. Axt and S. Mukamel, *Rev. Mod. Phys.* **70**, 145 (1998).
- [94] O. Dubovsky and S. Mukamel, *J. Chem. Phys.* **95**, 7828 (1991).
- [95] E. Schwegler, M. Challacombe, and M. Head-Gordon, *J. Chem. Phys.* **106**, 9708 (1997).
- [96] M. C. Strain, G. E. Scuseria, and M. J. Frisch, *Science* **271**, 5245 (1996).
- [97] S. Tretiak, V. Chernyak, and S. Mukamel, *Chem. Phys. Lett.* **287**, 75 (1998).
- [98] S. Tretiak, V. Chernyak, and S. Mukamel, *Phys. Rev. Lett.* **77**, 4656 (1996).
- [99] G. Zerbi, E. Galbiati, M. C. Gallazzi, C. Castiglioni, M. D. Zoppo, R. Schenk, and K. J. Mölen, *J. Chem. Phys.* **105**, 2509 (1996).
- [100] G. A. Korn and T. M. Korn, *Mathematical Handbook* (McGraw-Hill Book Company, New York, 1968).
- [101] G. H. Golub and C. F. V. Loan, *Matrix Computation* (Jonh Hopkins University Press, Baltimore, Maryland, 1983).
- [102] V. Chernyak and S. Mukamel, *J. Chem. Phys.* **108**, 5812 (1998).
- [103] L. D. Landau and E. M. Lifshitz, *Mechanics, 3rd ed.* (Pergamon Press, Oxford, New York, 1976).
- [104] S. Mukamel, S. Tretiak, T. Wagersreiter, and V. Chernyak, *Science* **277**, 781 (1997).
- [105] G. P. Agrawal, C. Cojan, and C. Flytzanis, *Phys. Rev. B* **17**, 776 (1978).
- [106] Z. Shuai and J. L. Brédas, *Phys. Rev. B* **44**, 5962 (1991).



- [107] D. Beljonne, Z. Shuai, and J. L. Brédas, *J. Chem. Phys.* **98**, 8819 (1993).
- [108] F. S. Spano and Z. G. Soos, *J. Chem. Phys.* **99**, 9265 (1993).
- [109] C. Bubeck, *Nonlinear Optical Material: Principles and Applications*, edited by V. Degiorgio and C. Flytzanis (IOS Press, Amsterdam 1995), p.359.
- [110] A. Mathy, K. Ueberhofen, R. Schenk, R. Garay, K. Millen, and C. Bubeck, *Phys. Rev. B* **53**, 4367 (1996).
- [111] I. D. W. Samuel, I. Ledoux, C. Dhenaut, J. Zyss, H. H. Fox, R. R. Schrock, and R. J. Silbey, *Science* **265**, 1070 (1994).
- [112] J. P. Hermann and J. Ducuing, *J. Appl. Phys.* **45**, 5100 (1974).
- [113] H. Kuhn, *Fortschr. Chem. Org. Naturstoffe* **17**, 404 (1959).
- [114] E. F. McIntyre and H. F. Hamerka, *J. Chem. Phys.* **68**, 3481 (1978).
- [115] D. N. Beratan, J. N. Onuchic, and J. W. Perry, *J. Chem. Phys.* **91**, 2696 (1987).
- [116] B. M. Pierce, *Physica D* **68**, 51 (1993).
- [117] G. S. W. Graig, R. E. Cohen, R. R. Schrock, C. Dhenaut, I. Ledoux, and J. Zyss, *Macromolecules* **27**, 1875 (1994).
- [118] C. Flytzanis and J. Huttler, *Contemporary Nonlinear Optics*, Edited by G. P. Agrawal and R. W. Boyd (Academic Press, San Diego, 1992).
- [119] D. Neher, A. Kaltbeitzel, A. Wolf, C. Bubeck, and G. Wegner, *Conjugated Polymeric Materials: Opportunities in Electronics, Optoelectronics and Molecular Electronics*, edited by J. L. Brédas, R. R. Chance, (NATO ASI E 182, Kluwer, 1990).

- [120] V. Chernyak and S. Mukamel, *J. Chem. Phys.* **103**, 7640 (1995).
- [121] R. Silbey, *Conjugated Polymeric Materials: Opportunities in Electronics, Optoelectronics and Molecular Electronics*, edited by J. L. Brédas, R. R. Chance, (NATO ASI E 182, Kluwer, Dordrecht, 1990).
- [122] T. W. Hagler, K. Pakbaz, K. F. Voss, and A. J. Heeger, *Phys. Rev. B* **44**, 8652 (1991).
- [123] D. D. C. Bradley, R. H. Friend, H. Lindemberger, and S. Roth, *Polymer* **27**, 1709 (1986).
- [124] D. A. Halliday, P. L. Burn, R. N. Friend, D. D. C. Bradley, A. B. Holmes, and A. Kraft, *Synthetic Metals* **55-57**, 954 (1993).
- [125] A. Sakamoto, Y. Furukawa, and M. Tasumi, *J. Chem. Phys.* **96**, 1490,3870 (1992).
- [126] B. Tian, G. Zerbi, R. Schenk, and K. Müllen, *J.Chem.Phys.* **95**, 3191,3198 (1991).
- [127] U. Rauscher, H. Bässler, D. D. C. Bradley, and M.Hennecke, *Phys. Rev. B* **42**, 9830 (1990).
- [128] J. L. Brédas, R. R. Chance, R. H. Baughman, and R.Silbey, *J. Chem. Phys.* **76**, 3673 (1982).
- [129] J. Cornil, D. Beljonne, R. H. Friend, and J. L. Brédas, *Chem. Phys. Lett.* **223**, 82 (1994).
- [130] W. Z. Wang, A. Saxena, and A. R. Bishop, *Phys. Rev. B* **50**, 6068 (1994).
- [131] M. Chandross, S. Mazumdar, S. Jeglinski, X. Wei, Z. V. Vardeny, E. W. Kwock, and T. M. Miller, *Phys. Rev. B* **50**, 14702 (1994).

- [132] A. K. Ghosh, D. L. Morel, T. Feng, R. F. Shaw, and C. R. Rowe, *J. Appl. Phys.* **45**, 230 (1974).
- [133] P. da Costa *et.al.*, *Synthetic Metals* **55**, 4320 (1993).
- [134] O. Straub, *Key to Carotenoids* (Basel, Boston, 1987).
- [135] G. Britton, S. Liaaen-Jensen, H. Pfander, and (ed.), *Carotenoids* (Basel, Boston: Birkhauser, 1995).
- [136] Y. Koyama and Y. Mukai, *Biomolecular Spectroscopy, Part B, Edited by R. J. H. Clark and R. E. Hester* (John Willey & Sons Ltd, New York, 1993).
- [137] A. Young and G. Britton, *Carotenoids in Photosynthesis, George (ed.)* (Chapman and Hall, London, 1993).
- [138] R. A. Mathies, C. H. B. Cruz, W. T. Pollard, and C. V. Shank, *Science* **240**, 777 (1988).
- [139] W. L. Wilson, P. S. Szajowski, and L. E. Brus, *Science* **262**, 1242 (1993).
- [140] L. E. Brus, *J. Chem. Phys.* **98**, 3575 (1994).
- [141] A. P. Alivisatos, *MRS bulletin* **20**, 23 (1995).
- [142] A. P. Alivisatos, *Science* **271**, 993 (1996).
- [143] M. Nirmal, D. J. Norris, M. Kuno, M. G. Bawendi, A. L. Efros, and M. Rosen, *Phys. Rev. Lett.* **75**, 3728 (1995).
- [144] M. Yan, L. J. Rothberg, F. Papadimitrakopoulos, M. E. Galvin, and T. M. Miller, *Phys. Rev. Lett.* **72**, 1104 (1994).
- [145] M. Yan, L. J. Rothberg, F. Papadimitrakopoulos, M. E. Galvin, and T. Miller, *Phys. Rev. Lett.* **73**, 744 (1994).

- [146] M. Yan, L. J. Rothberg, E. W. Kwock, and T. M. Miller, *Phys. Rev. Lett.* **75**, 1992 (1975).
- [147] A. J. Heeger, S. Kivelson, J. R. Schrieffer, , and W. P. Su, *Rev. Mod. Phys.* **60**, 781 (1988).
- [148] A. Takahashi and S. Mukamel, *J. Chem. Phys.* **103**, 7144 (1995).
- [149] F. Meyers, S. R. Marder, B. M. Pierce, and J. L. Brédas, *J. Am. Chem. Soc.* **116**, 10703 (1994).
- [150] S. R. Marder, J. W. Perry, B. G. Tiemann, C. B. Gorman, S. Gilmour, S. L. Biddle, and G. Bourhill, *J. Am. Chem. Soc.* **115**, 2524 (1993).
- [151] D. A. Tomalia, A. M. Naylor, and W. A. Goddard, *Angew. Chem. Int. Edn. Engl.* **29**, 138 (1990).
- [152] D. L. Jiang and T. Aida, *Nature* **338**, 454 (1997).
- [153] S. Mukamel, *Nature* **338**, 425 (1997).
- [154] M. A. Fox, W. E. Jones, and D. M. Watkins, *Chem. Eng. News* **71**, 38 (1993).
- [155] A. Bar-Haim, J. Klafter, and R. J. Kopelman, *J. Am. Chem. Soc.* **119**, 6197 (1997).
- [156] D. M. Junge and D. V. McGrath, *Chem. Commun.*, 1997.
- [157] M. Shortreed, S. F. Swallen, Z.-Y. Shi, W. Tan, Z. Xu, , C. Devadoss, S. S. Moore, and R. J. Kopelman, *J. Phys. Chem.* **101**, 6318 (1997).
- [158] D. Gust, *Nature* **386**, 21 (1997).
- [159] M. Shortreed, Z.-Y. Shi, and R. Kopelman, *Mol. Cryst. Liq. Cryst.* **283**, 95 (1996).

- [160] C. Devadoss, P. Bharathi, and J. S. Moore, *J. Am. Chem. Soc.* **118**, 9635 (1996).
- [161] M. Pope and C. E. Swenberg, *Electronic Processes in Organic Crystals* (Clarendon Press, Oxford University Press, Oxford, New York, 1982).
- [162] E. A. Silinsh and V. Čápek, *Organic Molecular Crystals* (AIP Press, American Institute of Physics, New York, 1994).
- [163] M. van Burgel, D. A. Wiersma, and K. Duppen, *J. Chem. Phys.* **102**, 20 (1995).
- [164] K. Sauer, R. J. Cogdell, S. M. Prince, A. A. Freer, N. Isaak, and H. Scheer, *Photochem. Photobiol.* **64**, 564 (1996).
- [165] H. Scheer, *Chlorophylls* (CRC Press, Boca Raton Ann Arbor, Boston London, 1991).
- [166] *Iron porphyrins*, edited by A. B. P. Lever (Addison-Wesley press, Reading, MA, 1983).
- [167] *Porphyrins: excited states and dynamics*, edited by M. Gouterman, P. M. Rentzepis, and K. D. Straub (American Chemical Soc., Washington, D.C., 1986).
- [168] C. Weiss, H. Kobayashi, and M. Gouterman, *J. Mol. Spectr.* **16**, 415 (1965).
- [169] W. D. Edwards and M. Zerner, *Int. J. of Quan. Chem.* **23**, 1407 (1983).
- [170] C. Rimington, S. F. Mason, and O. Kennard, *Spectrochim. Acta* **12**, 65 (1958).
- [171] P. Dupuis, R. Roberge, and C. Sandorfy, *Chem. Phys. Lett.* **75**, 434 (1980).

- [172] L. Edwards, D. H. Dolphin, M. Gouterman, and A. D. Adler, *J. Mol. Spectrosc.* **38**, 16 (1971).
- [173] L. Edwards, D. H. Dolphin, M. Gouterman, and A. D. Adler, *J. Mol. Spectrosc.* **35**, 90 (1970).
- [174] J. D. Baker and M. C. Zerner, *Chem. Phys. Lett.* **175**, 192 (1990).
- [175] D. C. Rawlings, E. R. Davidson, and M. Gouterman, *Theoret. Chim. Acta* **61**, 227 (1982).
- [176] D. C. Rawlings, E. R. Davidson, and M. Gouterman, *Int. J. Quantum Chem.* **26**, 237, 251 (1984).
- [177] D. C. Rawlings, E. R. Davidson, M. Gouterman, and D. Feller, *Int. J. Quantum Chem.* **28**, 773, 797, 823 (1985).
- [178] H. Nakatsuji, J. Hasegawa, and M. Hada, *Chem. Phys. Lett.* **104**, 2321 (1996).
- [179] S. R. Gwaltney and R. J. Bartlett, *J. Chem. Phys.* **108**, 6790 (1998).
- [180] W. T. Simpson, *J. Chem. Phys.* **17**, 1218 (1949).
- [181] H. Kuhn, *J. Chem. Phys.* **17**, 1198 (1949).
- [182] M. Gouterman, *J. Mol. Spectr.* **6**, 138 (1961).
- [183] M. Gouterman, G. H. Wagniere, and L. C. Snyder, *J. Mol. Spectr.* **11**, 108 (1963).
- [184] J. Hasegawa, M. Hada, M. Nonoguchi, and H. Nakatsuji, *Chem. Phys. Lett.* **250**, 159 (1996).
- [185] C. Kratky and J. D. Dunitz, *Acta Crystallogr. B* **31**, 1586 (1975).

- [186] D. C. Easter, R. L. Whetten, and J. E. Wessel, *J. Chem. Phys.* **94**, 3347 (1991).
- [187] D. C. Easter, J. T. Khoury, and R. L. Whetten, *J. Chem. Phys.* **97**, 1681 (1992).
- [188] D. C. Easter, A. P. Baronavski, and R. L. Whetten, *J. Chem. Phys.* **99**, 4942 (1993).
- [189] J. A. Syage and J. E. Wessel, *J. Chem. Phys.* **89**, 5962 (1988).
- [190] J. E. Wessel and J. A. Syage, *J. Chem. Phys.* **94**, 737 (1990).
- [191] M. N. Berberan-Santos, J. Canceill, J.-C. Brochon, L. Jullien, J.-M. Lehn, J. Pouget, P. Tauc, and B. Valeur, *J. Am. Chem. Soc.* **114**, 6227 (1992).
- [192] M. N. Berberan-Santos, J. Pouget, P. Tauc, B. Valeur, J. Canceill, L. Jullien, and J.-M. Lehn, *J. Phys. Chem.* **97**, 11376 (1993).
- [193] M. N. Berberan-Santos, J. Canceill, E. Gratton, L. Jullien, J.-M. Lehn, P. So, J. Sutin, and B. Valeur, *J. Phys. Chem.* **100**, 15 (1996).
- [194] Special Issue on Light-Harvesting Physics Workshop, *J. Phys. Chem. B*, **101**, 1997.
- [195] V. Sundström and R. van Grondelle, in *Anoxygenic Photosynthetic Bacteria*, p.349, edited by R. E. Blankenship, M. T. Madiga, and C. E. Baner (Kluwer Academic, Dordrecht, 1995).
- [196] G. D. Scholes, K. P. Ghiggino, A. M. Oliver, and M. N. Paddon-Row, *J. Am. Chem. Soc.* **115**, 4345 (1993).
- [197] A. H. A. Clayton, G. D. Scholes, K. P. Ghiggino, and M. N. Paddon-Row, *J. Phys. Chem.* **100**, 10912 (1996).

- [198] P. Hobra, H. L. Selzle, and E. W. Schlag, *J. Am. Chem. Soc.* **116**, 3500 (1994).
- [199] K. O. Börsen, S. H. Lin, H. L. Selzle, and E. W. Schlag, *J. Chem. Phys.* **90**, 1299 (1989).
- [200] P. Čársky, H. L. Selzle, and E. W. Schlag, *Chem. Phys.* **125**, 166 (1988).
- [201] G. C. Bazan, J. W. J. Oldham, R. J. Lachicotte, S. Tretiak, V. Chernyak, and S. Mukamel, *J. Am. Chem. Soc.* **1**, 1 (1998).
- [202] W. J. Oldham, . Y.-J. M. Jr, R. Lachicotte, and G. C. Bazan, *J. Am. Chem. Soc.* **1**, 1 (1997).
- [203] S. Canuto and M. C. Zerner, *J. Am. Chem. Soc.* **112**, 2114 (1990).
- [204] S. Iwata, K. Fuke, M. Sasaki, S. Nagakura, T. Otsubo, and S. Misumi, *J. Mol. Spectr.* **46**, 1 (1973).
- [205] The term 'Davydov splitting' usually refers to the splitting of degenerate states in molecular aggregates and crystals in which intermolecular interactions are electrostatic, and are described by the Frenkel exciton Hamiltonian. In contrast, the coupling between electronic modes in dimers includes electrostatic as well as exchange interactions, which result in interchromophore electronic coherence. These may not be described by Frenkel exciton Hamiltonian.
- [206] B. I. Greene, R. M. Hochstrasser, and R. B. Weisman, *Chem. Phys.* **48**, 289 (1980).
- [207] S. Speiser, *Chem. Rev.* **96**, 1954 (1996).
- [208] J. O. Morley, *J. Chem. Soc. Perkins Trans.* **II**, 1351 (1987).
- [209] J. O. Morley and D. Pugh, *Spec. Publ. - R. Soc. Chem* **69**, 28 (1989).



- [210] J. O. Morley, *J. Chem. Soc. Faraday Trans.* **87**, 3009 (1991).
- [211] S. R. Marder, B. Kippelen, A. K.-Y. Jen, and N. Peyghambarian, *Nature* **388**, 845 (1997).
- [212] N. Matsuzawa and D. A. Dixon, *Int. J. Quantum Chemistry* **44**, 497 (1992).
- [213] G. M. Carter, J. V. Hryniewicz, M. Thakur, Y. Chen, and S. Meyler, *Appl. Phys. Lett.* **49**, 998 (1986).
- [214] J. M. Huxley, P. Mataloni, R. W. Schoenlein, J. G. Fujimoto, E. P. Ippen, , and G. M. Carter, *Appl. Phys. Lett.* **56**, 1600 (1990).
- [215] R. Kersting, U. Lemmer, R. F. Mahrt, K. Leo, H. Kurz, H. Bässler, and E. Göbel, *Phys. Rev. Lett.* **70**, 3820 (1993).
- [216] U. Lemmer, R. F. Mahrt, Y. Wada, A. Greiner, H. Bässler, and E. Göbel, *Chem. Phys. Lett.* **209**, 243 (1993).
- [217] R. Kersting, U. Lemmer, M. Deussen, H. J. Bakker, R. Mahrt, H. Kurz, V. I. Arckhipov, H. Bässler, and E. O. Göbel, *Phys. Rev. Lett.* **73**, 1440 (1994).
- [218] S. K. Ghoshal, P. Chopra, B. P. Singh, J. Swiatkiewicz, and P. Prasad, *J. Chem. Phys.* **90**, 5078 (1989).
- [219] M. Samoc and P. Prasad, *J. Chem. Phys.* **91**, 6643 (1989).
- [220] T. A. Pham, A. Daunois, J.-C. Merle, J. L. Moigne, and Y.-V. Bigot, *Phys. Rev. Lett.* **74**, 904 (1995).
- [221] T. Meier and S. Mukamel, *Phys. Rev. Lett.* **77**, 3471 (1996).

- [222] A. J. Heeger, S. Kivelson, J. Schrieffer, , and W.-P. Su, *Rev. Mod. Phys.* **60**, 781 (1988).
- [223] M. Wegener, D. S. Chemla, S. Schmitt-Rink, and W. Schäfer, *Phys. Rev. A* **42**, 5675 (1990).
- [224] S. Schmitt-Rink, S. Mukamel, K. Leo, J. Shah, and D. S. Chemla, *Phys. Rev. A* **44**, 2124 (1991).
- [225] M. Lindberg, R. Binder, and S. W. Koch, *Phys. Rev. A* **45**, 1865 (1992).
- [226] S. Weiss, M.-A. Mycek, J.-Y. Bigot, S. Schmitt-Rink, and D. Chemla, *Phys. Rev. Lett.* **69**, 2685 (1992).
- [227] D.-S. Kim, J. Shah, T. C. Damen, W. Schäfer, F. Jahnke, S. Schmitt-Rink, and K. Köhler, *Phys. Rev. Lett.* **69**, 2725 (1992).
- [228] K. Bott, O. Heller, D. Bennhardt, S. T. Cundiff, P. T. E. J. Mayer, G. O. Smith, R. Eccleston, J. Kuhl, and K. Ploog, *Phys. Rev. B* **49**, 7817 (1993).
- [229] E. J. Mayer *et al.*, *Phys. Rev. B* **50**, 14730 (1994).
- [230] J. A. Leegwater and S. Mukamel, *J. Chem. Phys.* **101**, 7388 (1994).
- [231] O. Kühn, V. Chernyak, and S. Mukamel, *J. Chem. Phys.* **105**, 8586 (1996).
- [232] G. Chen and S. Mukamel, *Chem. Phys. Lett.* **240**, 296 (1995).
- [233] D. S. Chemla, J.-Y. Bigot, M.-A. Mycek, S. Weiss, and W. Schäfer, *Phys. Rev. B* **50**, 8439 (1994).
- [234] L. Allen and J. H. Eberly, *Optical Resonances and Two-Level Atoms* (Wiley, New York, 1975).

- [235] T. Yajima and Y. Taira, *J. Phys. Soc. Jpn.* **47**, 1620 (1979).
- [236] The geometry optimization enters into the Hamiltonian by a term  $\frac{1}{2} \sum_n K(x_n - \bar{x})^2$ , where  $x_n$  is the  $n$ -th bond length, we have used a force constant of  $K = 21eV\text{\AA}$  ( $K = 38eV\text{\AA}$ ) for the Hückel (PPP) model and an equilibrium bond length of  $\bar{x} = 1.41\text{\AA}$  for both models, see Ref. [55].
- [237] W. Huhn and A. Stahl, *Phys. Status Solidi B* **124**, 167 (1984).
- [238] S. Schmitt-Rink, D. S. Chemla, and H. Haug, *Phys. Rev. B* **37**, 941 (1988).
- [239] M. Lindberg and S. W. Koch, *Phys. Rev. B* **38**, 3342 (1988).
- [240] F. Jahnke, M. Koch, T. Meier, J. Feldmann, W. Schäfer, P. Thomas, S. W. Koch, E. Göbel, and H. Nickel, *Phys. Rev. B* **50**, 8114 (1994).
- [241] J.-Y. Bigot, M.-A. Mycek, S. Weiss, R. G. Ulbrich, and D. S. Chemla, *Phys. Rev. Lett.* **70**, 3307 (1993).
- [242] Selected papers on coherence and fluctuations of light, with bibliography, 1970, edited by L. Mandel and E. Wolf, (Dover Publications),.
- [243] L. Cohen, *Proc. IEEE* **77**, 941 (1989).
- [244] W. E. Torruelas, D. Neher, R. Zandoni, G. I. Stegeman, and F. Kajzar, *Chem. Phys. Lett.* **175**, 11 (1990).
- [245] M. Cha, W. E. Torruelas, G. I. Stegeman, H. X. Wang, A. Takahashi, and S. Mukamel, *Chem. Phys. Lett.* **228**, 73 (1994).
- [246] M. Díaz-García, I. Ledoux, F. Fernández-Lázaro, A. Sastre, T. Torres, F. Agulló-López, and J. Zyss, *J. Phys. Chem.* **98**, 4495 (1994).

- [247] M. Díaz-García, I. Ledoux, F. Fernández-Lázaro, J. A. Duro, T. Torres, F. Agulló-López, and J. Zyss, *J. Phys. Chem.* **98**, 8761 (1994).
- [248] S. Mukamel and R. Loring, *J. Opt. Soc. B* **3**, 595 (1986).